DEVELOPING LATTICE-CONFINED CHEMISTRY: SYNTHESIS AND APPLICATION OF BINUCLEAR REACTION SITES

A Dissertation

by

CHEN-HAO WANG

Submitted to the Office of Graduate and Professional Studies of
Texas A&M University
in partial fulfillment of the requirements for the degree of

DOCTOR OF PHILOSOPHY

Chair of Committee,	David C. Powers
Committee Members,	François P. Gabbaï
	Michael B. Hall
	Michael Nippe
	Emily Pentzer
Head of Department,	Simon W. North

August 2020

Major Subject: Chemistry

ABSTRACT

The selective functionalization of simple hydrocarbons would provide opportunities to utilize currently-wasted hydrocarbon fractions as chemical fuels and chemical feedstocks. We are interested in lattice-confined chemistry which confines reactive species inaccessible in molecular analogs.

To this end, we demonstrate the use of ion metathesis chemistry to provide access to novel binuclear platforms to explore M–M cooperation in catalysis. We have utilized ion metathesis within pre-formed coordination polymers to prepare metastable $Pd_2(O_2CR)_4$ sites in which the confined Pd–Pd interaction is evidenced by its short bond distance. The demonstration of templated ion metathesis to generate specific metastable coordination sites that are inaccessible in solution phase chemistry represents a new opportunity to interrogate the chemistry of specific polynuclear metal aggregates. Nitrogen-atom transfer (NAT) from a lattice-confined Ru_2 nitride to toluene to generate benzylamine is realized. Analogous chemistry is unavailable at molecule site mimics since the side reactions take place when the reactive center in not confined. *In operando* analysis of intra- and intermolecular deuterium kinetic isotope effect (KIE) establishes the relative rates of substrate diffusion and interstitial chemistry. We utilize KIEs to directly evaluate the impact of material mesoporosity on substrate diffusion during catalysis. The use of KIEs as a tool enables the interrogation of substrate diffusion rate relative to the reaction rate during chemical reaction.

CONTRIBUTORS AND FUNDING SOURCES

Contributors

This work was supervised by a dissertation committee consisting of Professors David C. Powers, François P. Gabbaï, Michael B. Hall, and Michael Nippe of the Department of Chemistry and Professor Emily Pentzer of the Department of Materials Science and Engineering.

Yu-Sheng Chen acquired and analyzed single-crystal X-ray diffraction described in Chapter II. Qing Ma analyzed a portion of the extended X-ray absorption fine structures in Chapter II. Gregory S. Day carried out TGA-MS measurements in Chapter II. Nattamai Bhuvanesh carried out SQUID measurement of diruthenium complexes in Chapter III. Wen-Yang Gao carried out and analyzed the window size of porous materials in Chapter III. Anuvab Das carried out the synthesis and reactivity of molecular diruthenium complexes in Chapter III. Anuvab Das, Wen-Yang Gao, and Ian Riddington acquired and analyzed GC-MS experiments in Chapter III. Eric D. Bloch acquired toluene vapor adsorption isotherms in Chapter IV. Nattamai Bhuvanesh and Wen-Yang Gao carried out and analyzed crystallite size by PXRD line-shape analysis in Chapter IV. Guan-Wen Liu acquired and analyzed the SEM images described in Chapter IV. Je-Ruei Wen acquired and analyzed the TEM images described in Chapter IV. Thomas R. Cundari and Ahmad Najafian calculated and analyzed the potential energy surface of ruthenium complexes in Chapter IV. Doyong Kim, Yohannes H. Rezenom, and Bo Wang acquired ESI-MS data in Chapters III and IV. Elemental analyses were performed by Atlantic Microlab (Norcross, GA).

Funding Sources

This work was funded by Texas A&M University, the Welch Foundation (A-1907), and the U.S. Department of Energy (DOE), Office of Science, Office of Basic Energy Sciences, Catalysis Program under Award Number DE-SC0018977. Portions of this work were performed at the DuPont-Northwestern-Dow Collaborative Access Team (DND-CAT) located at Sector 5 of the Advanced Photon Source (APS). DND-CAT is supported by Northwestern University, E.I. DuPont de Nemours & Co., and The Dow Chemical Company. This research used resources of the Advanced Photon Source, a U.S. Department of Energy (DOE) Office of Science User Facility operated for the DOE Office of Science by Argonne National Laboratory under Contract No. DE-AC02-06CH11357. Single-crystal X-ray diffraction was collected at NSF's ChemMatCARS Sector 15 which is principally supported by the Divisions of Chemistry (CHE) and Materials Research (DMR), National Science Foundation, under grant number NSF/CHE-1346572.

TABLE OF CONTENTS

Page

LIST OF FIGURES

Page

LIST OF TABLES

Page

CHAPTER I

INTRODUCTION: LATTICE-CONFINED CHEMISTRY

I.1 Introduction

Enzymatic catalysts often accomplish challenging chemical transformations (*e.g.* formation of methanol from methane by selective C–H bond oxidation and formation of ammonia from dinitrogen by nitrogen fixation) with high reactivity and selectivity. Enzymatic catalysis involves substrate diffusion, substrate gating, protein dynamics, and substrate binding to a catalytically active site.[1,2] Confinement effects play an important role in enzymatic catalysis. For example, selective C–H bond oxidation to synthesize methanol from methane with incorporation of one oxygen atom from O_2 can be achieved by soluble monooxygenase (sMMO) and intermediate Q is the key reactive species. The structure of intermediate Q (**Figure I-1**) has been studied extensively and an $Fe_2^{IV}(\mu\text{-}O_2)$ diamond core structure has been proposed by using extended X-ray absorption fine structure and Mössbauer spectroscopy.[3] Clusters mimicking intermediate Q have been synthesized but none of them exhibits selective methane oxidation comparative to sMMO.[4-6] The selectivity for methanol over other oxidation products, such as formaldehyde or CO_2, has been attributed to enzyme-gated diffusion to and from the active

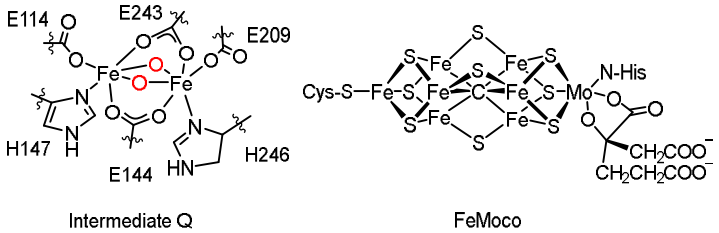

Figure I-1. Chemical structures of intermediate Q and FeMoco.

site.[7] Similarly, nitrogenases catalyze the formation of ammonia from dinitrogen. Nitrogenases can be classified into three known types based on the metal contents of their cofactors: MoFe, VFe, and FeFe proteins. The Mo-dependent nitrogenases, which have both higher reactivity for nitrogen reduction and require less ATP than the other three isozymes,[8] can be viewed as a [$MoFe_3S_3$] and an [Fe_4S_3] cluster bridged by three sulfides and an interstitial μ_6-carbide.[9,10] While the clusters featuring some aspects of FeMoco (**Figure I-1**) have been synthesized, none of them is active for N_2 reduction.[11-13] In addition, FeMoco extracted from MoFe protein by polar solvents also shows no dinitrogen reduction reactivity .[10,14] These examples highlight the significance of confinement effect in enzymes which is essential for high reactivity and selectivity during catalysis.

In the context of synthetic catalysis, confinement effects have been studied extensively in molecular cages,[15,16] carbon nanotubes (CNT),[17] two-dimensional materials,[18,19] and biological enzymes[20] as supports to encapsulate reactive centers and/or substrates. Confinement offers a variety of advantages, including enhancing the stability of the catalyst and high product selectivity. For example, confinement of the catalyst or intermediates during chemical reactions can enhance stability (*i.e.* the prevention of bimolecular side reactions) and thus prolong activity. Substrate confinement allows selective functionalization and also changes the transition states by varying the distance between reactants and reaction centers.[17] Confinement effect illustrates the increased reactivity due to proximity of substrates and reaction center when the pore size is optimal.[21]

One of the most important criteria to either confine a catalyst or a substrate is the pore size.[22-24] Pore size is a parameter which governs reactivity and selectivity for chemical reaction with diffusion limitation and confinement effect.[25] Diffusional limitations exclude substrates from accessing reaction sites and thus decrease overall reaction rates when the pore size is narrow (*i.e.* mass-transport controlled regime).

I.2 Confinement Effects

Substrate confinement is a strategy to increase the reaction rate and selectivity for chemical reactions. When a substrate enters a pore within a confined space, the environments around the substrate is different to the environment in the bulk solvent (**Figures I-2** and **I-3**). The substrate adopts conformational change to change its geometry

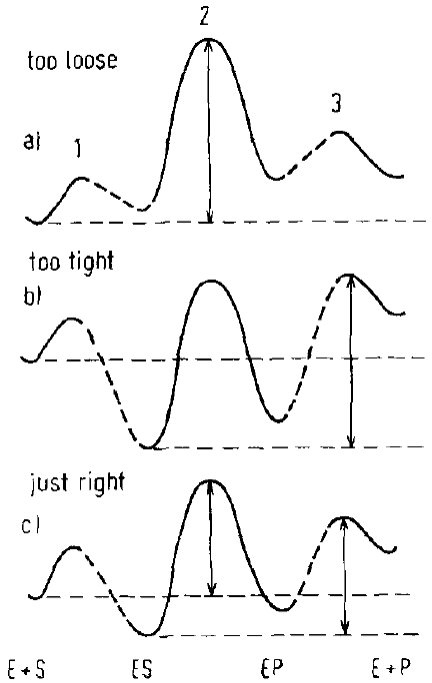

Figure I-2. Generic free energy profiles for reactions confined in enzymes. (a) The transition state 2 is high in a loose environment; (b) intermediate ES is too low in a tight environment; (c) optimal environment in which the activation energy is lowered. Reprinted from reference 29. Copyright 1977 Wiley-VCH Verlag GmbH & Co.

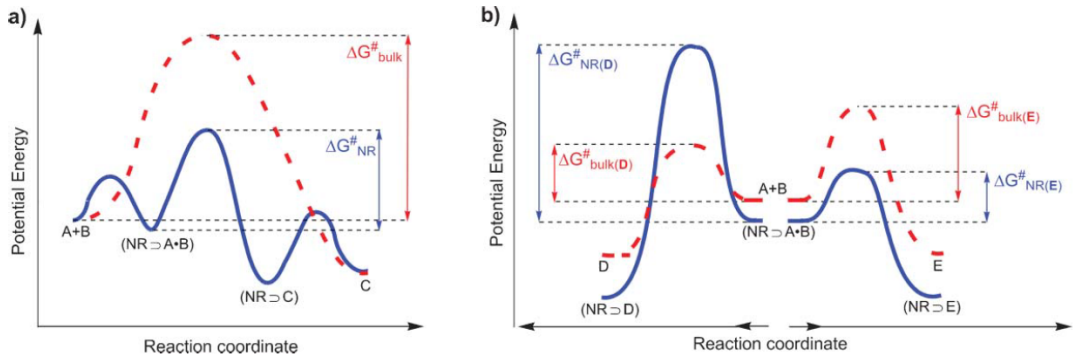

Figure I-3. The free energy profiles in bulk solution and confined molecular cage. (a) Simplified reaction profiles of a reaction in the bulk solution (dashed red line) and of a reaction within a molecular cage (nanoreactor in the graph) (blue line); (b) simplified reaction profiles of a reaction leading to product D which is destabilized by the nanoreactor (blue line) compared to the bulk solution (dashed red line), and of a reaction leading to product E which is stabilized by the nanoreactor (blue line) compared to the bulk solution (dashed red line). Reprinted from reference 27. Copyright 2008 The Royal Chemistry Society.

to fit in the confined space and its motion is limited in the pore, resulting in a decrease in entropy.[26] The limited orientation and the proximity to reaction center can render selectivity during catalysis.[27] The energy of the transition state varies depending on the confinement of the substrate.[28] In enzymes, the optimal cavity size leads to a low-energy transition state which kinetically favors the formation of product (**Figure I-2**).[29] In **Figure I-3a**, confinement provides access to new and stable transition states and thus lowers the activation energy required for the chemical reaction. **Figure I-3b** depicts the free energy profiles of a reaction involving reactants A + B and products D + E with (blue line) and without confinement (dashed red line). Product D is favored without confinement due to the lower activation energy. With confinement, the transition state to form product D is destabilized and the intermediate to form product E is stabilized, resulting in a different

selectivity. The concentration of substrate around the reaction center is increased by confinement and thus the rate of a non-zero-order reaction is expected to increase.

In order to achieve high reaction rate and selectivity comparable to enzymatic catalysis, significant effort has been exerted to harness confinement effects for inorganic and organometallic chemistry. Both of the solid- (*e.g.* metal-organic frameworks (MOFs)) and solution-state (*e.g.* molecular cages) compounds are candidates to accommodate these catalysts since the tunability of the pore size allows the development of an optimal cavity for a chemical reaction. The correlation between reactivity/selectivity and pore size is important for catalyst design. The use of molecular cages,[15,16] MOFs,[30] and mesoporous silicas[31] as platforms to explore the impact of confinement on catalysis will be introduced in the following sections. The impact of confinement on reactivity and selectivity will be discussed. Emphasis is given to examples disclosed in the last five years that have not been cited by the leading reviews.[15,16,30,31]

I.3 Molecular Cages

Confinement effects are encountered in the organometallic chemistry of cage compounds, which provide the opportunity for the activation energy of a reaction to be lowered by housing catalyst and substrate in a confined environment (**Figure I-3**).[27] Confining either substrates or a catalyst in a microenvironment requires ligand design (*e.g.* molecular cages) to house substrates and catalyst. There are different strategies to encapsulate a catalyst in a confined environment such as self-assembly by multi-dentate ligands, coordination chemistry by multi-dentate ligands, and transmetalation of a pre-formed structure.

Fujita and co-workers utilized coordination chemistry to synthesize an octahedral cage with Pd(II) (compound **I-1**) as catalysts on the nodes which catalyzed Diels-Alder reaction at the terminal anthracene ring in a high regioselectivity (**Figures I-4 and I-5**).[32] A control catalyst (compound **I-2**), in which confinement effects were removed, yielded typical Diels-Alder reaction on central anthracene ring under same condition. These

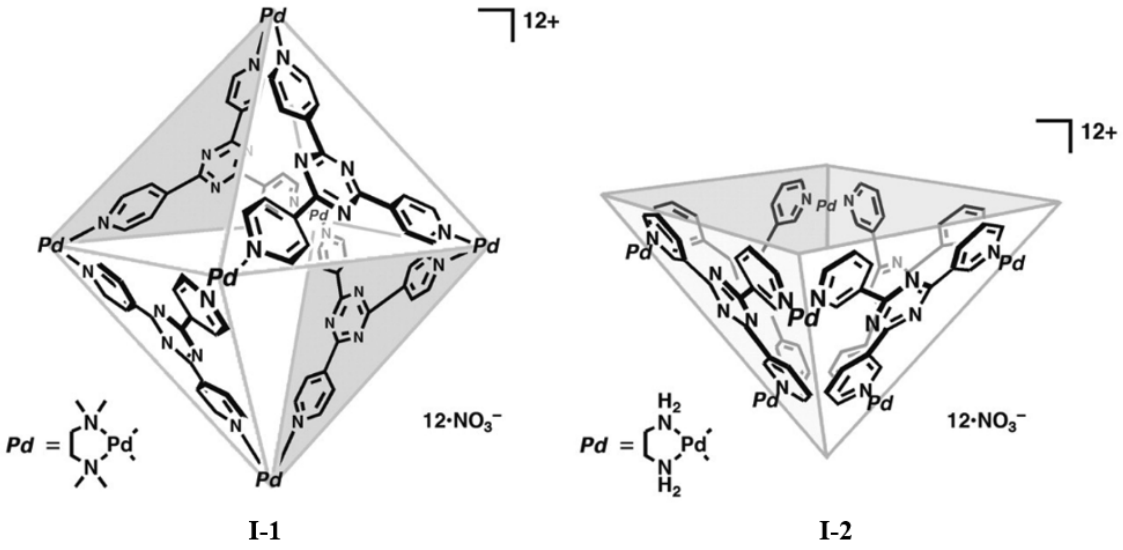

I-1 **I-2**

Figure I-4. Coordination complexes create a confined space. Reprinted from reference 32. Copyright 2006 American Association for the Advancement of Science.

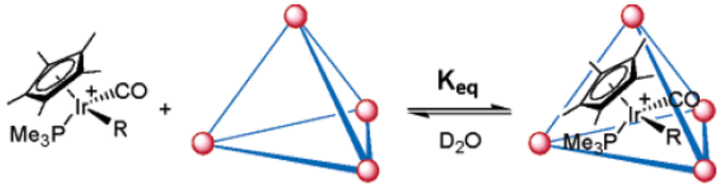

I-3 $Ga_4L_6^{12-}$

Figure I-5. Molecular cage as a confined space to encapsulate the catalyst. Reprinted from reference 34. Copyright 2006 American Chemical Society.

observations exemplify the substrate conformational change in transition state during catalysis in a confined environment. Molecular cages synthesized by supramolecular

assembly provide unique microenvironment and internal cavity to host both small substrates and catalytic metal centers.[33]

The Raymond tetrahedron has been studied extensively and its hydrophobicity and dodecanionic charge render it a soluble cage in polar solvents. This system has been applied to catalysis of a wide variety of reactions.[15,27,33] Raymond and co-workers utilized dodecanionic tetrahedral cage to confine the cationic metal complex. **Figure I-5** shows an example in which a half-sandwich iridium cationic complex (compound **3**) is confined within a $Ga_4L_6^{12-}$ (L = bis-bidentate catechol amide) cage for selective C–H bond activation.[34]

Of particular note for our purposes, the Raymond tetrahedron catalyzed three-component aza-Darzens reaction in basic aqueous solution (**Figure I-6**).[35] Solvent exclusion of the Raymond tetrahedron allowed the encapsulation of hydrolytically unstable iminium ions within the cage. Larger alkyl groups (*e.g.* propyl group) on the substrates inhibited product formation which suggested that the substrate encapsulation was essential for catalytic reaction (see **Figure I-7** for proposed reaction mechanism). Similar reaction in a bulk solvent yielded *cis*-isomers which was in contrast to the *trans*-isomers observed using molecular cage to confine the catalyst.

Transannular 1,5-hydride transfer in a bimolecular aza-Prins cyclization was also realized by confinement within **I-4** (**Figure I-8**). Kinetic studies and deuterium isotopic labeling experiment revealed that the rate-limiting step was the encapsulation of the transient iminium ion. The double bond of the encapsulated iminium ion preferred axial

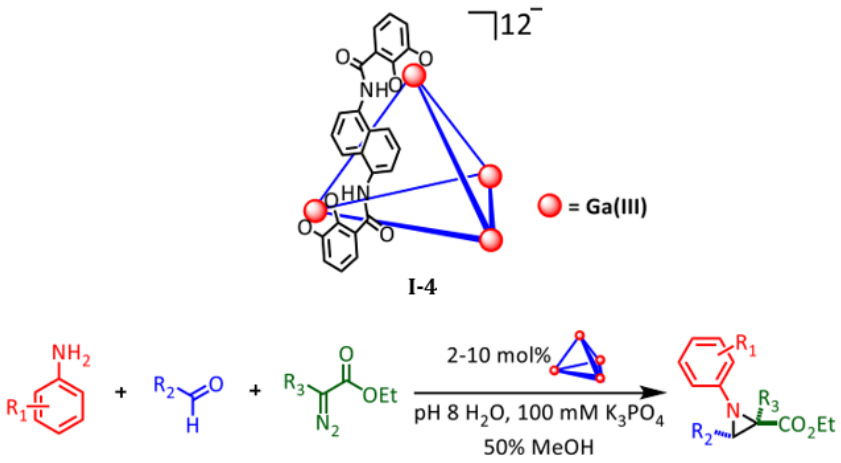

Figure I-6. The molecular cage and three-component aza-Darzens reaction. Reprinted from reference 35. Copyright 2020 American Chemical Society.

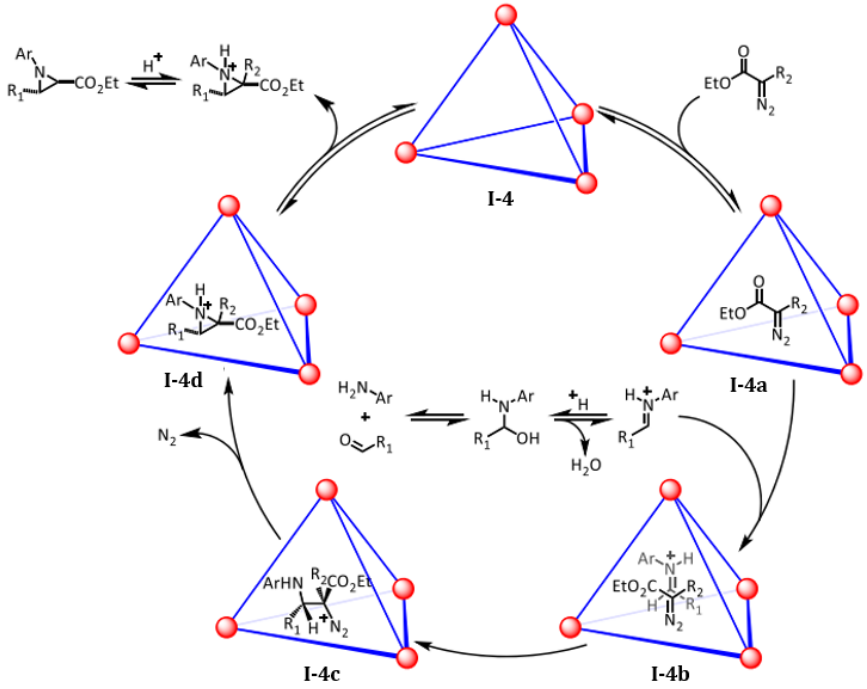

Figure I-7. Proposed mechanism for three-component aza-Darzens reaction catalyzed by the Raymond tetrahedron. Reprinted from reference 35. Copyright 2020 American Chemical Society.

orientation in the transition state which resulted in a product that was in contrast to that obtained in bulk solution. The temperature required for the reaction in a confined

environment (23 °C) was much lower than that of bulk solution (100 °C). Confinement restricted the geometry of the substrate during catalysis and it changed the stereoselectivity and reactivity.[36]

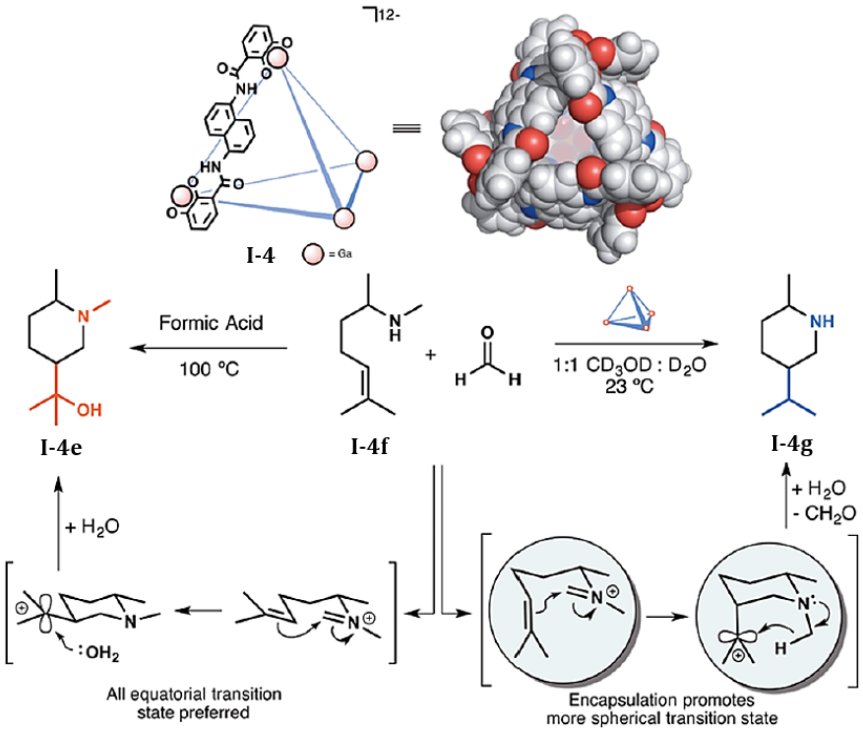

Figure I-8. Unusual selectivity of aza-Prins cyclization in a confined cage. Reprinted from reference 36. Copyright 2015 American Chemical Society.

The reactivity of metal complexes encapsulated within the Raymond tetrahedron was examined and shown to induced unusual confinement-induced reactivity.[37] Selective olefin hydrogenation was achieved by the encapsulation of a cationic Rh(I) complex in the Raymond tetrahedron (**Figure I-9**, compound **I-5**), which was not observed in the parent Rh(I) complex in bulk solution. The reported data evidenced that the rate of hydrogenation depended solely on the double bond encapsulated. The olefin coordinated to the Rh(I) complex inside the cage and the conformation of olefin in the cage was limited due to confinement, resulting in good regioselectivity (**Figure I-10**). Hydrogenation of

olefins catalyzed by Rh(I) complex in the cage yielded cis-alkanes. The microenvironment in the cage was relevant to the selectivity of hydrogenation. When a longer alkyne was mixed with a suitable alkene, Rh(I) in the cage selectively hydrogenated alkene despite

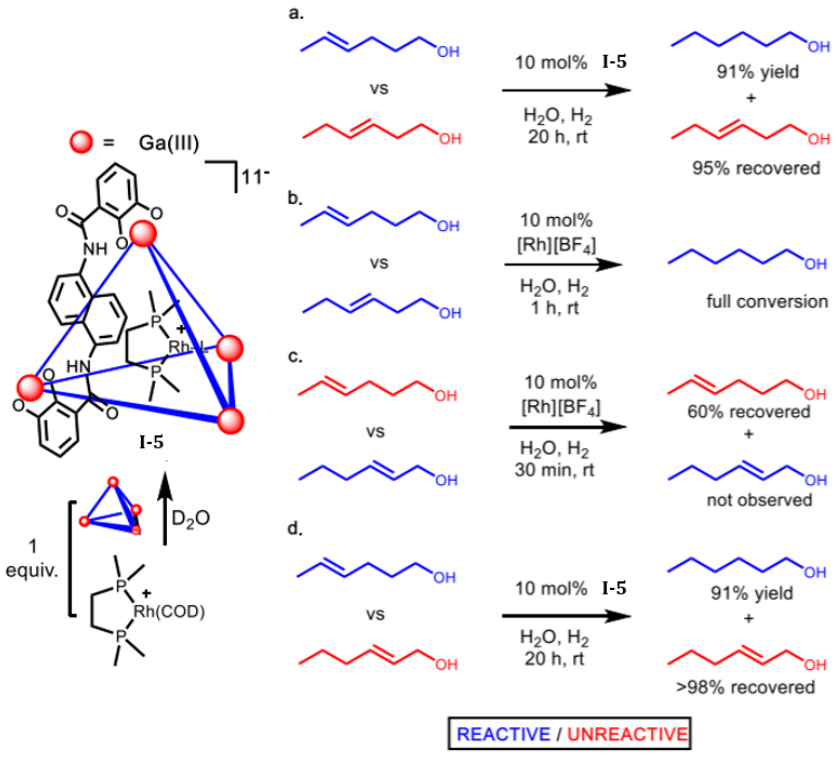

Figure I-9. Selective olefin hydrogenation by molecular cage. Reprinted from reference 37. Copyright 2019 American Chemical Society.

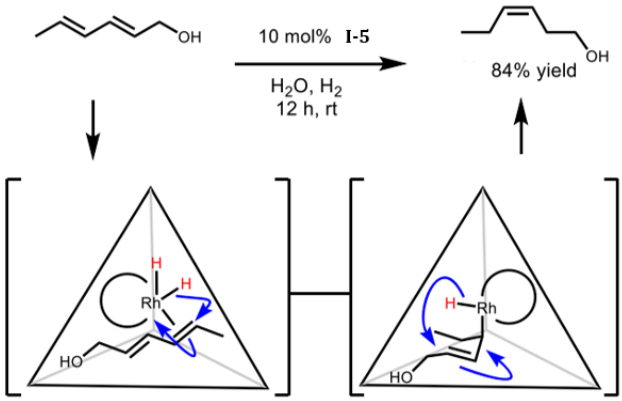

Figure I-10. Proposed mechanism for selective olefin hydrogenation. Reprinted from reference 37. Copyright 2019 American Chemical Society.

the fact that the alkyne was more reactive. The high size- and site- selectivity highlighted the role of substrate confinement during catalysis.

The impact of the cage charge was investigated by using Si(IV) as the nodes of the cage in place of Ga(III), which results in an octaanionic cage (compound **I-6**). The silicon-based tetrahedron was isostructural to Raymond tetrahedron. The reaction rate of silicon-containing tetrahedron (k_{Si}) was compared to that of Raymond tetrahedron (k_{Ga}) for aza-Cope rearrangement and Nazarov cyclization (**Figure I-11**).[38] In aza-Cope rearrangement, the formal charge of the substrate remained the same during the transition state so the rates for Ga- and Si-catalyzed reaction were similar. On the other hand, the formal charge for the intermediate in Nazarov cyclization increased by one (0 to +1) in the transition state. The inherent stabilization of the positive-charge intermediate by the Raymond tetrahedron resulted in a 680-fold increase in reaction rate.

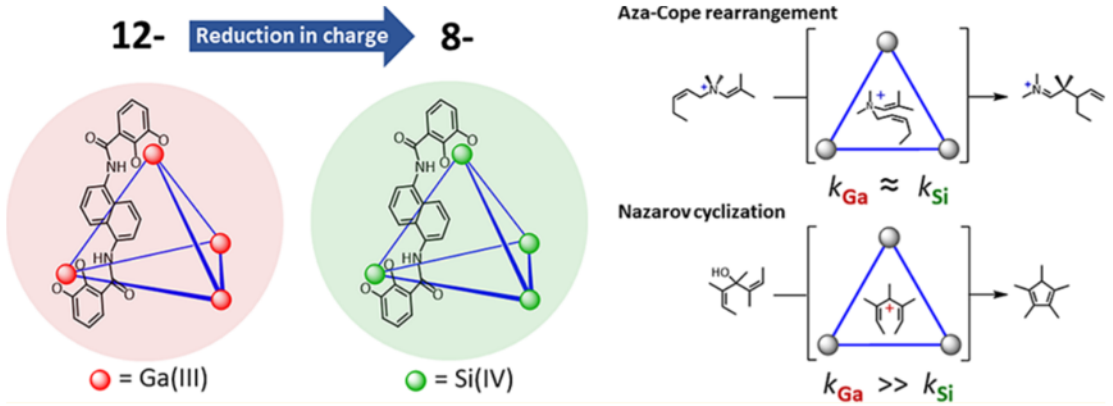

I-6

Figure I-11. Raymond tetrahedron and its octaanionic isostructure. The reduce of the negative charge largely retards the reaction in Nazarov cyclization in which a positive-charge intermediate is involved during catalysis. Reprinted from reference 38. Copyright 2018 American Chemical Society.

I.4 Selected Examples of Confinement on Catalysis with Metal-Organic Frameworks*

Metal-organic frameworks (MOFs) are porous materials comprised of polytopic organic ligands and metal-containing secondary building units.[39,40] In analogy to zeolitic catalysts, which are heterogeneous catalysts based on porous aluminosilicate materials commonly employed in large-scale catalytic applications,[41-43] the ability to generate single-site catalysts in MOFs has led to the development of MOF catalysts for a variety of commodity-scale chemical transformations. [44-50] In analogy to enzymatic catalysis, in which substrate confinement within enzyme active sites can alter the chemo- and stereoselectivity of substrate functionalization, the potential to systematically tune the topology and chemical functionality of molecular-scale pores within materials (*e.g.* MOFs) has inspired application of MOF catalysts to chemical transformations of relevance to fine chemicals.[51-54]

The relative abundance of interstitial sites may lead to the assumption that catalysis with highly porous MOF catalysts proceeds at the far more abundant interstitial sites. However, if substrate diffusion is slower than catalyst turnover, and the activity of interfacial and interstitial catalyst sites is similar, then the reaction will proceed at or near the surface of catalyst particles and very few interstitial catalyst sites will contribute to the observed catalysis (**Figure I-12a**).[55,56] In contrast, if diffusion is faster than catalyst turnover, most or all the catalytic active sites will participate in the observed catalysis

*Portions of the data, figures, and text in this chapter were adapted with permission from reference Gao, W.-Y.[+]; Cardenal, A. D.[+]; Wang, C.-H.; Powers, D. C. *Chem. Eur. J.* **2019**, *25*, 3465–3476, copyright 2019 Wiley-VCH Verlag GmbH & Co.

(**Figure I-12b**). The ability to access and utilize interstitial sites for substrate functionalization catalysis depends intimately on the relative rates of substrate functionalization and diffusion.

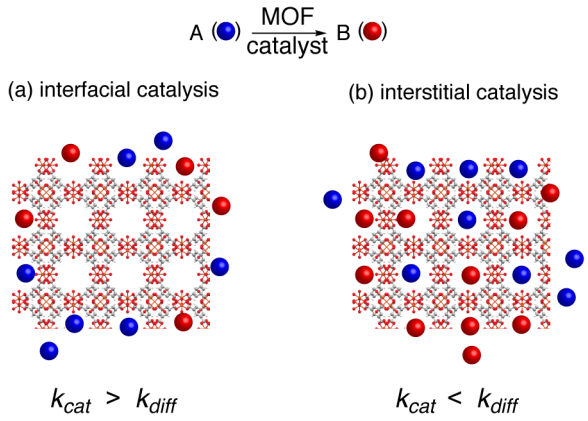

Figure I-12. Impact of relative rates of diffusion and catalyst turnover. The relative rates of substrate diffusion and catalyst turnover dictate the fraction of potential catalyst sites that are utilized in catalysis. (a) If diffusion is slower than catalyst turnover, only interfacial catalyst sites will participate in catalysis. (b) If diffusion is faster than catalyst turnover, interstitial catalyst sites will contribute to catalysis. Copyright 2019 Wiley-VCH Verlag GmbH & Co.

Molecular diffusivity (*i.e.* the diffusion coefficient) is a molecule-specific descriptor of the propensity of a given molecule to diffuse through a given medium.[57,58] Diffusivity depends on the mean-free-path of the diffusing species, which is the average distance a molecule travels between successive intermolecular collisions. In bulk, the mean-free-path of a diffusing molecule is limited by collisions with other molecules. In porous materials, the mean-free-path of a diffusing molecule is limited by collisions with other diffusing molecules as well as by collisions with the pore walls. The introduction of collisions between diffusing molecules and pore walls inherently depresses the diffusivity of molecules in porous materials relative to the bulk phase. The extent to which the

diffusivity is inhibited within a porous material is referred to as the degree of confinement.[59,60] Related concept, such as the tortuosity factor has been developed to describe the impact of pore confinement on diffusing small molecules in porous substrates.[61,62]

In porous materials, the substrate diffusion rate is critical to achieving interstitial catalysis. Experimentally, diffusional barriers can be interrogated by measuring reaction rate as a function of pore size. The diffusivity of small molecules in porous materials has received substantial attention, both from experimental and theoretical investigators.[60] Significant effort has been dedicated to developing experimental tools to quantify diffusion rates in porous materials.[63] Diffusion processes can be classified as either transport diffusion or self-diffusion. Transport diffusion is the net flux of molecules across a concentration gradient, such as the uptake of small-molecule sorbates into activated MOFs. Self-diffusion is the process by which molecules translate in space in the absence of a concentration gradient. An example of self-diffusion is the exchange of position between two sorbate molecules resulting from random Brownian motion. Broadly, the available experimental techniques to measure diffusivity can be categorized as non-equilibrium measurements, which probe transport diffusion—including spectroscopic methods,[64-67] gravimetric methods (gravimetric or quartz crystal microbalance),[68-71] zero-length column,[72,73] and coherent quasi-elastic neutron scattering (QENS)[74,75]—or equilibrium measurements, which evaluate self-diffusion—such as pulsed-field gradient (PFG) NMR,[76,77] incoherent QENS,[74] and other labeling experiments.[78,79] Depending on the length scale of diffusion that is probed by a given technique, experiments are further

classified as either macroscopic techniques (e.g., gravimetric methods and zero-length column), which evaluate diffusion over hundreds of micrometers,[80] or microscopic techniques (*e.g.* PFG NMR, QENS, interference microscopy, and IR microimaging), which typically evaluate diffusion over distances of a few micrometers or less.[81] Macroscopic techniques can probe both surface barriers and diffusional barriers within the pore, whereas microscopic experiments investigate a much smaller domain with focus on diffusion within the pore. Thus, unsurprisingly, discrepancies in diffusivities have been observed when rates derived from macroscopic and microscopic measurements are compared.[63]

Turnover frequency (TOF), representing intrinsic kinetic effect, is a key parameter to assess the performance of a catalyst and determine the diffusivity of the substrate. Turnover number (TON) is utilized to determine the longevity of the catalysis and a higher TON does not necessarily correlate to higher reactivity. Although TON is often found in the papers regarding solid-state catalysis, the use of TON as a proxy for TOF is not rigorously true to describe the efficacy of a catalyst. For example, Anwander and co-authors investigated the catalysis of the Meerwein–Ponndorf–Verley (MPV) reaction to reduce aromatic aldehydes to form alcohols by Lewis bases such as aluminum(III) alkoxides. Aluminum alkoxides were grafted to silicas with varying pore sizes and the conversions of reduction of benzaldehyde and 1-pyrenecarboxaldehyde were measured (**Figure 1-13**).[82] The parent material, $AlEt_x$@Aerosil 380, reduced both aldehydes in a similar rate, indicating that both of the substrates were not diffusional limited during the reaction (**Figure 1-13a**). When the pore size was decreased to 16 Å by using $AlEt_x$@SBA-

15, the conversion of 1-pyrenecarboxaldehyde decreased due to its larger size compared to that of benzaldehyde (**Figure 1-13b**). Longer alky chains were grafted to the silica by co-condensation reaction. The alky chains blocked the pores, resulting in smaller pore sizes. The difference of conversion between the two aldehydes was even greater when the pore size was further decreased to 14 Å by introducing a longer alkyl chain (**Figure 1-13c**). The material became non-porous when the alkyl chain was too long which blocked the pore and shut down the reactivity (**Figure 1-13d**).

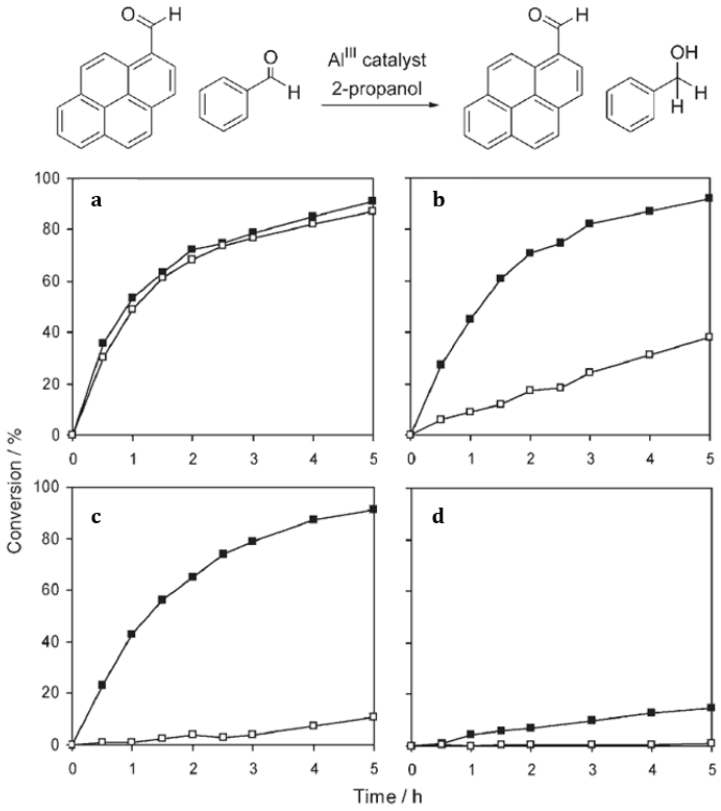

Figure I-13. Conversion of benzaldehyde (■) and 1-pyrenecarboxaldehyde (□) in MPV reductions over various Al(III) catalysts. (A) $AlEt_x$@Aerosil 380, (B) $AlEt_x$@SBA-1, (C) AlEtx@$SiMe_2C_8H_{17}$@SBA-1, (D) $AlEt_x$@$SiMe_2C_{18}H_{37}$@SBA-1. Reprinted from reference 82. Copyright 2007 Wiley-VCH Verlag GmbH & Co.

If diffusion is rate limiting, the concentration of product as a function of reaction time can be used as a probe to determine substrate diffusion rate. A higher conversion at a certain reaction time indicates that the substrate diffuses to and egresses from the reaction center with a lower diffusional barrier. Nitroaldol (Henry) reaction between 4-nitrobenzaldehyde and nitroalkanes could be catalyzed by Lewis base (**Figure I-14**).[83] A zinc paddlewheel MOF was synthesized and the axial position of zinc was coordinated by one of the N atom on DABCO. The free N atom on DABCO was a Lewis base which had affinity to coordinate Lewis-acidic substrates such as CO_2. Nitromethane (pK$_a$ = 10.24), nitroethane (pK$_a$ = 8.60), 2-nitropropane (pK$_a$ = 8.98), 1-nitropropane (pK$_a$ = 7.7-7.8), and nitrocyclohexane were chosen as substrates to systematically study the impact of substrate size on reactivity. The turnover numbers (TONs) were found to be 48.2, 20.5, 18.1, 11.4 and 7.2 for 120 h, respectively. Turnover frequency (TOF) which represents intrinsic

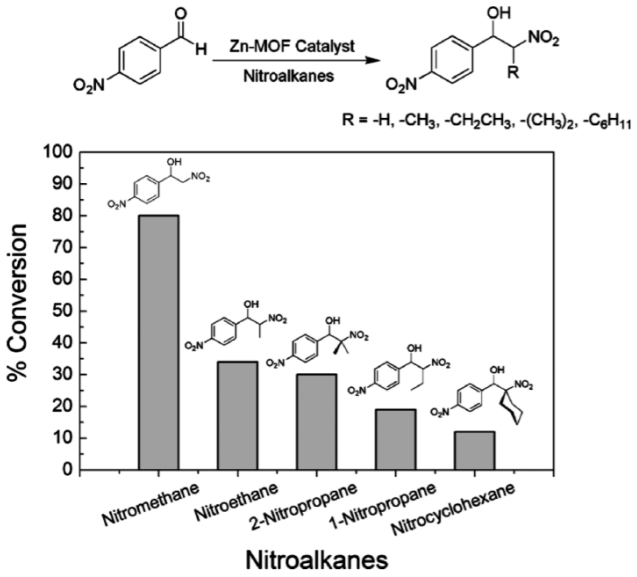

Figure I-14. Henry reaction with various nitroalkanes. The smaller nitroalkanes show better reactivity due to lower diffusional barrier. Reprinted from reference 83. Copyright 2011 Royal Society of Chemistry.

kinetic effect that we are interested in was not reported in the paper. The conversion for each substrate was 80%, 34%, 30%, 19% and 12%, respectively (**Figure I-14**). The TON and conversion decreased as the size of the nitroalkane decreased and both of the TON and conversion were not related to acidity. The decrease of TON and conversion was interpreted in the context of increased diffusional barrier as a function of substrate size.

The diffusion rate of the substrate depends on the size of the substrate which can be evidenced by the comparison of different substituents on the substrates and TOF. Knoevenagel condensation reaction was catalyzed by Lewis base.[84] Amino-functionalized MOF (UPC-30) was synthesized with a pore size of 16 Å and the Lewis acidic amino group catalyzes the Knoevenagel condensation reaction with various benzaldehydes and malanonitrile. By changing the size of the substituent on the substrate, the relationship between the substrate size and reaction yield can be investigated over a specific reaction time. Although TOF was not reported in this paper, the authors concluded that as the size of the substituent on benzaldehyde increased, the yields of the product decreased from 94.1% (R = Ph) to 0% (R = 4-PhPh) (**Table I-1**).

Table I-1. Knoevenagel Reactions Catalyzed by UPC-30. Copyright 2016 American Chemical Society.

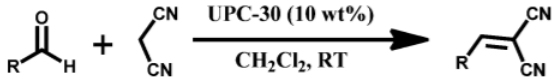

entry[a]	R	*t* (h)	yield (%)[b]
1	Ph	5	94.1
2	4-NO_2Ph	5	74.4
3	4-MePh	5	71.4
4	4-$C(CH_3)_3$Ph	5	21.5
5	1-naphthyl	5	18.9
6	4-FPh	5	18.4
7	4-PhOPh	5	16.6
8	4-MeOPh	5	5.1
9	4-PhPh	5	0

Studies on product distribution of a multi-step reaction gives insights into the mechanism. If diffusion is slower than other steps, the product distribution will depend on diffusion and the product distribution will be different compared to the diffusion-free reaction since a different equilibrium will be established based on diffusion rate. Studies of ruthenium-catalyzed ring-opening ring-closing metathesis (RO-RCM) of *cis*-cyclooctexne highlights this impact of confinement (**Figure I-15**). Monomers were polymerized to linear oligomers and linear polymers. The linear chains then underwent ring-closing metathesis to form cyclic oligomers. The distribution of products was monitored by GC as a function of conversion. For the homogeneous RO-RCM, the distribution of products as a function of conversion as well as selectivity was consistent with reported equilibrium distributions.[85] When the Grubb's catalyst was grafted on MCM-41, diffusion and confinement effect changed the equilibrium distribution. The selectivity for the liner polymer (**Figure I-16a**, red trace) was higher compared to that of the homogeneous reaction, indicating the oligomers slowly egressed from the pore and

thus they polymerized inside the pore. As reaction proceeded, they were converted to linear oligomers (**Figure I-16a**, green trace) and then cyclic oligomers by RO-RCM. The distribution of products of heterogenous reaction did not follow equilibrium distribution (**Figure I-16c**).

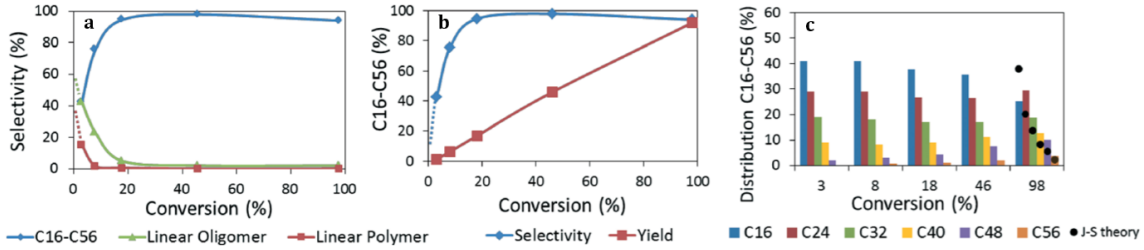

Figure I-15. Homogeneous RO-RCM of cis-cyclooctene. (A) Distribution of the cyclic oligomer/linear oligomer/linear polymer fraction as a function of conversion. (B) Yield and selectivity to C16–C56 with increasing conversion. (C) Distribution (wt%) of C16–C56 cyclic oligomers. Reprinted from reference 85. Copyright 2016 Royal Society of Chemistry.

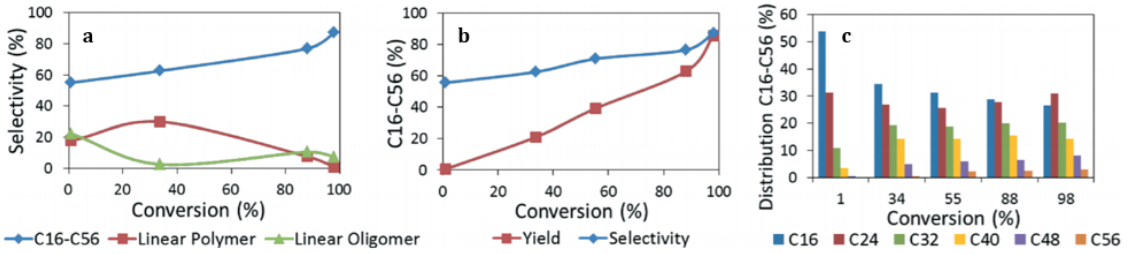

Figure I-16. Reaction profile of heterogeneous RO-RCM of cis-cyclooctene with HG2/MCM-41. (A) Distribution of the cyclic oligomer/linear oligomer/linear polymer fraction as a function of conversion. (B) Yield and selectivity to C16–C56 with increasing conversion. (C) Distribution of C16–C56 cyclic oligomers (wt%). Reprinted from reference 85. Copyright 2016 Royal Society of Chemistry.

I.5 Outlook

Analogous to enzymatic catalysis, confinement effect can be applied to organometallic and materials chemistry. Confinement of the metal center creates a microenvironment in which the metals are not proximal to on another, avoiding decomposition pathway (*i.e.*, bimolecular reaction to form stable and unreactive dimeric compound). Substrates in the confined space are not allowed to move freely and the change of the transition state of the intermediates during the catalysis leads to unusual reactivity or high chemoselectivity, which are found in various systems such as molecular cages and MOFs. The degree of the confinement can be controlled by the size of the cavity/pore by employing ligands or linkers with different lengths.

Diffusion is the key parameter in the confined system and understanding diffusion rate during reaction is important to catalysis. Relative substrate diffusion rate can be determined by the comparison of TOFs. The assessment of reactivity in materials chemistry is sometimes misleading in the literature. The use of TON as a surrogate for TOF to interrogate the reactivity of a catalyst is not always true since TON represents the longevity of a catalyst. Physical measurement of diffusion rate has been studied extensively but the measurement of diffusion during the reaction is lacking. *In operando* measurement evaluates substrate diffusion rate relative to the reaction rate and this information is meaningful to designing new catalyst systems. The development of confinement chemistry will contribute to both advancing the fundamental chemistry and chemical synthesis by catalysis.

CHAPTER II

TEMPLATING METASTABLE DIPALLADIUM CARBOXYLATE AGGRAGATES*

II.1 Introduction

Inspired by the facility of small molecular activation at multinuclear enzyme active sites[86-89] and the enhanced reactivity of high nuclearity defect sites in heterogeneous catalysts,[90,91] substantial effort has been directed towards developing multinuclear synthetic catalysts.[92-97] Leveraging the potential opportunities for chemical catalysis that arise from cooperative redox chemistry between transition metal ions (i.e. M–M cooperation) requires synthetic access to polynuclear aggregates that feature specific nuclearity and geometry that engender efficient metal–metal (M–M) cooperation.[98] Extant polynuclear catalysts are accessed by either (1) design and synthesis of multidentate ligands that enforce specific aggregation size and geometry,[99-104] or (2) by self-assembly of transition metal ions with simple bridging ligands. These strategies are inherently limiting with respect to the structures that can be evaluated as potential catalysts because (1) the ligands required to stabilize targeted complexes may not be compatible with catalytic applications (*i.e.* N–N coupling has been observed following oxidation in guanidinate-supported complexes[105]), and (2) the self-assembled structures may not give rise to the geometry required for efficient M–M interaction.

* Data, figures, and text in this chapter were adapted with permission from reference Wang, C.-H.; Gao, W.-Y; Ma, Q.; Powers, D. C. *Chem. Sci.* **2019**, *10,* 1823–1830, copyright 2019 the Royal Chemical Society.

In the context of developing new oxidation catalysts, we have become interested in controlling the aggregation state of transition metal ions in oxidatively resistant ligand scaffolds, such as all-oxygen fields (i.e. metal carboxylates). Examination of the self-assembled aggregates of metal carboxylates highlights both the diversity of aggregation sizes and geometries available to simple combinations of metals and ligands, and the challenge inherent in relying on self-assembled aggregates in catalysis. Rh(II) acetate self-assembles as a dimer (*i.e.* $Rh_2(OAc)_4$) due to the presence of a Rh–Rh bond (**Figure II-1a**).[106,107] The activity of $Rh_2(OAc)_4$ in carbene group transfer catalysis has been ascribed to M–M cooperation mediated through the M–M bond.[108] Isostructural complexes of Group 10 metals are unavailable: $Ni(OAc)_2$ is a solvated monomer under many conditions,[109,110] $Pd(OAc)_2$ is an acetate-bridged timer in both solution- and solid-state (*i.e.* $Pd_3(OAc)_6$),[111-117] (a polymeric crystal structure has also been reported,[118] but this structure has not been widely studied) and $Pt(OAc)_2$ is tetrameric (*i.e.* $Pt_4(OAc)_8$).[111,119] The self-assembled, thermodynamically preferred aggregates of these salts do not provide

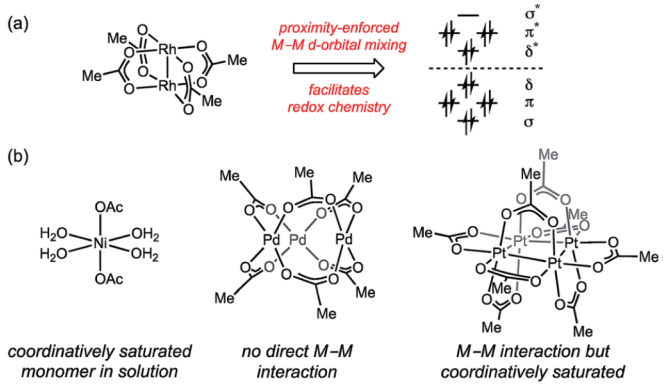

Figure II-1. Exapamles of metal aggregates. (a) $Rh_2(OAc)_4$ features a Rh–Rh single bond, which both enforces formation of a binuclear complex and mediates the redox cooperation between the metal centers responsible for M–M cooperation. (b) Group 10 metal acetates display a range of aggregation sizes and geometries, none of which supports both substrate binding and cooperative redox chemistry.

platforms that engender cooperative M–M interactions (**Figure II-1b**).

Pd_2 intermediates supported by oxygen-rich ligand environments have been proposed in electrochemical methane oxidation,[120] directed C–H oxidation chemistry,[121-126] and are of interest as models for PdO combustion catalysts.[127,128] **Figure II-2** illustrates the small family of acetate-rich Pd_2 aggregates that have been described. Stahl[129] and Sanford[130] have independently reported that pyridyl donors can support acetate-bridged complexes (**II-1–3**). Acetate-bridged cyclometallated complexes (*i.e.* **II-4**) have been observed during, and isolated from, directed C–H oxidation reactions.[121-126] $Pd_2(OAc)_2(acac)_2$ (**II-5**) has been obtained by treatment of $Pd_3(OAc)_5(NO_2)$ with acetylacetone (acac = acetylacetonate).[131] Related acetate-bridged Pd_2 species supported by γ-Keggin silicodecatungstate ligands have been characterized.[132] In the presence of

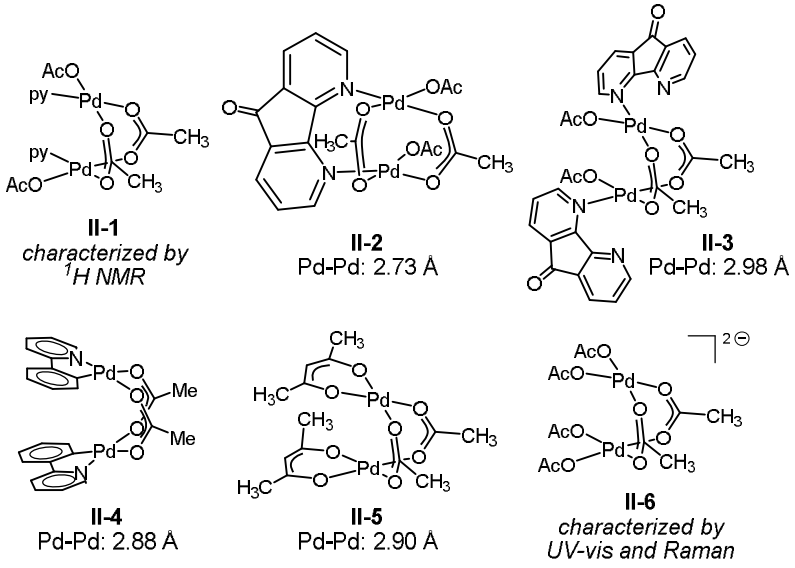

Figure II-2. Available oxygen-rich Pd_2 complexes. The structure of complex 1 was assigned by ^{1}H NMR spectroscopy. Complexes **II-2-5** have been characterized crystallographically and the structure of $[Pd_2(OAc)_6^{2-}]$ (**II-6**) has been proposed based on UV-vis and Raman spectroscopies.

exogenous acetate ion-conditions relevant to the Wacker-type conversion of ethylene to vinyl acetate-concentration-dependent Pd aggregation has been observed. At intermediate acetate concentration, the dimer $[Pd_2(OAc)_6^{2-}]$ (**II-6**) has been characterized by UV-vis and Raman spectroscopies; at high acetate concentrations, $[Pd(OAc)_4^{2-}]$ speciation has been suggested (see *II.5.5 Additional Data* for the attempts to isolation of $[Pd_2(OAc)_6^{2-}]$).[133,134] While $Pd_2(OAc)_4$ structures that are isostructural to $Rh_2(OAc)_4$ have been the subject of numerous theoretical investigations,[130,135-138] this aggregation mode has not been observed or characterized experimentally.

We are interested in Pd_2 tetracarboxylate sites as potential redox catalysts based on the dual hypotheses that d-orbital mixing will give rise to cooperative redox chemistry in these structures[98] and that the unavailability of $Pd_2(OAc)_4$ aggregates has prevented evaluation of the chemistry of this structural motif. Post-synthetic ion metathesis[47,139-142] in metal–organic frameworks (MOFs) — a process in which metal sites in a template porous lattice are exchanged with exogenous ions — has been demonstrated to be a method that can enable access to novel coordination geometries.[143-147] There are a limited number of examples of d^0 and d^{10} ions (*i.e.* Hf(IV)[148] and Cd(II)[149-151]) in the second and third row that have been demonstrated to participate in ion metathesis chemistry and ion metathesis chemistry has not been demonstrated for the introduction of 2nd- or 3rd-row transition metals. Here, we demonstrate that ion metathesis of binuclear transition metal sites in pre-formed porous crystalline materials provides a targeted strategy to rationally access Pd_2 sites that are metastable in solution-phase chemistry. The new Pd_2-based lattice is characterized by a combination of powder- (PXRD) and single-crystal X-ray diffraction

(SCXRD), X-ray absorption spectroscopy (X-ray absorption near edge structure (XANES) and extended X-ray absorption fine structure (EXAFS)), and gas adsorption analysis. We demonstrate that proximity-enforced Pd–Pd interaction gives rise to cooperative binding of substrates, such as CS_2, which is not observed for $Pd_3(OAc)_6$.

II.2 Results

II.2.1 Computational Evaluation of Pd Carboxylate Aggregation

We have evaluated the isodesmic aggregation equilibria illustrated in **Figure II-3**. Geometry optimizations were carried out with B3LYP functional[152-155] with LANL2TZ + f (1.472) basis set and corresponding ECP for Pd[156-158] and 6-31G(d) basis set for other atoms (coordinates of optimized structures are tabulated in **Tables II-10–13**).[159-161] Frequency calculations at this level of theory confirmed that optimized geometries represent ground state structures. Single-point energy calculations were carried out using the M06 functional[162] with sdd basis set for Pd[163,164] and the 6-311++G(d,p) basis set for light atoms.[165] Single-point solvation energies in acetonitrile were calculated using the SMD solvation model.[166] These methods reproduce available structural data for $Pd_3(OAc)_6$ and have been demonstrated to provide reliable energies for related Pd carboxylate systems.[136] Initial geometries for Pd_2 and Pd_4 aggregates were supplied as Pd substitution of known $Rh_2(OAc)_4$ and $Pt_4(OAc)_8$ structures, respectively.[106,119] The

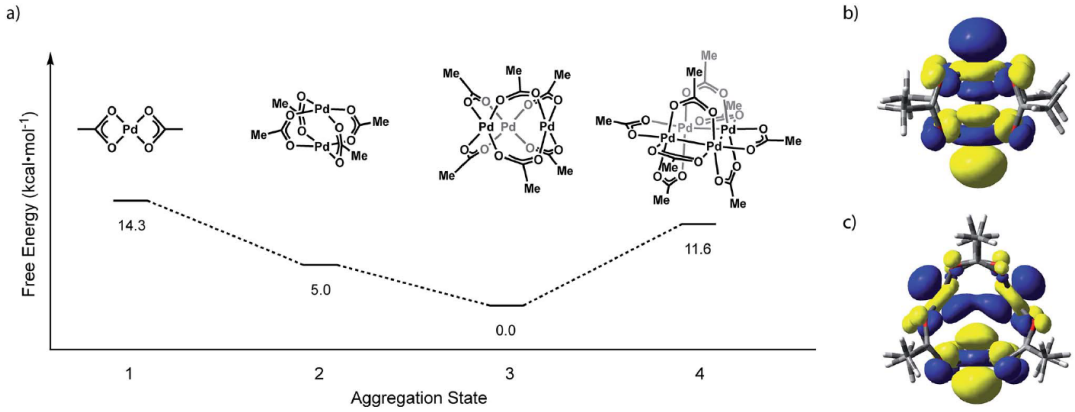

Figure II-3. Calculation of oxygen-rich Pd aggregates. (a) Plot of free energy versus aggregate size for the aggregation equilibria available to $Pd(OAc)_2$. Illustrations of the HOMO of (b) $Pd_2(OAc)_4$ and (c) $Pd_3(OAc)_6$.

geometry of $Pd_3(OAc)_6$ was based on its reported X-ray structure.[112] Consistent with solid-state and solution-phase measurements, these calculations indicate that trimeric $Pd_3(OAc)_6$ (Pd–Pd: 3.23 Å) is the thermodynamically preferred aggregate. $Pd_2(OAc)_4$ (Pd–Pd: 2.62 Å), the next-most stable aggregate, is +5.0 kcal·mol^{-1} relative to $Pd_3(OAc)_6$. The highest occupied molecular orbitals (HOMOs) of $Pd_2(OAc)_4$ and $Pd_3(OAc)_6$ are dominated by $4d_z^2$ contributions from each of the Pd centers (**Figures II-3b and c**). The σ* interaction highlighted in the HOMO of $Pd_2(OAc)_4$ aggregates are responsible for the relative instability of $Pd_2(O_2CR)_4$ sites and alleviation of these interactions drives the observed trimeric structure of Pd carboxylates.

II.2.2 Synthesis of Pd_2-Based Materials by Ion Exchange

We initiated our investigations of ion metathesis to generate metastable Pd_2 aggregates using M_3btc_2 (btc = 1,3,5-benzenetricarboxylate) networks because (1) these networks feature carboxylate-bridged binuclear sites, (2) a variety of metal ions have been demonstrated to give rise to isostructural networks,[167]and (3) we have an ongoing interest in the group-transfer chemistry of M_2 sites housed in this class of materials.[168,169] We specifically identified Zn_3- and Cu_3btc_2 networks based on the similarity of the ionic radii of Zn, Cu, and Pd within carboxylate ligand frameworks.[170,171] Molecular heterobimetallic complexes $PdZn(OAc)_4·H_2O$ and $PdCu(OAc)_4·H_2O$ are known,[172] and the Pd–O distances in these structures are well matched: Pd–O for $PdZn(OAc)_4·H_2O$ = 2.007 Å, Pd–O for $PdCu(OAc)_4·H_2O$ = 2.000 Å, Cu–O = 1.997 Å, and Zn–O = 2.057 Å.

Ion metathesis experiments were carried out by soaking preformed template lattices in solutions containing Pd(II) sources. The soaking solution was refreshed weekly. The extent of ion exchange was evaluated by inductively coupled plasma-mass spectrometry (ICP-MS) analysis of solutions prepared by exhaustively washing exchanged materials with both the solvent used in the soaking experiment and MeCN followed by digestion of the solid material with aqueous HNO_3 (experiments in which substantial Pd(0) formation was observed, either visually or by the diagnostic PXRD signal at ~40° were not included). We initiated our experiments by examining potential ion exchange chemistry into Cu_3btc_2. We examined a variety of Pd sources ($Pd(OAc)_2$, $Pd(O_2CCF_3)_2$, $PdCl_2$, and $[Pd(CH_3CN)_4][BF_4]_2$) in a series of reaction solvents ($CHCl_3$, CH_3CN, MeOH, EtOH, and DMF) between 23–80 °C. Under no condition were we able to detect substantial Pd(II) incorporation into the Cu-based network (<1% exchange; these experiments are summarized in **Table II-1**).[170,171] Based on the demonstration that Zn sites can be fluxional in the Zn_4O nodes of MOF-5,[173] we turned our attention to exchange experiments with Zn_3btc_2. Treatment of Zn_3btc_2 with $CHCl_3$ solutions of $Pd_3(OAc)_6$ for 20 d results in ~35% exchange of Zn for Pd. While further soaking with Pd^{2+} solutions did not result in increased Pd incorporation, the partially exchanged material was isomorphous with Zn_3btc_2 (for PXRD, see **Figure II-4a**) which indicated the viability of Pd exchange into lattice sites of M_2-based materials. **Figure II-4b** compares the PXRD patterns obtained for Zn_3btc and Pd-exchanged btc-based networks with the PXRD pattern that would be following network reorganization accommodate trigonal prismatic nodes (*i.e.*

Table II-1 Examination of cation metathesis in btc-supported networks

Template Network	Pd Source	Temp / °C	Solvent	Result
Zn_3btc_2	$Pd(O_2CCF_3)_2$	23	$CHCl_3$	Pd black after 5 d
Zn_3btc_2	$Pd(OAc)_2$	55	$CHCl_3$	Pd black after 2 d
Zn_3btc_2	$Pd(OAc)_2$	80	MeCN	Pd black after 1 d
Zn_3btc_2	$PdCl_2$	80	MeCN	Pd black after 1 d
Zn_3btc_2	$Pd(O_2CCF_3)_2(DMSO)_2$	23	$CHCl_3$	Pd black after 3 d
Zn_3btc_2	$[Pd(MeCN)_4][(BF_4)_2]$	23	$CHCl_3$	Pd black after 4 d
Zn_3btc_2	$Pd(OAc)_2$	23	$CHCl_3$	35% exchange after 20 d
Cu_3btc_2	$Pd(OAc)_2$	23	$CHCl_3$	<1% exchange after 150 d
Cu_3btc_2	$Pd(OAc)_2$	23	MeOH	Pd black after 3 h
Cu_3btc_2	$Pd(OAc)_2$	23	EtOH	Pd black after 3 h
Cu_3btc_2	$Pd(OAc)_2$	23	DMF	Pd black after 5 h
Cu_3btc_2	$Pd(OAc)_2$	75	DMF	Pd black after 1 h
Cu_3btc_2	$Pd(OAc)_2$	80	MeCN	Pd black after 2 d
Cu_3btc_2	$PdCl_2$	23	MeOH	Pd black after 5 h
Cu_3btc_2	$PdCl_2$	23	EtOH	Pd black after 7 h
Cu_3btc_2	$PdCl_2$	23	DMF	Pd black after 7 h
Cu_3btc_2	$PdCl_2$	75	DMF	Pd black after 1 h
Cu_3btc_2	$Pd(O_2CCF_3)_2$	23	$CHCl_3$	Pd black after 5 d
Cu_3btc_2	$Pd(OAc)_2$	55	$CHCl_3$	Pd black after 2 d
Cu_3btc_2	$Pd(OAc)_2$	80	MeCN	Pd black after 1 d
Cu_3btc_2	$PdCl_2$	80	MeCN	Pd black after 1 d
Cu_3btc_2	$Pd(O_2CCF_3)_2(DMSO)_2$	23	$CHCl_3$	Pd black after 3 d
Cu_3btc_2	$[Pd(MeCN)_4][(BF_4)_2]$	23	$CHCl_3$	Pd black after 4 d

analogous to the structure of $Pd_3(OAc)_6$), and demonstrates that the extended M_2-based lattice is not changed upon ion metathesis. To access materials with greater Pd incorporation, we examined the ion metathesis chemistry of other Zn_2-based porous materials (data summarized in **Tables II-2 and II-3**).

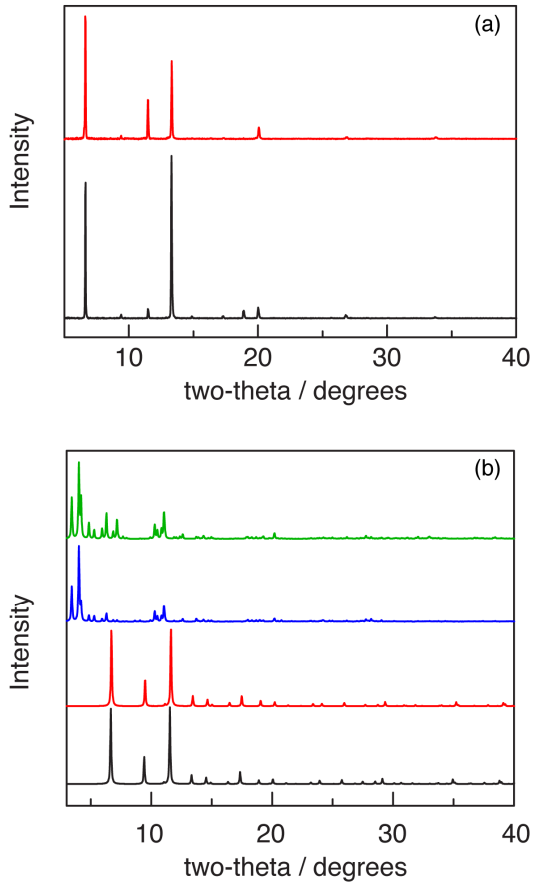

Figure II-4. PXRD patterns for btc-MOFs. (a) PXRD patterns for Zn_3btc_2 (—) and for Pd-exchanged material (—). (b) Simulated PXRD of Pd substituted MIL-101 structure (trigonal prismatic Pd_3 nodes, —), simulated PXRD of MIL-100 ($Cr_3(btc)_2$, —), simulated PXRD of $Cu_3(btc)_2$ (—), and simulated PXRD of $Zn_3(btc)_2$ (—).

Table II-2 Examination of cation metathesis in other networks

Template Network	Pd Source	Temp / °C	Solvent	Result
Zn_3abtc (**II-S8**)	$Pd(OAc)_2$	23	$CHCl_3$	54 % 161 d
II-S9	$Pd(OAc)_2$	23	$CHCl_3$	46 % 161 d
II-S10	$Pd(OAc)_2$	23	$CHCl_3$	29 % 161 d

Table II-3 Examination of cation metathesis in btei-supported networks

Template Network	Pd Source	Temp / °C	Solvent	Result
Zn_3btei (crystalline)	$Pd(O_2CCF_3)_2$	23	$CHCl_3$	Pd black after 5 d
Zn_3btei (microcrystalline)	$Pd(O_2CCF_3)_2$	23	$CHCl_3$	Pd black after 5 d
Cu_3btei	$Pd(OAc)_2$	23	$CHCl_3$	20% exchange after 56 d

Large families of metal–organic frameworks are available in which carboxylate linkers support the targeted M_2 coordination sites, and the extent of ion exchange has previously been reported to correlate with linker flexibility.[144] Among the Zn-based porous frameworks that were investigated, Zn_3btei (btei = 5,5',5''-(benzene-1,3,5-triyltris(ethyne-2,1-diyl))triisophthalate)[174,175] was identified as participating in the most efficient ion metathesis chemistry, affording 79% Pd exchange after 112 d (**Figure II-5a**, black trace). The Pd-exchanged material is isomorphous to Zn_3btei based on powder X-ray diffraction analysis (**Figure II-5b**). Soaking the exchanged materials in $CHCl_3$ for 14 days resulted in no Pd leaching (ICP-MS analysis). Consistent with our observations with Zn_3btc_3 and Cu_3btc_2, as well as observations of others regarding the relative facility of ion metathesis of Cu and Zn sites,[144] exchange into Cu_3btei afforded 20% exchange after 56 d. Ion metathesis of Pd^{2+} into Zn_3btei is reversible. Exposure of the Pd-exchanged material to CH_3CN solutions of $Zn(NO_3)_2$ led to the back exchange to regenerate Zn_3btei (**Figure II-5b**).

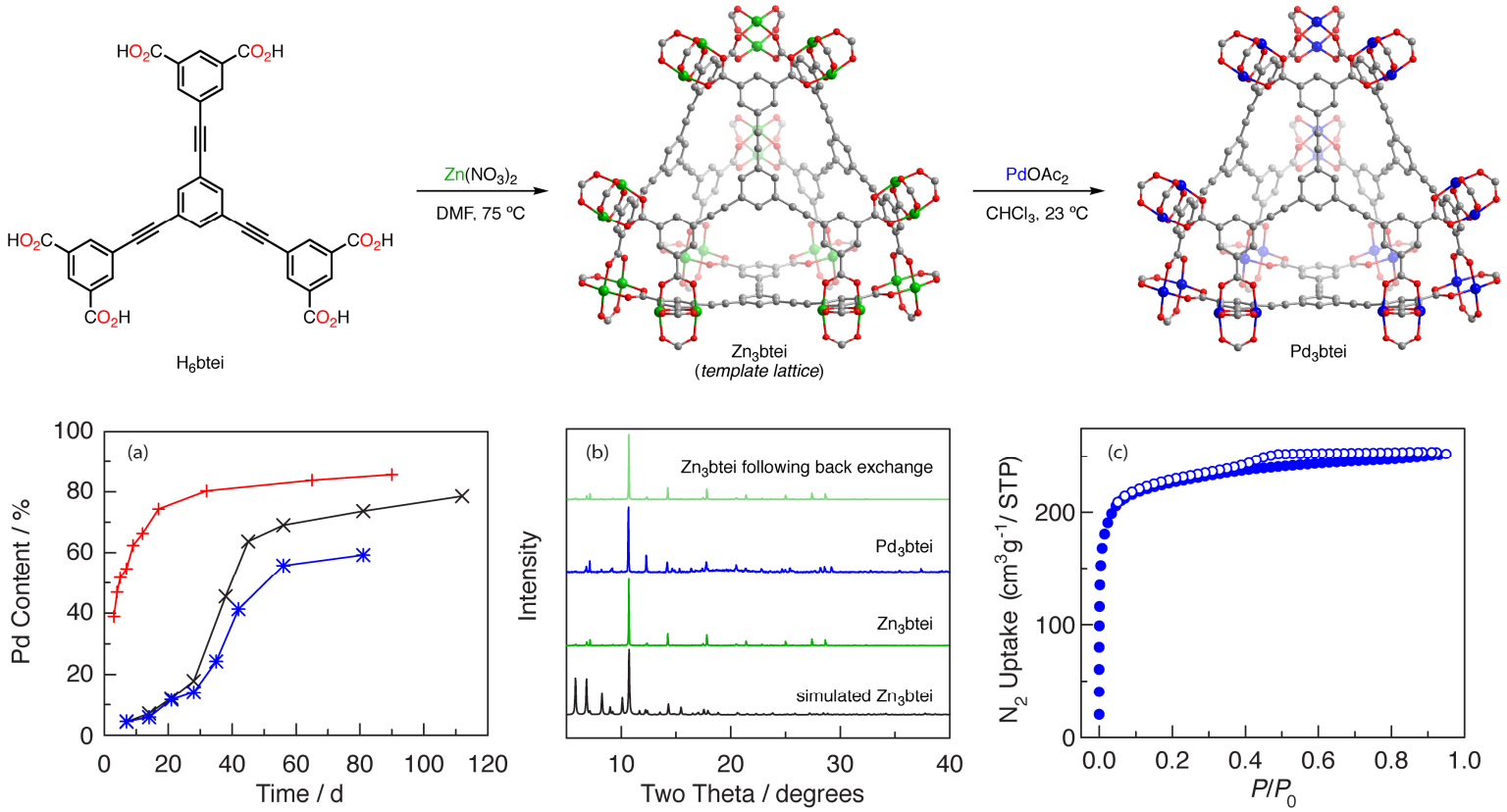

Figure II-5. Synthesis of Zn_3btei and ion exchange with Pd(II) to generate Pd_3btei. (a) Plot of Pd incorporation into Zn_3btei as a function of time. Data plotted for soaking into a microcrystalline powder of Zn_3btei (—), crystalline Zn_3btei (—), and Zn_3btei that was solvent-activated with $CHCl_3$ (—). (b) From bottom to top: simulated PXRD of Zn_3btei, experimental PXRD of as synthesized Zn_3btei, experimental PXRD of Pd_3btei, and PXRD of Zn_3btei obtained by back exchange of Pd_3btei with Zn(II). (c) N_2 adsorption isotherm of Pd_3btei (adsorption (●), desorption (○)) obtained at 77 K.

II.2.3 Impact of solvation on ion metathesis

Ion metathesis reactions are often stymied by slow exchange kinetics.[142] We were intrigued by the observed (and reproducible) sigmoidal exchange profile pictured in **Figure II-5a**. **Figure II-5a** illustrates that exchange is slow for the first ~30 days, after which point substantially more rapid Pd incorporation is observed. The sigmoidal kinetics behavior is not related to sample morphology: two preparations, one using $Zn(NO_3)_2$ and the other based on $ZnBr_2$, have been reported and afford Zn_3btei as either a microcrystalline powder or as single crystals.[174,175] Examination of these two samples resulted in similar exchange vs. time plots (**Figure II-5a**, black vs. blue traces).

The IR spectrum of as-synthesized Zn_3btei displays a stretching frequency at 1650 cm^{-1}, which has been assigned as Zn-bound DMF ligands (**Figure II-6**).[170,171,176] As exchange chemistry is carried out in $CHCl_3$, the intensity of this feature diminishes over the course of ~30 days. Thermogravimetric analysis-mass spectrometry (TGA-MS) analysis of samples obtained following exposure to $CHCl_3$ for varying lengths of time

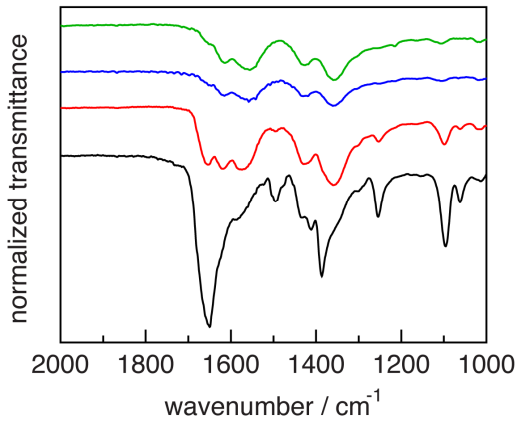

Figure II-6. IR spectra. IR spectra of Zn_3btei in DMF (—), Zn_3btei in $CHCl_3$ for 1 hour (—), Zn_3btei in $CHCl_3$ for 1 day (—), and Zn_3btei in $CHCl_3$ for 3 days (—).

confirms that concurrent with the disappearance of the carbonyl stretching mode from the IR spectrum, DMF solvent is removed from the Zn material; after 27 days of soaking, DMF is no longer observed (**Figure II-7**). Similar activation of metal sites by chlorinated solvents has been observed by treating DMF-solvated Cu_3btc_2 with CH_2Cl_2.[177]

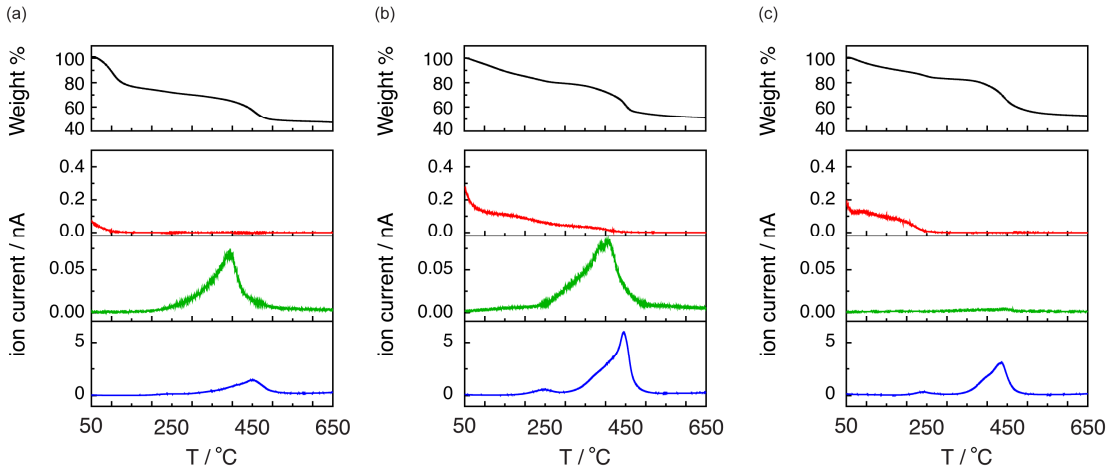

Figure II-7. TGA-MS data. TGA-MS spectra (—) of Zn_3btei exchanged in $CHCl_3$ for (a) 1 h; (b) 1 d; and (c) 28 d. Mass loss was attributed to $CHCl_3$ (—), DMF (—), and CO_2 (—).

We hypothesized that the DMF ligated Zn sites that are present in as-synthesized Zn_3btei participate in exchange more slowly than sites with weak donors, such as $CHCl_3$, that are generated by solvent activation of Zn_3btei. To interrogate this hypothesis, we soaked a sample of Zn_3btei in $CHCl_3$ for 30 days, after which time we exposed the solvent-activated sample to Pd(II) sources (**Figure II-4a**, red trace). In this exchange reaction, no induction period for Zn-to-Pd exchange is observed and 86% Pd incorporation is achieved after 90 days (**Figure II-7a**). Using solvent-exchanged materials, the rate of Pd incorporation is dependent on the Pd salt used for exchange. For example, ion exchange with $Pd(NO_3)_2$ is much faster than with $Pd(OAc)_2$ (88% incorporation is observed after 10

days, **Figure II-8b**). The faster uptake is associated with a loss of material crystallinity (see additional data, **Figure II-21**) so in subsequent experiments we have utilized Pd_3btei prepared from exchange with $Pd(OAc)_2$.

II.2.4 Gas Adsorption

Zn_3btei has been reported to be a non-porous material, which has been attributed to network collapse upon desolvation;[174,175] see **Figure II-9** for gas adsorption analysis of Zn_3btei. The N_2-adsorption isotherm obtained for a sample of Pd_3btei activated under the same conditions used for Zn_3btei (evacuation at 23 °C, see **Figure II-9** for other activation protocols) provided a BET surface area of 857 m^2 g^{-1} (a Langmuir surface area of 991 m^2 g^{-1}; **Figure II-9**). While substantially higher than the surface area measured for Zn_3btei, the BET surface area of Pd_3btei is less than that of the isostructural Cu_3btei material (reported BET surface area of 3730 m^2 g^{-1};[174] theoretical surface area is 3677 m^2 g^{-1}, see *experimental details* for the details of calculation).

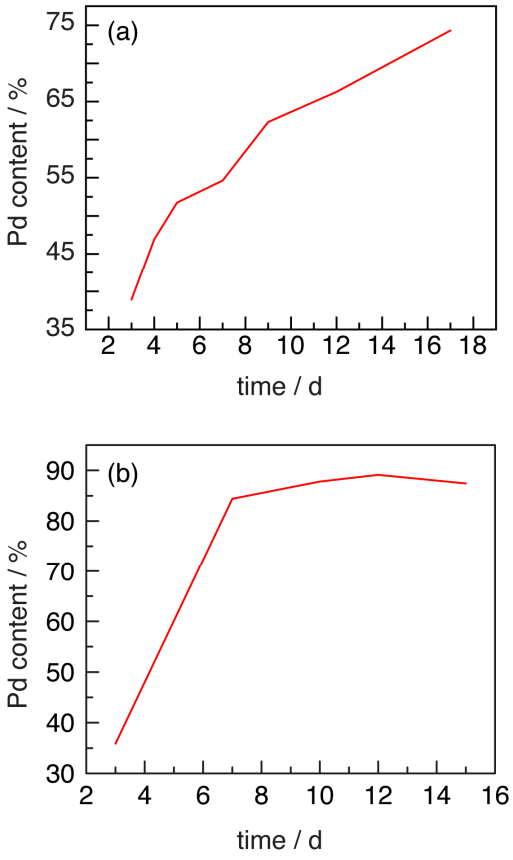

Figure II-8. Exchange rate profile and PXRD after Pd(II) exchange. (a) Plot of $Pd(OAc)_2$ exchange into Zn_3btei that was pre-soaked in $CHCl_3$ for 28 d. (b) Plot of $Pd(NO_3)_2$ exchange into Zn_3btei that was pre-soaked in $CHCl_3$ for 28 d. (c) PXRD pattern of material obtained following $Pd(NO_3)_2$ exchange with Zn_3btei.

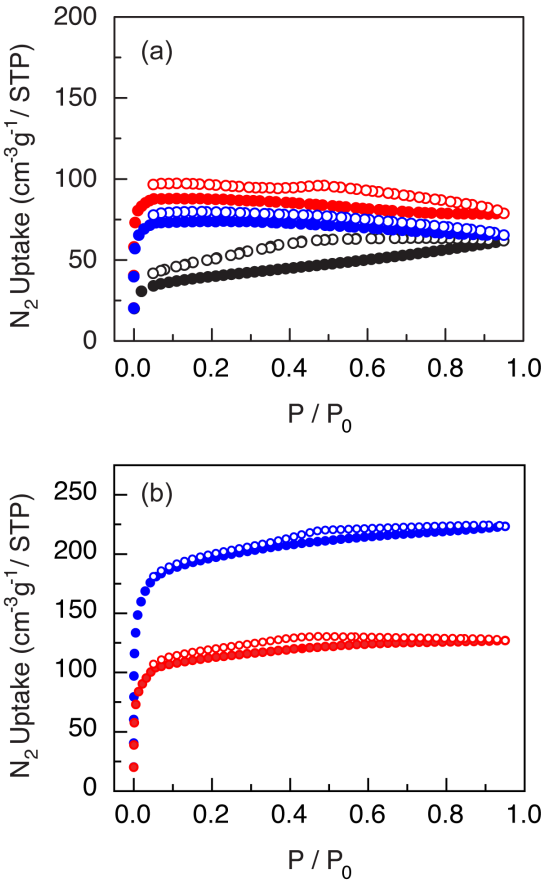

Figure II-9. N_2 adsorption isotherms for Zn_3btei and Pd_3btei at different conditions. Supercritical CO_2 activation and heating (45 °C) were incapable of access higher gas uptake capacity. N_2 adsorption isotherms collected at 77 K (a) for Zn_3btei that was activated by vacuum twice at 23 °C (adsorption (●;●), desorption (○;○)) and by supercritical CO_2 (adsorption (●), desorption (○)); (b) for Pd_3btei that was activated at 45 °C for 16 h (absorption (●), desorption (○)); and, for Pd_3btei that was activated by supercritical CO_2 (absorption (●), desorption (○)).

Table II-4 Surface areas for Zn_3btei and Pd_3btei at different conditions

Samples	BET surface area (m^2/g)	Langmuir surface area (m^2/g)
Zn_3btei/23 °C-1	348	386
Zn_3btei/23 °C-2	N/A	175
Zn_3btei/supercritical CO_2	290	325
Pd_3btei/45 °C	741	858
Pd_3btei/supercritical CO_2	425	493

II.2.5 Single-Crystal X-ray Diffraction

Zn_3btei (**rht**-topology) crystallizes in the *F*m-3m space group and the asymmetric unit contains two Zn ions.[174,175] We have examined a single crystal that was isolated following partial Pd exchange (the Pd content of the sample from which the crystal was isolated was 49% (ICP-MS); crystallography details are compiled in **Table II-14**). Refinement of metal site occupancy in this partially exchanged crystal indicated exchange of one of the symmetry inequivalent Zn sites: Zn(1) has not undergone any exchange while Zn(2) has been ~40% exchanged. Concurrent with exchange, the occupancy of the apical ligand associated with the site undergoing exchange decreases. This observation is consistent with five-coordinate Zn(II) ions being replaced by four-coordinate, square planar Pd(II) ions. While PXRD measurements of fully exchange Pd_3btei indicated that bulk crystallinity is maintained during exchange, single crystallinity was not maintained during complete exchange, which prevented acquisition of SCXRD data for fully exchanged btei networks.

II.2.6 X-ray Absorption Spectroscopy

Extended X-ray absorption fine structure (EXAFS) analysis was pursued to interrogate the coordination environment of the metal sites during and after ion exchange. We have analyzed Zn_3btei, Pd_3btei, as well as partially exchanged sample (~50% exchange). In addition, we have examined $PdZn(OAc)_4 \cdot H_2O$ as a molecular model of partially exchange heterobimetallic Pd–Zn sites. Data and fitting parameters are collected in **Figures II-10–II-14** and **Tables II-5–9**.

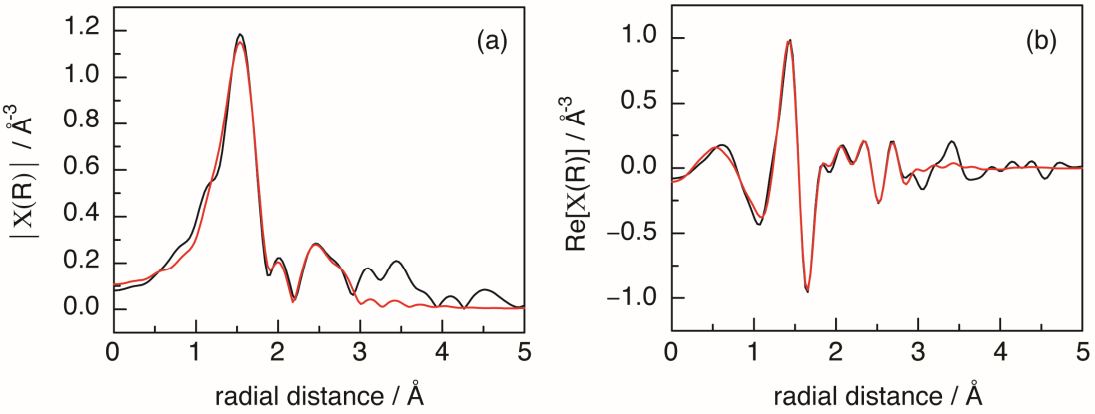

Figure II-10. EXAFS Pd K-edge data (window range 1.0 Å – 3.3 Å) for Pd_3btei. Experimental data (—) and fit (—) using the FEFF9 code. Fourier transforms (FT) of the Pd K-edge EXAFS data measured on the sample following 86% Pd exchange. Left: the FT moduli; right: real parts of the FTs. The metal–metal interaction around Pd is dominated by the Pd–Pd ones at 2.72 ± 0.03 Å.

Table II-5 EXAFS data analysis of Pd_3btei. N, coordination number. S_0^2, amplitude reduction factor. R, the distance between absorber and scatterer; σ^2, the Debye-Waller factor; ΔE_0, the energy shift. R-factor is 0.008.

Path	N	S_0^2	R / Å	σ^2 / Å^2	ΔE_0 / eV
Pd–O	4.00	1.018	2.01 ± 0.01	0.0051	8.45 ± 1.25
Pd–Pd	1.00	1.018	2.72 ± 0.03	0.0103	8.45 ± 1.25
Pd–C	4.00	1.018	2.94 ± 0.03	0.0034	8.45 ± 1.25
Pd–O	4.00	1.018	3.14 ± 0.04	0.0088	8.45 ± 1.25

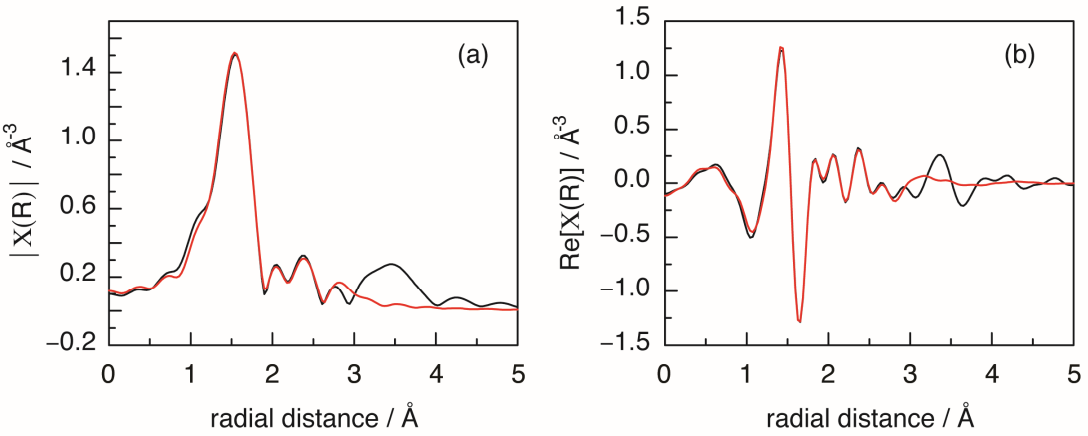

Figure II-11. EXAFS Pd K-edge data (window range 1.0 Å – 3.0 Å) for $PdZn(OAc)_4 \cdot H_2O$. Experiment data (—) and fit (—) using the FEFF9 code. Left: the FT moduli; right: real parts of the FTs.

Table II-6 EXAFS data analysis of $PdZn(OAc)_4 \cdot H_2O$. N, coordination number. S_0^2, amplitude reduction factor. R, the distance between absorber and scatterer; σ^2, the Debye-Waller factor; ΔE_0, the energy shift. R-factor is 0.005.

Path	N	S_0^2	R / Å	σ^2 / Å^2	ΔE_0 / eV
Pd–O	4.00	1.022	2.01 ± 0.01	0.0024	9.21 ± 1.27
Pd–Zn	1.00	1.022	2.61 ± 0.05	0.0107	9.21 ± 1.27
Pd–C	2.00	1.022	2.92 ± 0.03	0.0015	9.21 ± 1.27
Pd–C	2.00	1.022	2.98 ± 0.03	0.0015	9.21 ± 1.27
Pd–O	2.00	1.022	3.07 ± 0.04	0.0086	9.21 ± 1.27
Pd–O	2.00	1.022	3.13 ± 0.04	0.0086	9.21 ± 1.27

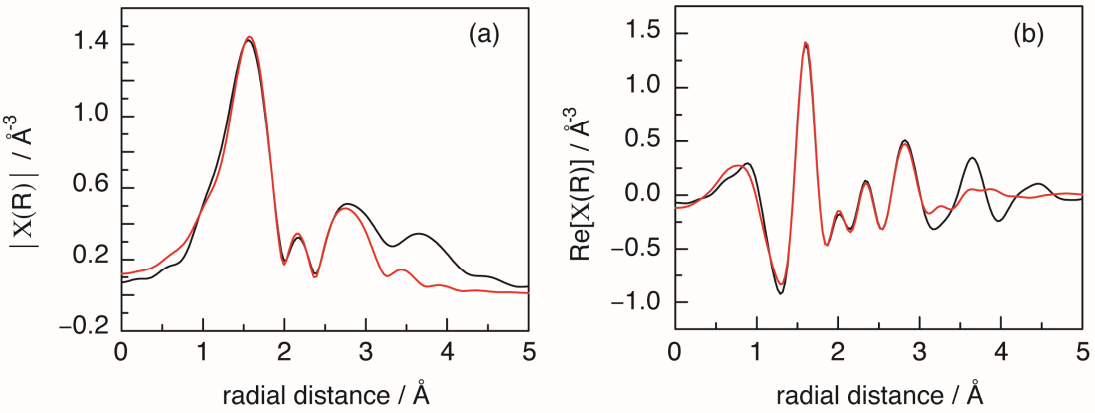

Figure II-12. EXAFS Zn K-edge data (window range 1.0 Å – 3.3 Å) for $PdZn(OAc)_4 \cdot H_2O$. Experiment data (—) and fit (—) using the FEFF9 code. Left: the FT moduli; right: real parts of the FTs.

Table II-7 EXAFS data analysis of $PdZn(OAc)_4 \cdot H_2O$. N, coordination number. S_0^2, amplitude reduction factor. R, the distance between absorber and scatterer σ^2, the Debye-Waller factor; ΔE_0, the energy shift. R-factor is 0.014.

Path	N	S_0^2	R / Å	σ^2 / Å^2	σE_0 / eV
Zn–O	2.00	0.976	2.05 ± 0.03	0.0074	8.97 ± 2.38
Zn–O	2.00	0.976	2.08 ± 0.03	0.0074	8.97 ± 2.38
Zn–Pd	1.00	0.976	2.61 ± 0.07	0.0055	8.97 ± 2.38
Zn–C	4.00	0.976	3.03 ± 0.09	0.0032	8.97 ± 2.38
Zn–O	4.00	0.976	3.23 ± 0.08	0.0035	8.97 ± 2.38

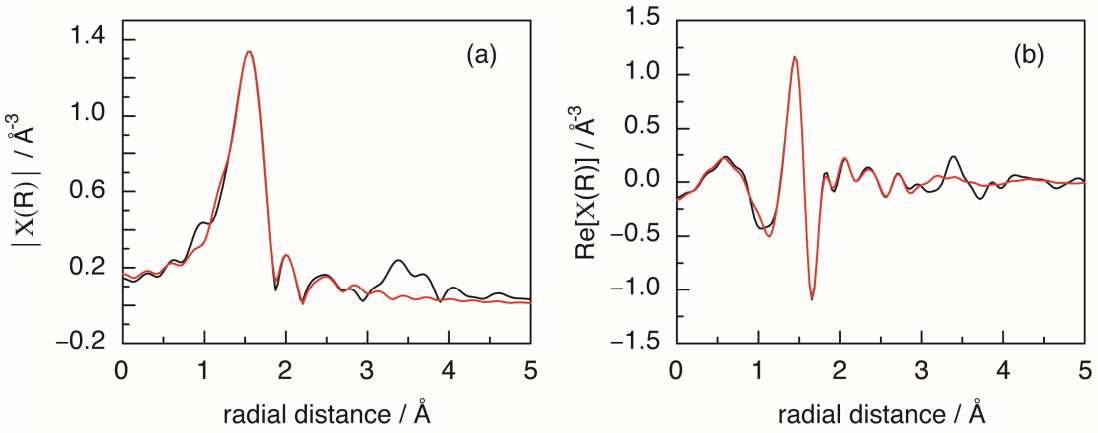

Figure II-13. EXAFS Pd K-edge data (window range 1.0 Å – 3.3 Å) for $(PdZn)_{1.5}$btei. Experiment data (—) and fit (—) using the FEFF9 code. Fourier transforms (FT) of the Pd K-edge EXAFS data measured on the sample following 50% Pd exchange. Left: the FT moduli; right: real parts of the FTs.

Table II-8 EXAFS data analysis of $(PdZn)_{1.5}$btei. N, coordination number S_0^2, amplitude reduction factor. R, the distance between absorber and scatterer; σ^2, the Debye-Waller factor; ΔE_0, the energy shift. R-factor is 0.016.

Path	N	S_0^2	R / Å	σ^2 / Å^2	ΔE_0 / eV
Pd–O	4.00	1.037	2.01 ± 0.01	0.0034	6.11 ± 1.50
Pd–Zn	0.50	1.037	2.65 ± 0.07	0.0097	6.11 ± 1.50
Pd–Pd	0.50	1.037	2.70 ± 0.07	0.0097	6.11 ± 1.50
Pd–C	4.00	1.037	2.96 ± 0.03	0.0052	6.11 ± 1.50
Pd–O	4.00	1.037	3.16 ± 0.07	0.0149	6.11 ± 1.50

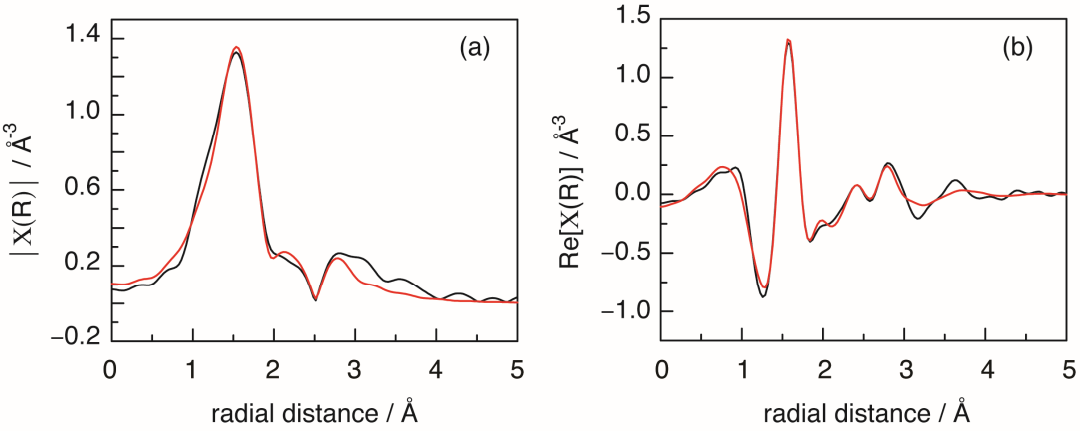

Figure II-14. EXAFS Zn K-edge data (window range 1.0 Å – 3.8 Å) for $(PdZn)_{1.5}$btei. Experiment data (—) and fit (—) using the FEFF9 code. Fourier transforms (FT) of the Pd K-edge EXAFS data measured on the sample following 50% Pd exchange. Left: the FT moduli; right: real parts of the FTs.

Table II-9 EXAFS data analysis of $(PdZn)_{1.5}$btei. N, coordination number S_0^2, amplitude reduction factor. R, the distance between absorber and scatterer; σ^2, the Debye-Waller factor; ΔE_0, the energy shift. R-factor is 0.020.

Path	N	S_0^2	R / Å	σ^2 / Å^2	ΔE_0 / eV
Zn–O	4.00	1.019	2.01 ± 0.01	0.0063	8.05 ± 1.14
Zn–O	1.00	1.019	2.18 ± 0.01	0.0063	8.05 ± 1.14
Zn–Pd	0.50	1.019	2.60 ± 0.06	0.0072	8.05 ± 1.14
Zn–Zn	0.50	1.019	2.90 ± 0.06	0.0051	8.05 ± 1.14
Zn–C	4.00	1.019	3.11 ± 0.06	0.0228	8.05 ± 1.14

The Zn K-edge data obtained for Zn_3btei indicate that the coordination environment about Zn is comprised of four Zn–O distances at 2.00 Å, one Zn–O distance at 2.17 Å, and a Zn–Zn distance of 2.86 Å, which is consistent with the known pentacoordinate Zn environment in solvated Zn_3btei.

EXAFS data collected following partial Pd exchange were fit as a mixture of Zn_2, PdZn, and Pd_2 sites (1 : 2 : 1 ratio). The Zn K-edge data indicated the Zn coordination environment in partially exchanged samples displays four Zn–O distances at 2.01 Å and one Zn–O distance at 2.18 Å. The Zn_2 sites display a Zn–Zn distance of 2.90 Å and the PdZn sites display a Pd–Zn separation of 2.60 Å. The Pd K-edge data collected for the same sample were fit with four Pd–O distances of 2.01 Å. The PdZn sites display a Pd–Zn separation of 2.65 Å and the Pd_2 sites show a Pd–Pd distance of 2.70 Å. The Pd–Zn distance determined from this sample is consistent with the Pd–Zn separation in the molecular site mimic $PdZn(OAc)_4 \cdot H_2O$ (2.576 Å (SCXRD), 2.61 Å (EXAFS)).[172]

The Pd K-edge data obtained for Pd_3btei indicated the coordination environment of Pd is comprised of four Pd–O distances at 1.98 Å and one Pd–Pd distance at 2.72 Å. The obtained EXAFS data set is dominated by Pd–Pd scattering and the best fit does not incorporate a Pd–Zn interaction.

Analysis of the X-ray absorption near edge structure (XANES) data for both partially and completely exchanged samples indicate that Pd is incorporated into the M_3btei network in the +II oxidation state (**Figure II-15**).[178] Based on comparison of the edge energy for $Pd_3(OAc)_6$, Pd_3btei, $PdZn(OAc)_4$, and Pd metal, the edge energy is inconsistent with the presence of Pd(0) in the exchanged samples.

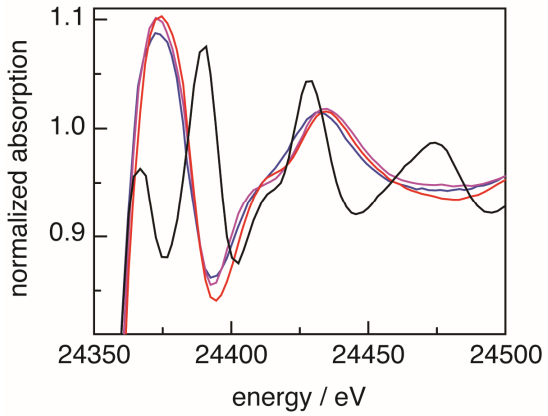

Figure II-15. XANES spectra of Pd_3btei (—), $Pd(OAc)_2$ (—), $PdZn(OAc)_4 \cdot H_2O$ (—), and Pd(0) (—). The edge energy in Pd(II) species is higher than that in Pd(0), which is inconsistent with reduction of the Pd_2 sites upon transmetalation.

II.2.7 Reactivity of Lattice-Confined Pd_2 Sites

We examined the hypothesis that proximity-enforced Pd–Pd interaction would raise the HOMO and result in a more nucleophilic and more easily oxidized Pd site in comparison to Pd carboxylates in which such Pd–Pd proximity is not enforced (*i.e.* the trinuclear structure of $Pd_3(OAc)_6$). To evaluate this hypothesis, we examined the interaction of Pd_3btei with CS_2. Electron donation into CS_2 is expected to manifest as a weakening of the C–S π-bonds and a low-energy shift in the associated IR stretching frequency.[179] The IR spectrum of CS_2-impregnated Pd_3btei displays an 11 cm^{-1} red shift in the IR stretching frequency (**Figure II-16**). No similar changes were observed upon CS_2 update in Zn3btei or upon treatment of $Pd_3(OAc)_6$ with CS_2.

We have evaluated the reactivity of Pd_3btei towards a variety of reaction conditions. The Pd–O linkages in Pd_3btei are susceptible to protonation: treatment of Pd_3btei with weak acids such as AcOH leads to the digestion of the extended lattice

and the evolution of free H_6btei and soluble Pd salts. The protolytic instability of the Pd–O bonds in Pd_3btei can give rise to reaction chemistry with protic substrates: treatment of Pd_3btei with benzyl alcohol resulted in the evolution of benzaldehyde with the concurrent formation of Pd(0). This observation is consistent with protonation of the Pd–O bond followed by β-hydride elimination of the incipient Pd(II) alkoxide. We have also carried out a series of experiments in which Pd_3btei was treated with oxidants, such as peracetic

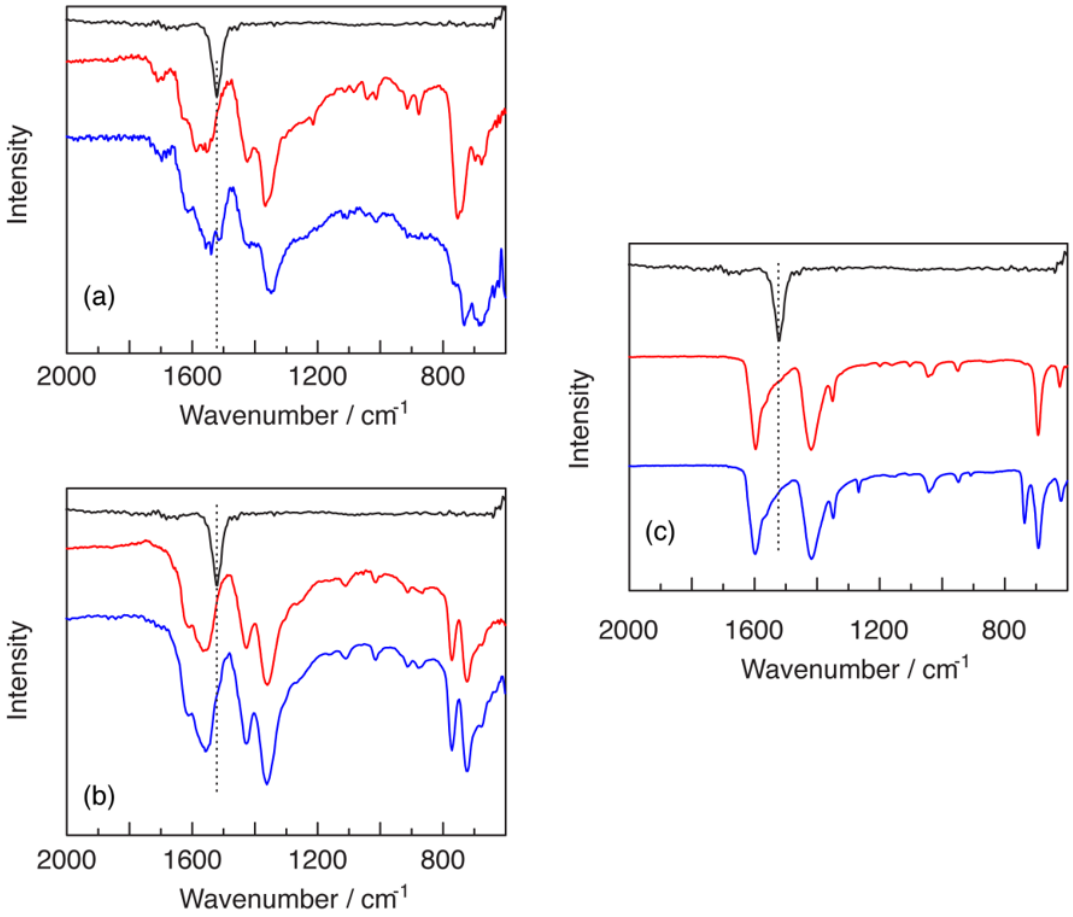

Figure II-16. IR spectra of CS_2 experiments. (a) CS_2 (—), Pd_3btei (—), and Pd_3btei treated with CS_2 (—); (b) CS_2 (—), Zn_3btei (—), and Zn_3btei treated with CS_2 (—); (c) CS_2 (—), $Pd(OAc)_2$ (—), and $Pd(OAc)_2$ treated with CS_2 (—).

acid and 2-tert-butylsulfonyl iodosylbenzene. Despite attempts to introduce exogenous substrates that might participate in C–H functionalization of olefin oxidation, in all conditions examined, the exclusive oxidation product obtained is 1,3,5-benzene tricarboxylic acid, which is the product of oxidative cleavage of the alkynyl groups in btei ligand. Similar treatment of H_6btei and Zn_3btei also generates 1,3,5-benzene tricarboxylic acid.

II.3 Discussion

$Pd(OAc)_2$ is a ubiquitous catalyst and precatalyst in organic synthesis, and as such the structure of this important molecule has been the focus of sustained interest. Single-crystal X-ray diffraction, EXAFS, and solid-state NMR experiments have confirmed that $Pd(OAc)_2$ exhibits a trimeric structure (*i.e.* $Pd_3(OAc)_6$) in the solid state (**Figure II-1**).[112,113] A combination of NMR, Raman, and IR spectroscopies as well as EXAFS data and ebulliometry measurements indicate that the trimeric structure is maintained upon dissolution in many common solvents.[111,113-115] Trinuclear aggregation simultaneously satisfies the proclivity for square planar coordination about Pd(II) ions and minimizes overlap of filled $4d_z^2$ orbitals (**Figure II-3**).

The close Pd–Pd interactions in acetate-bridged binuclear Pd complexes, such as complex **II-4** (**Figure II-2**), are credited for Pd–Pd cooperation and facile redox events in some Pd-catalyzed C–H oxidation chemistry.[121-126] *A priori*, one might expect that attractive $d^8 \cdots d^8$ interactions, which arise from symmetry allowed mixing of the 4d orbitals with the 5s and 5p orbitals, could stabilize Pd_2 aggregate.[180] However, in

comparison to Rh, Ir, and Pt, for which attractive $d^8 \cdots d^8$ interactions have been documented, Pd exhibits an anomalously large energy gap between the 4d and 5s and 5p orbitals, which attenuates the impact of symmetry-allowed orbital mixing.[178] The potential stabilization of mixing of the 4d with 5p and 5s orbitals is more than compensated for by the enforced filled-filled $4d_z^2$ interactions in Pd_2 aggregates. The kinetic instability of Pd_2 aggregation can be overcome with strong donor ligands such as formamidinate and guanidinate ligands,[181] but the use of such basic ligands can introduce potential ligand-based redox chemistry.[105] With interest in oxidation catalysis, we have been attracted to identifying strategies to stabilize Pd_2 aggregates in the absence of strongly basic nitrogen donors and have focused on the potential to isolate these structures in oxidation-resistant oxygen ligand fields.

Here, we demonstrate that ion metathesis of Pd(II) into preformed Zn(II)-based porous materials enables the synthesis and stabilization of thermodynamically metastable Pd_2 tetracarboxylate sites confined with a porous lattice (**Figure II-5**). Extended exposure of Zn_2-based materials to Pd(II)-containing solutions results in the replacement of lattice Zn(II) with Pd(II). Based on a combination of SCXRD and EXAFS analysis, the templated Pd_2 sites are installed by sequential replacement of the Zn ions in the template lattice. Pd exchange efficiency depends on both the templating metal ion-Pd exchange is more efficient in Zn_2-based materials than those comprised of Cu_2 sites-and the structure of the organic linkers-Pd exchange into Zn_3btc_2 proceeds only to ~35% Pd incorporation while use of the larger linking group btei enabled exchange reactions to proceed to ~80% Pd incorporation. This observation is consistent with previous reports that larger, potentially

more flexible organic linkers, support greater ion metathesis chemistry, which may be due to the ability of these more flexible structures to accommodate the subtle structural differences between materials before and after ion metathesis chemistry.[144]

Cation exchange in porous materials has begun to emerge as a powerful strategy to access materials that are unavailable from solvothermal synthetic methods. Based on XANES analysis, the generated Pd_2-based materials are comprised of Pd(II) ions, and the isolated materials do not contain Pd(0). This observation is in contrast to previous solvothermal approaches to Pd_2-containing materials, which result in formation of Pd(0) nanoparticles intercalated within the MOF structure.[182] These observations highlight the importance of low-temperature cation exchange to generate Pd-based MOFs: facile reduction of Pd(II) at high temperature and in the presence of many of the coordinating solvents typically employed in solvothermal synthesis of porous materials mandates that low-temperature synthetic methods to be developed to introduce Pd(II) sites.

While cation exchange chemistry is an important approach towards designer porous materials, often, the lack of mechanistic information regarding ion metathesis chemistry prevents predictive application of cation exchange reactions to target porous structures. Analysis of the time-dependent reaction progress of Pd exchange into Zn sites has revealed the presence of a kinetic induction period for ion exchange when DMF-solvated Zn templates were employed. At early reaction times, exchange proceeds slowly. At later times, substantially faster exchange is observed (**Figure II-5a**). IR spectroscopy and TGA-MS experiments, carried out during the kinetic induction period indicated that during this reaction regime, Zn-bound DMF ligands were being removed. The more rapid

exchange chemistry was observed once DMF ligands were completely removed. The importance of network solvation was confirmed by pre-soaking materials in $CHCl_3$. Ion exchange on these preactivated materials resulted in ion exchange with no induction period. We hypothesize that the observed solvation-dependent exchange chemistry reflects the increased Lewis acidity of under-ligated Zn(II) ions and the increased proclivity of these ions to bind incoming carboxylate ions delivered by $Pd_3(OAc)_6$.

The unique electronic structure of the Pd_2 site that is conferred by proximity-enforced Pd–Pd interaction is evidenced by the observation of CS_2 binding. The HOMO-energy-raising impact of d_z^2 mixing provides enhanced Lewis basicity and thus binding of Lewis acidic substrates which is not observed in either Zn_3btei or $Pd_3(OAc)_6$. Oxidative lability of the alkynyl linkers in the btei ligands has thus far precluded examination of the impact of HOMO-raising on oxidation catalysis with lattice-confined substrates.

II.4 Conclusions

The scope of polynuclear complexes that can be evaluated as potential catalyst platforms would be greatly expanded if general strategies to control the size and geometry of discrete aggregates supported by simple ligands were available. Here, we have demonstrated that cation metathesis within porous MOFs can be leveraged to prepare and stabilize Pd_2 tetracarboxylate sites that are metastable in solution-phase chemistry. These studies have revealed the important role that lattice solvation can exert on the course of ion metathesis chemistry. We anticipate that the development of predictive models for when cation exchange chemistry will be facile in combination with access to new

templated polynuclear aggregates housed in oxidatively stable ligand environments will contribute to the development of new families of polynuclear catalysts.

II.5 Experimental Details

II.5.1. General Considerations

Materials Solvents were obtained as ACS reagent grade. Unless otherwise noted, all chemicals and solvents were used as received. Ethyl acetate, magnesium sulfate, and dimethyl sulfoxide were obtained from EMD Millipore. Thionyl chloride, potassium iodide, triphenylphosphine, triethylamine, hydrazine monohydrate, dimethyl-5-hydroxyisophthalate, and 5-aminoisophthalic acid were obtained from Alfa Aesar. Diethyl ether (Et_2O), bis(triphenylphosphine)palladium(II) dichloride, 5-nitroisophthalic acid, 1,3,5-benzenetricarbonyl trichloride, copper(II) nitrate trihydrate, tetrafluoroboric acid solution (48% w/w), glucose, methanol, tetrahydrofuran (THF), *N*-methyl-2-pyrrolidone (NMP), peracetic acid solution (39% in acetic acid) and hexanes were obtained from Sigma Aldrich. Silica gel (0.060–0.200 mm, 60 Å for column chromatography), benzene, and *N*,*N*-dimethylformamide (DMF) were obtained from Acros Organics. Palladium(II) acetate, palladium(II) chloride, zinc nitrate hexahydrate, and copper(I) iodide were obtained from Strem Chemicals. (Trimethylsilyl)acetylene was obtained from Chem Impex. Diisopropylamine, glacial acetic acid, cesium fluoride, 1,3,5-tris(bromomethyl)benzene, and tribromobenzene were obtained from Beantown Chemical. Dichloromethane (CH_2Cl_2), acetonitrile (MeCN), potassium carbonate, and chloroform ($CHCl_3$) were obtained from Fisher Scientific. Ethanol was obtained from Koptec.

Potassium hydroxide and sodium hydroxide were obtained from BDH Analytical Chemicals. *N,N*-dimethylacetamide (DMA) was obtained from TCI. Sodium nitrite and hydrochloric acid were obtained from Macron Chemicals. Sodium bicarbonate was obtained from Aqua Solutions. $Pd(PPh_3)_4$[183] and 2-*tert*-butylsulfonyl iodosylbenzene (**S11**) were prepared according to literature methods.[184] NMR solvents was purchased from Cambridge Isotope Laboratories and were used as received. UHP-grade N_2, CO_2, Ar, and He, used in gas adsorption and thermogravimetric measurements, were obtained from Airgas. All reactions were carried out under ambient atmosphere unless otherwise noted.

Characterization Details NMR spectra were recorded on Mercury 300 at 299.92 MHz for ^{1}H and at 74.98 MHz for ^{13}C acquisitions and were referenced against solvent signals: $CDCl_3$ (7.26 ppm, ^{1}H; 77.16 ppm, ^{13}C) and DMSO-d_6 (2.50 ppm, ^{1}H).[185] ^{1}H NMR data are reported as follows: chemical shift (δ, ppm), (multiplicity: s (singlet), d (doublet), t (triplet), m (multiplet), br (broad), integration). IR spectra were recorded on ATI Mattson Genesis Series FTIR with ATR spectrometer. Spectra were blanked against air and were determined as the average of 64 scans. IR data are reported as follows: wavenumber (cm^{-1}), (peak intensity: s, strong; m, medium; w, weak). Elemental analyses were performed by Atlantic Microlab (Norcross, GA). TGA-MS analyses were performed at a temperature ramp of 20 °C/min on Mettler-Toledo TGA/ DSC 1 with an attached Pfeiffer Vacuum ThermoStar Mass Spectrometer under Ar flow. Diffuse reflectance UV-vis-NIR spectra were recorded by Hitachi U-4100 UV-vis-NIR spectrophotometer with Praying Mantis diffuse reflectance accessory. The spectra were obtained from samples of solids mixed with $BaSO_4$.

X-ray Absorption Details X-ray absorption spectroscopy (XAS) data were collected at the Pd K-edge (~24.3 keV) using the bending magnet beamline of the DuPont-Northwestern-Dow Collaborative Access Team (5-BM-D) at the Advanced Photon Source of Argonne National Laboratory. X-ray energy scans were performed using a Si(111) double-crystal monochromator detuned to 65% of the maximum intensity to reject harmonics. During these measurements, the APS storage ring was run in the top-up mode with the electron beam current at 102 mA. The vertical size of the beam entering the monochromator was 0.3 mm for maximum energy resolution. The vertical beam size that irradiated the samples was 0.6 mm due to natural beam divergence. The horizontal beam size was set to 10 mm. Samples were prepared by finely dispersing powdered material on Scotch® tape. The XAS data were collected in fluorescence mode using three identical ionization chambers (Oxford Danfysik) operating in their linear regimes. The first ion chamber (I_0) is used to monitor the incident beam intensity. The samples of interest were placed in between the first and second ion chambers (I_T). A Ru metal foil was placed in between the second and third ion chambers (I_{T2}) for energy verification. Each ionization chamber was filled with gas mixtures that absorbed given percentages of the incident beam in order to optimize signal-to-noise ratio, *i.e.*, 10% and 25% absorption in I_0 and I_T respectively (94% N_2/6% Ar in both chambers), and 65% absorption in I_{T2} (100% Ar). XAS data were analyzed using Demeter 0.9.26.

Powder X-ray Diffraction Details Powder X-ray diffraction (PXRD) measurements were carried out on a Bruker D8 Advance Eco X-ray diffractometer (Cu Kα, 1.5418 Å; 40 kV, 25 mA) fitted with LynxEye detector. The angular range was measured from 5.00 to

40.00° (2θ) with steps of 0.020° and a measurement time of 0.5 second per step. Simulated PXRD patterns were calculated with Mercury 3.9.

Gas Adsorption Details Gas adsorption isotherms for pressures in the range 0−1.0 bar were measured volumetrically using a Micromeritics ASAP 2020 instrument. Samples were transferred under an N_2 atmosphere to pre-weighed analysis tubes. The samples were evacuated at room temperature until the outgas rate was <10 μbar/min and further maintained for 16 h. Then the tube was weighed to determine the mass of the activated sample. The tube was transferred to the analysis port of the instrument. UHP-grade (99.999% purity) N_2 and He were used for all adsorption measurements. For all isotherms, both warm and cold free-space measurements were carried out with He; N_2 isotherms were measured at 77 K.

Inductively Coupled Plasma Mass Spectrometry (ICP-MS) Details ICP-MS measurements were carried out on a PerkinElmer NexION 300D Quadruple in pulse mode with ASX-520 AutoSampler. The collected data were analyzed by NexIon software Version 1.3. ^{108}Pd, ^{64}Zn and ^{63}Cu concentrations were measured five times to yield the average with ^{103}Rh as the internal standard. Calibration curves were made by five different concentrations between 10 and 200 ppb or 5 and 100 ppb (for leaching experiment) with $R^2 > 0.9995$; standards were prepared by dilution of analytical standards obtained from BDH Chemicals. Analysis of ion-metathesis samples was accomplished by washing M_3btei (2.0 mg) with MeCN (1.0 mL × 3) and $CHCl_3$ (1.0 mL × 3). The solids were digested in conc. HNO_3 by sonication and diluted with ultrapure water to make 2% HNO_3 solution.

II.5.2 Synthesis

Synthesis of Diethyl 5-Aminoisophthalate (II-S1).

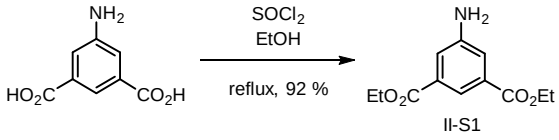

II-S1

Compound **II-S1** was prepared according to the following modification of literature methods.[186] A 500-mL round-bottom flask was charged with 5-aminoisophthalic acid (10.0 g, 55.2 mmol, 1.00 equiv) and EtOH (100 mL). The reaction mixture was cooled to 0 °C and $SOCl_2$ (12.0 mL, 165 mmol, 3.00 equiv) was added dropwise to the reaction vessel. The resulting mixture was heated at reflux for 5 h. Volatiles were removed *in vacuo* and EtOAc (100 mL) was added to the residue. A saturated aqueous solution of $NaHCO_3$ (100 mL) was added and the resulting suspension was stirred until the precipitate dissolved. The organic layer was separated and the aqueous layer was extracted with EtOAc (30 mL × 3). The combined organic layers were dried over Na_2SO_4. Solvent was removed *in vacuo* to afford 12.0 g of title compound as a white solid (92% yield). ^{1}H NMR (δ, 23 °C, $CDCl_3$): 8.06 (t, J = 1.4 Hz, 1H), 7.52 (d, J = 1.4 Hz, 2H), 4.37 (q, J = 7.1 Hz, 4H), 3.91 (bs, 2H), 1.40 (t, J = 7.1 Hz, 6H). IR (cm^{-1}): 3053 (w), 2918 (w), 1639 (w), 1599 (m), 1464 (s), 1395 (s), 1175 (m), 1070 (m), 1026 (m), 845 (m), 685 (s). Recorded ^{1}H NMR data was identical to that reported in the literature.[186]

Synthesis of Diethyl 5-Iodoisophthalate (II-S2).

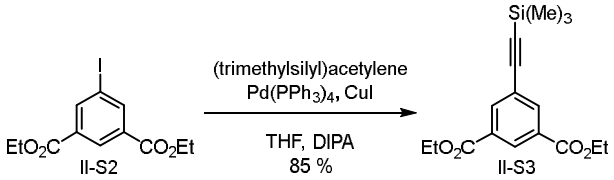

Compound **II-S2** was prepared according to the following modification of literature methods.[186] A 500-mL round-bottom flask was charged with compound **II-S1** (10.0 g, 42.2 mmol, 1.00 equiv) and 2 M HCl (45.0 mL, 90.0 mmol, 2.14 equiv). Sodium nitrite (3.50 g, 50.7 mmol, 1.20 equiv) in H_2O (30 mL) was added dropwise at 0 °C. After stirring at 0 °C for 45 min, a solution of potassium iodide (10.5 g, 63.3 mmol, 1.50 equiv) in H_2O (100 mL) was added dropwise. Dichloromethane (150 mL) was added to the dark-red mixture and the resulting mixture was stirred at 23 °C for 4 h. The layers were separated, the aqueous layer was extracted with dichloromethane (30 mL × 4), and the combined organic layers were dried over $MgSO_4$. Solvent was removed *in vacuo* and the orange residue was purified by SiO_2 chromatography (hexanes/ethyl acetate = 9/1) to afford 10.2 g of title compound as a white solid (70% yield). ^{1}H NMR (δ, 23 °C, $CDCl_3$): 8.63 (t, J = 1.4 Hz, 1H), 8.53 (d, J = 1.4 Hz, 2H), 4.41 (q, J = 7.1 Hz, 4H), 1.41 (t, J = 7.1 Hz, 6H). Recorded ^{1}H NMR data was identical to that reported in the literature.[186]

Synthesis of Diethyl 5-((Trimethylsilyl)ethynyl)isophthalate (II-S3).

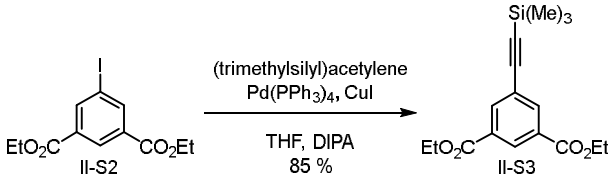

Compound **II-S3** was prepared according to the following modification of literature methods.[187] A 250-mL Schlenk flask was charged with compound **II-S2** (9.00 g, 25.9 mmol, 1.00 equiv), tetrakis(triphenylphosphine)palladium(0) (0.900 g, 0.779 mmol, 0.0301 equiv), copper(I) iodide (0.300 g, 1.58 mmol, 0.0610 equiv), THF (45.0 mL), and diisopropylamine (45.0 mL). The resulting mixture was degassed by three freeze-pump-thaw cycles and was then cooled to 0 °C. A 25-mL Schlenk flask was charged with (trimethylsilyl)acetylene (9.90 mL, 71.5 mmol, 2.76 equiv). The (trimethylsilyl)acetylene was degassed by three freeze-pump-thaw cycles and was transferred to the reaction mixture (0 °C) via cannula. The reaction mixture was allowed to warm to 23 °C at which temperature it was stirred for 15 h. At this time, solids were removed by filtration and were washed with hexanes (90 mL). The filtrate was concentrated to give dark-yellow oil, which was purified by SiO_2 chromatography (hexanes/ethyl acetate = 8/2) to afford 7.01 g of title compound as a light-yellow solid (85% yield). ^{1}H NMR (δ, 23 °C, $CDCl_3$): 8.60 (t, J = 1.7 Hz, 1H), 8.28 (d, J = 1.7 Hz, 2H), 4.41 (q, J = 7.1 Hz, 4H), 1.42 (t, J = 7.1 Hz, 6H), 0.27 (s, 9H). Recorded ^{1}H NMR data was identical to that reported in the literature.[187]

Synthesis of Hexaethyl 5,5',5''-(Benzene-1,3,5-triyltris(ethyne-2,1-diyl))-triisophthalate (II-S4).

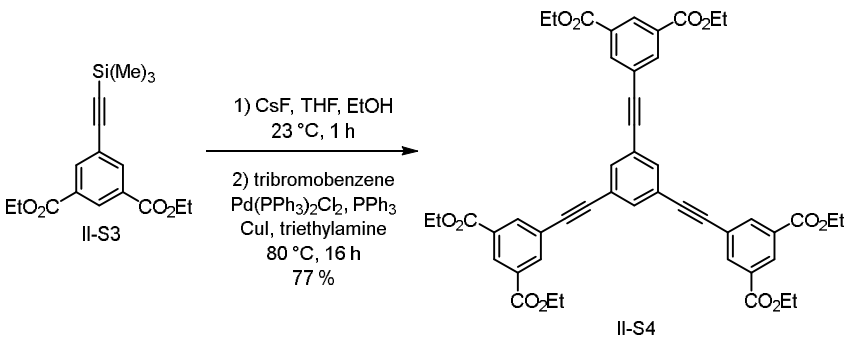

Compound **II-S4** was prepared according to the following modification of literature methods.[175,187] A 100-mL round-bottom flask was charged with compound **II-S3** (2.07 g, 6.52 mmol, 1.00 equiv), THF (25 mL), and EtOH (12.5 mL). Cesium fluoride (1.00 g, 6.58 mmol, 1.01 equiv) was added to the reaction mixture and the reaction was stirred at 23 °C for 1 h. At the time, the solids were removed by filtration and washed with CH_2Cl_2 (10 mL). The filtrate was concentrated *in vacuo* in a 100-mL Schlenk flask. To this reaction vessel was added tribromobenzene (0.430 g, 1.37 mmol, 0.208 equiv), bis(triphenylphosphine)palladium(II) dichloride (0.100 g, 0.142 mmol, 0.0216 equiv), triphenylphosphine (0.0765 g, 0.292 mmol, 0.0448 equiv), and triethylamine (50 mL). The resulting mixture was degassed by three freeze-pump-thaw cycles before CuI (0.0550 g, 0.289 mmol, 0.0443 equiv) was added. The reaction vessel was sealed under an N_2 atmosphere and heated to reflux for 16 h. At this time, volatiles were removed *in vacuo*, the dark-yellow residue was taken up in chloroform (100 mL) and washed with water (75 mL). The layers were separated, the aqueous layer was extracted with chloroform (30 mL × 4), the combined organic layer was dried over $MgSO_4$, and solvent was removed *in*

vacuo to afford dark-yellow solids. The crude solids were purified by SiO_2 chromatography (hexanes/ethyl acetate = 8/2) to afford 0.851 g of title compound as a light-yellow solid (77% yield based on tribromobenzene). ^{1}H NMR (δ, 23 °C, $CDCl_3$): 8.66 (t, *J* = 1.6 Hz, 3H), 8.38 (d, *J* = 1.6 Hz, 6H), 7.74 (s, 3H), 4.44 (q, *J* = 7.1 Hz, 12H), 1.44 (t, *J* = 7.1 Hz, 18H). Recorded ^{1}H NMR data was identical to that reported in the literature.[175,187]

Synthesis of 5,5',5''-(Benzene-1,3,5-triyltris(ethyne-2,1-diyl))triisophthalic acid (H_6btei).

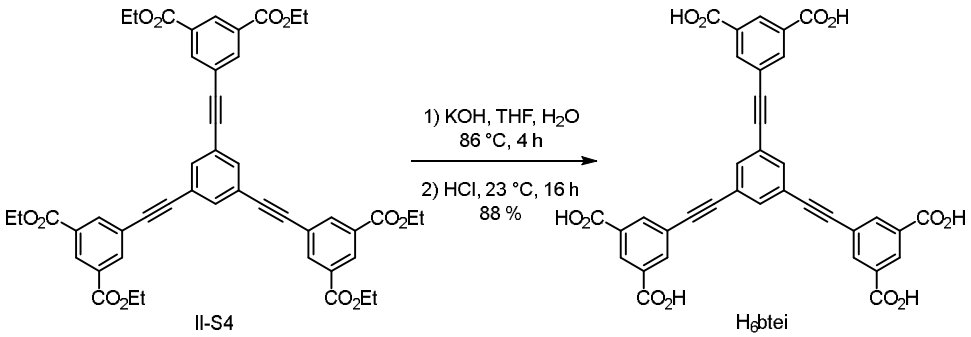

H_6btei was prepared according to the following modification of literature methods.[175] A 100-mL round-bottom flask was charged with compound **II-S4** (0.600 g, 0.740 mmol, 1.00 equiv), THF (12 mL), and 1M KOH solution (18 mL). The resulting solution was heated to reflux for 4 h. After this time, 12 M HCl was added until pH = 1 and the reaction mixture was stirred at 23 °C for 16 h. Solids were collected and washed with H_2O to afford 0.418 g of title compound as an amber solid (88% yield). ^{1}H NMR (δ, 23 °C, d_6-DMSO): 13.64 (bs, 6H), 8.48 (t, *J* = 1.6 Hz, 3H), 8.32 (d, *J* = 1.6 Hz, 6H), 8.01 (s, 3H). Recorded ^{1}H NMR data was identical to that reported in the literature.[175]

Synthesis of H_4abtc (II-S5).

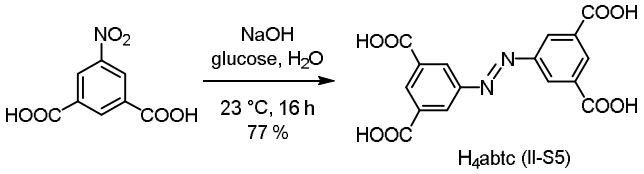

Compound **II-S5** (H_4abtc) was prepared according to literature methods.[188] A 250-mL round-bottom flask was charged with 5-nitroisophthalic acid (4.75 g, 22.5 mmol, 1.00 equiv), NaOH (12.5 g, 313 mmol, 13.9 equiv), and H_2O (63 mL). The reaction mixture was stirred at 60 °C for 1 h. A solution of glucose (25.0 g, 139 mol, 6.18 equiv) in H_2O (37 mL) was prepared at 60 °C and was slowly added to the reaction mixture. The brown mixture was cooled to 23 °C and air was bubbled through the reaction mixture for 16 h. At this time, the reaction mixture was cooled to 0 °C, and solids were isolated by filtration. The solids were dissolved in H_2O (50 mL) and the aqueous solution was acidified with conc. HCl to pH < 1. The resulting solids were isolated by filtration, washed with H_2O, and dried at 120 °C to afford 3.09 g of title compound as an orange solid (77% yield). ^{1}H NMR (δ, 23 °C, *d*$_6$-DMSO): 8.64 (s, 2H), 8.63 (s, 4H). Recorded ^{1}H NMR data was identical to that reported in the literature.[189]

Synthesis of 5,5',5''-((Benzene-1,3,5-tricarbonyl)tris(azanediyl))triisophthalic Acid (II-S6).

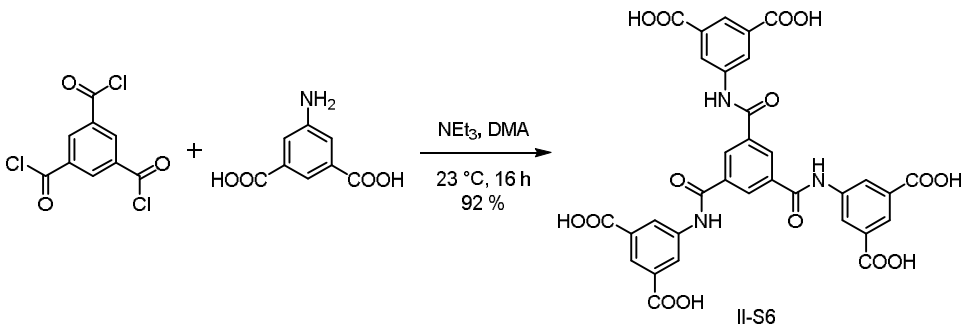

Compound **II-S6** was prepared according to the following modification of literature methods.[190] A 250-mL round-bottom flask was charged with 5-aminoisophthalic acid (2.08 g, 11.5 mmol, 3.05 equiv), triethylamine (1.68 mL, 12.1 mmol, 3.21 equiv), and DMA (25 mL) under an N_2 atmosphere. 1,3,5-Benzenetricarbonyl trichloride (1.00 g, 3.77 mmol, 1.00 equiv) was added dropwise and the reaction mixture was stirred at 23 °C for 16 h. At this time, H_2O (150 mL) was added and the solids were collected by filtration and washed with acetone, H_2O, MeOH, and Et_2O to afford 2.42 g of title compound as a yellow solid (92% yield). ^{1}H NMR (δ, 23 °C, d_6-DMSO): 13.33 (bs, 6H), 8.84 (s, 3H), 8.73 (d, J = 1.4 Hz, 6H), 8.26 (t, J = 1.4 Hz, 3H). Recorded ^{1}H NMR data was identical to that reported in the literature.[190]

Synthesis of 5,5',5''-((Benzene-1,3,5-triyltris(methylene))tris(oxy))triisophthalic Acid (II-S7).

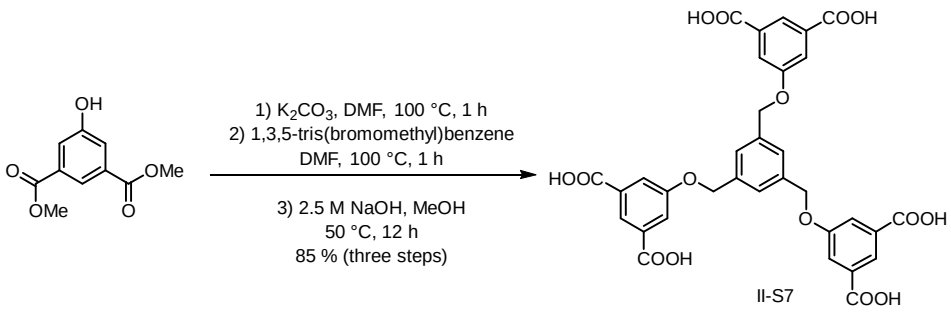

Compound **II-S7** was prepared according to the following modification of literature methods.[191] A 1-L round-bottom flask was charged with dimethyl-5-hydroxyisophthalate (6.35 g, 30.2 mmol, 7.49 equiv), potassium carbonate (13.0 g, 94.1 mmol, 23.4 equiv), and DMF (125 mL) and the reaction mixture was heated at 100 °C for 1 h. At this time, 1,3,5-tris(bromomethyl)benzene (1.44 g, 4.03 mmol, 1.00 equiv) and DMF (5 mL) was added and the reaction mixture was heated to 100 °C for 1 h. At this time, H_2O (400 mL) was added to the reaction mixture and the resulting white solids were isolated by filtration and washed with cold water. The solids were taken up in MeOH (125 mL) and a sodium hydroxide was added as a 2.0 M aqueous solution (30.0 mL, 60.0 mmol, 14.9 equiv). The reaction mixture was heated to 50 °C for 12 h. The reaction mixture was cooled to the mixture was acidified by conc. HCl until pH < 1. The solids were filtered and washed with cold H_2O to afford 2.25 g of the title compound (85% yield). ^{1}H NMR (δ, 23 °C, d_6-DMSO): 8.10 (s, 3H), 7.75 (s, 6H), 7.60 (s, 3H), 5.28 (s, 6H). Recorded ^{1}H NMR data was identical to that reported in the literature.[191]

Synthesis of $PdZn(OAc)_4 \cdot H_2O$.

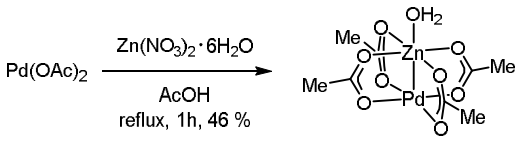

$PdZn(OAc)_4 \cdot H_2O$ was prepared according to literature methods.[172] A 10-mL round-bottom flask was charged with $Pd(OAc)_2$ (0.100 g, 0.445 mmol, 1.00 equiv), zinc acetate hexahydrate (0.135 g, 0.454 mmol, 1.02 equiv), and glacial acetic acid (3 mL). The resulting mixture was heated to reflux for 1 h. After this time, the reaction mixture was allowed to stand at 23 °C for 16 h and brown crystals formed. Solids were collected and washed with cold benzene and hexanes to afford 0.087 g of title compound as yellow crystals (46% yield). The PXRD pattern obtained for $PdZn(OAc)_4 \cdot H_2O$ matched the pattern simulated for single-crystal X-ray diffraction (**Figure II-17**).

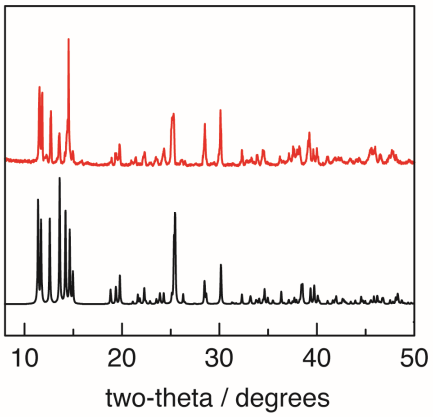

Figure II-17. Experimental (—) and calculated (—) PXRD pattern of $PdZn(OAc)_4 \cdot H_2O$.

II.5.3 MOF Synthesis as the Template for Transmetalation

Synthesis of Cu_3btc_2.

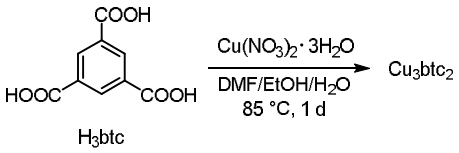

Cu_3btc_2 was prepared according to literature methods.[73] A 150-mL thick-walled vessel was charged with H_3btc (1.50 g, 7.14 mmol, 1.00 equiv), copper(II) nitrate trihydrate (3.00 g, 12.4 mmol, 1.74 equiv), DMF (25 mL), EtOH (25 mL), and water (25 mL). The resulting mixture was sonicated until a homogeneous solution was obtained and the reaction solution was allowed to stand at 85 °C for 1 d. At this time, the hot mother liquor was decanted and the obtained crystalline solids were washed with DMF (20 mL × 2) and dichloromethane (20 mL × 2). The solids were soaked in dichloromethane for 6 d and the solvent was refreshed two times per day. Solvent was removed *in vacuo* to afford 2.53 g of the title compound as a purple solid. The PXRD pattern of synthesized Cu_3btc_2 was consistent with reported data.[73]

Synthesis of Zn_3btc_2.

Zn_3btc_2 was prepared according to literature methods.[73] A 48-mL thick-walled vessel was charged with H_3btc (0.316 g, 1.50 mmol, 1.00 equiv), zinc nitrate hexahydrate (0.682 g,

2.29 mmol, 1.53 equiv), and DMF (40 mL). The resulting mixture was sonicated until a homogeneous solution was obtained and the reaction solution was allowed to stand at 85 °C for 16 h. At this time, the reaction was cooled to 23 °C and solvent was decanted. The crystalline solids were washed with DMF (20 mL × 2) to afford 74.0 mg of title compound as a white solid. The PXRD pattern of synthesized Zn_3btc_2 was consistent with reported data.[73]

Synthesis of Zn_2abtc (II-S8).

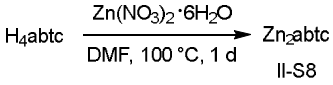

Zn_2abtc was prepared according to the following modification of literature methods.[192] A vial was charged with H_4abtc (35.8 mg, 0.100 mmol, 1.00 equiv), zinc nitrate hexahydrate (89.2 mg, 0.300 mmol, 3.00 equiv), and DMF (2.5 mL). The reaction mixture was sonicated until a homogeneous solution was obtained and the reaction solution was allowed to stand at 100 °C for 1 d. At this time, the reaction was cooled to 23 °C and solvent was decanted. The crystalline solids were washed with DMF (1.0 mL × 3) to afford title compound as an orange solid. The PXRD pattern of synthesized Zn_2abtc was consistent with reported literature data.[192]

Synthesis of Zn_3(II-S6) (II-S9).

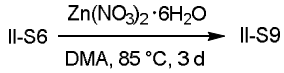

Compound **II-S9** was prepared according to literature methods.[193] A vial was charged with compound **II-S6** (50.0 mg, 0.0715 mmol, 1.00 equiv), zinc nitrate hexahydrate (170 mg, 0.571 mmol, 7.99 equiv), and DMA (3.5 mL). The reaction mixture was sonicated until a homogeneous solution was obtained and the reaction solution was allowed to stand at 85 °C for 3 d. At this time, the reaction was cooled to 23 °C and solvent was decanted. The crystalline solids were washed with DMA (1.0 mL × 3) to afford title compound as a colorless solid. The PXRD pattern of synthesized II-**S9** was consistent with reported literature data.[193]

Synthesis of Zn_3(II-S7) (II-S10).

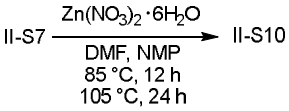

Compound **II-S10** was prepared according to the following modification of literature methods.[191] A vial was charged with compound II-**S7** (18.0 mg, 0.0273 mmol, 1.00 equiv), zinc nitrate hexahydrate (12.0 mg, 0.0403 mmol, 1.48 equiv), NMP (1.0 mL), and DMF (1.0 mL). The reaction mixture was sonicated until a homogeneous solution was obtained and the reaction solution was allowed to stand at 85 °C for 12 h and then 105 °C for 24 h. At this time, the reaction was cooled to 23 °C and solvent was decanted. The crystalline

solids were washed with DMF (1.0 mL × 3) to afford title compound as a colorless solid. The PXRD pattern of synthesized **II-S9** was consistent with reported literature data.[191]

Synthesis of Zn_3btei.

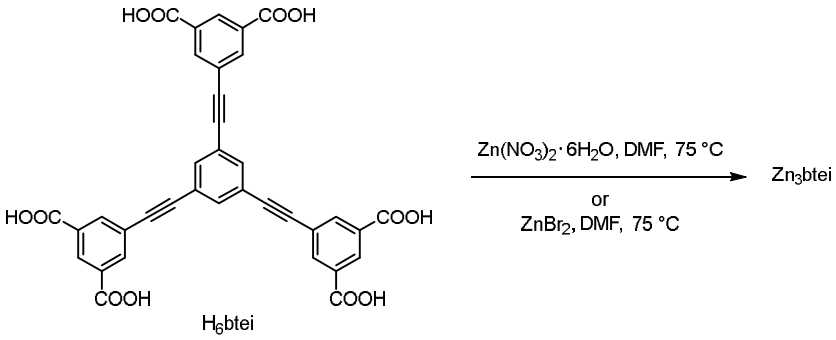

Microcrystalline Zn_3btei was prepared according to the following modification of literature methods.[174] A 1-dram vial was charged with H_6btei (8.00 mg, 0.0125 mmol, 1.00 equiv), zinc nitrate hexahydrate (12.0 mg, 0.0403 mmol, 3.22 equiv), and DMF (0.5 mL). The reaction mixture was sonicated until a homogeneous solution was obtained and the reaction solution was allowed to stand at 75 °C for 2 d. At this time, the reaction was cooled to 23 °C and solvent was decanted. The crystalline solids were washed with DMF (0.5 mL × 3) to afford 7.90 mg of title compound as an amber solid. The PXRD pattern of synthesized Zn_3btei was consistent with reported literature data.[174]

Crystalline Zn_3btei was prepared according to literature methods.[175] A 2-dram vial was charged with H_6btei (10.0 mg, 0.0156 mmol, 1.00 equiv), zinc bromide (30.0 mg, 0.133 mmol, 8.53 equiv), and DMF (1.5 mL). The reaction mixture was sonicated until a homogeneous solution was obtained and the reaction solution was allowed to stand at 75 °C for 3 d. At this time, the reaction was cooled to 23 °C and solvent was decanted. The

crystalline solids were washed with DMF (1.5 mL × 3) to afford 7.40 mg of title compound as amber solids. Elemental Analysis (EA) for $[Zn_3(btei)(H_2O)_9(C_3H_7NO)_{1.7}(CHCl_3)_{1.35}]$: calcd. C, 39.83; H, 3.41; N, 1.86; Cl, 11.22; found C, 39.25; H, 2.78; N, 1.86; Cl, 11.14. The PXRD pattern of synthesized Zn_3btei was consistent with reported literature data.[175]

II.5.4 Transmetalation as a Strategy to Synthesize Pd_2 Species and Its Reactivity

Transmetalation of Zn_3btei.

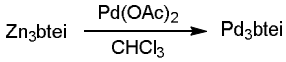

Zn_3btei was soaked in $CHCl_3$ for 3 d or 28 d and the solvent was refreshed three times per day. $Pd(OAc)_2$ was purified prior to use. $Pd(OAc)_2$ was dissolved in $CHCl_3$, filtered through Celite, and $CHCl_3$ was removed under vacuum. A 0.5-dram vial was charged with Zn_3btei (7.4 mg), $Pd(OAc)_2$ (2 mg), and chloroform (0.5 mL) and the Pd solution was refreshed weekly. Elemental Analysis (EA) for $[Pd_{2.25}Zn_{0.75}(btei)(H_2O)_{13}(C_3H_7NO)_{0.6}(CHCl_3)_{0.4}]$: calcd. C, 38.18; H, 3.57; N, 0.70; Cl, 3.57; found C, 37.03; H, 2.64; N, 0.71; Cl, 3.47. Transmetalation reactions between other MOFs and $Pd(OAc)_2$ were conducted using similar procedures.

Back-Exchange of Pd_3btei with Zn(II).

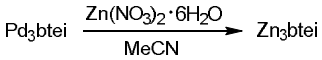

A 0.5-dram vial was charged with Pd_3btei (7.40 mg), zinc nitrate hexahydrate (50.0 mg) and MeCN (0.5 mL) and the mixture was allowed to stand for 7 d.

Digestion of Pd_3btei with AcOH. A 1-dram vial was charged with Pd_3btei (5.0 mg) and AcOH (1.0 mL). After sonication at 23 °C for 3 min, the solution was discarded. The solids were washed with MeOH (0.5 mL × 3) and the volatiles were removed *in vacuo*. ^{1}H NMR of the solids corresponded to that of H_6btei.

Treatment of Pd_3btei with BnOH.

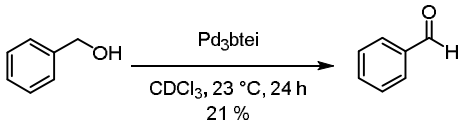

An NMR tube was charged with Pd_3btei (6.30 mg, 0.00677 mmol, 1.00 equiv), benzyl alcohol (2.00 μL, 0.0192 mmol, 2.84 equiv), mesitylene (2.00 μL, 0.0145 mmol, 2.14 equiv), and $CDCl_3$ (0.45 mL). The reaction mixture was agitated using a mechanical shaker for 24 h at 23 °C. At this time, benzaldehyde was detected by ^{1}H NMR and the yield was determined to be 21% by integration against the resonances of mesitylene.

General procedure for oxidation with peracetic acid.

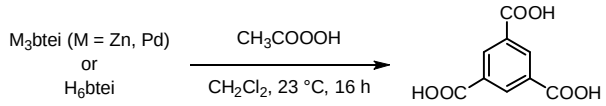

A one-dram vial was charged with Pd_3btei (0.00445 mmol, 1.00 equiv), peracetic acid (39% in acetic acid, 8.08 μL, 0.0472 mmol, 10.6 equiv), and CH_2Cl_2 (0.30 mL). After stirring at 23 °C for 16 h, solution turned light yellow and most of the solids dissolved. Water (0.30 mL) was added and the aqueous layer was collected and filtered. $[C_9H_5O_6]^-$ was observed by mass spectrometry (ESI negative, calc: 209.0081; expt m/z: 209.0087). Similar experiments were conducted with Zn_3btei and H_6btei using peracetic acid. $[C_9H_5O_6]^-$ was observed by mass spectrometry in each of these experiments.

General procedure for oxidation with 2-*tert*-butylsulfonyl iodosylbenzene (II-S11).

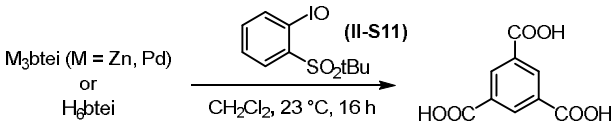

A one-dram vial was charged with Pd_3btei (0.00445 mmol, 1.00 equiv), hypervalent iodine reagent **II-S11** (15.0 mg, 0.0441 mmol, 9.90 equiv), and CH_2Cl_2 (0.30 mL). After stirring at 23 °C for 16 h, solution turned light yellow and some of the solids remained undissolved. DCM was decanted and water (0.30 mL) was added and the solution was filtered. $[C_9H_5O_6]^-$ was observed by mass spectrometry (ESI negative, calc: 209.0085; expt m/z: 209.0087). Similar experiments were conducted with Zn_3btei and H_6btei using **II-S11**. $[C_9H_5O_6]^-$ was observed by mass spectrometry in each of these experiments.

General procedure for CS_2 experiment A one-dram vial was charged with Pd_3btei (2.0 mg), CS_2 (0.01 mL), and CH_2Cl_2 (0.5 mL). The reaction mixture was allowed to sit for 1 h at 23 °C. At this time, the reaction solvent was decanted and IR spectra were recorded for the remaining solids. Similar experiments were conducted with Zn_3btei and $Pd(OAc)_2$ using CS_2. For $Pd(OAc)_2$, the reaction was allowed to air dry prior to acquisition of the IR spectrum.

Attempt to Directly Synthesize Pd_3btei under Cation Exchange Conditions.

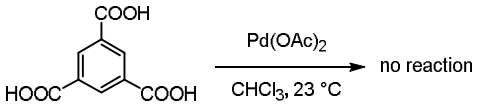

A 20-mL vial was charged with $Pd(OAc)_2$ (60.0 mg, 0.267 mmol, 4.01 equiv), H_3btc (14.0 mg, 0.0666 mmol, 1.00 equiv), and $CHCl_3$ (15.0 mL). After standing at 23 °C for 24 h, solvent was removed *in vacuo* to afford white and orange solids. PXRD analysis of the solids did not display any of the signals attributable to M_3btei frameworks.

II.5.5 Additional Data

Attempts to Crystallize of [$Pd_2(OAc)_6^{2-}$] We have synthesized and characterized [$Pd_2(OAc)_6^{2-}$] by the addition of LiOAc to $Pd_3(OAc)_6$ in AcOH / Ac_2O. The concentration of LiOAc changed the speciation of the equilibrium reaction and the equilibrium was reached after 16 h. When the concentration of LiOAc was 160 mM, a peak at 385 nm was observed which represented the formation of [$Pd_2(OAc)_6^{2-}$]. As the concentration of LiOAc increased, the peak shifted to 360 nm which was attributed to the formation of $[Pd(OAc)_4]^{2-}$.[133-135] Two isosbestic points at 325 nm and 380 nm were observed during equilibrium which were consistent with the literature (**Figure II-18**).[133-135] $Pd_3(OAc)_6$ (1.2 mM) with 160 mM LiOAc was chosen to be the condition for further studies. The attempts to crystallization of [$Pd_2(OAc)_6^{2-}$] failed by diffusing various solvents (*i.e.* pentane, hexanes, diethyl ether, and benzene).

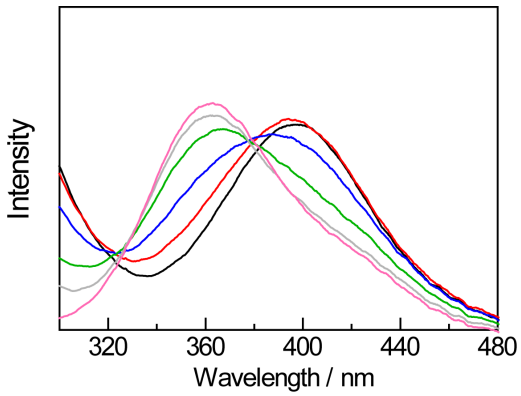

Figure II-18. UV-Vis spectra of titration experiment. $Pd_3(OAc)_6$ (1.2 mM) with 0 mM (—), 80 mM (—), 160 mM (—), 200 mM (—), 600 mM (—), and 1.6 M (—) LiOAc in AcOH / Ac_2O (v / v = 9 : 1).

II.5.5.1 PXRD patterns

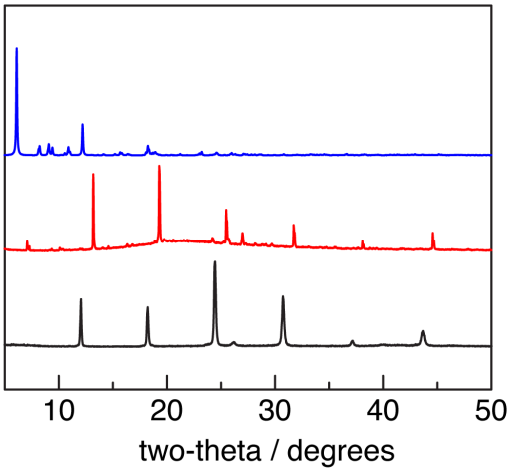

Figure II-19. PXRD patterns of calculated II-S8 (—), as-synthesized II-S8 (—), and Pd-exchanged II-S8 (—).

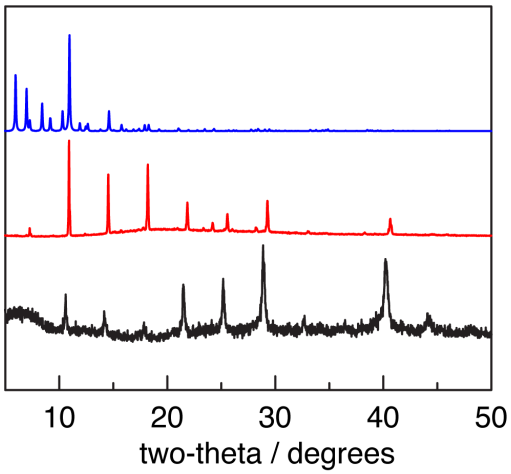

Figure II-20. PXRD pattern of calculated II-S9 (—), as-synthesized II-S9 (—), and Pd-exchanged II-S9 (—).

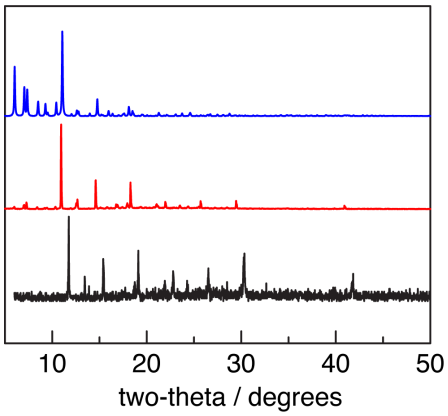

Figure II-21. PXRD pattern of calculated II-S10 (—), as-synthesized II-S10 (—), and Pd-exchanged II-S10 (—).

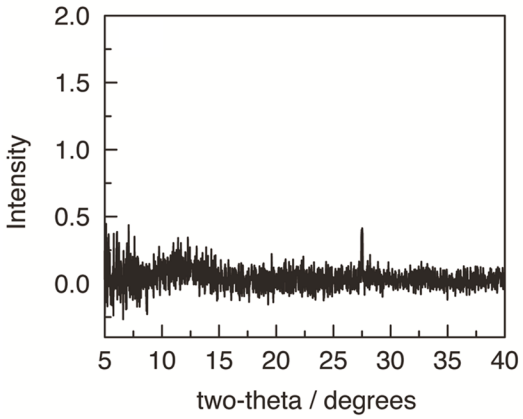

Figure II-22 PXRD pattern using $Pd(NO_3)_2$. $Pd(NO_3)_2$ exchange into Zn_3btei that was pre-soaked in $CHCl_3$ for 28 d.

II.5.5.2 Computational Coordinates

Table II-10 Coordinates for optimized geometry of $Pd(OAc)_2$

Atom	X	Y	Z
O	1.756794	1.087321	0.019089
O	–1.756708	–1.087420	–0.019125
C	2.430258	–0.000395	0.018232
C	–2.430303	0.000161	–0.018173
O	1.756668	–1.087876	0.019087
O	–1.756838	1.087754	–0.019085
C	3.926593	0.000022	–0.014726
H	4.261525	0.020976	–1.058672
H	4.313085	0.889949	0.487586
H	4.313509	–0.907879	0.453627
C	–3.926666	–0.000140	0.014902
H	–4.261542	–0.005236	1.059062
H	–4.313646	0.901003	–0.466402
H	–4.313223	–0.897111	–0.474553
Pd	0.000036	0.000047	–0.000039

Table II-11 Coordinates for optimized geometry of $Pd_2(OAc)_4$

Atom	X	Y	Z
O	–1.456793	1.432494	–1.147017
O	1.455459	–1.447963	–1.142675
O	–1.438447	–1.463812	–1.144355
O	1.442007	1.448162	–1.144394
C	–1.853951	1.828375	–0.002515
C	–1.834874	–1.859626	0.000712
C	1.856609	–1.838020	0.002689
C	1.832426	1.850038	0.000600
O	–1.458304	1.432559	1.142832
O	–1.438991	–1.463457	1.145610
O	1.455278	–1.446397	1.147295
O	1.440523	1.449852	1.145462
C	–2.930161	–2.905455	–0.001983
H	–3.898581	–2.398783	–0.087877
H	–2.816829	–3.568131	–0.862644
H	–2.917012	–3.473802	0.929734
C	–2.901375	2.922323	0.000154
H	–2.398032	3.890144	0.108973
H	–3.456259	2.922075	–0.939658
H	–3.576293	2.795439	0.849480
C	2.965438	–2.869471	0.001071
H	3.927498	–2.349662	–0.077670
H	2.955336	–3.441608	0.930524
H	2.865164	–3.530128	–0.862725
C	2.864652	2.958321	–0.001990
H	2.345843	3.920708	–0.083297
H	3.435762	2.949774	0.928117
H	3.526140	2.856121	–0.864943
Pd	–0.000448	–0.006211	1.309424
Pd	0.000640	–0.007323	–1.309043

Table II-12 Coordinates for optimized geometry of $Pd_3(OAc)_6$

Atom	X	Y	Z
Pd	1.619339	–0.929252	0.014006
C	–0.063527	–2.607519	1.868932
O	1.046467	–2.409266	1.293111
O	–1.174028	–2.047058	1.620059
C	–2.270779	1.267057	–1.892147
O	–1.528187	2.119232	–1.320660
O	–2.364702	0.027496	–1.640214
C	–3.178158	1.797375	–2.984445
H	–3.445016	0.997916	–3.678150
H	–4.097632	2.174483	–2.521305
H	–2.696088	2.623911	–3.510415
C	–0.077932	–3.658332	2.961265
H	0.912599	–3.758400	3.408479
H	–0.821832	–3.403082	3.719043
H	–0.361423	–4.620238	2.518104
Pd	–0.000013	1.867439	–0.000017
C	–2.277021	1.349145	1.834966
O	–2.651907	0.290927	1.246865
O	–1.243670	2.042684	1.594708
C	0.063702	–2.607749	–1.868759
O	1.174224	–2.047313	–1.619923
O	–1.046320	–2.409312	–1.293058
C	0.078015	–3.658857	–2.960809
H	–0.911720	–3.756345	–3.410385
H	0.824469	–3.405920	–3.716824
H	0.357531	–4.621458	–2.516624
C	–3.159641	1.823424	2.972363
H	–2.972965	1.191910	3.848399
H	–2.939589	2.861650	3.225049
H	–4.211469	1.708379	2.698582
Pd	–1.619309	–0.929275	–0.014030
C	2.276994	1.349213	–1.835011
O	2.651813	0.290911	–1.247027
O	1.243674	2.042783	–1.594697
C	3.159490	1.823504	–2.972499
H	2.970243	1.194055	–3.849485
H	2.941442	2.862654	–3.223146
H	4.211357	1.705552	–2.700179
C	2.270730	1.267241	1.892075
O	2.364612	0.027680	1.640159
O	1.528161	2.119436	1.320574
C	3.178091	1.797565	2.984386

Table II-12 Continued

Atom	X	Y	Z
H	4.097347	2.175156	2.521209
H	2.695803	2.623787	3.510655
H	3.445334	0.998013	3.677832

Table II-13 Coordinates for optimized geometry of $Pd_4(OAc)_8$

Atom	X	Y	Z
Pd	1.643894	–0.726051	0.128975
Pd	–0.725647	–1.642710	–0.128703
Pd	–1.643790	0.726026	0.128793
Pd	0.725698	1.642585	–0.129296
O	2.199496	–2.944158	0.075640
O	0.092868	–3.525427	–0.532630
C	1.340545	–3.761549	–0.336568
C	1.782990	–5.173964	–0.677347
O	1.339982	–0.922483	2.127993
O	–0.598143	–2.046739	1.846620
C	0.375170	–1.633647	2.549387
C	0.395146	–2.040605	4.001783
O	–2.943249	–2.199346	–0.073016
O	–3.526350	–0.092614	0.532529
C	–3.761316	–1.340595	0.337805
C	–5.173848	–1.784247	0.676451
O	–0.923277	–1.339405	–2.127671
O	–2.048761	0.597931	–1.846353
C	–1.635613	–0.375424	–2.548849
C	–2.043237	–0.396502	–4.001006
O	–2.198990	2.944228	0.075132
O	–0.092521	3.525349	–0.533871
C	–1.339934	3.761728	–0.337071
C	–1.783936	5.173694	–0.677711
O	–1.339834	0.923139	2.127728
O	0.598198	2.047376	1.845869
C	–0.375115	1.634578	2.548758
C	–0.394969	2.041926	4.001035
O	2.943264	2.199337	–0.073843
O	3.526381	0.092845	0.532471
C	3.761353	1.340724	0.337106
C	5.173617	1.784709	0.676411
O	0.923190	1.338644	–2.128160
O	2.048909	–0.598401	–1.846209

Table II-13 Continued

Atom	X	Y	Z
C	1.635827	0.374746	–2.548964
C	2.042833	0.395228	–4.001298
H	2.648444	–5.451693	–0.071525
H	0.965270	–5.883195	–0.531376
H	2.077761	–5.199939	–1.732946
H	–0.623503	–2.155149	4.377749
H	0.906786	–3.006735	4.082960
H	0.950199	–1.309207	4.592756
H	–5.459815	–2.632143	0.049787
H	–5.193613	–2.108635	1.723475
H	–5.880214	–0.959918	0.557107
H	–2.165488	0.621470	–4.376231
H	–1.308548	–0.946286	–4.592853
H	–3.005486	–0.915541	–4.081841
H	–0.956626	5.878793	–0.572620
H	–2.123464	5.188501	–1.719946
H	–2.622415	5.465116	–0.040828
H	0.623681	2.157116	4.376798
H	–0.906954	3.007916	4.081828
H	–0.949578	1.310536	4.592420
H	5.880258	0.960555	0.557465
H	5.459727	2.632630	0.049840
H	5.192710	2.109167	1.723420
H	1.304457	0.939098	–4.594051
H	3.001797	0.920093	–4.083542
H	2.171058	–0.622701	–4.374589

II.5.5.3 Crystallographic Data

Table II-14 Crystal data and structure refinement for Pd_3btei

Crystal data	
Chemical formula	$0.02(C_{1152}H_{384}O_{460.8}Pd_{19.41}Zn_{76.59})$
Fw (g/mol)	597.24
Temperature (K)	100(2)
Crystal system, space group	Cubic, *Fm*-3*m*
a, *b*, *c* (Å)	43.149(5), 43.149(5), 43.149(5)
α, β, γ (°)	90, 90, 90
V (Å^3)	80337(27)
Z	48
Radiation type	Synchrotron, λ = 0.41328 Å
μ (mm^{-1})	0.268
Crystal size (mm)	0.02 × 0.02 × 0.02
Data collection	
Diffractometer	Pilatus3 X CdTe 1M
Absorption correction	Multi-scan, *SADABS*
No. of measured, independent and observed [I>2σ (I)] reflections	139206, 1544, 1121
R_{int}	0.128
$\sin(\theta/\lambda)_{max}$ (Å^{-1})	1.12
Refinement	
$R[F^2 > 2\sigma(F^2)]$, $wR(F^2)$, S	0.043, 0.134, 1.06
No. of reflections	1544
No. of parameters	99
H-atom treatment	H-atom parameters constrained $w = 1/[\sigma^2(F_o^2) + (0.0638P)^2 + 222.7243P]$ where $P = (F_o^2 + 2F_c^2)/3$
r_{max}, r_{min} (e Å^{-3})	0.26, –0.19

CHAPTER III

PROBING SUBSTRATE DIFFUSION IN INTERSTITIAL MOF CHEMISTRY WITH KINETIC ISOTOPE EFFECTS*

III.1 Introduction

We have shown a strategy to confine metastable bimetallic Pd_2 in a lattice-confined scaffold which is inaccessible in solution-state analog in Chapter II. We use the same solid support (MOF) to lattice-confine a reactive metal nitride to prevent side reactions observed in solution-phase analog.

Reactive metal–ligand (M–L) multiply bonded complexes are critical intermediates in many biological C–H functionalization reactions. Intermediate Q, a diiron(IV) bis-m-oxo complex embedded in the active site of soluble methane monooxygenase (sMMO), is responsible for the partial oxidation of methane to methanol in methanotrophic bacteria (**Figure III-1**).[7,194-196] Soluble MMO achieves selective partial methane oxidation by conformationally gated substrate diffusion to, and product egress from, the enzyme active site.[197,198] Analysis of kinetic isotope effects (KIEs), which measure the impact of isotopic substitution on reaction rates, can provide direct evidence for conformationally gated diffusion. For example, sMMO-catalyzed C–H hydroxylation often exhibits large intramolecular KIEs (i.e., k_H/k_D = 4.2,[199] measured using partially deuterated ethane, where k_H/k_D is the ratio of the rates of C–H and C–D functionalization)

* Data, figures, and text in this chapter were adapted with permission from reference Wang, C.-H.; Das, A.; Gao, W.-Y; Powers, D. C. *Angew. Chem. Int. Ed.* **2018**, 57, 3676–3681, copyright 2018 Wiley-VCH Verlag GmbH & Co.

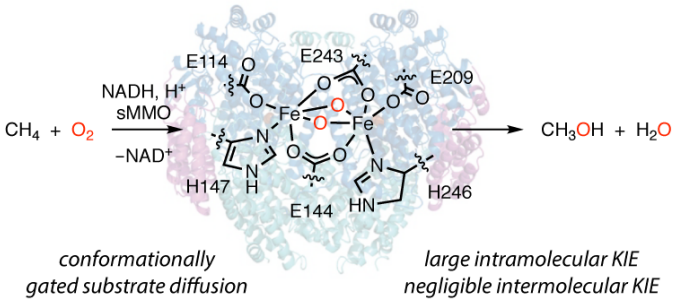

Figure III-1. Confinement of intermediate Q within the active site of sMMO is critical to intermolecular C–H oxidation in biology. Substrate flux to and product egress from the active site are carefully controlled by conformationally gated diffusion. For many substrates, the relative magnitudes of the intramolecular deuterium KIE, determined for the oxidation of partially deuterated substrates, and the intermolecular KIE, determined by competitive oxidation of a mixture of perdeuterated and nondeuterated substrate, indicate that conformationally gated substrate diffusion is turnover-limiting. Reprinted from reference 7. Copyright 2011 American Chemical Society.

but negligible intermolecular KIEs (i.e., k_H/k_D = 1.0,[200,201] measured using mixtures of perdeuterated and nondeuterated substrates).[202,203] The combination of large intramolecular KIEs and small intermolecular KIEs has been interpreted to indicate that while C–H cleavage is involved in hydroxylation, diffusional barriers, which are not sensitive to isotopic substitution, are rate-determining. Similar experimental data indicate that substrate access to compound I, the oxoiron intermediate in cytochrome P450s,[204-206] can also be diffusion-limited.

In the absence of a protein superstructure, reactive M–L multiply bonded complexes can participate in a variety of decomposition reactions, such as ligand oxidation chemistry, bimolecular dimerization, and solvent oxidation reactions, which prevent the utilization of these reactive structures for intermolecular C–H functionalization reactions.[207-209] For example, diruthenium nitride **III-2** generated *in situ* by the photolysis of diruthenium azide **III-1** participates in facile intramolecular C–H amination of proximal

ligand-based C–H bonds to afford amido complex **III-3** (**Figure III-2a**).[210-212] Metal–organic frameworks (MOFs), which are porous materials based on metal ions and organic linking groups, have been advanced as catalysis platforms based on catalyst site isolation and because the pore space provides an opportunity to localize substrates in proximity to catalyst sites.[46,213-216] To leverage many of the unique opportunities of MOFs in catalysis, substrates must diffuse to interstitial lattice-confined catalyst sites. Whereas indirect evidence is available for the impact of diffusion on substrate functionalization in some cases,[217-219] experimental tools to directly evaluate substrate diffusion through porous materials during interstitial chemistry are lacking.

We were attracted to the hypothesis that confinement of Ru_2 nitride intermediates that are isoelectronic to **III-2** within porous coordination lattices could enable intermolecular C–H amination. The development of an amination reaction by lattice-confined carboxylate-supported Ru_2 sites was guided by the following design principles: 1) M–M cooperation in a Ru_2 nitride intermediate would provide access to highly reactive M–L multiply bonded intermediates,[168,220] **III-2**) unlike the formamidinate ligands that are used to stabilize **III-2**, carboxylate ligands would not present ligand-based C–H bonds in proximity to reactive M–L multiple bonds, **III-3**) confinement of reactive intermediates[221-223] as structural elements of a MOF lattice would suppress bimolecular nitride coupling reactions,[224] and 4) material porosity could colocalize the substrate in proximity to the

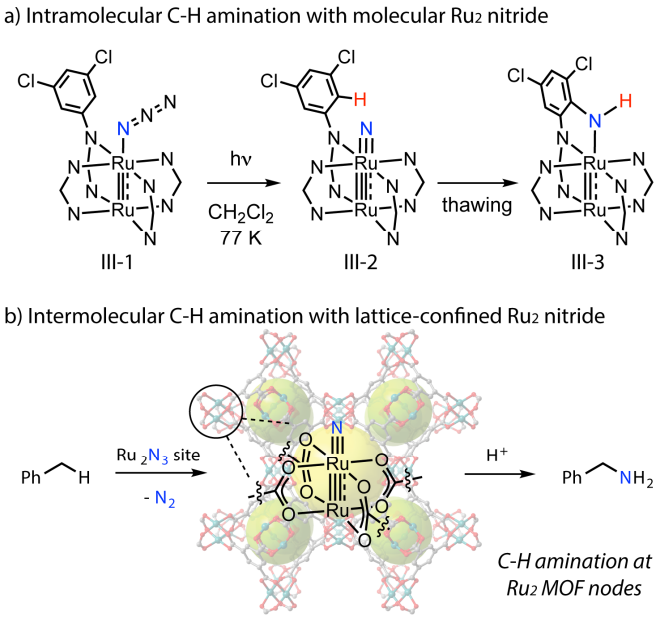

Figure III-2**. Nitrogen-atom transfer reactions.** a) Molecular Ru_2 nitride III-2 participates in facile C–H amination of proximal ligand-based C–H bonds. This chemistry exemplifies a challenge that is frequently encountered in leveraging reactive M–L multiple bonds for intermolecular C–H functionalization. b) Lattice confinement of reactive intermediates within porous materials can enable intermolecular group transfer chemistry. Herein, we disclose toluene amination at a Ru_2 MOF node. Similar to sMMO, slow substrate diffusion, as evidenced by the disparity of the intra- and intermolecular KIEs, is operative in this system.

reactive Ru_2 nitride to facilitate intermolecular nitrogen atom transfer (NAT). Herein, we report the intermolecular amination of toluene at a Ru_2 nitride intermediate confined as part of a MOF lattice (**Figure III-2b**). Furthermore, using the relative magnitudes of the intra- and intermolecular KIEs for toluene amination, we demonstrate that substrate diffusion in the developed porous material is slower than C–H amination. We anticipate that the developed kinetic tools will be useful to the ongoing development of catalysis with porous materials.

III.2 Results

We initiated our examination of the potential of lattice-confined intermolecular group transfer chemistry with $[Ru_6btc_4Cl_3]$, a porous MOF comprising $Ru_2^{II,III}$ nodes and 1,3,5-benzenetricarboxylate (btc^{3-}) linkers.[167,225,226] $[Ru_6btc_4Cl_3]$ is isomorphous with Cu_3btc_2 (HKUST-1).[170] M_3btc_2 networks display a three-dimensional channel structure and feature three distinct pore environments.[227] The smallest pore displays an 8.1 Å M-to-M separation and is accessed via a 4.0 Å aperture (M–M distance minus two van der Waals radii of Ru). The two larger pores feature M-to-M separations greater than 11.4 Å and are accessed through a 7.3 Å aperture (M–M distance minus two van der Waals radii of Ru). In situ X-ray diffraction studies have demonstrated that while small guests, such as methanol (kinetic diameter: 3.7 Å[228]), can access all three pores, larger guests, such as toluene (kinetic diameter: 5.9 Å[228]), only access the two larger pores (**Figure III-3**).[227]

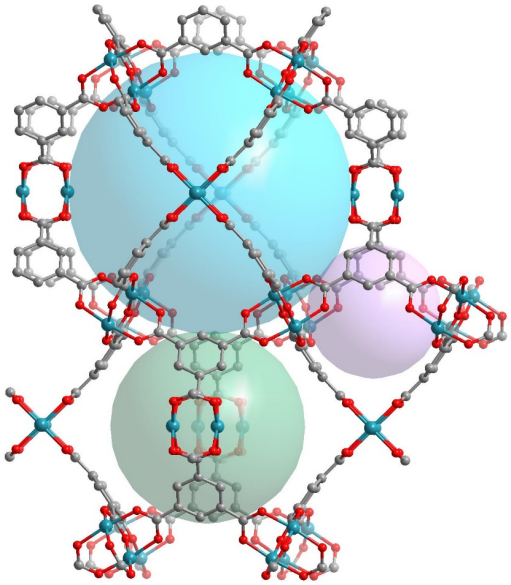

Figure III-3. Structure of M_3btc_2. M_3btc_2 materials are a three-dimensional porous network composed of three different types of pores. Detailed analysis (*Chem. Mater*. 2014, *26*, 4712) has demonstrated that toluene (kinetic diameter: 5.9 Å) molecules cannot be adsorbed into the smallest pore (light pink) due to the molecular sieving effect. The other two pores (light green and light blue) offer the same aperture size (Ru···Ru distance: 11.4 Å; Ru···Ru distance minus van der Waals radii: 7.3 Å) for substrate access. The window size of the smallest pore is 4.0 Å (Ru...Ru distance minus van der Waals radii).

Solvothermal combination of $Ru_2(OAc)_4Cl$ and H_3btc in H_2O and AcOH at 160 °C afforded $[Ru_6btc_4Cl_3]$ (**Figure III-4a**).[225] Powder X-ray diffraction (PXRD) of the as-synthesized material indicated that the obtained network is isostructural with Cu_3btc_2 (HKUST-1, **Figure III-4b**; see **Figure III-5** for a comparison of experimental and computed PXRD patterns[170,225]). Elemental analysis of $[Ru6btc_4Cl_3]$ indicated a 2:1 mixture of Cl and OH ligands on the Ru_2 sites, which is consistent with previous reports on this material (empirical formula: $[Ru_6btc_4Cl_2OH]$).[225] N_2 sorption experiments indicated a BET surface area of 746 $m^2\,g^{-1}$ (Langmuir surface area of 1056 $m^2\,g^{-1}$, Figure

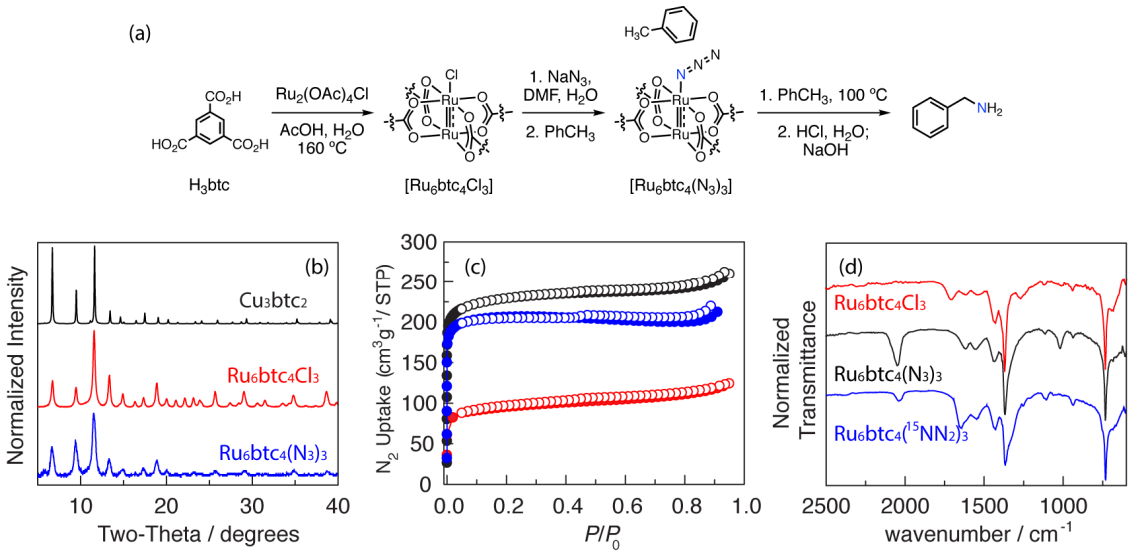

Figure III-4. Synthesis and characterization of Ru_6btc_4Cl, $Ru_6btc_4(N_3)_3$, and $Ru_6btc_4(^{15}NN_2)_3$. (a) Synthesis of $[Ru_6btc_4(N_3)_3]$ and use as a platform for intermolecular nitrogen-atom transfer chemistry. (b) PXRD patterns of $[Ru_6btc_4(N_3)_3]$ and $[Ru_6btc_4Cl_3]$, which are isostructural to Cu_3btc_2. (c) N_2 sorption isotherms for $[Ru_6btc_4Cl_3]$ activated at 150 °C (adsorption (●), desorption (○)), for $[Ru_6btc_4Cl_3]$ activated at 25 °C (adsorption (●), desorption (○)), and for $[Ru_6btc_4(N_3)_3]$ activated at 25 °C (adsorption (●), desorption (○)). (d) IR spectra of $[Ru_6btc_4Cl_3]$, $[Ru_6btc_4(N_3)_3]$, and $[Ru_6btc_4(^{15}NN_2)_3]$.

3c (black)), which is in good agreement with the literature (BET surface area=704 $m^2\ g^{-1}$ and Langmuir surface area=891 $m^2\ g^{-1}$).[225]

N_3-for-Cl exchange was accomplished by soaking $[Ru_6btc_4Cl_3]$ in an aqueous N,N-dimethylformamide (DMF) solution of NaN_3. Exchange of chloride in preference to hydroxide at Ru_2 lattice sites was evidenced by elemental analysis, which was consistent with a $[Ru_6btc_4Cl_{0.26}(N_3)_{1.44}(OH)_{1.3}]$ formulation, and may arise from the relative dissociation energies of Ru–Cl and Ru–OH bonds.[229] In an alternative synthetic route, a material with the empirical formula $[Ru_6btc_4(N_3)_3]$ was accessed by treatment of $[Ru_6btc_4Cl_3]$ first with trimethylsilyl triflate (TMSOTf) in CH_2Cl_2 followed by NaN_3 in aqueous DMF solution. The azide-exchanged materials obtained from these two

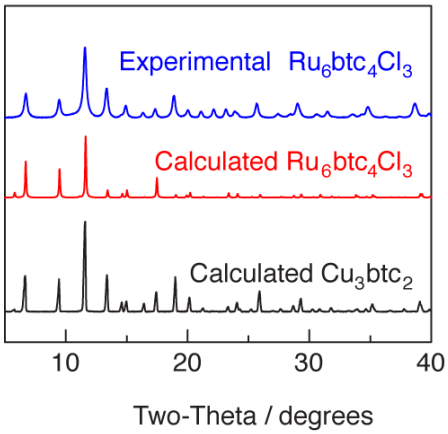

Figure III-5. PXRD patterns of M_3btc_2 isostructures. PXRD patterns of [$Ru_6btc_4Cl_3$] (experimental) and [$Ru_6btc_4Cl_3$]. Comparison with calculated PXRD pattern of Cu_3btc_2.

procedures displayed identical amination chemistry (*vide infra*). Prior to subsequent use, the extent of azide exchange in each batch was assessed by elemental analysis. The IR spectrum of [$Ru_6btc_4(N_3)_3$] displays an isotope-sensitive signal at 2048 cm^{-1}, which is shifted to 2031 cm^{-1} in [$Ru_6btc_4(_{15}NN_2)_3$] (prepared using $Na^{15}NN_2$; **Figure III-4d**). Ligand exchange was accompanied by a bathochromic shift of the solid-state UV-Vis absorption features, similar to the UV-Vis spectral changes observed during N_3-for-Cl ligand exchange in the synthesis of compound **III-1** (**Figure III-6**). [$Ru_6btc_4(N_3)_3$] is isomorphous with [$Ru_6btc_4Cl_3$] based on PXRD (**Figure III-4b**). Extensive soaking of [$Ru_6btc_4(N_3)_3$] in MeOH followed by soaking in CH_2Cl_2 allowed for low-temperature activation of this material and determination of a BET surface area of 619 m^2 g^{-1} (**Figure III-4c**, red curve; see **Figure III-7** and **Table III-1** for an additional discussion of the activation of [$Ru_6btc_4(N_3)_3$]). For comparison, activation of [$Ru_6btc_4Cl_3$] under identical low-temperature conditions yielded a BET surface area of 662 m^2 g^{-1} (**Figure III-4c**, blue curve). X-ray absorption near edge structure (XANES) and magnetometry data collected

for $[Ru_6btc_4(N_3)_3]$ indicate that the S = 3/2 $Ru_2^{II,III}$ sites in $[Ru_6btc_4Cl_3]$ were maintained following ion exchange[230] (**Figures III-8** and **III-S9**, respectively).

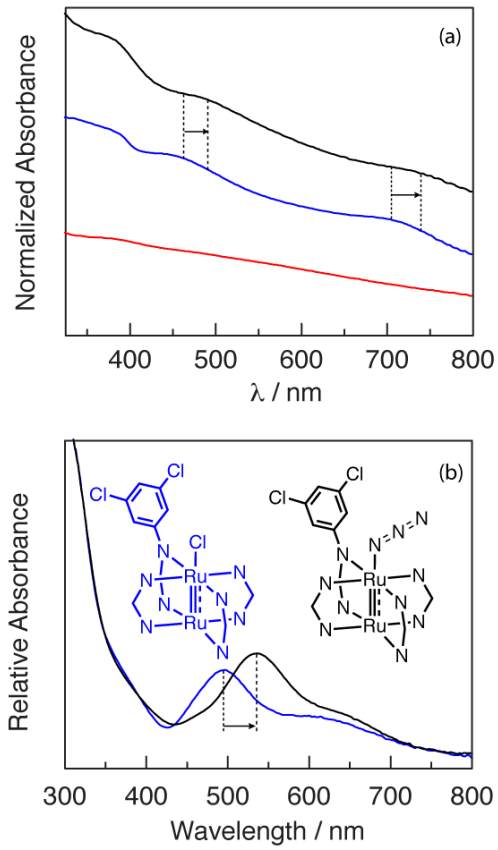

Figure III-6. Solid-state UV-Vis spectra of Ru_2 paddlewheels. (a) Solid-state UV-vis spectra collected for $[Ru_6btc_4(N_3)_3]$ (—), $[Ru_6btc_4Cl_3]$ (—), $[Ru_6btc_4]$ (—). A bathochromic shift of the absorbances of $[Ru_4btc_6Cl_3]$ is observed in $[Ru_4btc_6(N_3)_3]$. (b) A similar bathochromic shift upon exchange of Cl (—) for N_3 (—) is observed in the illustrated formamidinate supported Ru_2 complexes.

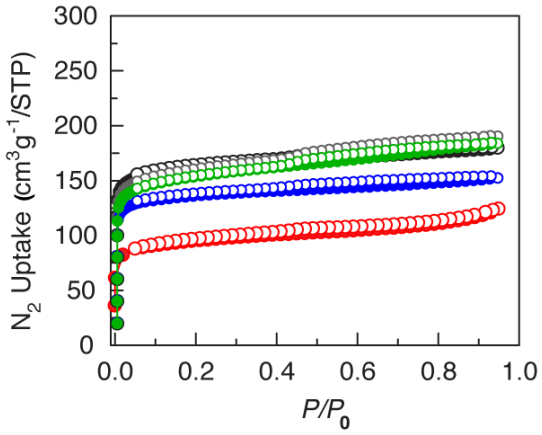

Figure III-7. Comparison of various activation conditions for [$Ru_6btc_4(N_3)$]. N_2 sorption isotherms collected at 77 K for [$Ru_6btc_4(N_3)_3$] that was (a) soaked in MeOH and activated at 25 °C ((adsorption (●), desorption (○)), (b) soaked in MeOH and activated using supercritical CO_2 ((adsorption (●), desorption (○)), (c) soaked in PhH and activated by lyophilization ((adsorption (●), desorption (○)), (d) soaked in acetone and activated at 25 °C ((adsorption (●), desorption (○)), and, (e) soaked in CH_2Cl_2 and activated at 25 °C ((adsorption (●), desorption (○)).

Table III-1 Surface areas for Zn_3btei and Pd_3btei at different conditions

Activation Protocol	MeOH soaked	CH_2Cl_2 soaked	Acetone soaked	PhH lyophilization	Super critical CO_2
BET (m^2 g^{-1})	281	619	607	581	523
Langmuir (m^2 g^{-1})	440	700	692	663	590

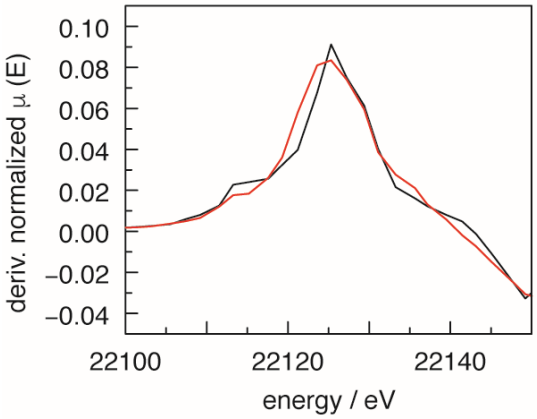

Figure III-8. XANES spectra of [$Ru_6btc_4Cl_3$] (—) and [$Ru_6btc_4(N_3)_3$] (—). The edge energy in [$Ru_6btc_4(N_3)_3$] is slightly higher than that in [$Ru_6btc_4Cl_3$], which is inconsistent with reduction of the Ru_2 sites upon azide addition. Reduction of [Ru_6btc_4Cl] to [Ru_6btc_4] is expected to result in ~5 eV shift lower in energy of the maximum of the above plot.

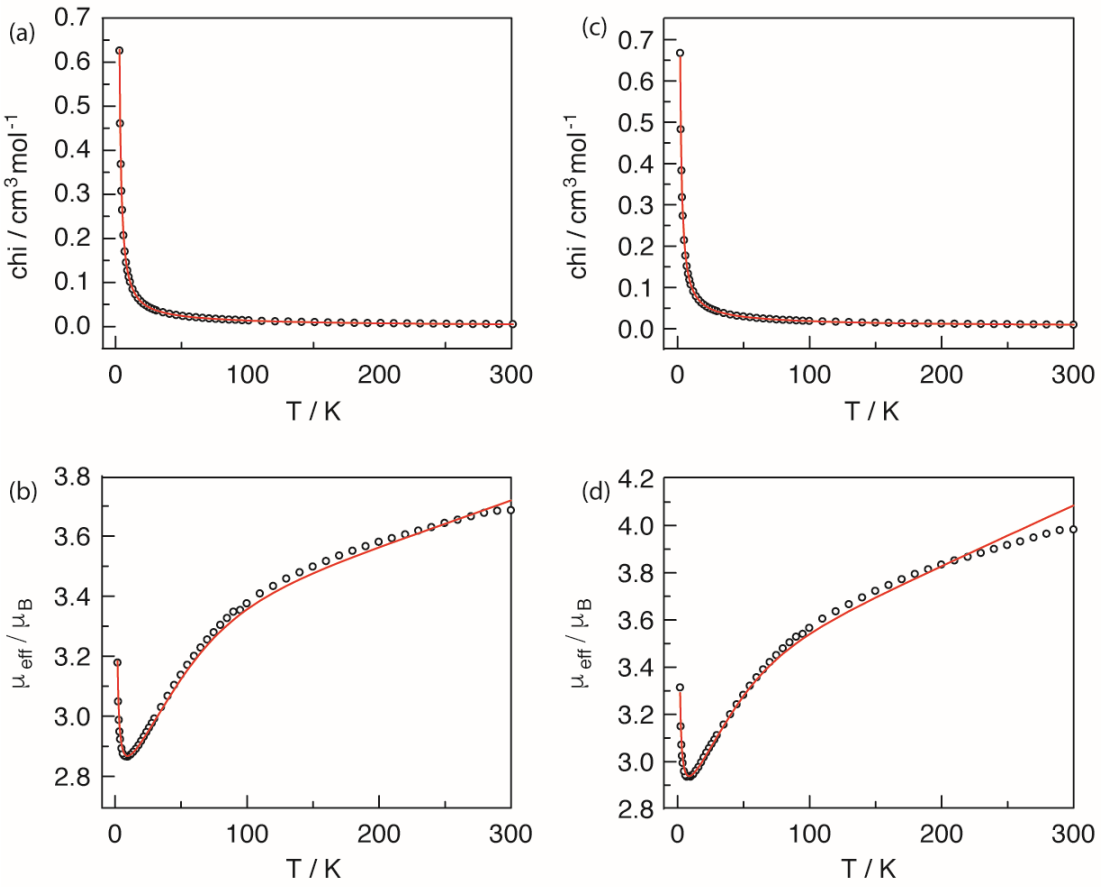

Figure III-9. Magnetic susceptibility experiment and fit. (a) χ vs. T for $[Ru_6btc_4(N_3)_3]$; experiment (○) and fit (—). (b) μ_{eff} / μ_B vs. T for $[Ru_6btc_4(N_3)_3]$; experiment (○) and fit (—). (c) (a) χ vs. T for $[Ru_6btc_4Cl_3]$; experiment (○) and fit (—). (d) μ_{eff} / μ_B vs. T for $[Ru_6btc_4Cl_3]$; experiment (○) and fit (—).

Table III-2 Parameters for magnetic susceptibility fitting

	g	D (cm^{-1})	zJ (cm^{-1})	TIP ($cm^3\ mol^{-1}$)	P
$[Ru_6btc_4Cl_3]$	1.93	73	0.29	3.60×10^{-3}	0.200
$[Ru_6btc4(N_3)_3]$	1.93	90	0.27	2.15×10^{-3}	0.215

bond dissociation energy (BDE) of $PhCH_2$–H: 90 kcal mol^{-1})[231] into the porous material by soaking $[Ru_6btc_4(N_3)_3]$ in $PhCH_3$ for 6 h. Heating the $PhCH_3$-impregnated material ($PhCH_3$@$[Ru_6btc_4(N_3)_3]$) to 100 °C resulted in the disappearance of the azide stretching mode (2048 cm^{-1}) in the IR spectrum (**Figure III-10**).

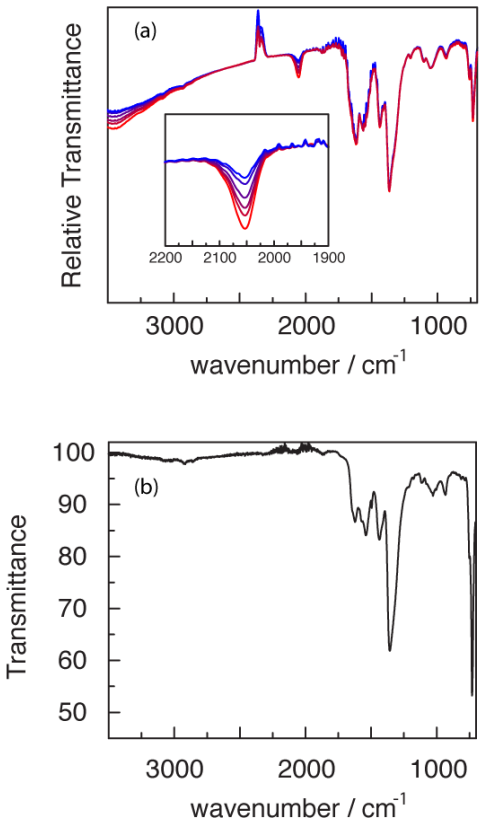

Figure III-10. *In situ* solid-state IR spectra of $[Ru_6btc_4(N_3)_3]$. (a) *In situ* IR spectra collected while heating $[Ru_6btc_4(N_3)_3]$ in a KBr pellet at 90 °C. Spectra were collected at the following times: 0 h (—), 1 h (—), 3 h (—), 6 h (—), 24 h (—), and 48 h (—). (b) IR spectrum collected following thermolysis of $PhCH_3$@$[Ru_6btc_4(N_3)_3]$.

Following acidic work-up, benzylamine was observed in 32% yield based on available Ru_2N_3 sites. We speculated that the low yield may be due to inefficient substrate diffusion to all available Ru_2N_3 sites, for example, because of size exclusion from the smallest pores in M_3btc_2.[227] The generated benzylamine was characterized by gas chromatography (GC) co-injection (**Figure III-11**), ^{1}H NMR analysis (**Figure III-12**), and electrospray ionization mass spectrometry (ESI-MS; *m/z* = 108.0805, calculated *m/z* = 108.0808 ($PhCH_2NH_3^+$); **Figure III-13**).

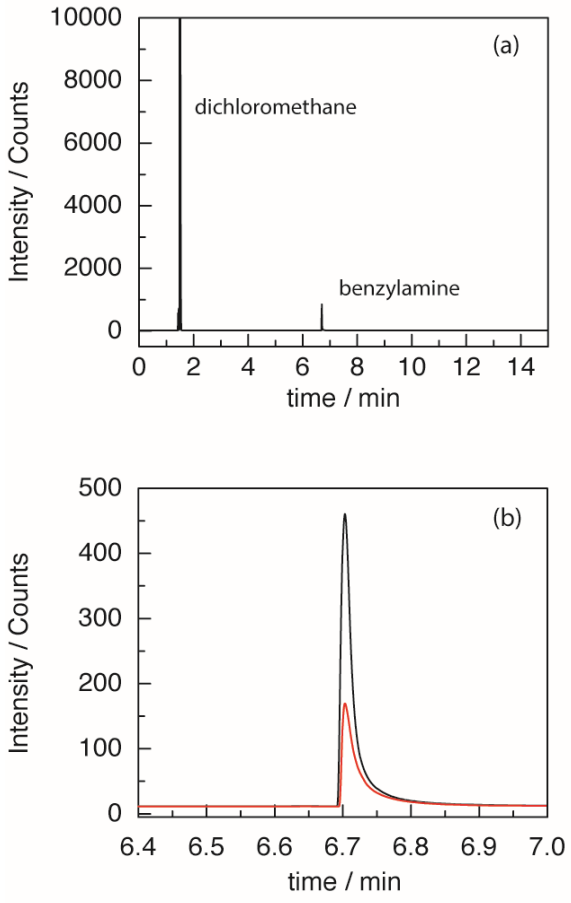

Figure III-11. GC trace of product and benzylamine. (a) GC trace of the thermolysis of $PhCH_3$@[$Ru_6btc_4(N_3)_3$]. (b) Co-injection of thermolysis of $PhCH_3$@[$Ru_6btc_4(N_3)_3$] (—) with an authentic sample of benzylamine (—) confirms the evolution of benzylamine.

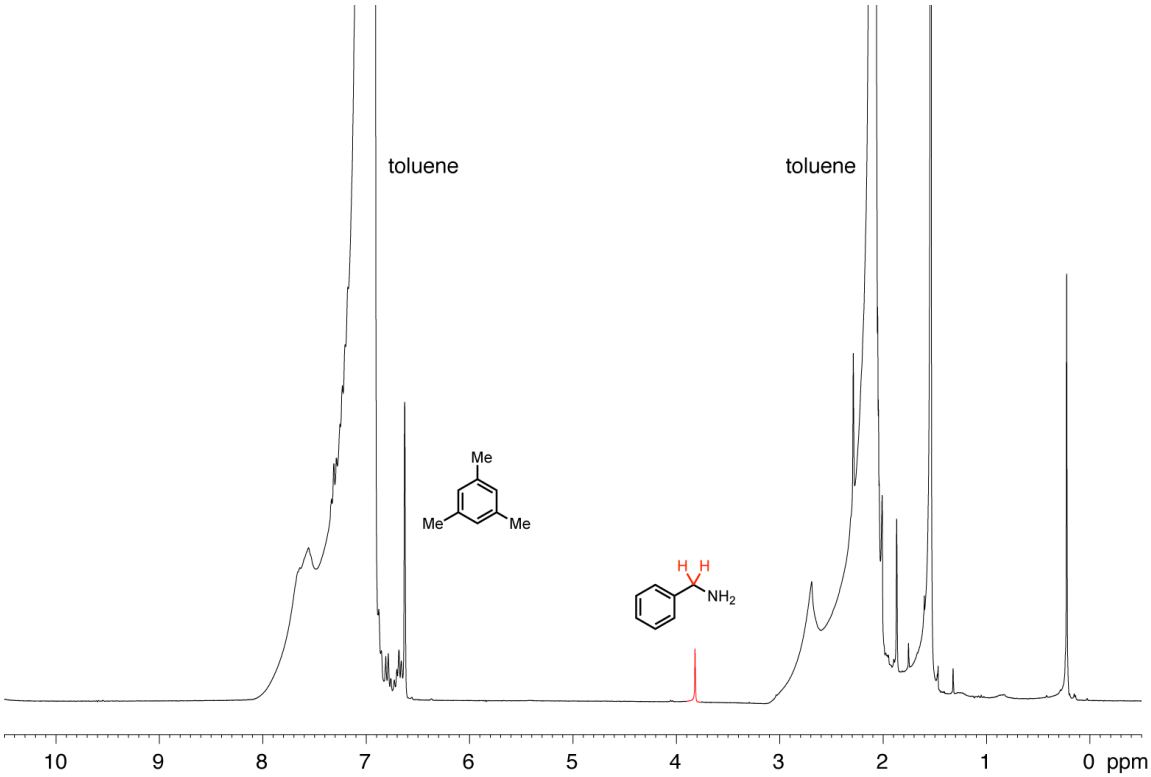

Figure III-12. ^{1}H NMR of the product mixture. ^{1}H NMR of the product mixture derived from the stoichiometric reaction of $[Ru_6btc_4(N_3)_3]$ with toluene. The yield of benzylamine was calculated by comparison of the intensity of the benzylamine signal at ~3.8 ppm with the intensity of the signal at ~6.6 ppm resulting from the addition of a known amount of mesitylene to the NMR sample.

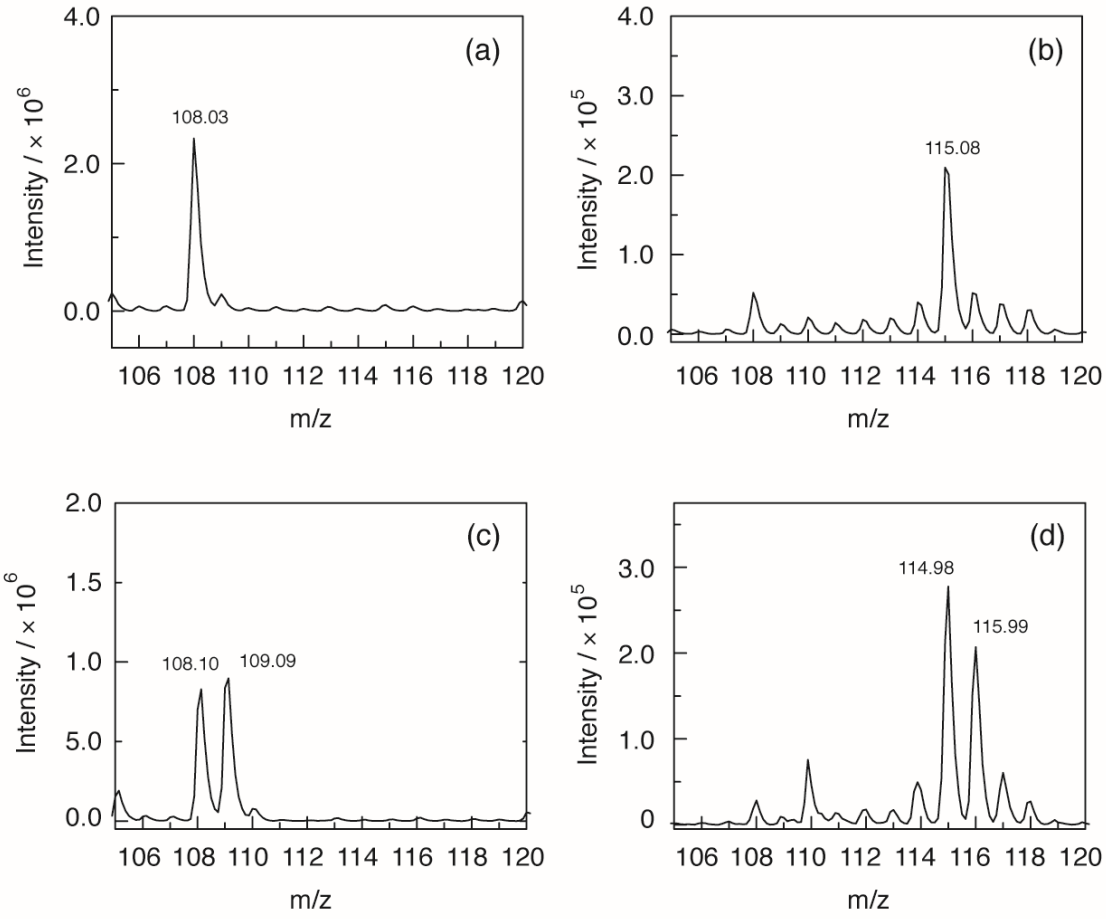

Figure III-13. Plots of ESI MS data showing the amination products obtained from thermolysis of $[Ru_6btc_4(N_3)_3]$ and $[Ru_6btc_4(^{15}NN_2)_3]$ in toluene. (a) Product mixture obtained from $[Ru_6btc_4(N_3)_3]$ and toluene; (b) product mixture obtained from $[Ru_6btc_4(N_3)_3]$ and d_8-toluene; (c) product mixture obtained from $[Ru_6btc_4(^{15}NN_2)_3]$ and toluene; and (d) product mixture obtained from $[Ru_6btc_4(^{15}NN_2)_3]$ and d_8-toluene. High-resolution MS confirms the exact mass of each of the obtained isotopomers.

Based on PXRD (**Figure III-14**) and gas sorption (**Figure III-15**) analyses of the spent Ru_2-based material, framework crystallinity and porosity are maintained following thermolysis.

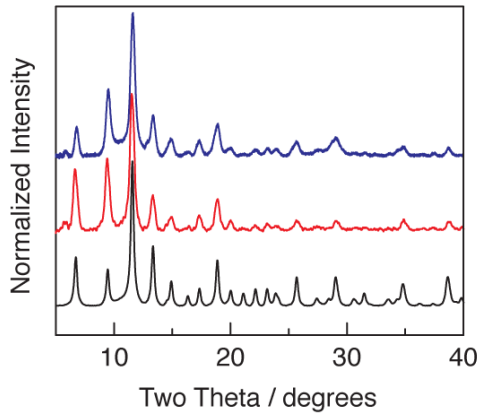

Figure III-14. PXRD patterns of $[Ru_6btc_4Cl_3]$ (—), $[Ru_6btc_4(N_3)_3]$ (—), and $PhCH_3@[Ru_6btc_4(N_3)_3]$ following thermolysis (—). The similarity of the PXRD patterns suggests that the crystallinity of the material is not substantially altered during thermolysis.

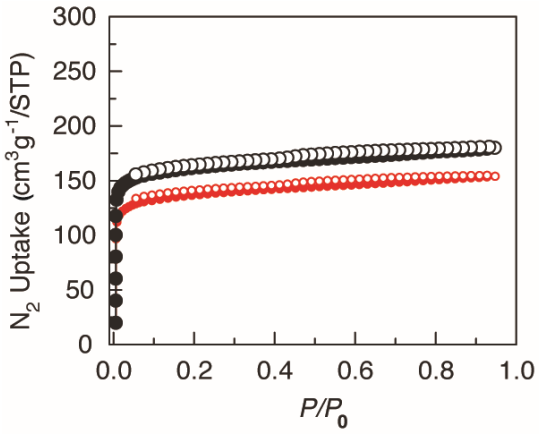

Figure III-15. N_2 sorption isotherms. N_2 sorption isotherms collected at 77 K for (a) $[Ru_6btc_4(N_3)_3]$ that was soaked in CH_2Cl_2 and activated at 25 °C ((adsorption (●), desorption (○)) and (b) $PhCH_3@[Ru_6btc_4(N_3)_3]$ that was thermolyzed, soaked in CH_2Cl_2, and activated at 25 °C ((adsorption (●), desorption (○)). The BET surface area for $PhCH_3@[Ru_6btc_4(N_3)_3]$ following thermolysis was determined to be 532 m^2/g (Langmuir surface area = 602 m^2/g).

To confirm that intermolecular amination of toluene had occurred, we carried out a series of isotope labeling experiments. First, using toluene-d_8 resulted in the observation of benzylamine-d_7 (*m/z*=115.1246, calculated *m/z*=115.1247 ($C_6D_5CD_2NH^{3+}$)). Second, amination of toluene with [$Ru_6btc_4(^{15}NN_2)_3$] led to a 1:1 mixture of ^{14}N- and ^{15}N-benzylamine, which was expected because $^{15}NN_2$ can bind via either the labeled or the unlabeled terminus (ESI-MS data are summarized in **Figure III-13**). Control experiments in which the NaN_3 soaking solution was decanted and heated in the presence of toluene resulted in no benzylamine, which confirmed that the observed amination chemistry proceeds in the solid state. The observation of benzylamine and the described isotope labeling experiments confirmed the viability of intermolecular group transfer chemistry with the developed Ru_2-based materials.

Cyclohexane and benzene do not participate in amination with [$Ru_6btc_4(N_3)_3$], which may be due to the C–H bond strength of these substrates (BDEs: C_6H_{11}–H: 96 kcal mol^{-1};[232] C_6H_5–H: 113 kcal mol^{-1})[231]. ortho-Xylene is a competent substrate for amination (ca. 5% yield). In addition, meta- and para-xylene do not participate in amination, which we hypothesized to be due to restricted diffusion into the porous Ru_2 material (*vide infra*).

Unlike lattice-isolated $Ru_2^{II,III}$ sites, analogous molecular $Ru_2^{II,III}$ carboxylate complexes do not participate in toluene amination chemistry. We carefully examined the reaction chemistry of the $Ru_2^{II,III}$ complex $Ru_2(OBz)_4Cl$ with NaN_3 to better understand the dichotomy between lattice-isolated and homogeneous complexes (OBz = benzoate). Treatment of $Ru_2(OBz)_4Cl$, or the more soluble analogue $Ru_2(OBz)_4BF_4$, with NaN_3 resulted in rapid one-electron reduction to generate the $Ru_2^{II,II}$ complex $Ru_2(OBz)_4$ with

concurrent evolution of N_2 (detected by GC analysis; **Figure III-16**). Formation of $Ru_2(OBz)_4$ was indicated by ^1H NMR, IR, and UV-Vis spectroscopy (**Figures III-17**, **III-18**, and **III-19**, respectively), and the structure of $Ru_2(OBz)_4$ was confirmed by X-ray diffraction.

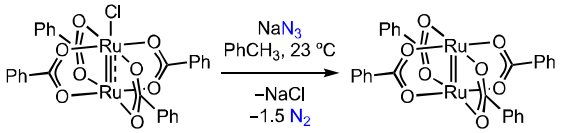

Figure III-16. Reductive decomposition of molecular analog. In contrast to lattice confined Ru_2 tetracarboxylates, which support Ru_2 azide sites (*i.e.* $[Ru_6btc_4(N_3)_3]$), molecular site analogs participate in rapid reductive decomposition reactions. Treatment of $Ru_2(OBz)_4Cl$ with NaN_3 results in rapid reduction of the Ru_2 core to generate $Ru_2(OBz)_4$ with concurrent evolution of N_2.

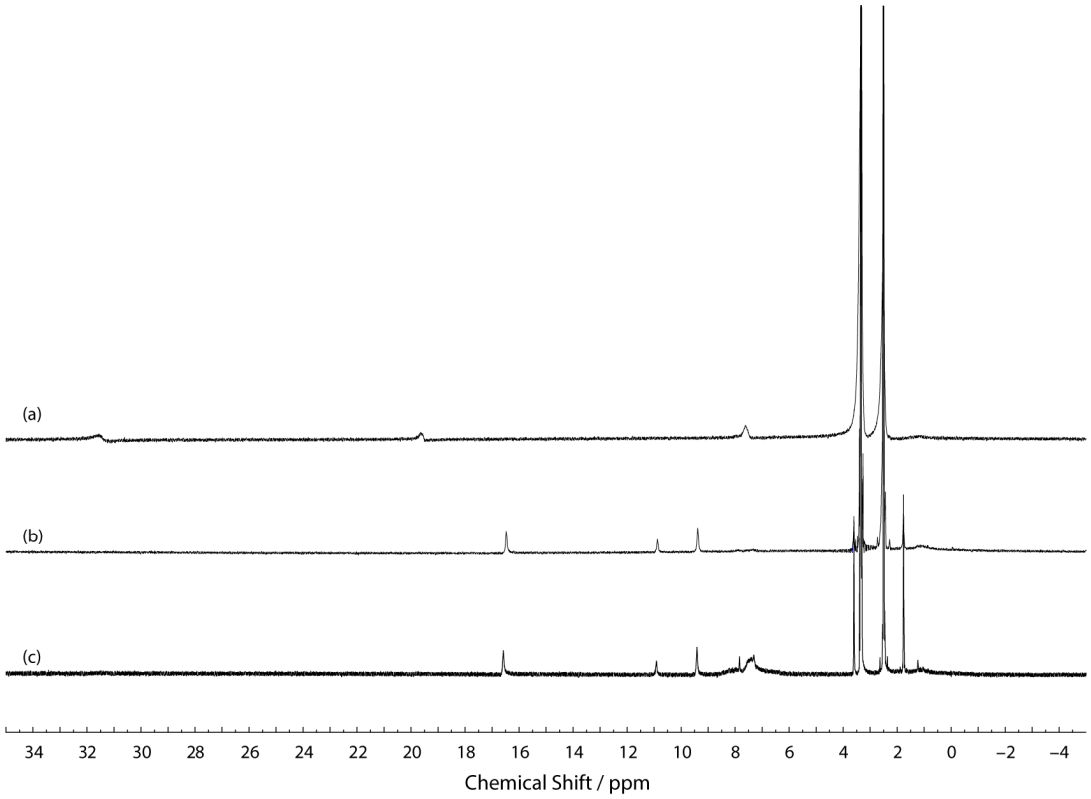

Figure III-17. ^{1}H NMR of reductive decomposition of molecular analog. (a) ^{1}H NMR of $Ru_2(OBz)_4Cl$ acquired at 23 °C in d_6-DMSO. (b) ^{1}H NMR of $Ru_2(OBz)_4(THF)_2$ acquired at 23 °C in d_6-DMSO. (c) ^{1}H NMR of $Ru_2(OBz)_4BF_4$ + NaN_3 acquired at 23 °C in d_6-DMSO.

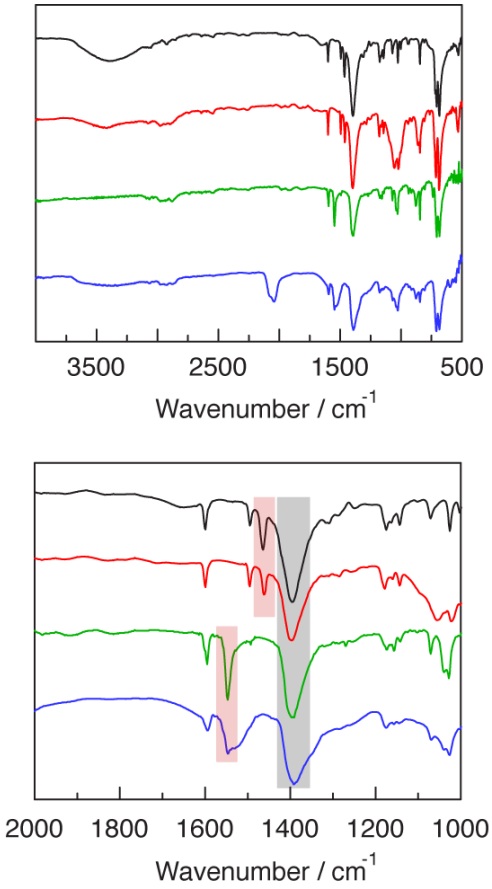

Figure III-18. IR spectra of reductive decomposition of molecular analog. IR spectra of $Ru_2(OBz)_4Cl$ (—; ν_{asym}=1464, ν_{sym}=1394), $Ru_2(OBz)_4BF_4$ (—; ν_{asym}=1461, ν_{sym}=1396), $Ru_2(OBz)_4(THF)_2$ (—; ν_{asym}=1547, ν_{sym}=1393), and $Ru_2(OBz)_4BF_4$ + NaN_3 (—; ν_{asym}=1545, ν_{sym}=1391).

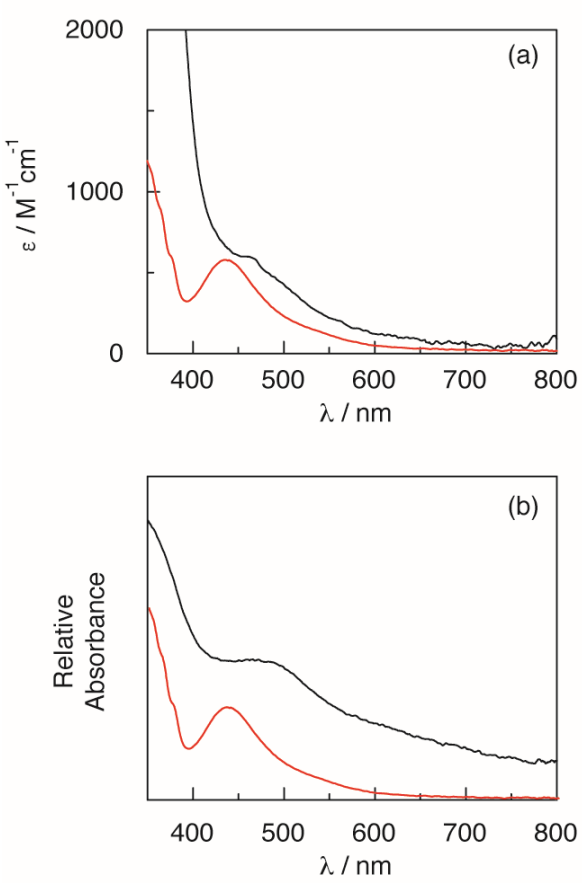

Figure III-19. UV-Vis spectra of reductive decomposition of molecular analog. (a) Extinction spectra for $Ru_2(OBz)_4BF_4$ (—) and $Ru_2(OBz)_4(THF)_2$ (—) measured in THF. (b) Relative absorbance of $Ru_2(OBz)_4BF_4$ (—) and $Ru_2(OBz)_4BF_4$ with NaN_3 added (—); the higher baseline in the NaN_3 addition experiment is due to sample heterogeneity (NaN_3 is not completely soluble under these conditions).

We hypothesized that the evolution of N_2 proceeds through azide binding, extrusion of one equivalent of N_2 to generate a reactive nitride, and subsequent nitride coupling to generate an additional 0.5 equivalents of N_2. Consistent with this hypothesis, analysis of the N_2 evolved upon treatment of $Ru_2(OBz)_4BF_4$ with $Na^{15}NN_2$ revealed substantial formation of $^{15}N^{15}N$ (**Figure III-20**). Formation of $^{15}N^{15}N$ implies a bimolecular N_2-forming reaction from monolabeled $^{15}NN_2$. In contrast to the evolution of $^{15}N^{15}N$ from $Ru_2(OBz)_4BF_4$, no $^{15}N^{15}N$ was detected in the headspace following treatment of $Ru_6btc_4Cl_3$ with $Na_{15}NN_2$.

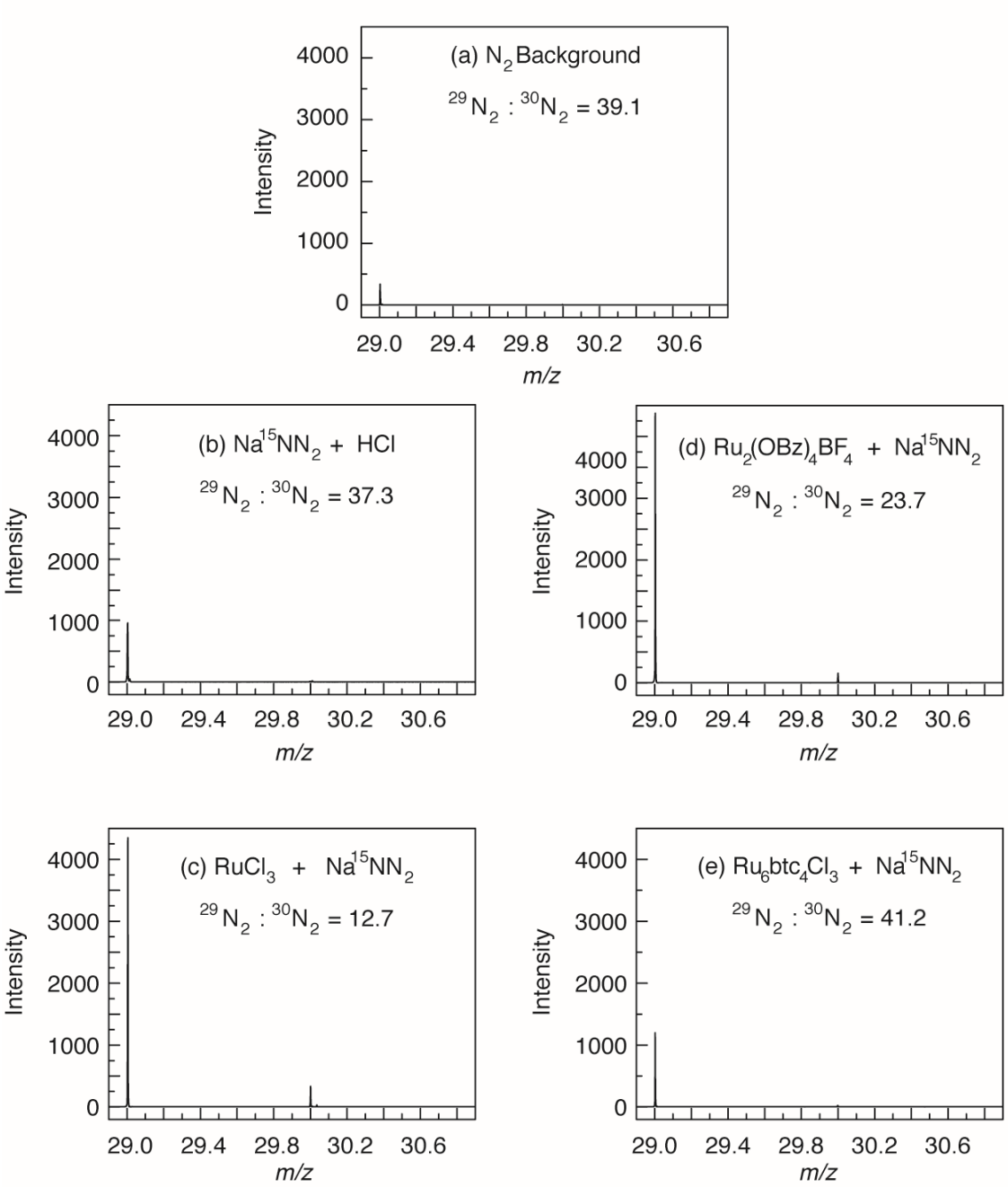

Figure III-20. MS data for N_2 evolution experiments. Only $^{29}N_2$ and $^{30}N_2$ are shown here. (a) EI MS of N_2 gas used in inert atmosphere gas manifolds. (b) EI MS of N_2 gas generated from HCl addition to $Na^{15}NN_2$. (c) EI MS of N_2 gas generated from addition of $Na^{15}NN_2$ to $RuCl_3$. (d) EI MS of N_2 gas generated from addition of $Na^{15}NN_2$ to $Ru_2(OBz)_4BF_4$. (e) EI MS of N_2 gas generated from addition of $Na^{15}NN_2$ to [$Ru_6btc_4Cl_3$].

To gain insight into the selectivity for benzylic versus aromatic C–H amination, we pursued a series of kinetic isotope effect (KIE) experiments (**Figure III-21**). Amination of toluene-d1 proceeded with an intramolecular k_H/k_D of 7.86(3) at 100 °C (Figure 5a; based on the Arrhenius equation, k_H/k_D = 13.2 would be expected at 25 °C). In contrast, amination of an equimolar mixture of toluene and toluene-d_8 at 100 °C afforded an intermolecular k_H/k_D of 1.02(2) (**Figure III-21b**). In these experiments, the benzylamine isotopomers were quantified by ESI-MS (data are collected in **Figures III-22a** and **III-23**). Control experiments using DCl to liberate benzylamine from our Ru_2 material confirmed that the determined KIEs are not influenced by the acidic work-up.

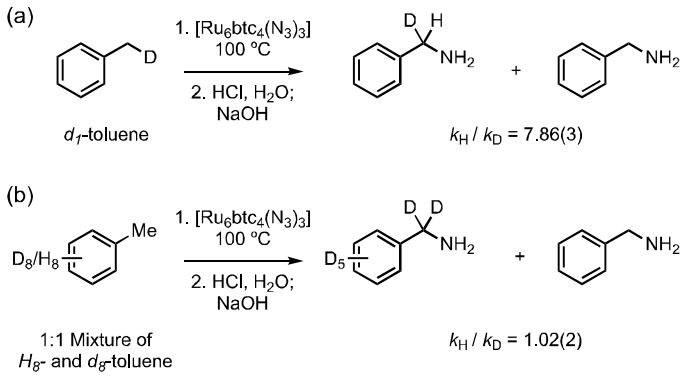

Figure III-21. KIEs of amination reaction. (a) The *intramolecular* KIE, measured with d_1-toluene, indicates that substantial C–H cleavage is involved in the C–H amination transition state. (b) The *intermolecular* KIE, measured with a 1:1 mixture of H_8- and d_8-toluene, indicates that substrate diffusion is slow relative to amination.

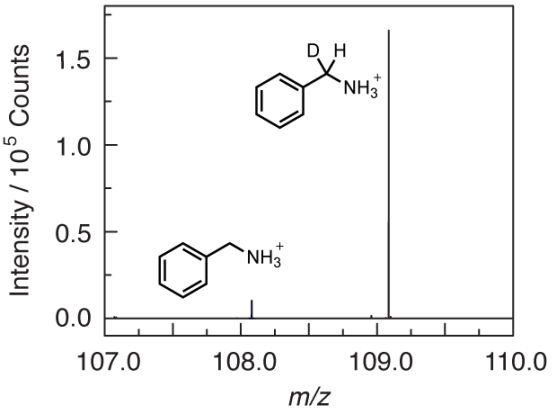

Figure III-22a. ESI MS data obtained following the amination of α-d_1-toluene with [$Ru_6btc_4(N_3)_3$].

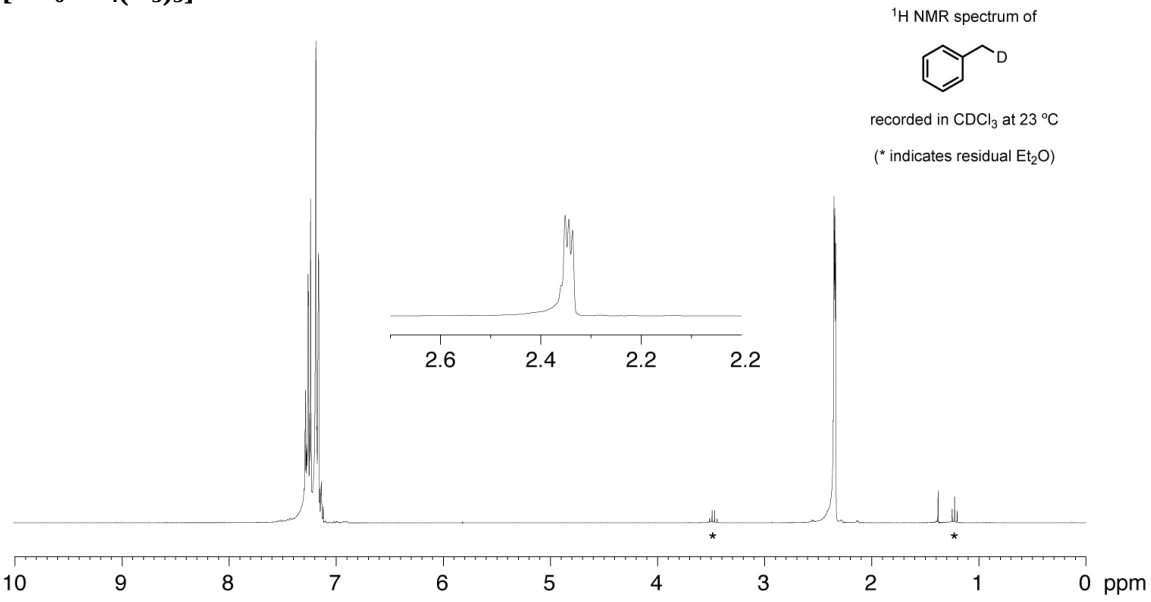

Figure III-22b. ^{1}H spectrum of the α-d_1-toluene used for the determination of the intramolecular KIE. The spectrum was recorded in $CDCl_3$ at 23 °C. Inset: Expansion of the benzylic signal which shows coupling to the deuterium label.

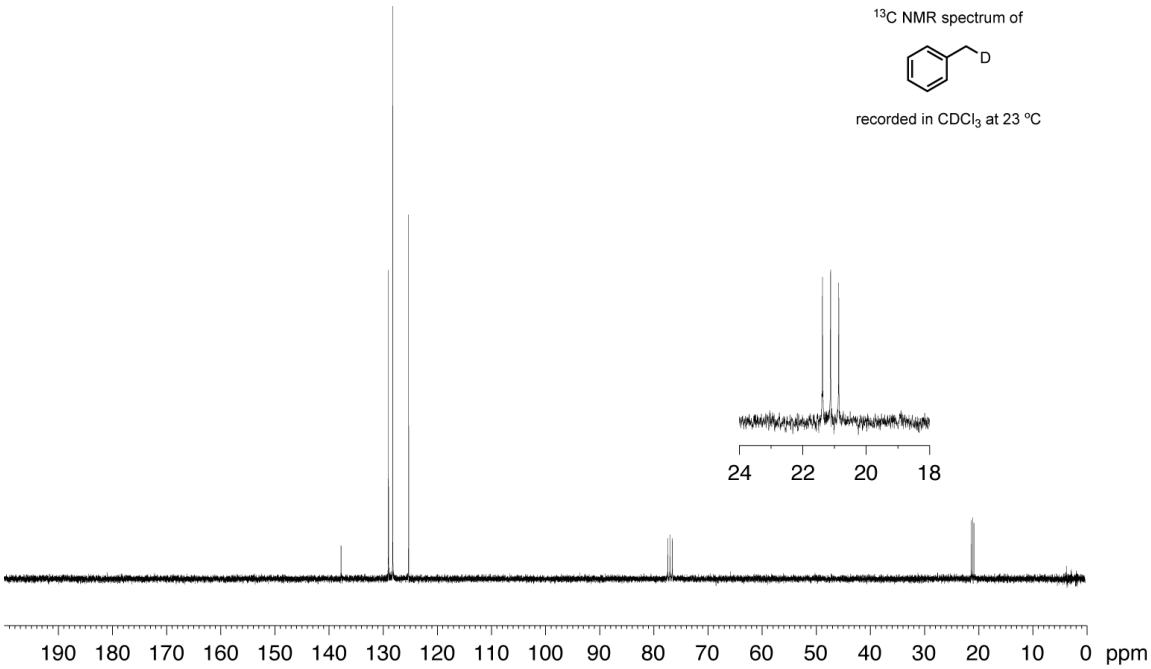

Figure III-22c. ^{13}C spectrum of the α-d_1-toluene used for the determination of the intramolecular KIE. The spectrum was recorded in $CDCl_3$ at 23 °C. Inset: Expansion of the benzylic signal which shows coupling to the deuterium label.

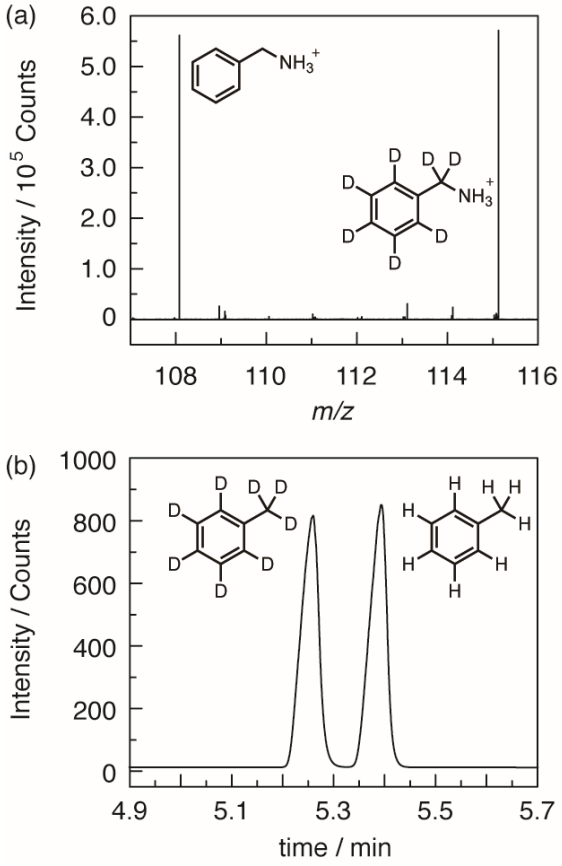

Figure III-23. Intermolecular KIE determination. (a) Integration of the MS signal at 108.0808 versus 115.1247 provided the ratio of C–H versus C–D cleavage. (b) The ratio of toluene and d_8-toluene in the substrate mixture was evaluated by gas chromatography. The elution order of toluene and d_8-toluene was determined by coinjection with authentic samples.

III.3 Discussion

The stoichiometric reactions described here constitute demonstration of a synthetic cycle for nitrogen-atom transfer to C–H bonds (**Figure III-24**). Lattice-confined Ru_2N_3 sites are generated by ion exchange into [$Ru_6btc_4Cl_3$] (step a). N_2 evolution from Ru_2N_3 sites provides access to a reactive nitride equivalent (step b) that is unable to participate in nitride dimerization, a process that is facile at molecular-site analogues (**Figure III-16**). Insertion of the lattice-confined nitride into a C–H bond of pore-localized toluene is believed to generate a benzylamido intermediate (step c). Subsequent protonation liberates benzylamine (step d). The observed amination of toluene at Ru_2 sites confined within a MOF lattice confirmed the hypothesis that lattice-confined Ru_2 nitrides participate in intermolecular C–H amination chemistry with pore-confined hydrocarbon substrates.

Given the demonstration of intermolecular NAT chemistry, and the observation that the crystallinity and porosity of the Ru_2-based material are maintained following thermolysis, one could envision achieving amination catalysis if appropriate proton and azide sources were available to regenerate the lattice-confined Ru_2 azide from a Ru_2 amido intermediate (steps d and a, **Figure III-24**).

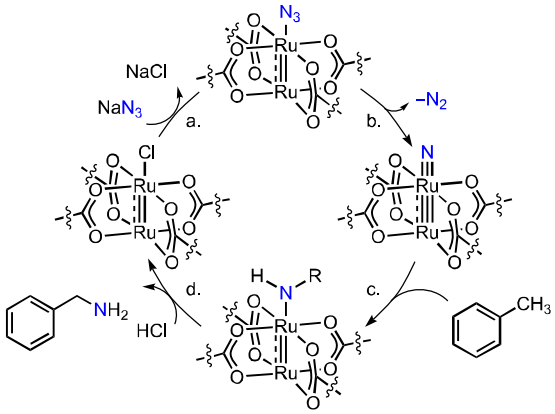

Figure III-24. A synthetic cycle for toluene amination. In single turnover experiments, each of the steps in the amination cycle has been demonstrated. Based on the relative magnitudes of *intra-* and *intermolecular* KIEs, lack of catalyst turnover is ascribed to restricted diffusion of substrates within $[Ru_6btc_4(N_3)_3]$.

Despite extensive experimentation, we have not yet identified conditions to achieve NAT catalysis. As each of the steps in the synthetic cycle illustrated in **Figure III-24** has been demonstrated in stoichiometric reactions, we speculated that restricted diffusion of substrates and reagents in the Ru_2 network may be responsible for the lack of observed catalyst turnover. Consistent with this hypothesis, prolonged presoaking of toluene into $[Ru_6btc_4(N_3)_3]$ was required to observe amination chemistry. Further, we determined by IR spectroscopy that exchange of toluene with toluene-d_8 in Ru_3btc_2-based materials is slow, and requires several hours for complete exchange (**Figure III-25**).

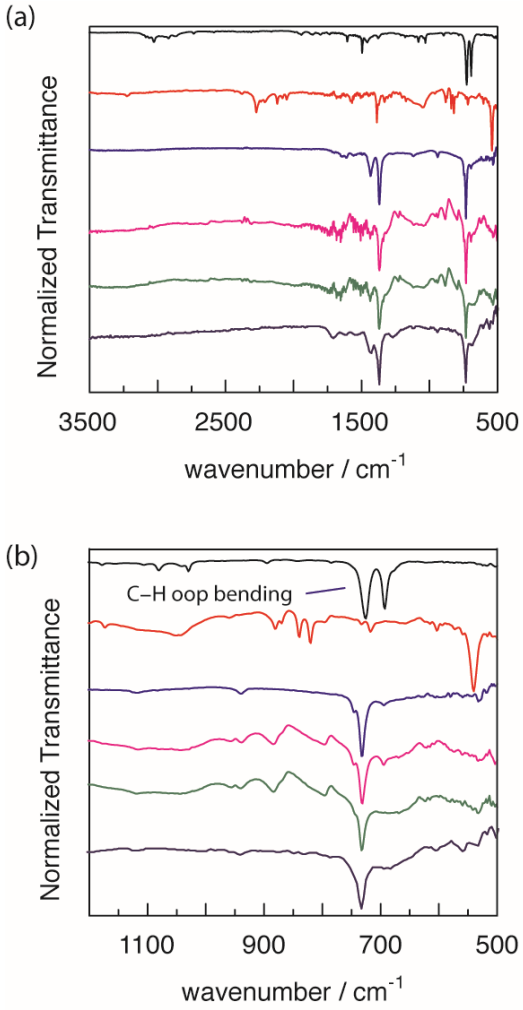

Figure III-25. Exchange of toluene with d_8-toluene was monitored by IR spectroscopy. An activated sample of [$Ru_3btc_2Cl_3$] was soaked in toluene for 20 h. Toluene was then decanted and d_8-toluene was added. Exchange of toluene took several hours as evidenced by the disappearance of the out-of-plane C–H bonding modes ~700 cm^{-1}. In both (a) and expansion (b): black: IR spectrum of toluene; red: IR spectrum of d_8-toluene; blue: IR spectrum of toluene soaked [$Ru_3btc_2Cl_3$]; pink: IR spectrum of toluene soaked [$Ru_3btc_2Cl_3$] after 3 h soaking in d_8-toluene; green: IR spectrum of toluene soaked [$Ru_3btc_2Cl_3$] after 20 h soaking in d_8-toluene; purple: IR spectrum of [$Ru_3btc_2Cl_3$] soaked in MeOH.

Inspired by the intra- and intermolecular KIE studies that have been used to elucidate the importance of conformationally gated substrate diffusion in enzymatic C–H oxidation chemistry, we evaluated the relative magnitudes of the intra- and intermolecular KIEs (**Figure III-21**) to probe the role of substrate diffusion during the amination of toluene. The measured intramolecular KIE value (7.86(3)) is above the classical limit for H/D isotope effects[233] and is consistent with significant C–H/D cleavage in the NAT transition state and the contribution of quantum-mechanical tunneling. These data suggest that amination proceeds by initial hydrogen atom abstraction, which is consistent with the observed selectivity for benzylic C–H functionalization. The measured intermolecular KIE (1.02(2)) indicates that C–H bond cleavage is not involved in the product-determining step in the amination of a mixture of toluene and toluene-d_8. Based on the relative magnitudes of the intra- and intermolecular KIEs, the lack of catalyst turnover was ascribed to restricted substrate diffusion within [$Ru_6btc_4(N_3)_3$]. The relative lack of discrimination between H and D reflected in the absence of an intermolecular KIE indicates that selection between H and D is not possible under these reaction conditions and that substrate diffusion in [$Ru_6btc_4(N_3)_3$] is slow relative to C–H amination.

III.4 Conclusions

In summary, we have demonstrated lattice confinement of reactive Ru_2 nitride intermediates as a strategy for intermolecular NAT chemistry. The site isolation of reactive Ru_2 nitride intermediates 1) prevents bimolecular nitride coupling, which is facile at homogeneous Ru_2 tetracarboxylate complexes, and 2) provides a platform for intermolecular C–H functionalization reactions that are challenging to achieve in the homogeneous milieu. The developed intermolecular C–H amination provides a venue to directly evaluate the impact of substrate diffusion on interstitial substrate functionalization. Comparison of the intra- and intermolecular KIEs reveals that while substantial C–H cleavage is involved in the C–H amination transition state, substrate diffusion through the microporous network is slow relative to the amination process. We believe that the presented KIE analysis represents a useful new tool in understanding the impact of substrate diffusion on interstitial chemistry and will provide critical guidance in designing new porous materials for interstitial MOF catalysis.

III.5 Experimental Details

III.5.1 General Considerations

Materials Solvents were obtained as ACS reagent grade and used as received. Unless otherwise noted, all chemicals and solvents were used as received. Ethyl acetate and sodium hydroxide were obtained from EMD Millipore. Trimesic acid (H_3btc) and PtO_2 were obtained from Alfa Aesar. Tetrabutylammonium azide, benzoic acid, isobutyronitrile, α,α'-dichloro-*m*-xylene, diethyl ether, methanol, THF, hexanes, lithium diisopropylamide, α,α,α',α'-tetramethyl-1,3-benzenedipropionitrile, ethylene glycol, benzyl bromide, magnesium, deuterium oxide, benzylamine, trimethylsilyl trifluoromethanesulfonate (TMSOTf), and acetic acid were obtained from Sigma Aldrich. LiCl was purchased from Alfa Aesar. Acetic anhydride and silica gel (0.060–0.200 mm, 60 Å for column chromatography) were obtained from Acros Organics, and $RuCl_3 \cdot \times H_2O$ and silver tetrafluoroborate were obtained from Strem Chemicals. Sodium azide was obtained from VWR. CH_2Cl_2, DMF and toluene were obtained from Fisher Scientific. Potassium hydroxide was obtained from BDH Analytical Chemicals. Hydrochloric acid was obtained from Macron Chemicals. Chlorobenzene was obtained from TCI. NMR solvents and sodium azide (1-^{15}N) were purchased from Cambridge Isotope Laboratories and were used as received. H_2 (99.995%) was obtained from Coastal Welding Supply. UHP-grade N_2, CO_2, and He, used in gas sorption measurements, were obtained from Airgas. Anhydrous THF was obtained from a drying column and stored over activated molecular sieves.[234] All reactions were carried out under ambient atmosphere unless otherwise noted.

Characterization Details NMR spectra were recorded on Inova 500 FT NMR operating at 499.53 MHz or Mercury 300 at 299.92 MHz for ^{1}H and ^{13}C acquisitions and were referenced against solvent signals: $CDCl_3$ (7.26 ppm, ^{1}H; 77.16 ppm, ^{13}C), D_2O (4.79 ppm, ^{1}H), d_8-THF (3.58 ppm and 1.72 ppm, ^{1}H), CD_3CN (1.94 ppm, ^{1}H), d_8-toluene (2.08 ppm, ^{1}H) and DMSO-d_6 (2.50 ppm, ^{1}H). ^{1}H NMR data are reported as follows: chemical shift (δ, ppm), (multiplicity: s (singlet), d (doublet), t (triplet), m (multiplet), br (broad), integration).[185] UV-vis spectra were recorded at 293 K in quartz cuvettes on an Ocean Optics Flame-S miniature spectrometer with DH-mini UV-vis NIR light source and were blanked against the appropriate solvent. Solid-state UV-vis spectra were recorded as mineral oil dispersions on glass slides using Hitachi U-4100 UV-vis-NIR spectrophotometer and were blanked against empty glass slides. IR spectra were recorded on either a Shimadzu FTIR/IRAffinity-1 spectrometer or an Agilent Cary 630a housed in an N_2-filled glovebox. *In situ* IR spectra in a KBr pellet were measured with a Bruker VERTEX 70. Spectra were blanked against air and were determined as the average of 32 scans. IR data are reported as follows: wavenumber (cm^{-1}), (peak intensity: s, strong; m, medium; w, weak). Magnetic data were obtained using a Quantum Design MPMS 3 SQUID magnetometer. DC measurements were acquired under a 1000 Oe applied field at a temperature range of 2–300 K. The measured DC susceptibility was corrected by Pascal's constants.[235] GC analysis was carried out using a Trace 1310 (Thermo Scientific) instrument equipped with a TraceGOLD TG-1M column from Thermo Scientific (length: 30 m, id: 0.53 mm, film thickness: 0.25 µm). For d_8/h_8-toluene, the column temperature was maintained at 31 °C for 0.1 min and raised to 40 °C at 0.5 °C/min. The final

temperature (40 °C) was held for 3 min. For benzylamine, the column temperature was maintained at 50 °C for 2 min and was raised to 200 °C at 10 °C/min. The final temperature (200 °C) was held for 5 min. Elemental analyses were done in Atlantic Microlab, Inc., Norcross, GA. Low-resolution mass spectrometry data were obtained using a Bruker AmaZon SL operating in positive mode. High-resolution mass spectrometry (HRMS) data were measured on a Thermo Scientific Orbitrap Fusion Tribrid in 3kV positive mode at 240000 mass resolution (3 sheath gas, 2 aux gas, 1 sweep gas, 5 μL/min syringe push). TGA experiments were performed on a TGA Q500 TA Instrument. Samples were heated from 23 °C to 760 °C at a heating rate of 20 °C/min under N_2.

X-ray Diffraction Details Powder X-ray diffraction (PXRD) measurements were carried out on a Bruker D8 Advance Eco X-ray diffractometer (Cu Kα, 1.5418 Å; 40 kV, 25 mA) fitted with LynxEye detector. The angular range was measured from 5.00 to 50.00° (2θ) with steps of 0.020° and a measurement time of 0.5 second per step. Simulated PXRD patterns were calculated with Mercury 3.9. Unit cells of single-crystal samples were determined using a Bruker ApexII CCD diffractometer equipped with microfocus copper source lμS (CuKα = 1.5418 Å) operating at 110 K.

Gas Sorption Details Gas adsorption isotherms for pressures in the range 0−1.0 bar were measured using a volumetric method using a Micromeritics ASAP 2020 or ASAP 2420 instrument. Samples were transferred under an N_2 atmosphere to pre-weighed analysis tubes. The samples were evacuated at 150 °C until the outgas rate was <10 μbar/min and further maintained for 16 h. Then the tube was weighed to determine the mass of the activated sample. The tube was transferred to the analysis port of the

instrument. UHP-grade (99.999% purity) N_2 and He were used for all adsorption measurements. For all isotherms, both warm and cold free-space measurements were carried out with He; N_2 isotherms were measured at 77 K.

Mass Spectrometry Analysis of N_2 Isotopomers Analysis of N_2 isotopomers was carried out with a Waters Micromass AutoSpec Ultima GCMS. The instrument used is a magnetic sector mass spectrometer interfaced with an Agilent Technologies 6890N Network gas chromatography system housed in the University of Texas-Austin Chemistry Department. Analysis was performed by loading a 2-mL vial with 0.023 mmol of the Ru_2 compound of interest and $Na^{15}NN_2$. The vial was sealed with a rubber septum and was purged with N_2 for 2 min. Solvent was added (THF for molecule Ru_2OBz_4Cl, 5:1 (v/v) DMF : water for $[Ru_6btc_4Cl_3]$ and $RuCl_3 \cdot \times H_2O$, and HCl for NaN_3) and the samples were allowed to stand for 1 h. The GC column was placed under vacuum, inserted directly into the headspace of the reaction vial, and the isotopic distribution of N_2 was determined.

III.5.2 Synthesis and Characterization

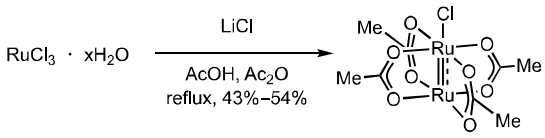

Synthesis of $Ru_2(OAc)_4Cl$ $Ru_2(OAc)_4Cl$ was prepared according to the following modification of literature methods.[236] A 100-mL round-bottom flask was charged with $RuCl_3 \cdot \times H_2O$ (0.506 g, 2.44 mmol, 1.00 equiv) and anhydrous LiCl (0.529 g, 12.6 mmol, 5.16 equiv). A mixture of glacial acetic acid (18.0 mL) and acetic anhydride (4.0 mL) was added to the reaction vessel and the resulting solution was heated at reflux for 6 h under a slow stream of N_2. The reaction mixture was cooled to 10 °C for 12 h at which time a red-brown precipitate was observed. The precipitate was isolated by vacuum filtration, washed with MeOH and Et_2O, and dried *in vacuo* to afford 250–310 mg of the title compound as a red-brown powder (43%–54% yield; 5 independent syntheses). ^1H NMR (δ, 23 °C, D_2O): –46.0 (s, 12H). IR (cm^{-1}): 2932 (w), 1437 (s), 1395 (s), 1356 (s), 1042 (m), 1014 (w), 943 (w), 689 (s), 630 (m).

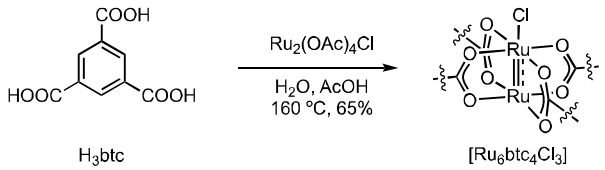

H_3btc $[Ru_6btc_4Cl_3]$

Synthesis of $[Ru_6btc_4Cl_3]$ $[Ru_6btc_4Cl_3]$ was prepared according to the literature.[226] A 20-mL Teflon-lined autoclave was charged with $Ru_2(OAc)_4Cl$ (0.310 g, 0.654 mmol, 1.00 equiv) and H_3btc (0.182 g, 0.866 mmol, 1.32 equiv). H_2O (7.3 mL) and acetic acid (1.2 mL) were added and the resulting mixture was heated at 160 °C for 3 d in a ventilated oven. The reaction mixture was cooled to 23 °C and the resulting solid was isolated by filtration. The solid was washed with H_2O (5.0 mL × 3) and ethanol (5.0 mL × 3) to afford 322 mg of the title complex. Thermal gravimetric analysis (TGA) of the solid obtained by this procedure indicated that 24% of the mass was due to entrapped solvent. When $[Ru_6btc_4Cl_3]$ was used in the synthesis of $[Ru_6btc_4(N_3)_3]$, $[Ru_6btc_4Cl_3]$ was not further purified. IR (cm^{-1}): 1708 (w), 1617 (w), 1431 (m), 1369 (s), 1271 (w), 1120 (w), 1009 (w), 939 (w), 732 (s), 690 (m). Elemental Analysis (EA) for $[Ru_6(btc)_4Cl_3]$: calcd. C, 19.71; H, 4.23; Cl, 3.09; found C, 19.73; H 4.31; Cl, 3.13. Based on the obtained EA data, the formula of $[Ru_6(btc)_4Cl_3]$ is calculated to be $[Ru_6(C_9H_3O_6)_4Cl_2(OH)]\cdot(H_2O)_{40}(CH_3COOH)_{0.8}$. This measured formula agrees well with literature reports of this material.[226] Based on the formula mass determined by EA, the yield of $[Ru_6btc_4Cl_3]$ in this synthesis is 65%. For gas sorption studies, $[Ru_6btc_4Cl_3]$ was activated under active vacuum at 150 °C for 24 h.

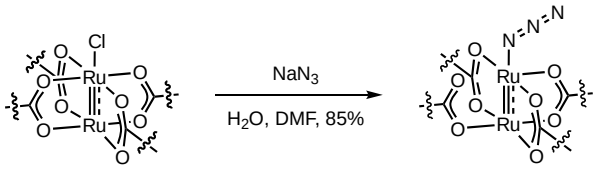

Synthesis of [$Ru_6btc_4(N_3)_3$] A 20-mL vial was charged with [$Ru_6btc_4Cl_3$] (0.0400 g, 0.0175 mmol, 1.00 equiv), NaN_3 (0.0400 g, 0.615 mmol, 35.1 equiv), H_2O (3.2 mL), and DMF (16.0 mL). The resulting mixture was allowed to stand at 23 °C for 3 d. At this time, the supernatant was decanted and the remaining solids were washed with MeOH (10.0 mL × 3). The solids were then soaked in MeOH (20.0 mL) at 23 °C for 3 d (refreshed three times per day), solvent was decanted, and the solids were allowed to air-dry to give 35.0 mg of the title compound as a dark brown powder. Thermal gravimetric analysis (TGA) of the solid obtained by this procedure indicated that 22% of the mass was due to solvent. IR (cm^{-1}): 2048 (m), 1618 (m), 1554 (m), 1435 (m), 1368 (s), 1114 (w), 1019 (m), 937 (w), 732 (s). Elemental Analysis (EA) for [$Ru_6(btc)_4(N_3)_3$]: calcd. C, 19.88; H, 4.46; N, 3.16; Cl, 0.39; found C, 19.82; H, 4.40; N, 3.14; Cl, 0.38. Based on EA data and synthetic procedures, the formula of [$Ru_6(btc)_4(N_3)_3$] is calculated to be $[Ru_6(C_9H_3O_6)_4Cl_{0.26}(N_3)_{1.44}(OH)_{1.3}]\cdot(H_2O)_{42}(C_3H_7NO)$ by optimizing the contents of Cl^-, N_3^-, OH^-, H_2O and DMF. This procedure affords [$Ru_6btc_4(N_3)_3$] in 85% based on the formula determined by elemental analysis. The similarity of the hydroxyl content in this material and in [$Ru_6btc_4Cl_3$] (see above) suggests that Cl^- exchange with azide is facile but OH^- exchange is not. For gas sorption studies, [$Ru_6btc_4(N_3)_3$] was soaked in CH_2Cl_2 for 2 d (refreshed three times per day) and then activated at 23 °C under active vacuum for 24 h. Additional activation protocol are presented in **Figure III-7**.

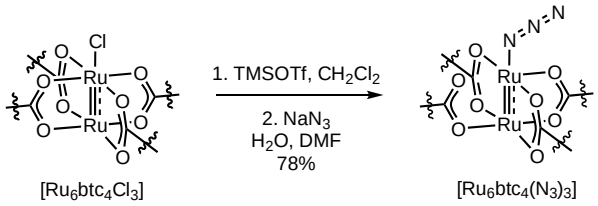

Synthesis of $[Ru_6btc_4(N_3)_3]$ with TMSOTf and NaN_3 Under N_2 atmosphere, a 20-mL vial was charged with $[Ru_6btc_4Cl_3]$ (0.0400 g, 0.0175 mmol, 1.00 equiv), TMSOTf (0.0200 g, 0.0900 mmol, 5.14 equiv) and CH_2Cl_2 (5.0 mL). The resulting mixture was allowed to stand at 23 °C for 7 d. At this time, the supernatant was decanted and the remaining solids were washed with CH_2Cl_2 (5.0 mL × 3). The solids were then soaked in CH_2Cl_2 (20.0 mL) at 23 °C for 3 d (refreshed three times per day), solvent was decanted, and the solids were allowed to dry under vacuum. NaN_3 (0.0400 g, 0.615 mmol, 35.1 equiv to $[Ru_6btc_4Cl_3]$), H_2O (3.2 mL), and DMF (16.0 mL) were added and the resulting mixture was allowed to stand for 3 d. The supernatant was decanted and the remaining solids were washed with MeOH (10.0 mL × 3). The solids were then soaked in MeOH (20.0 mL) at 23 °C for 3 d (refreshed three times per day), solvent was decanted, and the solids were allowed to air-dry to give 31.0 mg of the title compound as a dark brown powder. This procedure affords $[Ru_6btc_4(N_3)_3]$ in 78% based on the formula determined by elemental analysis. The material obtained from this procedure was spectroscopically identical to that produced from direct azide exchange into the chloride MOF. Elemental Analysis (EA) for $[Ru_6(btc)_4(N_3)_3]$: calcd. C, 27.93; H, 3.79; N, 9.02; Cl, 0; F, 0; S, 0; found C, 27.46; H, 3.67; N, 9.29; Cl, 0; F, 0; S, 0. Based on EA data and synthetic procedures, the formula of $[Ru_6(btc)_4(N_3)_3]$ is calculated to be $[Ru_6(C_9H_3O_6)_4(N_3)_3]\cdot(H_2O)_{17}(C_3H_7NO)_{5.7}$ by optimizing the contents of Cl^-, N_3^-, OH^-, H_2O and DMF.

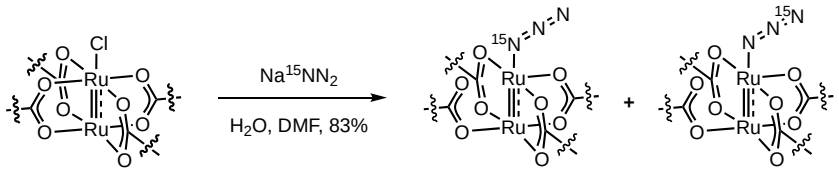

[$Ru_6btc_4Cl_3$] [$Ru_6btc_4(^{15}NN_2)_3$]

Synthesis of [$Ru_6btc_4(^{15}NN_2)_3$] A 20-mL vial was charged with [$Ru_6btc_4Cl_3$] (0.0200 g, 0.00873 mmol, 1.00 equiv), Na($^{15}NN_2$) (0.0220 g, 0.333 mmol, 38.1 equiv), H_2O (1.6 mL), and DMF (8.0 mL). The resulting mixture was allowed to stand at 23 °C for 3 d. At this time, the supernatant was decanted and the remaining solids were washed with MeOH (5.0 mL × 3). The solids were then soaked in MeOH (10.0 mL) at 23 °C for 3 d (refreshed three times per day), solvent was decanted, and the solids were allowed to air-dry to give 17.0 mg of the title compound as a dark brown powder (83% yield). IR (cm^{-1}): 2031 (m), 1623 (m), 1542 (m), 1433 (m), 1348 (s), 1118 (w), 1014 (w), 938 (w), 732 (s).

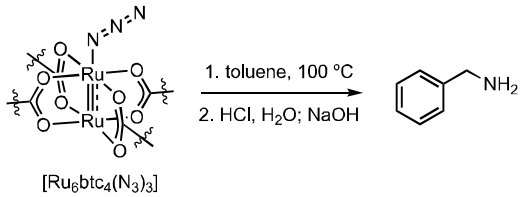

Acidic Workup to Generate Benzylamine In a Schlenk tube, toluene (1.00 mL, 9.41 mmol, 2219 equiv) was added to $[Ru_6btc_4(N_3)_3]$ (0.0100 g, 0.00424 mmol, 1.00 equiv). The toluene suspension was allowed to stand at 23 °C for 6 h.[i] The suspension was degassed three times by freeze-pump-thaw and then heated at 100 °C for 16 h. Two methods were used to analyze the reaction outcome. *Method A:* The supernatant was decanted and concentrated aqueous HCl (0.10 mL)[ii] was added to the remaining solid. The suspension was sonicated for 30 min. CH_2Cl_2 (1.0 mL) was added and the resulting mixture was basified by 2.5 M NaOH solution until pH > 10. The CH_2Cl_2 layer was collected and analyzed by GC and ESI-MS. *Method B:* Acetic acid (0.05 mL) was added to the reaction suspension and the suspension was sonicated for 30 minutes. d_8-Toluene was added and the reaction mixture was analyzed by ^{1}H NMR.

[i] Control experiments in which activated $[Ru_6btc_4(N_3)_3]$ was exposed to toluene at 100 °C without pre-soaking and in which $PhCH_3$@$[Ru_6btc_4Cl_3]$ was exposed to $[TBA]N_3$ did not result in the formation of significant quantities of benzylamine, which is consistent with slow substrate diffusion in these materials.
[ii] We have found that >3 M HCl and AcOH are able to extract the benzylamine from the Ru_2-based material. Hexafluoroisopropanol, NH_4Cl (up to 6 M), and MeOH do not extract benzylamine.

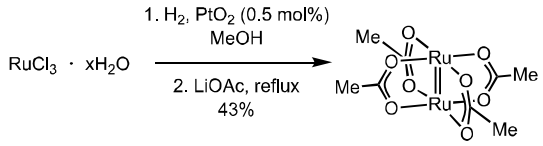

Synthesis of $Ru_2(OAc)_4$ Under N_2 atmosphere, $[Ru_2(OAc)_4]$ was prepared according to the following modification of literature methods.[237] A 100-mL Schlenk flask was charged with $RuCl_3 \cdot \times H_2O$ (1.00 g, 4.82 mmol, 1.00 equiv), PtO_2 (0.005 g, 0.020 mmol, 0.005 equiv) and methanol (10 mL). The flask was pressurized with 1.5 atm H_2 and the reaction mixture was stirred at 23 °C for 3 h to yield dark blue solution. Lithium acetate (1.18 g, 17.8 mmol, 3.69 equiv) was added and the mixture was refluxed for 18 h. The mixture was filtered hot and the solids were washed with methanol. The resulting solid was dried under vacuum at 80 °C to afford 445 mg of the title compound as an orange solid (43% yield). IR (cm^{-1}): 1635 (w), 1560 (s), 1426 (s), 1383 (m), 1321 (m), 1103 (m), 1009 (s), 937 (w), 681 (s), 622 (m). UV-vis (THF, λ_{max} (nm, ε (M^{-1} cm^{-1}))): 445 (600). These data are well-matched with reported spectral data.[237]

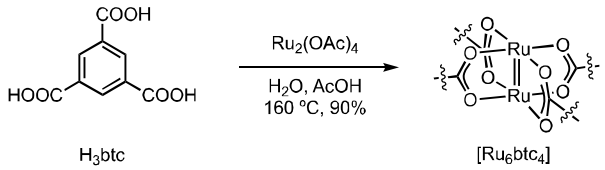

H_3btc $[Ru_6btc_4]$

Synthesis of [Ru_6btc_4] [Ru_6btc_4] was prepared according to literature methods.[238] Under an N_2 atmosphere, a 20-mL Teflon-lined autoclave was charged with $Ru_2(OAc)_4$ (0.100 g, 0.228 mmol, 1.00 equiv) and H_3btc (0.067 g, 0.319 mmol, 1.40 equiv). H_2O (2.7 mL) and acetic acid (0.47 mL) were added and the resulting mixture was heated at 160 °C for 3 d in a ventilated oven. The reaction mixture was cooled to 23 °C and the resulting solid was isolated by filtration. The solid was washed with H_2O (5.0 mL × 3) and ethanol (5.0 mL × 3), and activated under active vacuum at 150 °C for 24 h to afford 98 mg of the title complex (90% yield). IR (cm^{-1}): 1613 (w), 1538 (w), 1436 (m), 1369 (s), 1112 (w), 1026 (m), 936 (w), 731 (s).

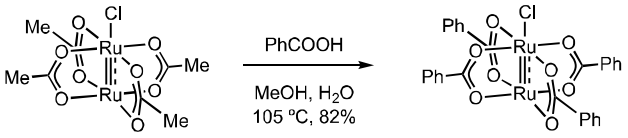

Synthesis of $Ru_2(OBz)_4Cl$ $Ru_2(OBz)_4Cl$ was prepared according to the following modification of literature methods.[239] A 100-mL round-bottom flask was charged with $Ru_2(OAc)_4Cl$ (0.150 g, 0.317 mmol, 1.00 equiv), $PhCO_2H$ (0.161 g, 1.33 mmol, 4.20 equiv), H_2O (10.0 mL), and MeOH (10.0 mL). The reaction vessel was fitted with a water-cooled reflux condenser and the reaction mixture was heated to reflux for 12 h. After this time, the reaction mixture was cooled to 23 °C and let stand at this temperature for 4 h, at which time solid precipitate was observed. The resulting solid was isolated by vacuum filtration and was washed thoroughly with Et_2O and MeOH. The resulting solid was dried to afford 186 mg of the title complex as a brick-red solid (82% yield). ^{1}H NMR (δ, 23 °C, d_6-DMSO): 31.58 (s, 1H), 19.61 (s, 1H), 7.61 (s, 3H). IR (cm^{-1}): 3053 (w), 2918 (w), 1639 (w), 1599 (m), 1464 (s), 1395 (s), 1175 (m), 1070 (m), 1026 (m), 845 (m), 685 (s). The recorded ^{1}H NMR spectrum is given in **Figure III-17a**.

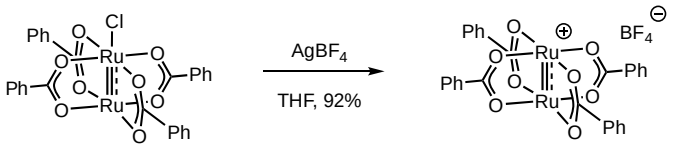

Synthesis of $Ru_2(OBz)_4BF_4$ $Ru_2(OBz)_4BF_4$ was prepared according to the following modification of literature methods.[240] $Ru_2(OBz)_4Cl$ (37.0 mg, 0.0512 mmol, 1.00 equiv) was dissolved in 10.0 mL THF under N_2 atmosphere. Simultaneously $AgBF_4$ (10.0 mg, 0.0513 mmol, 1.00 equiv) was also dissolved in 5.0 mL THF and were combined together and stirred at 23 °C for 24 h. After this time, the reaction mixture was filtered through a celite plug and the filtrate was concentrated under vacuum to afford 36.5 mg of the solid orange product (92%). ^{1}H NMR (δ, 23 °C, *d*$_8$-THF): 31.69 (s, 2H), 19.46 (s, 1H), 7.45 (s, 2H). IR (cm^{-1}): 2934 (w), 1650 (w), 1440 (s), 1395 (s), 1355 (m), 1022 (s), 860 (s), 686 (s). UV-vis (THF, λ_{max} (nm, ε (M^{-1} cm^{-1}))): 433 (1018).

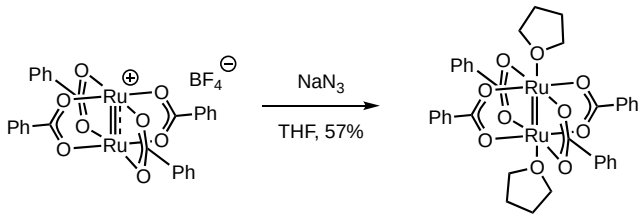

Treatment of $Ru_2(OBz)_4BF_4$ with NaN_3 A 20.0-mL vial was charged with $Ru_2(OBz)_4BF_4$ (50.0 mg, 0.0646 mmol, 1.00 equiv), NaN_3 (5.00 mg, 0.0769 mmol, 1.19 equiv) and 10.0 mL THF and stirred at 23 °C for 24h under N_2 atmosphere. After this time, the reaction mixture was filtered through a Celite plug and the filtrate was concentrated under vacuum to afford 25.3 mg of the dark brown solid (57% yield). ^{1}H NMR (δ, 23 °C, d_6-DMSO): 16.59 (s, 2H), 10.92 (s, 1H), 9.41 (s, 2H). IR (cm^{-1}): 2924 (m), 2851 (m), 2066 (m), 1528 (m), 1439 (s), 1403 (s), 1026 (s), 690 (s). UV-vis (THF, λ_{max} (nm)): 498. The recorded ^{1}H NMR spectrum is given in **Figure III-17c**. Single-crystals were obtained by slow diffusion of THF/pentane solution. Unit cell data was determined to be: $P2_1/n$, a = 10.214(1), b = 10.302(1), c = 16.011(2), α = 90°, β = 90.90(1)°, γ = 90°, V= 1684.1(4), which is well-matched to a reported structure.[239]

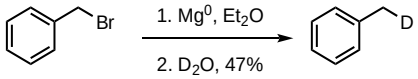

Synthesis of α-*d*$_1$-toluene A 100-mL round-bottom flask was charged with magnesium (1.80 g, 74.0 mmol, 2.00 equiv) and diethyl ether (30.0 mL). Benzyl bromide (4.40 mL, 37.0 mmol, 1.00 equiv) was added slowly and the resulting mixture was stirred at 23 °C for 3 h. Deuterium oxide (99.9%, 0.90 mL, 49.9 mmol, 1.35 equiv) was added slowly and the resulting mixture was stirred at 23 °C for 12 h. The solids were filtered off and the solution was distilled to yield 3.60 mL α-*d*$_1$-toluene (47% yield), which contained 0.9% residual diethyl ether. ^{1}H NMR (δ, 23 °C, $CDCl_3$): 7.23–7.30 (m, 2H), 7.15–7.21 (m, 3H), 2.34 (t, 2H, J = 2.3 Hz). ^{13}C NMR (δ, 23 °C, $CDCl_3$): 137.93 (t, J = 0.8 Hz), 129.17 (t, J = 0.8 Hz), 128.36 (s), 125.45 (s), 21.28 (t, J = 19.3 Hz). The recorded ^{1}H and ^{13}C spectra are shown in **Figure III-22b** and **Figure III-22c**. These data are well-matched with reported spectral data.[241,242]

CHAPTER IV

MEASURING AND MODULATING SUBSTRATE CONFINEMENT DURING NITROGEN-ATOM TRANSFER IN A RU_2-BASED METAL-ORGANIC FRAMEWORK*

IV.1 Introduction

Substrate confinement underpins the exquisite selectivities that characterize many enzymatic C–H oxidation reactions.[243-245] Substantial effort has led to the development of experimental probes to evaluate the interplay of substrate transport and substrate confinement in enzyme-catalyzed reactions. The relative magnitude of intramolecular molecular kinetic isotope effects (KIEs), obtained by challenging a catalyst with a partially labeled substrate, and intermolecular KIEs, obtained by challenging a catalyst with a mixture of perlabeled and unlabeled substrate, can report on transport barriers to substrate diffusion (*i.e.* the extent of substrate commitment to participate in a chemical step, Figure 1).[246] Further, large temperature-dependent intramolecular KIEs (*i.e.* $A_H/A_D < 0.7$ and $\Delta E_{D-H} > 1.2$ kcal·mol^{-1}) [247] are often encountered during enzymatic C–H functionalization and have been interpreted as evidence for significant quantum tunneling during C–H activation reactions (*i.e.* chemical barriers, **Figure IV-1**).[248] Together, analysis of both

* Portions of the data, figures, and text in this chapter were adapted with permission from reference Wang, C.-H.; Gao, W.-Y; Powers, D. C. *J. Am. Chem. Soc.* **2019**, *141*, 19203–19207, copyright 2019 The American Chemical Society.

intra- and intermolecular KIEs provides direct insight regarding substrate mobility during C–H functionalization.

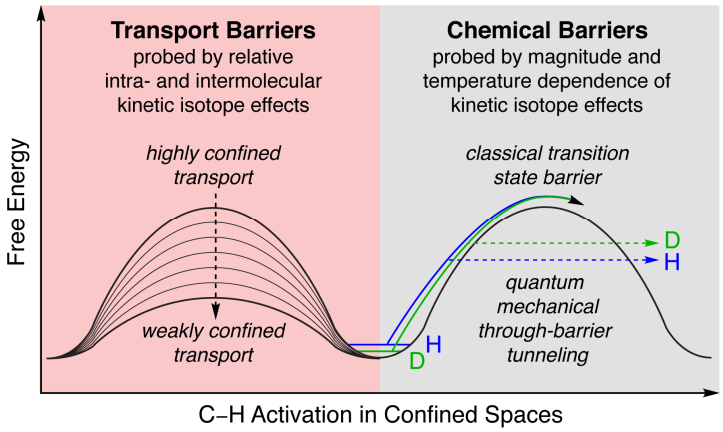

Figure IV-1. The degree of substrate confinement. Comparison of intra- and intermolecular kinetic isotope effects can provide information about the degree of substrate confinement in interstitial C–H functionalization. The magnitude and temperature dependence of the kinetic isotope effect provide information about the intimate details of the C–H cleavage event.

The combination of network porosity and synthetically tunable structure has motivated interest in utilizing metal-organic frameworks (MOFs) as enzyme-mimetic catalysts.[249-252] Unlike enzymes, which have evolved transport mechanisms to manage substrate flux to, and product egress from, the active site, MOF catalysts rely on diffusion to manage substrate and product migration to and from lattice-confined catalyst sites.[60] Due to the inherent challenges in measuring absolute diffusivity under catalytic conditions (*i.e.* multicomponent reaction conditions) and in establishing absolute catalyst turnover frequencies in these heterogeneous systems, substrate diffusivity on timescales relevant to interstitial reaction chemistry (*i.e.* the degree of substrate confinement) is typically unknown.[253,254] In 2018, we reported an analysis of intra- and intermolecular KIEs that indicated significant substrate confinement in the timescale of nitrogen-atom transfer

(NAT) in a Ru_2-based MOF.[169] Here, we apply this experimental strategy to directly evaluate the impact of network structure on substrate mobility during interstitial chemistry. In addition to revealing systematic tuning of substrate diffusivity, the data reported here also provide the first evidence for significant quantum tunneling during C–H activation chemistry in MOFs. We anticipate that the developed experimental approach for evaluating the impact of network structure on substrate mobility will be useful in the rational design of new MOF catalysts.

IV.2 Results

Synthesis and Characterization. We initiated our investigations by preparing a family of isostructural Ru_2-based materials with varying mesoporosities (**Figure IV-2**):[i] Solvothermal combination of $Ru_2(OAc)_4Cl$ with mixtures of 1,3,5-benzenetricarboxylic acid (H_3btc) and 3,5-pyridinedicarboxylic acid (H_2pydc) afforded a family of materials that are isostructural to $[Ru_6(btc)_4Cl_3]$ based on powder X-ray diffraction (PXRD) analysis (**Figure IV-3a** and **Tables IV-1** and **IV-2**).[255-257] For a given linker ratio used in the synthesis of $[Ru_6(btc)_x(pydc)_{4-x}Cl_3]$, the mesoporosity of the resulting material shows variability (**Tables IV-1** and **IV-22**). Combustion analyses and surface areas (derived from 77 K N_2 adsorption isotherms; **Figure IV-3b**) of the obtained materials were consistent with previous reports of $[Ru_6(btc)_x(pydc)_{4-x}Cl_3]$ materials.[257] Toluene vapor adsorption isotherms indicate that the gravimetric uptake of toluene is not substantially affected by introduction of mesopores and ~3 toluene molecules are adsorbed per Ru_2 site (**Figure**

[i] Ru_3btc_2-based materials exhibit the highest gas uptake and largest pores of available 3-dimensional Ru_2[II,III]-derived materials. See: Ribeiro, G.; Vichi, F. M.; de Oliveira Silva, D. Synthesis, Characterization and Adsorption Properties of Porous Mixed Valent Diruthenium(II,III)-Terephthalate and Diruthenium(II,III)-Adipate Polymers. *J. Mol. Struct.* **2008**, *890*, 209–214; Takamizawa, S.; Yamaguchi, K.; Mori, W. The Gas-Occlusion Properties of Dicarboxylate (Fumarate, trans-trans-Muconate and Terephthalate) Ruthenium(II,III) Dinuclear Complexes. *Inorg. Chem. Commun.* **1998**, *1*, 177–178; Kato, C. N.; Ono, M.; Hino, T.; Ohmura, T.; Mori, W. Room Temperature Oxidation of Alcohols with 1atm Dioxygen and Air Catalyzed by a Novel Three-Dimensional Microporous Ruthenium(II,III) 4,4′,4″,4‴-(21H,23H-Porphine-5,10,15,20-Tetrayl)tetrakisbenzoate Tetrafluoroborate. *Catal. Commun.* **2006**, *7*, 673–677; Miyazaki, Y.; Kataoka, Y.; Mori, W. Nitrogen and Hydrogen Gas Adsorption Properties of Microporous Ruthenium Coordination Polymers. *Trans. Mater. Res. Soc. Japan* **2010**, *35*, 665–667; Mori, W.; Takamizawa, S. Microporous Materials of Metal Carboxylates. *J. Solid State Chem.* **2000**, *152*, 120–129; Kataoka, Y.; Sato, K.; Miyazaki, Y.; Masuda, K.; Tanaka, H.; Naito, S.; Mori, W. Photocatalytic Hydrogen Production from Water Using Porous Material $[Ru_2(p\text{-}BDC)_2]_n$. *Energy Environ. Sci.* **2009**, *2*, 397–400. Families of porous coordination polymers have been developed in which Ru_2 dimers are bridged by chloride ligands, and are thus not available to participate in ligand exchange with azide. Additionally, 2-dimensional materials have been developed in which no structural elements connect the sheets of Ru_2-containing networks. Extensive attempts to apply reticular synthetic techniques to the synthesis of larger-pore materials have been unsuccessful.

IV-4).[258] $[Ru_6(btc)_x(pydc)_{4-x}(N_3)_3]$ materials were accessed by soaking the corresponding chloride MOFs in DMF/H_2O solutions of NaN_3. Azide-exchanged materials are isostructural to $[Ru_6(btc)_x(pydc)_{4-x}Cl_3]$ by PXRD analysis (**Figure IV-2**).

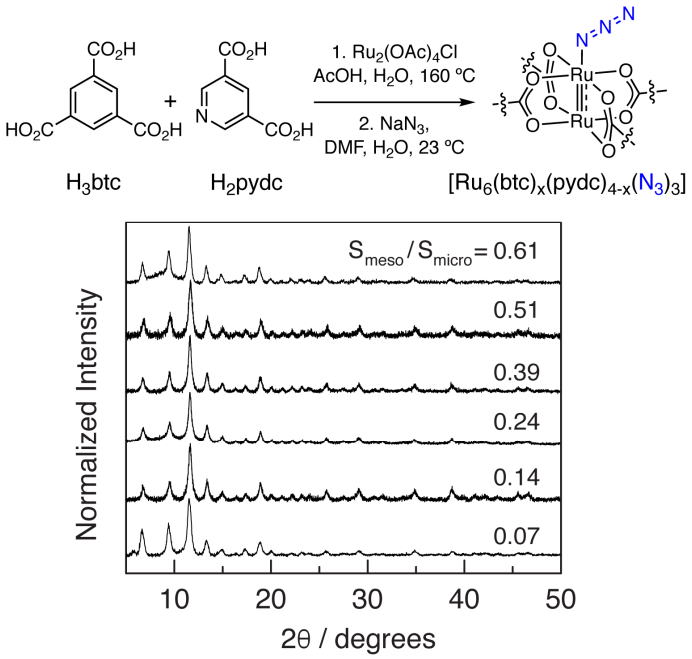

Figure IV-2. Synthesis of mesoporous $[Ru_6(btc)_x(pydc)_{4-x}(N_3)_3]$ via a mixed component strategy. The resulting materials are isostructural, as indicated by PXRD analysis, but display tunable mesoporosities, which are determined by fitting of the 77 K N_2 adsorption isotherms.

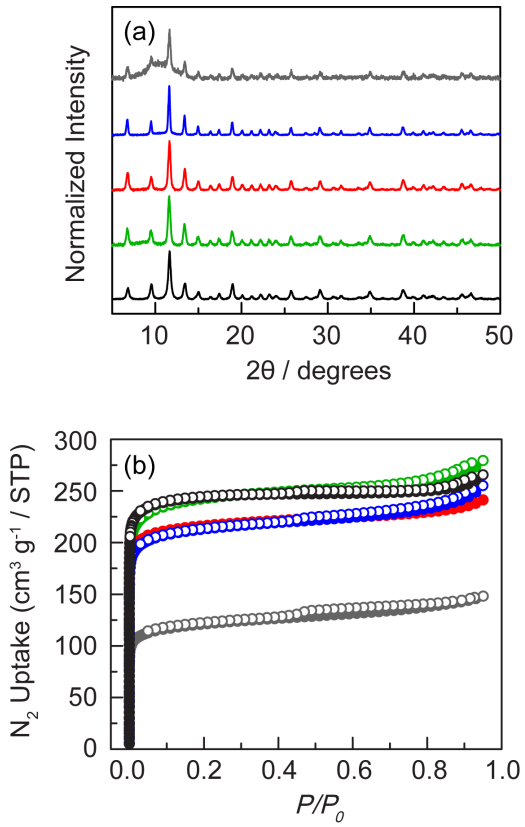

Figure IV-3. PXRD and gas sorption data of $[Ru_6(btc)_x(pydc)_{4-x}(N_3)_3]$. (a) Powder X-ray diffraction patterns for $[Ru_6(btc)_4Cl_3]$ (S_{meso}/S_{micro} = 0.06 (—)) and $[Ru_6(btc)_x(pydc)_{4-x}Cl_3]$: S_{meso}/S_{micro} = 0.28 (—); S_{meso}/S_{micro} = 0.40 (—); S_{meso}/S_{micro} = 0.39 (—); and S_{meso}/S_{micro} = 0.55 (—). (b) N_2 adsorption isotherms obtained at 77 K for $[Ru_6(btc)_4Cl_3]$ (S_{meso}/S_{micro} = 0.06, adsorption (●), desorption (○)) and $[Ru_6(btc)_x(pydc)_{4-x}Cl_3]$: S_{meso}/S_{micro} = 0.28, adsorption (●), desorption (○)); S_{meso}/S_{micro} = 0.40 (adsorption (●), desorption (○)); S_{meso}/S_{micro} = 0.39 (adsorption (●), desorption (○)); and S_{meso}/S_{micro} = 0.55 (adsorption (●), desorption (○)). Due to the substantially diminished surface area, we have not pursued chloride-to-azide exchange using materials with higher mesoporosities.

Table IV-1 Synthetic details for the preparation of $[Ru_6(btc)_x(pydc)_{4-x}Cl_3]$ materials

H_2pydc / (H_2pydc + H_3btc)	H_3btc (mg)	H_2pydc (mg)	Product (mg)	Formula derived from elemental analyses
0.05	57.6	2.4	112	$Ru_6(btc)_{3.83}(pydc)_{0.17}(OH)_{1.98}Cl_{1.02}(AcOH)_{1.5}(H_2O)_{10}$
0.10	54.4	4.8	110	$Ru_6(btc)_{3.60}(pydc)_{0.40}(OH)_{1.90}Cl_{1.10}(H_2O)_{13}$
0.30	42.3	14.4	102	$Ru_6(btc)_{2.80}(pydc)_{1.20}(OH)_{2.35}Cl_{0.65}(AcOH)_2(H_2O)_{17}$
0.50	30.2	24.0	91.4	$Ru_6(btc)_{2.10}(pydc)_{1.90}(OH)_{2.30}Cl_{0.70}(AcOH)_2(H_2O)_{20}$

Table IV-2 S_{meso}, S_{micro}, and BET surface areas for a series of independent syntheses of $[Ru_6(btc)_x(pydc)_{4-x}Cl_3]$ using a 9:1 H_3btc:H_2pydc ratio.

BET / m^2 g^{-1}	S_{meso} / m^2 g^{-1}	S_{micro} / m^2 g^{-1}	S_{meso}/S_{micro}
849	123	306	0.42
838	103	326	0.32
841	82	294	0.28
829	110	264	0.42
830	102	315	0.32

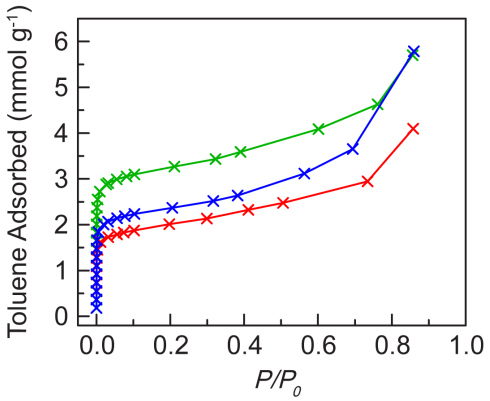

Figure IV-4. Toluene vapor adsorption isotherms. Toluene vapor adsorption isotherms obtained at 298 K for $[Ru_6(btc)_4Cl_3]$ (S_{meso}/S_{micro} = 0.12 (—)) and $[Ru_6(btc)_x(pydc)_{4-x}Cl_3]$ with S_{meso}/S_{micro} = 0.28 (—) and 0.59 (—)). The intermediate mesoporosity (S_{meso}/S_{micro} = 0.28) gives the smallest toluene adsorption (~2.0 molecules per Ru_2 site). To ensure that measured KIEs were not an artifact of low toluene loading we measured time-dependent KIEs with a similarly mesoporous sample (S_{meso}/S_{micro} = 0.24); data is summarized in **Table IV-4**.

Pore size distribution analysis, based on the 77 K N_2 adsorption isotherms, provided sample-dependent mesoporous (S_{meso}) and microporous (S_{micro}) surface areas:

The family of $[Ru_6(btc)_x(pydc)_{4-x}Cl_3]$ samples accessed in this study displayed S_{meso}/S_{micro} = 0.07−0.61 (**Figures IV-5−IV-7**, **Table IV-13**). Samples with higher mesoporosities are unavailable; attempts to access such samples resulted in decreased crystallinity. IR spectroscopy indicates that ν_{N3} is insensitive to network mesoporosity (ν_{N3} = 2048 cm^{-1}), which indicates the local Ru_2N_3 structure is conserved across the family of materials (**Figure IV-8**). Both PXRD line-broadening analysis (**Figure IV-9**) and electron microscopy (SEM **Figure IV-10**, TEM **Figure IV-11**) indicate that the average crystallite size is consistent across the family of mesoporous materials prepared.

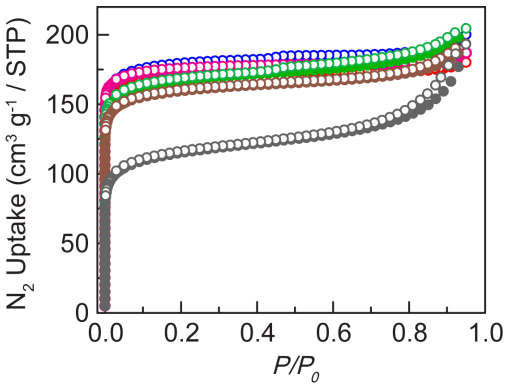

Figure IV-6. N_2 adsorption isotherms. N_2 adsorption isotherms obtained at 77 K for samples of $[Ru_6(btc)_4(N_3)_3]$ (S_{meso}/S_{micro} = 0.07, adsorption (●), desorption (○)) and $[Ru_6(btc)_x(pydc)_{4-x}(N_3)_3]$ with S_{meso}/S_{micro} = 0.14 (adsorption (●), desorption (○)); S_{meso}/S_{micro} = 0.24 (adsorption (●), desorption (○)); S_{meso}/S_{micro} = 0.39 (adsorption (●), desorption (○)); S_{meso}/S_{micro} = 0.51 (adsorption (●), desorption (○)); and S_{meso}/S_{micro} = 0.61 (adsorption (●), desorption (○)).

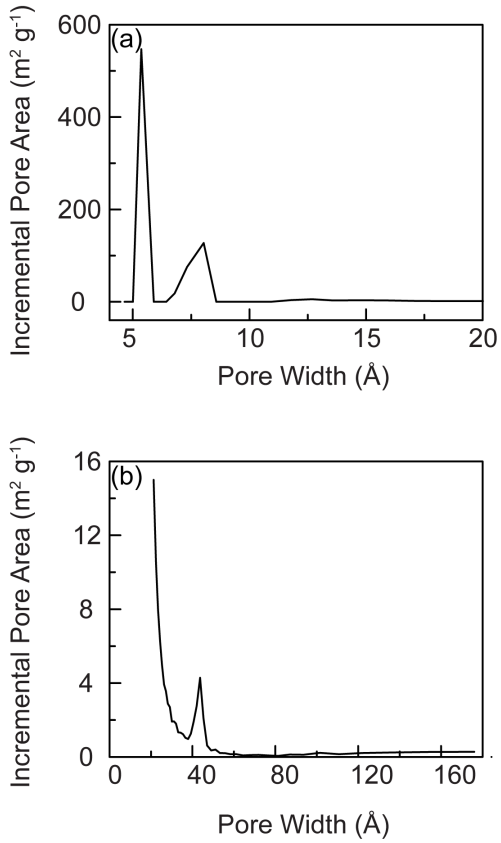

Figure IV-5. Example of pore size distribution analysis of $[Ru_6(btc)_x(pydc)_{4-x}(N_3)_3]$ (S_{meso}/S_{micro} = 0.35).

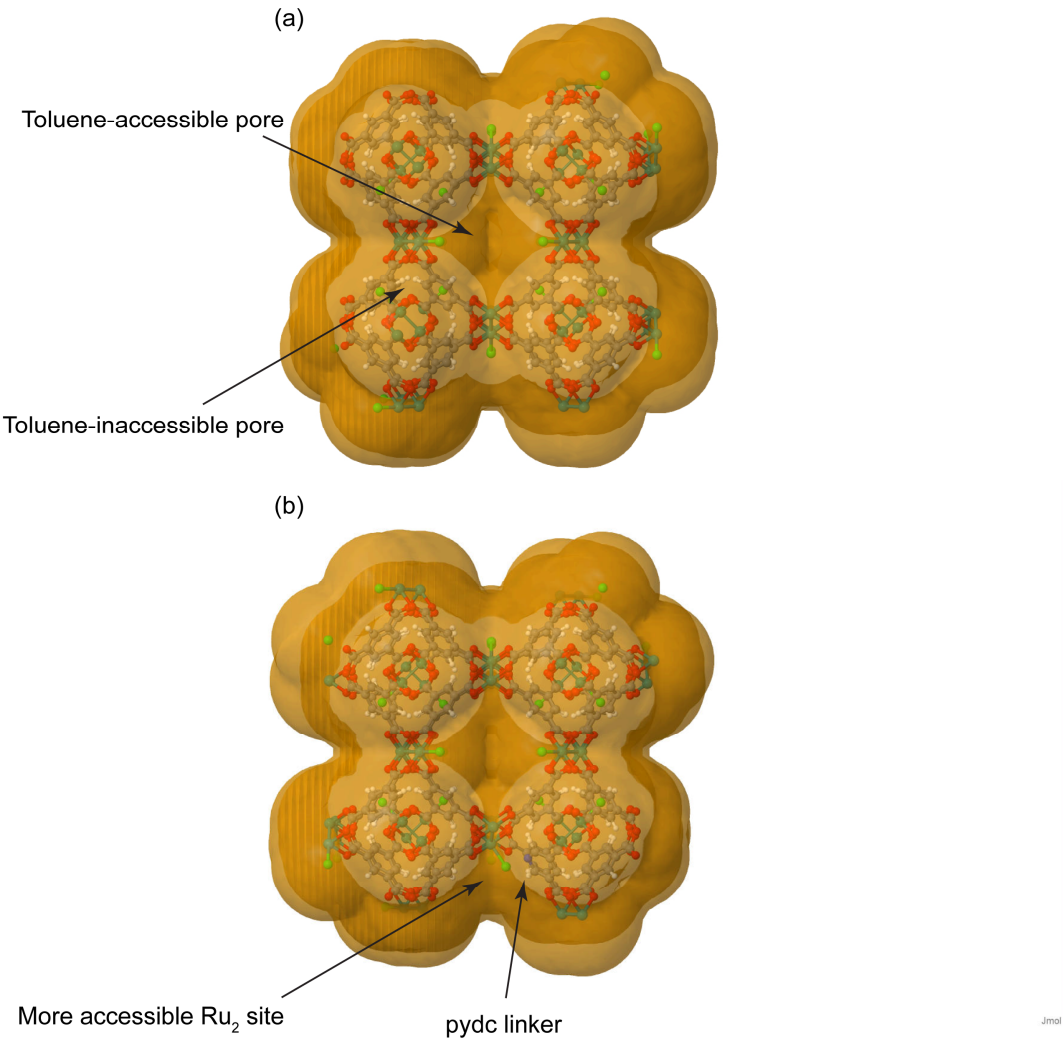

Figure IV-7. Simulation of toluene in materials. Simulation (teal: Ru; red: O; gray: C; green: Cl; white: H; and blue: N) of toluene in (a) $[Ru_6(btc)_4Cl_3]$ and (b) $[Ru_6(btc)_x(pydc)_{4-x}Cl_3]$. Dark yellow space-fills denote toluene solvent-accessible surfaces and light-yellow space-fills denote inaccessible surfaces. The Ru_2 paddlewheel proximal to pydc is more accessible compared to that of $[Ru_6(btc)_4Cl_3]$.

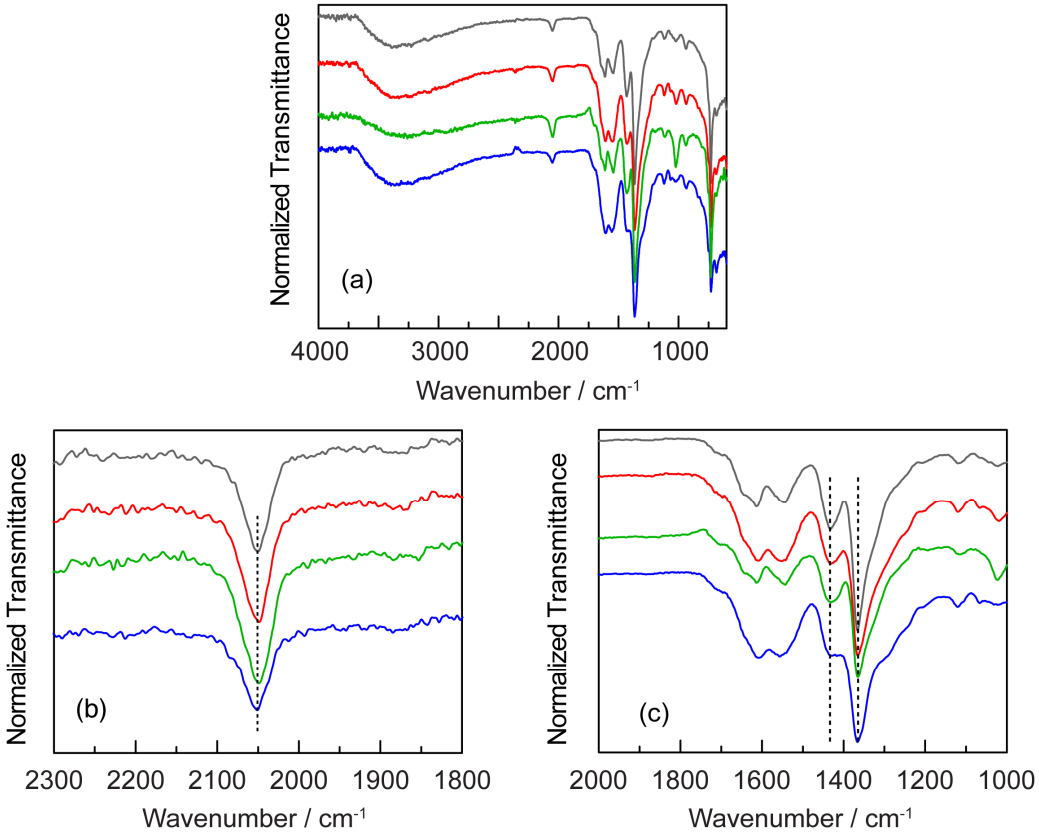

Figure IV-8. IR spectra of $[Ru_6(btc)_x(pydc)_{4-x}(N_3)_3]$. Spectra recorded as a function of mesoporosity (S_{meso}/S_{micro} = 0.41 (—); 0.29 (—); 0.39 (—); 0.58 (—)) used during synthesis of these materials. (a) Full spectral range; (b) expansion of azide and (c) carboxylate stretching (υ_{asym} = 1432 cm^{-1}, υ_{sym} = 1366 cm^{-1}) regions.

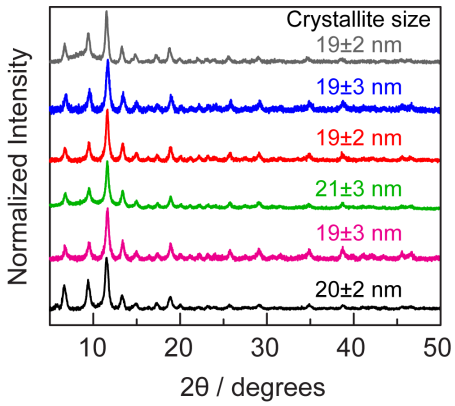

Figure IV-9. Analysis of crystallite size by PXRD line-shape analysis. Analysis of crystallite size by PXRD line-shape analysis for $[Ru_6(btc)_4(N_3)_3]$ (S_{meso}/S_{micro} = 0.07 (—)) and $[Ru_6(btc)_x(pydc)_{4-x}(N_3)_3]$ with S_{meso}/S_{micro} = 0.14 (—), 0.24 (—), 0.39 (—), 0.51 (—), and 0.61 (—). The average crystallite size D of the sample is calculated from the Scherrer equation: $D = K\lambda/(\beta\cos\theta)$, where K is the Debye-Scherrer constant (K = 0.9), λ is the X-ray wavelength (λ = 1.5406 Å), β is the peak width of half-maximum, and θ is the Bragg diffraction angle. Here, ten peaks with high intensity (2θ = 6.8, 9.5, 11.6, 13.4, 15.0, 18.9, 25.8, 29.1, 34.9, 38.8 °) were picked out to evaluate the crystallite size.

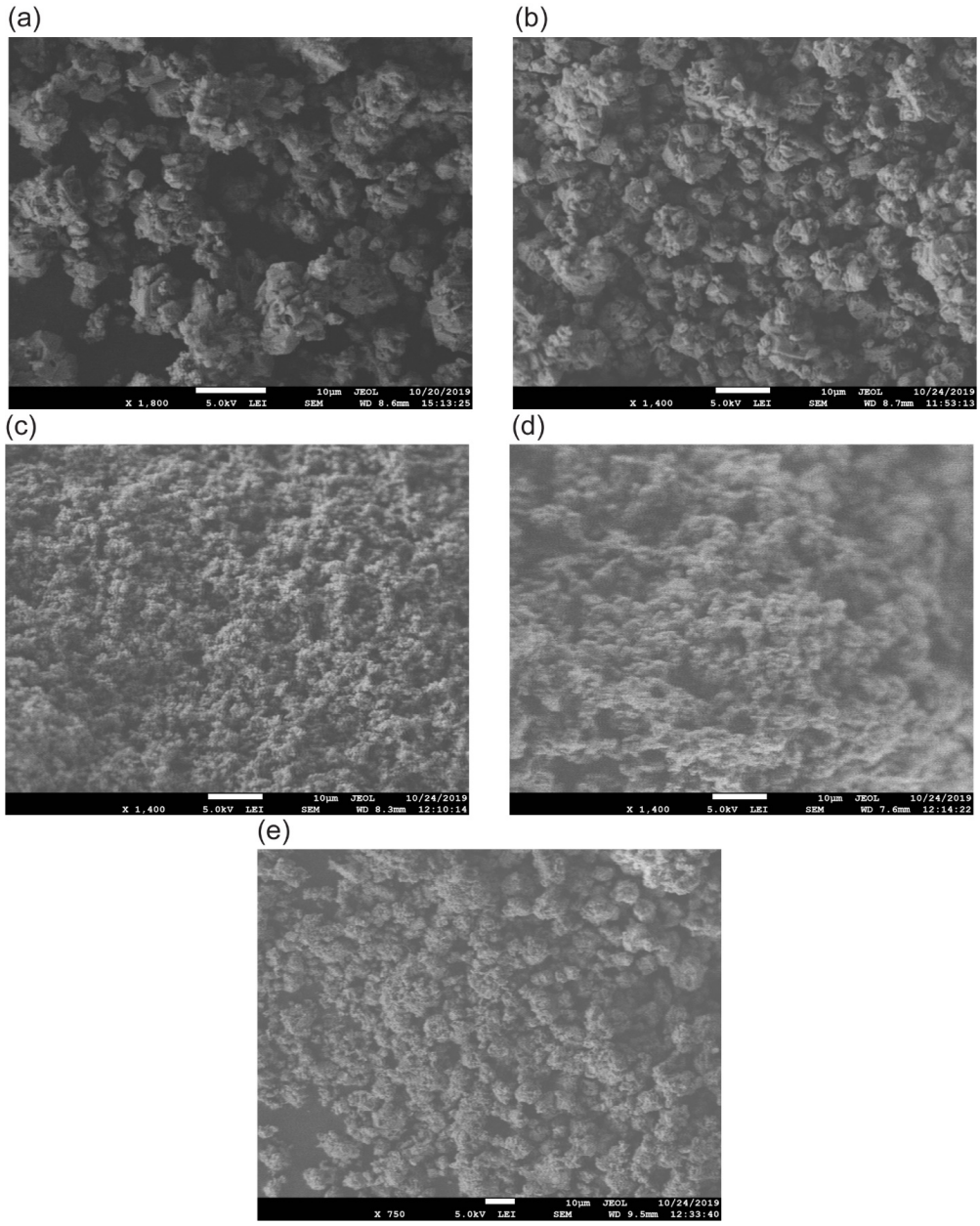

Figure IV-10. FE-SEM images. Field emission scanning electron microscopy (FE-SEM) images of $[Ru_6(btc)_4(N_3)_3]$ (S_{meso}/S_{micro} = (a) 0.07) and $[Ru_6(btc)_x(pydc)_{4-x}(N_3)_3]$ with S_{meso}/S_{micro} = (b) 0.14, (c) 0.24, (d) 0.41, and (e) 0.61.

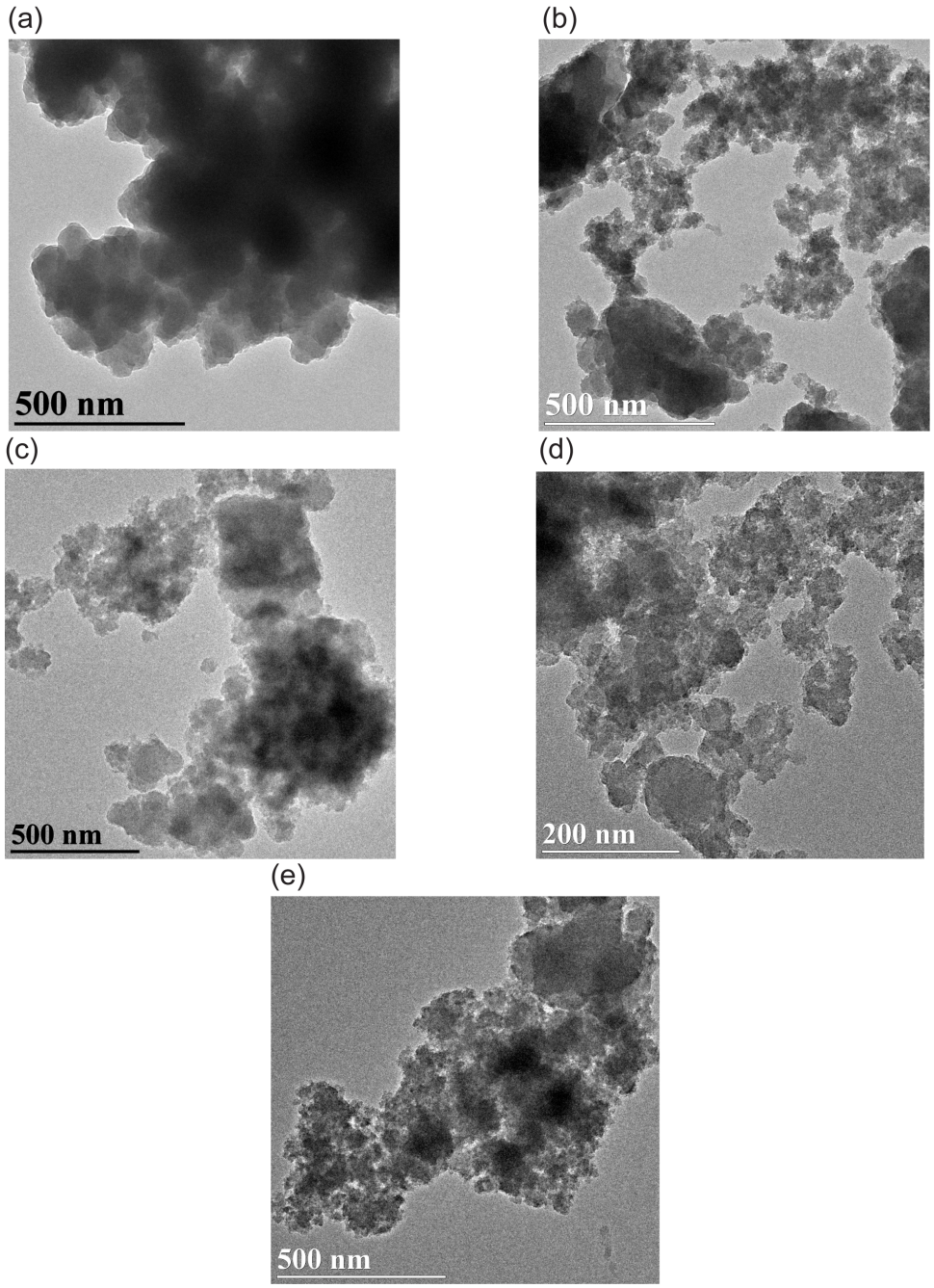

Figure IV-11. FE-TEM images. Field emission transmission electron microscopy (FE-TEM) images of $[Ru_6(btc)_4(N_3)_3]$ (S_{meso}/S_{micro} = (a) 0.07) and $[Ru_6(btc)_x(pydc)_{4-x}(N_3)_3]$ with S_{meso}/S_{micro} = (b) 0.14, (c) 0.24, (d) 0.41, and (e) 0.61.

Mesoporosity-Dependent Kinetic Isotope Effects. We have evaluated both intra- and intermolecular KIEs for NAT to toluene to generate benzylamine as a function of network mesoporosity; the data from these experiments are summarized in **Figure IV-12** (see **Table IV-3** for raw data). Each k_H/k_D value was determined by thermolysis of toluene-exchanged MOF samples at 100 °C. Presoaking the MOF samples is critical to amination chemistry. Thermolysis without soaking proceeds in 3% yield, whereas thermolysis following soaking affords benzylamine in 30% yield. These observations suggest that solvent-exposed surfaces of crystallites do not substantially contribute to the observed amination chemistry. After thermolysis, benzylamine was obtained by acidic workup and k_H/k_D was determined by integration of high-resolution mass spectrometry. Toluene amination in $[Ru_6(btc)_4(N_3)_3]$ (*i.e.* S_{meso}/S_{micro} = 0.07, "microporous" parent material) proceeds with an intramolecular k_H/k_D = 7.86(3) (after accounting for the 2:1 H:D ratio in d_1-toluene) and an intermolecular k_H/k_D = 1.02(2). The observed KIEs are consistent as a function of reaction progress (**Tables IV-4** and **IV-5**). These data are consistent with a scenario in which substrate self-exchange, which would mediate kinetic selection in an intermolecular competition experiment, is slow relative to NAT, and C−C rotation, which mediates kinetic selection in an intramolecular competition experiment, is faster than NAT.[259] With increasing network mesoporosity, the intermolecular KIE, measured for NAT to a 1:1 mixture of d_8- and H_8-toluene, steadily increases from 1.02(2) to 2.33(2) (**Figure IV-12**). In contrast, the intramolecular KIE decreases from 7.86(3) for the microporous parent material to 3.4(1) for the most mesoporous sample. Rapid N_2

evolution via nitride dimerization has prevented comparison of kinetic isotope effects measured in Ru_2-based materials with soluble molecular analogs.[169]

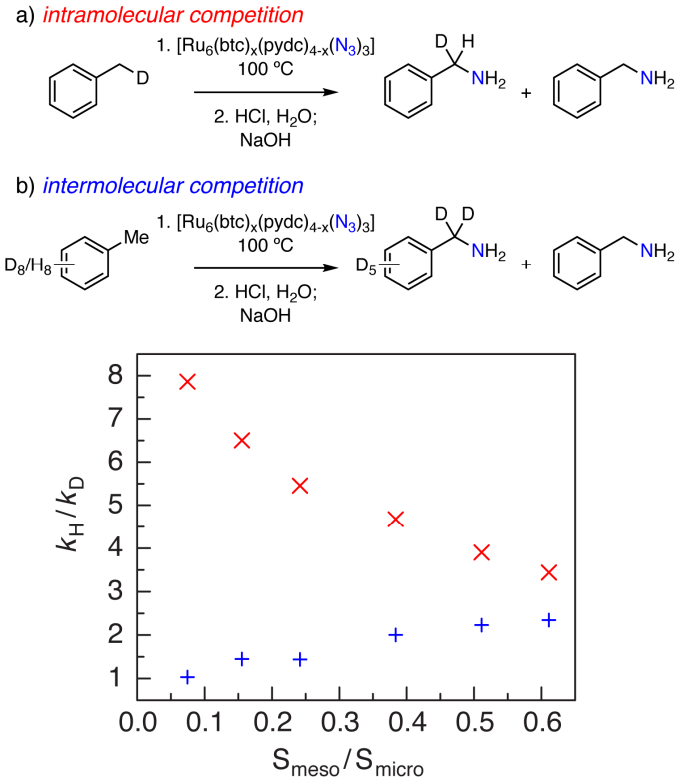

Figure IV-12. Plot of k_H/k_D as a function of network mesoporosity. Plot of k_H/k_D as a function of network mesoporosity for the a) amination of d_1-toluene (×) and b) the amination of a 1:1 mixture of H_8- and d_8-toluene (+).

Table IV-3 Summary of k_H/k_D for intra- and intermolecular amination of toluene using $[Ru_6(btc)_4(N_3)_3]$ (S_{meso}/S_{micro} = 0.07) and $[Ru_6(btc)_x(pydc)_{4-x}(N_3)_3]$ (S_{meso}/S_{micro} = 0.14, 0.24, 0.39, 0.51, and 0.61) at 100 °C

Sample S_{meso}/S_{micro}	Intramolecular k_H/k_D	Intermolecular k_H/k_D
0.07	7.86	1.02
0.14	6.50	1.44
0.24	5.45	1.42
0.39	4.67	1.99
0.51	3.89	2.22
0.61	3.43	2.31

Table IV-5 Time-dependent intermolecular KIEs at 75 °C

The data below were collected by heating a sample of $Ru_6(btc)_x(pydc)_{4-x}(N_3)_3$ (40 mg, S_{meso}/S_{micro} = 0.11 or 0.24) in a 1 : 1 mixture of toluene and d_8-toluene. At 12 h increments the reaction vial was removed from oil bath and allowed to cool to 23 °C. A portion of the $[Ru_6(btc)_x(pydc)_{4-x}(N_3)_3]$ or $[Ru_6(btc)_4(N_3)_3]$ (~10 mg) was removed and worked up as described above. The remaining reaction mixture was again heated at 75 °C. The KIE values tabulated below were determined by high resolution ESI. The data demonstrate that the measured KIEs are independent on the consumption of the substrates. The lower toluene adsorption (Figure S2) of the sample with intermediate mesoporosity (S_{meso}/S_{micro} = 0.24) does not impact intermolecular KIEs.

Sample S_{meso}/S_{micro}	Time / h	k_H/k_D
0.11	12	1.19
	24	1.20
	36	1.17
	48	1.20
0.24	12	1.40
	24	1.41
	36	1.41
	48	1.42

Table IV-4 Time-dependent intramolecular KIEs at 100 °C

The data below were collected by heating a sample of $Ru_6(btc)_x(pydc)_{4-x}(N_3)_3$ (40 mg, S_{meso}/S_{micro} = 0.41) in d_1-toluene. At 12 h increments the reaction vial was removed from oil bath and allowed to cool to 23 °C. A portion of the $[Ru_6(btc)_x(pydc)_{4-x}(N_3)_3]$ (~10 mg) was removed and worked up as described above. The remaining reaction mixture was again heated at 75 °C. The KIE values tabulated below were determined by high resolution ESI. The data demonstrate that the measured KIEs are independent on the consumption of the substrates.

Sample S_{meso}/S_{micro}	Time / h	k_H/k_D
0.41	12	7.63
	24	8.17
	36	7.32
	48	7.55

The average of k_H/k_D in this experiment is 7.7(3). The percent error is comparable to that of the most mesoporous material 3.4(1).

The data illustrated in **Figure IV-12** provide direct experimental evidence for the impact of network mesoporosity on substrate diffusivity during interstitial functionalization chemistry. The combination of large intramolecular and negligible intermolecular KIE observed in $[Ru_6(btc)_4(N_3)_3]$ is consistent with rate-determining N_2 extrusion to generate a Ru_2 nitride, and substantial substrate commitment to functionalization. In situ IR analysis indicates that the rate of ν_{N3} disappearance is insensitive to either the presence of substrate (toluene or d_8-toluene) or network mesoporosity (**Figures IV-13** and **IV-14**, respectively). These observations mirror the KIEs observed in conformationally gated enzymes[199,200] and in diffusionally limited zeolitic catalysts.[260] The convergence of intra- and intermolecular KIEs is consistent with enhanced substrate diffusivity as a function of increasing network mesoporosity. Importantly, diffusion barriers are still observed in the most mesoporous samples as evidenced by the differing intra- and intermolecular KIEs (3.4 vs 2.33).

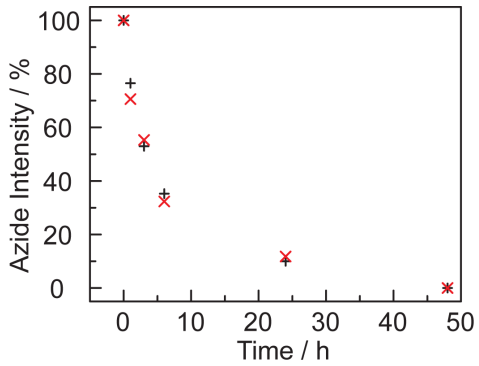

Figure IV-13. Azide thermolysis with and without toluene. Azide thermolysis of $[Ru_6(btc)_4(N_3)_3]$ (×) and toluene@$[Ru_6(btc)_4(N_3)_3]$ (×) in a KBr pellet at 75 °C. Azide intensity is calculated by its peak intensity monitored by *in-situ* IR.

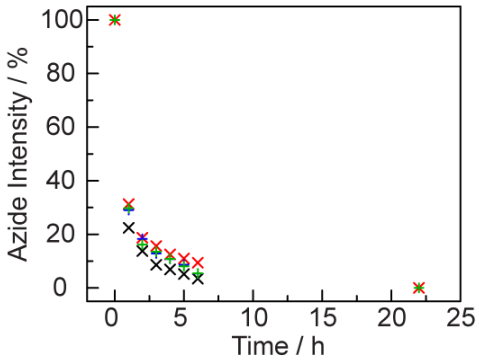

Figure IV-14. Azide thermolysis with d_8- and H_8- toluene. Azide thermolysis of d_8-toluene@$[Ru_6(btc)_4(N_3)_3]$ (×), toluene@$[Ru_6(btc)_4(N_3)_3]$ (×), d_8-toluene@$[Ru_6(btc)_x(pydc)_{4-x}(N_3)_3]$ (S_{meso}/S_{micro} = 0.51, +), and toluene@$[Ru_6(btc)_x(pydc)_{4-x}(N_3)_3]$ (S_{meso}/S_{micro} = 0.51, +) in a KBr pellet at 90 °C. Azide intensity is calculated by its peak intensity monitored by *in situ* IR.

Calculation of Potential Energy Surface. Geometry optimizations were were carried out using BP86-GD3/def2TZVP for Ru, N, O, and Cl, and def2SVP for C and H. Frequency calculations were performed with BP86-GD3/def2TZVPP/def2SVPP. Toluene (e = 2.38) was treated as a continuum solvent (SMD model).

We evaluated the potential energy surfaces relevant to pathways for the decomposition of Ru_2 azide sites (**Figure IV-15**). The barrier to N_2 via loss via a potential four-membered transition state (*i.e.* loss of N_α and N_β) is significantly higher (60.7 kcal mol^{-1}) than the barrier to direct loss of N_2 (*i.e.* loss of N_β and N_γ) (35.5 kcal mol^{-1}) to generate the ruthenium nitride (**Figure IV-15** and TS1 in **Figure IV-16**). The computed activation energy of 35.5 kcal mol^{-1} is consistent with the long reaction time required for amination of toluene. We are currently evaluating this barrier height experimentally via *in situ* IR spectroscopy of the thermolysis of $Ru_6btc_4(N_3)_3$. We also evaluated the possibility of the loss of an azide radical to form the unreactive $Ru^{II,II}$ complex (**Figure IV-15**). The

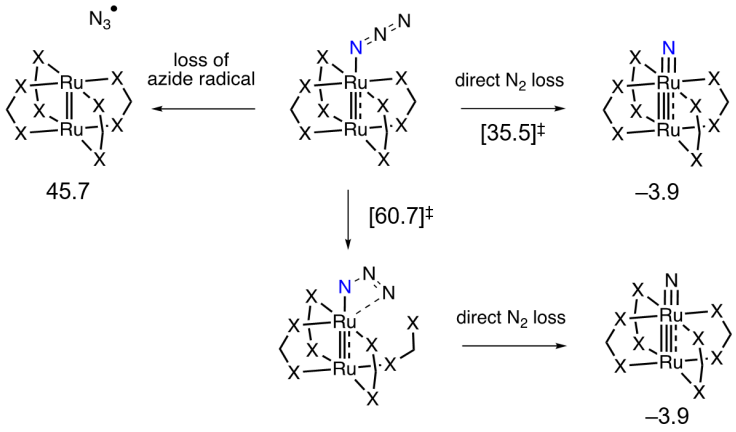

Figure IV-15. Pathway for the decomposition of azide as an azide radical or N_2. X = O–O. Energies are in kcal mol^{-1}.

loss of the azide radical to form a reduced ruthenium complex. Formation of the azide radical and thus is not facile under our reaction condition (100 °C).

Calculated structural and electronic properties of Ru_2 complexes are summarized in **Table IV-6**. The multiplicity changed from quartet (azide) to doublet (nitride) upon the formation of nitride. The calculated Ru–N bond orders for azide and nitride were computed to be 0.77 and 2.38 respectively, which indicated the bonding was labilized. The longer Ru–N bond distances for azide (2.07 Å) and nitride (1.68 Å) also suggested the labilization of Ru–N. This weak Ru–N bonding was supported by the calculation done by Berry and co-authors.[210]According to their calculation, the energy level of antibonding orbital was significantly raised due the interaction between N 2p orbitals and d_z^2 orbitals of three surface Ru atoms. The Ru–N bond was destabilized due to delocalized energy levels of the bulk Ru atoms acting as a buffer for electrons. We have found that the nitride complex was computed to have significant radical (nitridyl) character with a spin density of –0.24 on N and 0.09 on Ru. The features of these calculated intermediates were in good accordance with experimental and computational data in the literatures.[210,261-267]

Table IV-6 Summary of structural and electronic properties of ruthenium complexes.
[a]Calculation is undergoing.

Complex	Multiplicity	Calcd. Ru_a–Ru_b / Å	Calcd. Ru_a–N / Å	Ru_a–N bond order	ρ_{spin} on N / e^-	ρ_{spin} on Ru_a / e^-	ρ_{spin} on Ru_b / e^-
(O–O)Ru_2–N_3	quartet	2.33	2.07	0.77	0.06	1.25	1.43
(O–O)Ru_2–N	doublet	2.41	1.68	2.38	–0.24	0.09	0.98
(O–O)Ru_2–NH	singlet	2.28	1.78	1.49	–[a]	–[a]	–[a]
(O–O)Ru_2–NH (benzylic)	doublet	2.30	1.96	0.36	–0.12	0.36	0.75
(O–O)Ru_2–NH (aromatic)	doublet	2.31	2.00	–[a]	–0.13	0.40	0.81

The activation of sp^3 benzylic C–H bond had a much lower barrier (**Figure IV-16**, Int3, 21.3 kcal mol^{-1}) compared to that of sp^2 aromatic C–H bond (**Figure IV-17**, 42.0 kcal mol^{-1}). The formation of amido complex (**Figure IV-16**, Int3) via the activation of sp^3 benzylic C–H bond was thus favored and benzylamine was synthesized in a high selectivity.

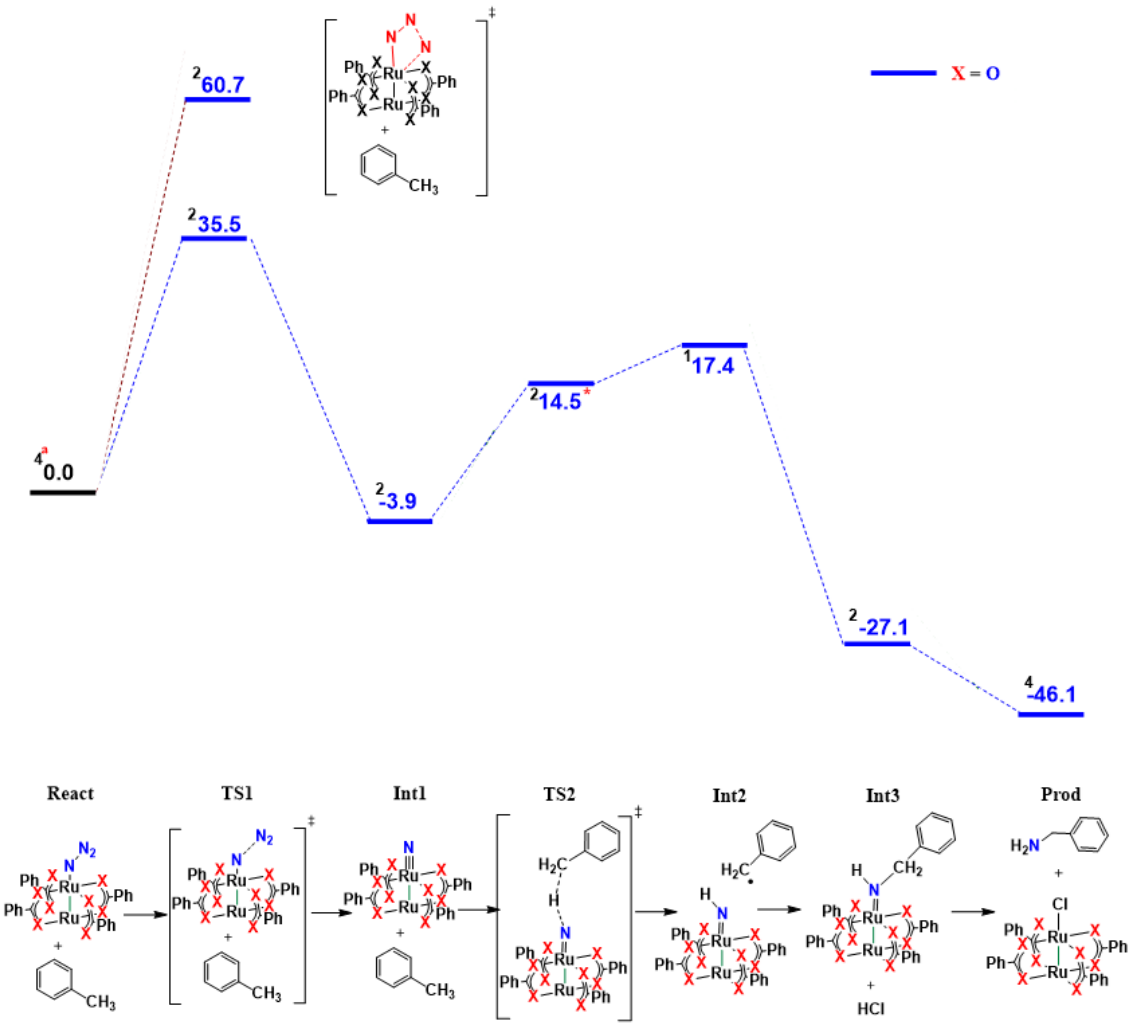

Figure IV-16. Energies of transition states and intermediates for sp^3 benzylic C–H activation. X = O–O. Energies are in kcal mol^{-1}. Numbers in superscript denote multiplicities.

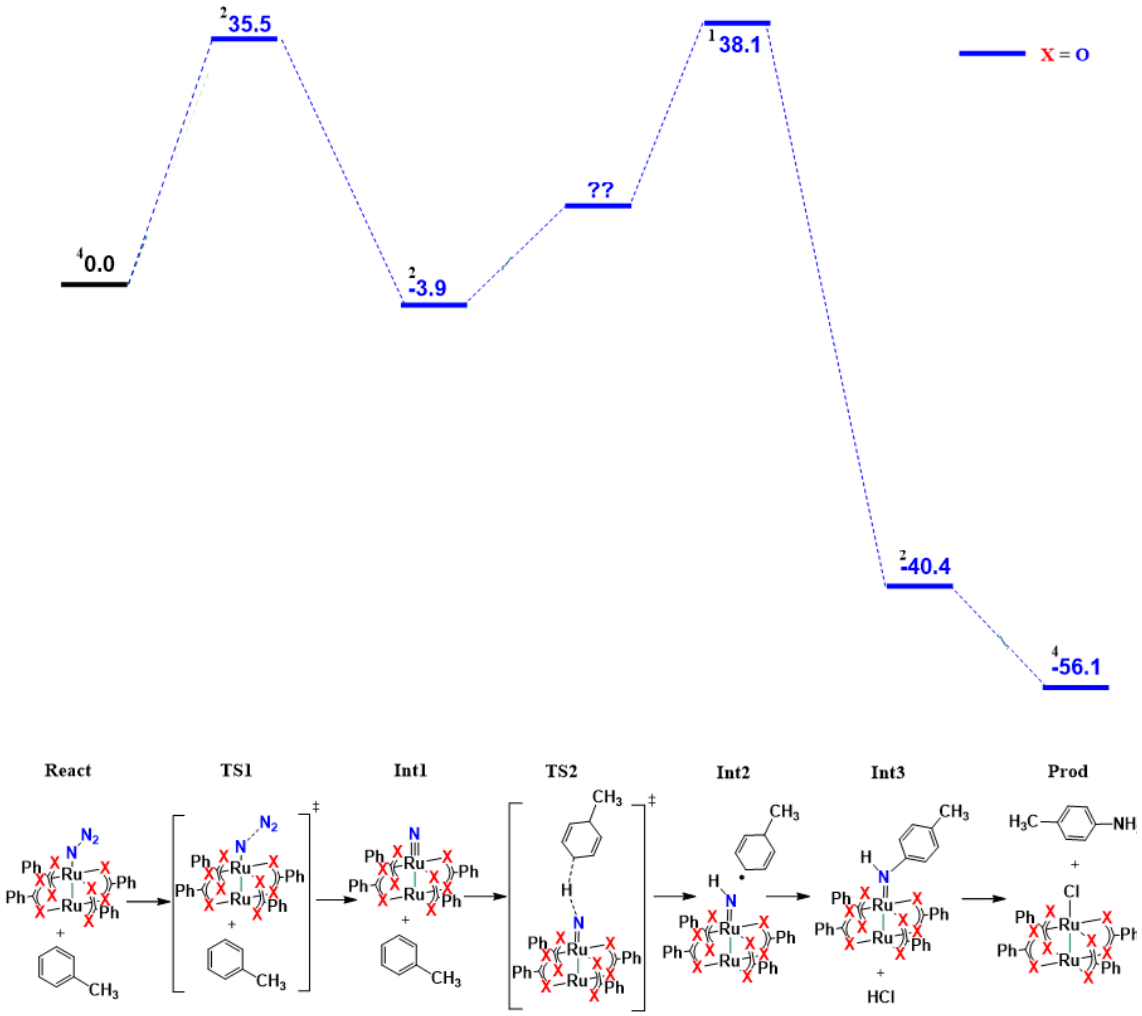

Figure IV-17. Energies of transition states and intermediates for sp^2 aromatic C–H activation. X = O–O. Energies are in kcal mol^{-1}. Numbers in superscript denote multiplicities. Calculation for TS2 is running.

The calculated KIE for toluene sp^3 benzylic C–H amination at 100 °C with no impact of diffusion was found to be 3.7, which was in good accordance with the convergence of the experimental curves of the intra- and intermolecular curves catalyzed by the most mesoporous $Ru_6btc_x(pydc)_{4-x}(N_3)_3$ (S_{meso}/S_{micro} = 0.61).

Temperature Dependence. In addition to the magnitude of kinetic isotope effects, the temperature dependence of these values can provide substantial mechanistic information regarding the intimate details of C−H cleavage. In particular, we examined the kinetic isotope effect of amination of d_1-toluene as a function of temperature (60−110 °C) with $[Ru_6(btc)_4(N_3)_3]$ (S_{meso}/S_{micro} = 0.07; **Figure IV-18**). We were specifically interested in the temperature dependence of this KIE because the measured intramolecular KIE (7.86(3)) exceeds the classical limit derived from C−H vs C−D stretching frequencies[iv-v] (KIE equivalent to ∼13.4 at 23 °C if treated classically). The intramolecular KIE increases substantially as the reaction temperature is decreased: amination of d_1-toluene proceeds with k_H/k_D = 4.87 at 110 °C, which increases to 18.8 at 60 °C (**Figure IV-18**, raw data collected in **Tables IV-7** and **IV-8**). The reaction is prohibitively slow at lower temperatures and thus lower-temperature data are unavailable. An Arrhenius plot

[iv]If one considers the differences in zero-point energy of the C−H and C−D stretching modes, the classical limit for k_H/k_D = 6.9. Larger values (15−20) are possible is one considers potential bending modes as well. See: Melander, L.; Saunders, W. H., Jr *Reaction Rates of Isotopic Molecules*; John Wiley & Sons: New York, 1980; pp 130−131.

[v]Important low-energy bending modes can give rise to large kinetic isotope effects for H-atom-transfer reaction involving M = E (E = O and N) fragments: Slaughter, L. M.; Wolczanski, P. T.; Klinckman, T. R.; Cundari, T. R. Inter- and Intramolecular Experimental and Calculated Equilibrium Isotope Effects for $(silox)_2(tBu_3SiND)TiR$ + RH (silox = tBu_3SiO): Inferred Kinetic Isotope Effects for RH/D Addition to Transient $(silox)_2Ti$ = $NSitBu_3$. *J. Am. Chem. Soc.* **2000**, *122*, 7953−7975.

(**Figure IV-19**) generated from these temperature-dependent KIEs provided A_H/A_D = 0.002 and $\Delta E_{D\text{-}H}$ = 6.2 ± 0.9 kcal·mol^{-1} (**Tables IV-9**), both of which are consistent with significant tunneling based on the criteria articulated by Kreevoy et al. (A_H/A_D < 0.7 and $\Delta E_{D\text{-}H}$ > 1.2 kcal·mol^{-1}).[247]

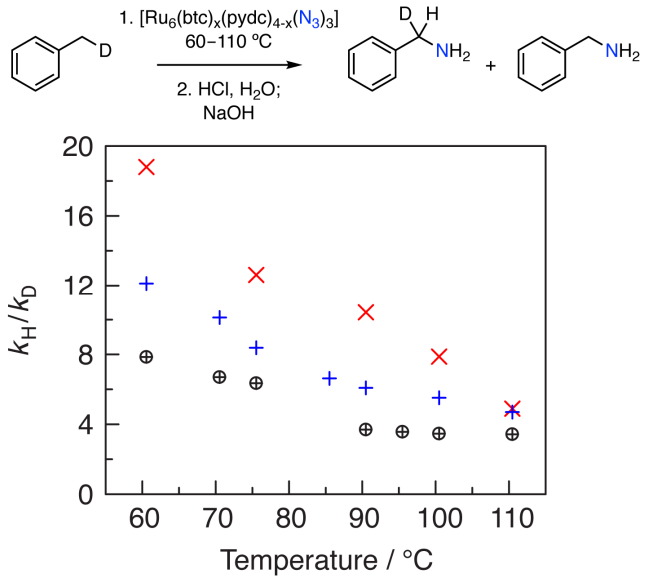

Figure IV-18. Temperature-dependent intramolecular KIEs. Temperature-dependent intramolecular KIEs for the amination of d_1-toluene in $[Ru_6(btc)_4(N_3)_3]$ (×, S_{meso}/S_{micro} = 0.07) and $[Ru_6(btc)_x(pydc)_{4-x}(N_3)_3]$ with S_{meso}/S_{micro} = 0.39 (+) and 0.61 (⊕).

Table IV-7 Summary of reaction times and temperatures used for thermolysis of $[Ru_6(btc)_x(pydc)_{4-x}(N_3)_3]$ in toluene, d_8/H_8-toluene mixture, and deuterated xylene isomers. The reaction time was monitored by the disappearance of azide stretching using IR.

Temperature / °C	Reaction Time / h
60	96
70	96
75	72
83	50
85	50
90	36
95	28
100	16
110	14
120	12
130	11

Table IV-8 Summary of k_H/k_D for intramolecular amination of toluene using $[Ru_6(btc)_4(N_3)_3]$ (S_{meso}/S_{micro} = 0.07) and $[Ru_6(btc)_x(pydc)_{4-x}(N_3)_3]$ (S_{meso}/S_{micro} = 0.39 and 0.61) at various temperatures.

Sample S_{meso}/S_{micro}	Temperature / °C	k_H/k_D
0.07	60	18.8
	75	12.6
	90	10.4
	100	7.86
	110	4.87
0.39	60	12.1
	70	10.1
	75	8.36
	85	6.61
	90	6.06
	100	5.49
	110	4.67
0.61	60	7.83
	70	6.67
	75	6.33
	90	3.67
	95	3.54
	100	3.43
	110	3.40

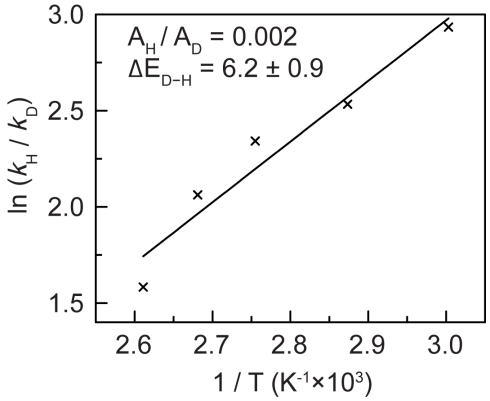

Figure IV-19. Arrhenius plot generated from intramolecular k_H/k_D values measured for amination of d_1-toluene with $[Ru_6(btc)_4(N_3)_3]$ (S_{meso}/S_{micro} = 0.07). Linear regression statistics collected in **Table IV-10**.

Table IV-9 Arrhenius parameters for C–H amination derived from temperature-dependent KIEs

S_{meso} / S_{micro}	A_H/A_D	ΔE_{D-H} (kcal·mol^{-1})	R^2
0.07	0.002	6.2 ± 0.9	0.94
0.39	0.007	4.9 ± 0.3	0.98
0.61 (>90 °C)	0.87	1.0 ± 0.3	0.84
0.61 (<90 °C)	0.001	6.1 ± 1.2	0.93

Further, we have analyzed the temperature dependence of the kinetic isotope effects as a function of material mesoporosity using samples with S_{meso}/S_{micro} = 0.39 and 0.61 (**Figure IV-18**). Amination of *d*$_1$-toluene with S_{meso}/S_{micro} = 0.39 [$Ru_6(btc)_x(pydc)_{4-x}(N_3)_3$] displays a temperature-dependent KIE: from 4.67 at 110 °C to 12.1 at 60 °C. The Arrhenius plot (**Figure IV-20**) generated from these data provided A_H/A_D = 0.007 and ΔE_{D-H} = 4.9 ± 0.9 kcal·mol^{-1}, which is also suggestive of a meaningful contribution of tunneling. In comparison, two temperature regimes were observed when k_H/k_D of *d*$_1$-toluene amination was determined using S_{meso}/S_{micro} = 0.61 [$Ru_6(btc)_x(pydc)_{4-x}(N_3)_3$] (Arrhenius plot presented in **Figure IV-21**). Between 90–110 °C, the observed NAT displays classical Arrhenius behavior (A_H/A_D = 0.87 and ΔE_{D-H} = 1.0 ± 0.3 kcal·mol^{-1}). Below 90 °C, temperature-dependent KIEs are observed and Arrhenius analysis suggests the contribution of tunneling (A_H/A_D = 0.001 and ΔE_{D-H} = 6.1 ± 1.2 kcal·mol^{-1}). These observations indicate that toluene confinement in the most mesoporous sample is relaxed such that NAT displays classical kinetic behavior at high temperature.

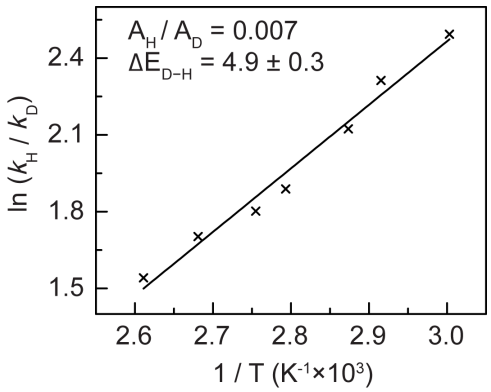

Figure IV-20. Arrhenius plot generated from intramolecular k_H/k_D values measured for amination of d_1-toluene with $[Ru_6(btc)_4(N_3)_3]$ (S_{meso}/S_{micro} = 0.39). Linear regression statistics collected in **Table IV-10**.

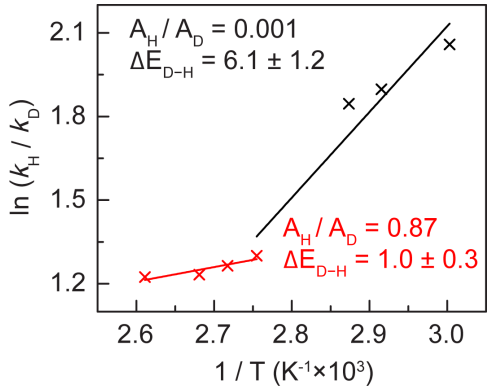

Figure IV-21. Arrhenius plot generated from intramolecular k_H/k_D values measured for amination of d_1-toluene with $[Ru_6(btc)_4(N_3)_3]$ (S_{meso}/S_{micro} = 0.61). Linear regression statistics collected in **Table IV-10**.

Table IV-10 Arrhenius fit for **Figures IV-19**, **IV-20**, and **IV-21** by fitting the Arrhenius equation $\ln(k_H/k_D) = (\Delta E_{D-H}/k)\,(1/T) + \ln(A_H/A_D)$

Mesoporosity	**$\ln(A_H / A_D)$**	**$(\Delta E_{D-H} / k)$**	**R^2**
0.07	–6.4915	3153.8	0.9419
0.39	–4.9866	2484.2	0.9799
0.61 (>90 °C)	–0.1408	518.74	0.8419
0.61 (<90 °C)	–7.0997	3074.4	0.9269

IV.3 Discussion

While low-energy vibrational modes can give rise to classical rationalizations for large KIEs,[268] the dependence of the intramolecular KIE–measured for the same chemical event (*i.e.* amination of toluene by a Ru_2 nitride)–on material mesoporosity suggests that (1) confinement effects, and not differences in vibrational modes, are responsible for the observed trends and (2) tunneling contributes meaningfully to the rate of H-atom abstraction (HAA) during NAT at lattice-confined Ru_2 nitrides. These results closely mirror those reported by Klinman *et al.* for HAA reactions mediated by I553X series of soybean lipoxygenase (SLO) variants which showed the tunneling effect was less substantial as pretunneling distance was increased.[269]

Further support for substantial substrate confinement and the contribution of tunneling to HAA chemistry mediated by lattice-confined Ru_2 nitride intermediates was obtained by examination of the amination of selectively labeled xylenes featuring one CH_3 and one CD_3 group. Labeled xylene isomers were prepared by Suzuki coupling between the appropriate tolylboronic acid and d_3-methyl iodide.[270] Using a sample of $[Ru_6(btc)_x(pydc)_{4-x}(N_3)_3]$ with $S_{meso}/S_{micro} = 0.61$, we have carried out amination of each of the labeled xylene isomers (**Table IV-11**). Each isomer participates in amination upon thermolysis at 100 °C to afford the corresponding methylbenzylamine and displays large kinetic isotope effect (k_H/k_D = 29.3 (*ortho*-xylene), 26.0 (*meta*), and 25.8 (*para*). The magnitude of these KIE values indicates that xylenes are not sufficiently constrained to prevent the methyl groups from sampling the Ru_2 nitride on the time scale of NAT. If xylene was sufficiently confined to restrict the methyl groups from sampling the nitride,

one might expect *p*-d_3-xylene to display a lower KIE than *o*-d_3-xylene. Each of the measured KIEs is highly temperature dependent: When thermolysis is carried out at 130 °C, k_H/k_D values of 15.4 (ortho), 11.9 (meta), and 12.8 (para) are obtained. The enhanced KIE values for xylene amination as compared to toluene suggest that xylenes (kinetic diameter (7.4 Å (ortho), 7.1 Å (meta), and 6.7 Å (para),[271] are more confined in a given network than toluene (kinetic diameter (5.9 Å)).[228]

Table IV-11 Temperature-dependent KIEs for NAT to isomeric d_3-xylenes using $[Ru_6(btc)_x(pydc)_{4-x}(N_3)_3]$ (S_{meso} / S_{micro} = 0.61).

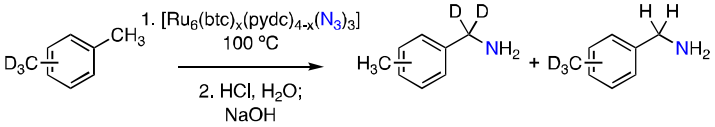

Substrate	k_H/k_D			
	100 °C	110 °C	120 °C	130 °C
o-d_3-xylene	29.3	27.7	15.8	15.4
m-d_3-xylene	26.0	22.1	19.9	11.9
p-d_3-xylene	25.8	20.4	14.5	12.8

IV.4 Conclusions

In conclusion, the described experimental results directly reveal the impact of network structure on the confinement of substrates during interstitial chemistry. Because the experiments provide direct observation of the relative rates of substrate diffusion and functionalization, this analysis is amenable to application in the commonly encountered defective frameworks that are utilized in MOF catalysis. In addition, these experiments have revealed that network-dependent substrate confinement gives rise to substantial quantum tunneling during interstitial C−H functionalization chemistry. These data highlight the similarity of pore-confined substrate functionalization with enzymatic C−H functionalization and serve as a stark example of the significant transport barriers that confront fine-chemical synthesis in microporous MOFs. We anticipate the described experiments will provide critical information regarding diffusivity that will inform rational development of designer MOF catalysts.

IV.5 Experimental Details

IV.5.1 General Considerations

Materials Solvents were obtained as ACS reagent grade. Unless otherwise noted, all chemicals and solvents were used as received. Magnesium sulfate ($MgSO_4$) and pyridine (py) were obtained from EMD Millipore. Diethyl ether (Et_2O), iodomethane-d_3 (CD_3I), trimethylsilyl trifluoromethanesulfonate (TMSOTf), 1,3-benzenedicarboxylic acid (1,3-H_2bdc), and methanol (MeOH) were obtained from Sigma Aldrich. Dimethylformamide (DMF) was obtained from Acros Organics. Tri(*o*-tolyl)phosphine (P(*o*-tolyl)$_3$) and palladium acetate ($Pd(OAc)_2$) were obtained from Strem Chemicals. *o*-Tolylboronic acid, *m*-tolylboronic acid, and *p*-tolylboronic acid were obtained from Chem Impex. Acetic acid (AcOH) was obtained from Beantown Chemical. Dichloromethane (CH_2Cl_2), toluene ($PhCH_3$), and potassium carbonate (K_2CO_3) were obtained from Fisher Scientific. 3,5-Pyridinedicarboxylic acid (H_2pydc) and 1,3,5-benzenetricarboxylic acid (H_3btc) were obtained from Alfa Aesar. Sodium hydroxide (NaOH) was obtained from BDH Analytical Chemicals. Hydrochloric acid (HCl) was obtained from Macron Chemicals. NMR solvents were purchased from Cambridge Isotope Laboratories and were used as received. UHP-grade N_2, CO_2, Ar, and He, used in gas adsorption and desorption were obtained from Airgas (UHP = ultra-high purity). All reactions were carried out under ambient atmosphere unless otherwise noted. $Ru_2(OAc)_4Cl$,[169] $[Ru_6(btc)_4]$,[169] $[Ru_6(btc)_4Cl_3]$,[226] $[Ru_6(btc)_4(N_3)_3]$,[169] α-d_1-toluene,[169] $[Ru_2(OBz)_4(THF)_2]BF_4$,[169] and $[Ru_6(btc)_x(1,3\text{-bdc})_{4-x}Cl_3]$[272] were prepared according to literature methods.

Characterization Details NMR spectra were recorded on a Bruker Ascend 400 at 400.09 MHz for ^{1}H and at 100.60 MHz for ^{13}C acquisitions and were referenced against residual solvent resonances: $CDCl_3$ (7.26 ppm, ^{1}H; 77.16 ppm, ^{13}C) and d_6-DMSO (2.50 ppm, ^{1}H).[185] ^{1}H NMR data are reported as follows: chemical shift (δ, ppm), (multiplicity: s (singlet), d (doublet), t (triplet), m (multiplet), br (broad), integration). IR spectra were recorded on either a Shimadzu FTIR/IRAffinity-1 spectrometer or an ATI Mattson Genesis Series FTIR spectrometer. *In situ* IR spectra in a KBr pellet were measured with a Bruker VERTEX 70. Spectra were blanked against air and were determined as the average of 64 scans. IR data are reported as follows: wavenumber (cm^{-1}), (peak intensity: s, strong; m, medium; w, weak). Electrospray ionization mass spectrometry (ESI-MS) experiments were performed using a Thermo Scientific Q Exactive Focus. Samples were introduced into the mass spectrometer by loop injection (10 µL) with a methanol mobile phase at a flow rate of 100 µL/min. The Q Exactive Focus HESI source was operated in full MS in positive mode. The mass resolution was tuned to 70000 FWHM at m/z 200. The spray voltage was set to 3.75 kV, and the sheath gas and auxiliary gas flow rates were set to 7 and 0 arbitrary units, respectively. The transfer capillary temperature was held at 250 °C and the S-Lens RF level was set at 50 V. Exactive Series 2.8 SP1/Xcalibur 4.0 software was used for data acquisition and processing. Kinetic isotope effects (k_H/k_D) were determined by integration of appropriate peaks in the mass spectrum. Elemental analyses were performed in Atlantic Microlab, Inc., Norcross, GA. Field emission scanning electron microscopy (FE-SEM) were obtained by a JEOL JSM-7500F at an accelerating voltage of 5.0 kV, an emission current of 10 μA and a probe current of 10 μA.

Transmission electron microscopy (TEM) images were taken on an FEI Tecnai G2 F20 ST FE-TEM operated at an accelerating voltage of 200 kV. Gas chromatography (GC) analysis for the ratio of d_8/H_8-toluene was carried out using a Trace 1310 (Thermo Scientific) instrument equipped with a TraceGOLD TG-1M column from Thermo Scientific (length: 30 m, id: 0.53 mm, film thickness: 0.25 μm). The column temperature was maintained at 31 °C for 0.1 min and raised to 40 °C at 0.5 °C/min. The final temperature (40 °C) was held for 3 min. Diffuse reflectance UV-vis-NIR spectra were recorded by a Hitachi U-4100 UV-vis-NIR spectrophotometer with Praying Mantis diffuse reflectance accessory at 293 K and were collected against a $BaSO_4$ blank.

Gas/Vapor Adsorption and Desorption Details Gas adsorption and desorption isotherms for pressures in the range 0−1.0 bar were measured volumetrically using a Micromeritics ASAP 2020 Plus instrument. Samples were transferred under an N_2 atmosphere to pre-weighed analysis tubes. The samples were evacuated at room temperature or 150 °C until the outgas rate was <10 μbar/min and further maintained for 24 h. At this time the tube was weighed to determine the mass of the activated sample. The tube was transferred to the analysis port of the ASAP 2020 Plus. UHP-grade (99.999% purity) N_2 and He were used for all adsorption measurements. For all isotherms, both warm and cold free-space measurements were carried out with He; N_2 isotherms were measured at 77 K. For toluene vapor adsorption isotherms, approximately 100 mg of each sample was loaded into a pre-weighed sample tube in an N_2 glovebox and capped with a Transeal. Samples were transferred to an activation station and heated under dynamic vacuum to a temperature of 150 °C until the static off-gas rate was <1 μbar/min. Activated samples

were weighed and transferred to a Micromeritics 3Flex gas adsorption analyzer equipped with a vapor dosing attachment. Samples were placed in a 25 °C bath for the adsorption experiments. Anhydrous toluene was placed in the vapor dosing tube and degassed on the instrument via three freeze−pump−thaw cycles. The vapor dosing tube was heated to 40 °C with a heating mantle for the duration of the experiment while the instrument manifold was kept at 45 °C. Toluene accessible surface areas were modeled using Jmol 14.29.25 using a solvent radius of 2.93 Å (kinetic diameter of toluene[228] is 5.85 Å). The optimized molecular coordinates of $[Ru_6(btc)_4Cl_3]$ and $[Ru_6(btc)_x(pydc)_{4-x}Cl_3]$ were obtained from the literature.[273]

Mesoporosities are reported as S_{meso}/S_{micro}, in which the microporous surface area (S_{micro}) is calculated using Density Functional Theory (DFT)[vi] fitting of the N_2 adsorption data (P/P_0 = 0.000000635—0.95), and the mesoporous surface area (S_{meso}) is calculated by Barrett–Joyner–Halenda (BJH)[274] analysis of the N_2 desorption data (P/P_0 = 0.04—0.9) with Kruk–Joyner–Sayari (KJS) correction.[275,vii] This strategy was utilized because the Density Functional Theory (DFT) package with ASAP 2020 Plus software calculates the pore size distribution based on the N_2 adsorption branch, which intentionally ignores the hysteresis loop observed in the N_2 desorption branch. Thus, to address this issue, we employ the BJH method to calculate the N_2 desorption branch to accurately evaluate the

[vi] We have used the slit-geometry model in this calculation, which has previously been validated for Cu_3btc_2 and Zn_3btc_2; see: Wang, T.; Li, X.; Dai, W.; Fang, Y.; Huang, H. J. *Mater. Chem. A* **2015**, *3*, 21044, Wang, W.; Yuan, D. *Sci. Rep.* **2014**, *4*, 5711. This calculation was carried out using Micromeritics software.

[vii] The same model was utilized to analyze mesopore size distribution of mesoporous Cu_3btc_2; see: Qiu, L.-G.; Xu, T.; Li, Z.-Q.; Wang, W.; Wu, Y.; Jiang, X.; Tian, X.-Y.; Zhang, L.-D. *Angew. Chem. Int. Ed.* **2008**, *47*, 9487, 12; Sun, L.-B.; Li, J.-R.; Park, J.; Zhou, H.-C. *J. Am. Chem. Soc.* **2012**, *134*, 126. This calculation was carried out using Micromeritics software.

mesopore range. The S_{micro} is defined and generated from pores with diameter between 6 Å and 20 Å; micropores with diameter of ~5.5 Å are not accessible by toluene molecules (kinetic diameter = 5.85 Å, see **Figure IV-7**)[228] and thus surface areas derived from these micropores were excluded. The S_{meso} is defined and generated from pores with diameters between 20 Å and 200 Å.

IV.5.2 Synthesis and Characterization

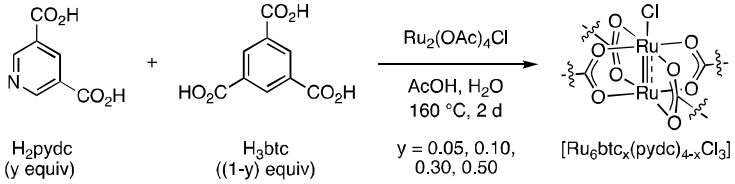

Synthesis of $[Ru_6(btc)_x(pydc)_{4-x}Cl_3]$ $[Ru_6(btc)_x(pydc)_{4-x}Cl_3]$ samples were prepared according to the following modification of literature procedures.[257] Here the procedure based on a 90:10 H_3btc:H_2pydc ligand feed is presented; details of synthesis with other H_3btc:H_2pydc ratios are summarized in Table S1. A 20-mL Teflon-lined autoclave was charged with a stir bar, $Ru_2(OAc)_4Cl$ (0.102 g, 0.215 mmol, 1.00 equiv), H_3btc (0.0544 g, 0.259 mmol, 1.20 equiv), and H_2pydc (0.0048 g, 0.029 mmol, 0.13 equiv). H_2O (2.40 mL) and acetic acid (0.42 mL) were added and the resulting mixture was heated in a pre-heated sand bath at 160 °C. After stirring for 30 min at this temperature, the autoclave was transferred to a well-ventilated oven at 160 °C. After 2 d, the reaction mixture was cooled to 23 °C and the resulting solid was isolated by filtration. The solid was washed with H_2O (15.0 mL × 5) and methanol (15.0 mL × 5) to afford 110 mg of the title material. $[Ru_6(btc)_x(pydc)_{4-x}Cl_3]$ was not purified further prior to use in the synthesis of $[Ru_6(btc)_x(pydc)_{4-x}(N_3)_3]$. IR ($cm^{-1}$): 1709 (m), 1611 (m), 1553 (m), 1430 (m), 1368 (s), 1264 (m), 1119 (w), 1018 (w), 939 (m), 731 (s), 684 (m). PXRD data for samples prepared by this procedure are collected in Figure S1a. For gas adsorption and desorption studies, $[Ru_6(btc)_x(pydc)_{4-x}Cl_3]$ was activated under high vacuum at 150 °C for 24 h. N_2 and toluene adsorption isotherms are collected in **Figures IV-3b** and **IV-4**, respectively.

Elemental analysis [viii] (EA) for S_{meso}/S_{micro} = 0.28 ($Ru_6(btc)_{3.83}(pydc)_{0.17}(OH)_{1.98}Cl_{1.02}(AcOH)_{1.5}(H_2O)_{10}$): found C, 25.91; H, 2.25; N, 0.12; Cl, 2.24; calcd. C; 26.27; H, 2.28; N, 0.13; Cl, 2.05; S_{meso}/S_{micro} = 0.40 ($Ru_6(btc)_{3.60}(pydc)_{0.40}(OH)_{1.90}Cl_{1.10}(H_2O)_{13}$): found C, 24.87; H, 2.52; N, 0.35; Cl, 2.37; calcd. C, 24.53; H, 2.33; N, 0.33; Cl, 2.26; S_{meso}/S_{micro} = 0.39 ($Ru_6(btc)_{2.80}(pydc)_{1.20}(OH)_{2.35}Cl_{0.65}(AcOH)_2(H_2O)_{17}$): found C, 24.88; H, 3.38; N, 0.93; Cl, 1.15; calcd. C, 24.10; H, 3.03; N, 0.90; Cl, 1.23; S_{meso}/S_{micro} = 0.55 ($Ru_6(btc)_{2.10}(pydc)_{1.90}(OH)_{2.30}Cl_{0.70}(AcOH)_2(H_2O)_{20}$): found C, 22.81; H, 3.43; N, 1.38; Cl, 1.28; calcd. C, 22.23; H, 3.26; N, 1.35; Cl, 1.24. The reported data for this material is well-matched to that previously reported.[257] The EA results from varying H_2pydc loadings are summarized in **Table IV-12**. For a given H_2pydc loading, the resulting mesoporosity shows variation; exemplary data are summarized in **Table IV-13** for syntheses carried out with 10% H_2pydc loading.

[viii] Elemental analysis has previously been utilized to characterize the presence of Cl, and OH ligands in $[Ru_6(btc)_4Cl_3]$ (see references *Angew. Chem. Int. Ed.* **2018**, *57*, 3676–3681 and *Nat. Commun.* **2019**, *10*, 2076–2083). The observed ligand distributions here are in agreement with those previously reported.

Table IV-12 Synthetic details for the preparation of $[Ru_6(btc)_x(pydc)_{4-x}Cl_3]$ materials

H_2pydc / (H_2pydc + H_3btc)	H_3btc (mg)	H_2pydc (mg)	Product (mg)	Formula derived from elemental analyses
0.05	57.6	2.4	112	$Ru_6(btc)_{3.83}(pydc)_{0.17}(OH)_{1.98}Cl_{1.02}(AcOH)_{1.5}(H_2O)_{10}$
0.10	54.4	4.8	110	$Ru_6(btc)_{3.60}(pydc)_{0.40}(OH)_{1.90}Cl_{1.10}(H_2O)_{13}$
0.30	42.3	14.4	102	$Ru_6(btc)_{2.80}(pydc)_{1.20}(OH)_{2.35}Cl_{0.65}(AcOH)_2(H_2O)_{17}$
0.50	30.2	24.0	91.4	$Ru_6(btc)_{2.10}(pydc)_{1.90}(OH)_{2.30}Cl_{0.70}(AcOH)_2(H_2O)_{20}$

Table IV-13 S_{meso}, S_{micro}, and BET surface areas for a series of independent syntheses of $[Ru_6(btc)_x(pydc)_{4-x}Cl_3]$ using a 9:1 H_3btc:H_2pydc ratio.

BET / $m^2\ g^{-1}$	S_{meso} / $m^2\ g^{-1}$	S_{micro} / $m^2\ g^{-1}$	S_{meso}/S_{micro}
849	123	306	0.42
838	103	326	0.32
841	82	294	0.28
829	110	264	0.42
830	102	315	0.32

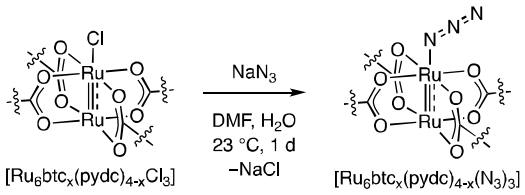

Synthesis of $[Ru_6(btc)_x(pydc)_{4-x}(N_3)_3]$ A 20-mL vial was charged with $[Ru_6(btc)_x(pydc)_{4-x}Cl_3]$ (0.0400 g), NaN_3 (0.0400 g, 0.615 mmol, > 30.0 equiv),[ix] H_2O (3.20 mL), and DMF (16.0 mL). The resulting mixture was allowed to stand at 23 °C for 1 d. At this time, the supernatant was decanted and the remaining solids were washed with MeOH (10.0 mL × 3). The solids were then soaked in MeOH (20.0 mL) at 23 °C for 3 d (refreshed three times per day), solvent was decanted, and the solids were allowed to air-dry to give 33.0 mg of the title compound as a dark brown powder. IR (cm^{-1}): 2048 (m), 1611 (m), 1544 (m), 1430 (m), 1366 (s), 1116 (w), 1019 (m), 937 (w), 732 (s), 684 (w).[x] PXRD data for samples prepared by this procedure are collected in **Figure IV-2**. For gas adsorption studies, $[Ru_6(btc)_x(pydc)_{4-x}(N_3)_3]$ was soaked in CH_2Cl_2 for 2 d (refreshed three times per day) and then activated at 23 °C under active vacuum for 24 h. N_2 adsorption isotherms are collected in **Figure IV-3**. Elemental analysis[xi] (EA) for S_{meso}/S_{micro} = 0.41 ($Ru_6(btc)_{3.83}(pydc)_{0.17}(OH)_{1.98}Cl_{0.54}(N_3)_{0.48}(H_2O)_{23}$): found C, 22.44; H, 2.71; N, 1.03; Cl, 0.92; calcd. C, 22.37; H, 3.16; N, 1.18; Cl, 1.00; S_{meso}/S_{micro} = 0.29 ($Ru_6(btc)_{3.60}(pydc)_{0.40}(OH)_{1.90}Cl_{0.31}(N_3)_{0.44}(H_2O)_{30}$): found C, 20.75; H, 3.73; N, 1.10; Cl,

[ix] We have previously utilized TMSOTf to remove OH and OAc ligands from Ru_2-based materials (*Angew. Chem. Int. Ed.* **2018**, *57*, 3676). Application of these methods to $[Ru_6(btc)_x(pydc)_{4-x}Cl_3]$ resulted in amorphous materials.

[x] Treatment of Ru_2(II,II)-based $[Ru_6(btc)_4]$ with NaN_3 did not result in the observation of any stretching frequency associated with azides was observed in the obtained solids.

[xi] EA analyses were performed on H_2pydc / (H_2pydc + H_3btc) = 0.05, 0.10, 0.30, 0.50 samples. The assignments of apical ligands and the solvents were based on EA analyses on $[Ru_6(btc)_x(pydc)_{4-x}Cl_3]$ and the fact that sodium azide exchanges only the chloride ligands (*Angew. Chem. Int. Ed.* **2018**, *57*, 3676).

0.50; calcd. C, 20.93; H, 3.69; N, 1.19; Cl, 0.54; S_{meso}/S_{micro} = 0.39 ($Ru_6(btc)_{2.80}(pydc)_{1.20}(OH)_{2.35}Cl_{0.23}(N_3)_{0.42}(H_2O)_{24}$): found C, 22.68; H, 3.65; N, 1.80; Cl, 0.39; calcd. C, 21.44; H, 3.34; N, 1.83; Cl, 0.43; S_{meso}/S_{micro} = 0.58 ($Ru_6(btc)_{2.10}(pydc)_{1.90}(OH)_{2.30}Cl_{0.35}(N_3)_{0.35}(H_2O)_{23}$): found C, 21.92; H, 3.35; N, 2.12; Cl, 0.58; calcd. C, 21.07; H, 3.31; N, 2.25; Cl, 0.68. **Table IV-14** summarizes the gas sorption data for the obtained family of mesoporous materials; mesoporosity is not well-correlated with the nomical ligand ratio used in synthesis.

Table IV-14 S_{meso}, S_{micro}, BET surface area, and the ratios of H_2pydc for $[Ru_6(btc)_x(pydc)_{4-x}(N_3)_3]$ and $[Ru_6(btc)_x(pydc)_{4-x}Cl_3]$ (in parentheses)

S_{meso}/S_{micro}	S_{meso} / m^2 g^{-1}	S_{micro} / m^2 g^{-1}	BET / m^2 g^{-1}	H_2pydc / (H_2pydc + H_3btc)
0.07 (0.12)	38 (43)	582 (356)	699 (959)	0
0.14 (0.23)	35 (75)	255 (326)	678 (838)	0.05
0.24 (0.20)	62 (60)	263 (294)	690 (841)	0.05
0.39 (0.19)	82 (74)	206 (287)	646 (826)	0.30
0.51 (0.33)	95 (85)	188 (264)	618 (829)	0.10
0.61	111	183	430	0.30

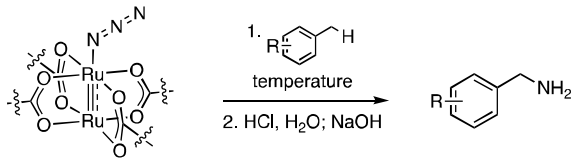

Thermolysis of $[Ru_6(btc)_x(pydc)_{4-x}(N_3)_3]$ A one-dram vial was charged with $[Ru_6(btc)_x(pydc)_{4-x}(N_3)_3]$ (10 mg). Substrate (0.25 mL) was added to the solids and the suspension was allowed to sit for 3 hours. The flask was then heated (reaction temperature and times are summarized in **Table IV-15**) by oil bath. The reaction vessels were cooled to 23 °C and substrate was removed by pipette. Concentrated HCl (0.20 mL) was added to the solids and the resulting suspension was sonicated for five minutes. CH_2Cl_2 (0.20 mL) was added and NaOH (2.50 M in H_2O) was added until pH > 10. The biphasic mixture was filtered through a Celite plug. The layers were separated and the KIE was determined by high-resolution ESI-MS analysis of the organic layer.

Table IV-15 Summary of reaction times and temperatures used for thermolysis of $[Ru_6(btc)_x(pydc)_{4-x}(N_3)_3]$ in toluene, d_8/H_8-toluene mixture, and deuterated xylene isomers. The reaction time was monitored by the disappearance of azide stretching using IR.

Temperature / °C	Reaction Time / h
60	96
70	96
75	72
83	50
85	50
90	36
95	28
100	16
110	14
120	12
130	11

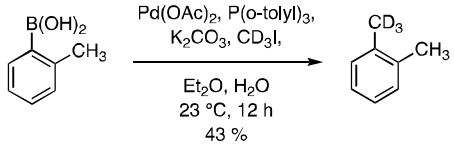

Synthesis of *o*-d_3-Xylene *o*-d_3-Xylene was prepared according to the following modification of literature.[270] A 100-mL Schlenk flask was charged with *o*-tolylboronic acid (2.04 g, 15.0 mmol, 1.00 equiv), $Pd(OAc)_2$ (168 mg, 0.750 mmol, 0.0500 equiv), tri(*o*-tolyl)phosphine (0.571 g, 1.88 mmol, 0.125 equiv), and K_2CO_3 (4.15 g, 30.0 mmol, 2.00 equiv). The headspace of the reaction vessel was evacuated and refilled with N_2. Degassed Et_2O (50.0 mL), H_2O (0.540 mL, 30.0 mmol, 2.00 equiv), and CD_3I (1.40 mL, 22.5 mmol, 1.50 equiv) were added. The reaction mixture was stirred at 23 °C for 12 h. *o*-d_3-Xylene was isolated by fractional distillation and was dried over $MgSO_4$ to afford 0.705 g title compound as a colorless liquid (43% yield). ^{1}H NMR (δ, 23 °C, $CDCl_3$): 7.01–7.07 (m, 4H), 2.19 (s, 3H). ^{13}C NMR (δ, 23 °C, $CDCl_3$): 136.7 (s), 136.5 (s), 129.7 (s), 125.9 (s), 125.9 (s), 19.8 (s), 19.1 (septet, J = 19.0 Hz). The recorded ^{1}H and ^{13}C spectra are shown in **Figures IV-22** and **IV-23**. The measured spectral data are in excellent agreement with *o*-xylene with the exception of the signals attributable to sites of deuteration.[276]

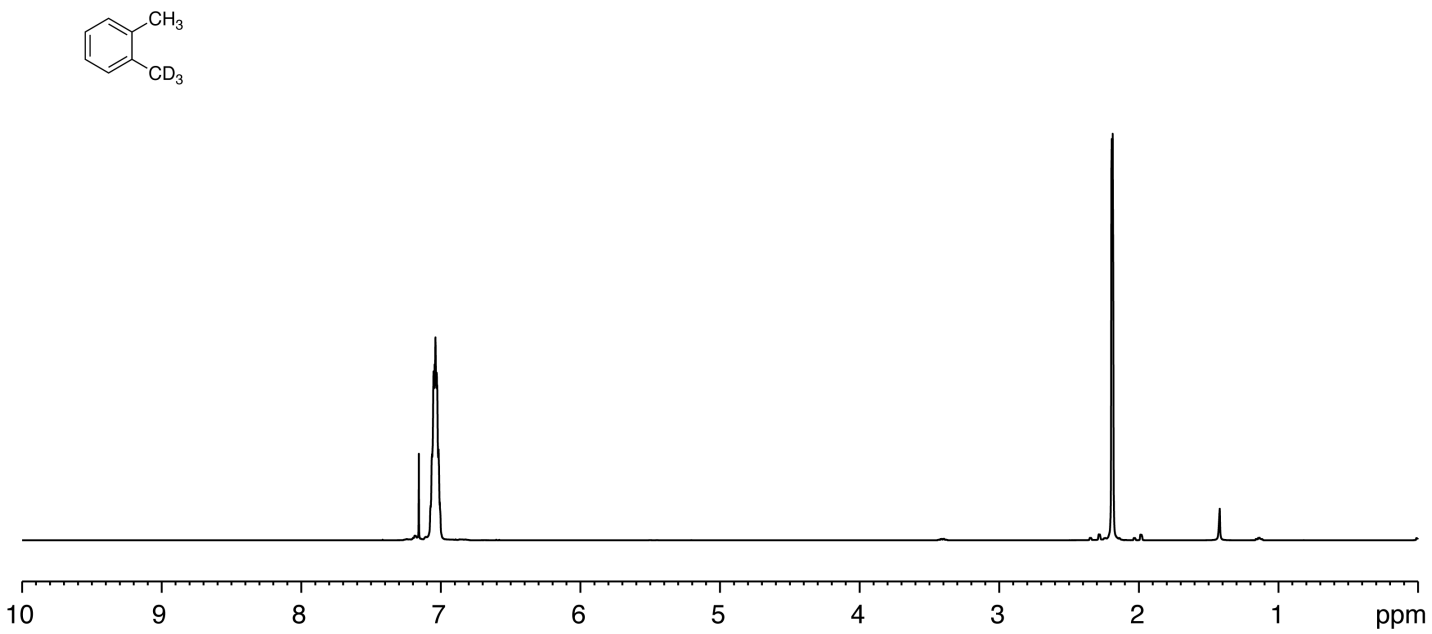

Figure IV-22. ^{1}H NMR spectrum of *o*-d_3-xylene acquired at 23 °C in $CDCl_3$.

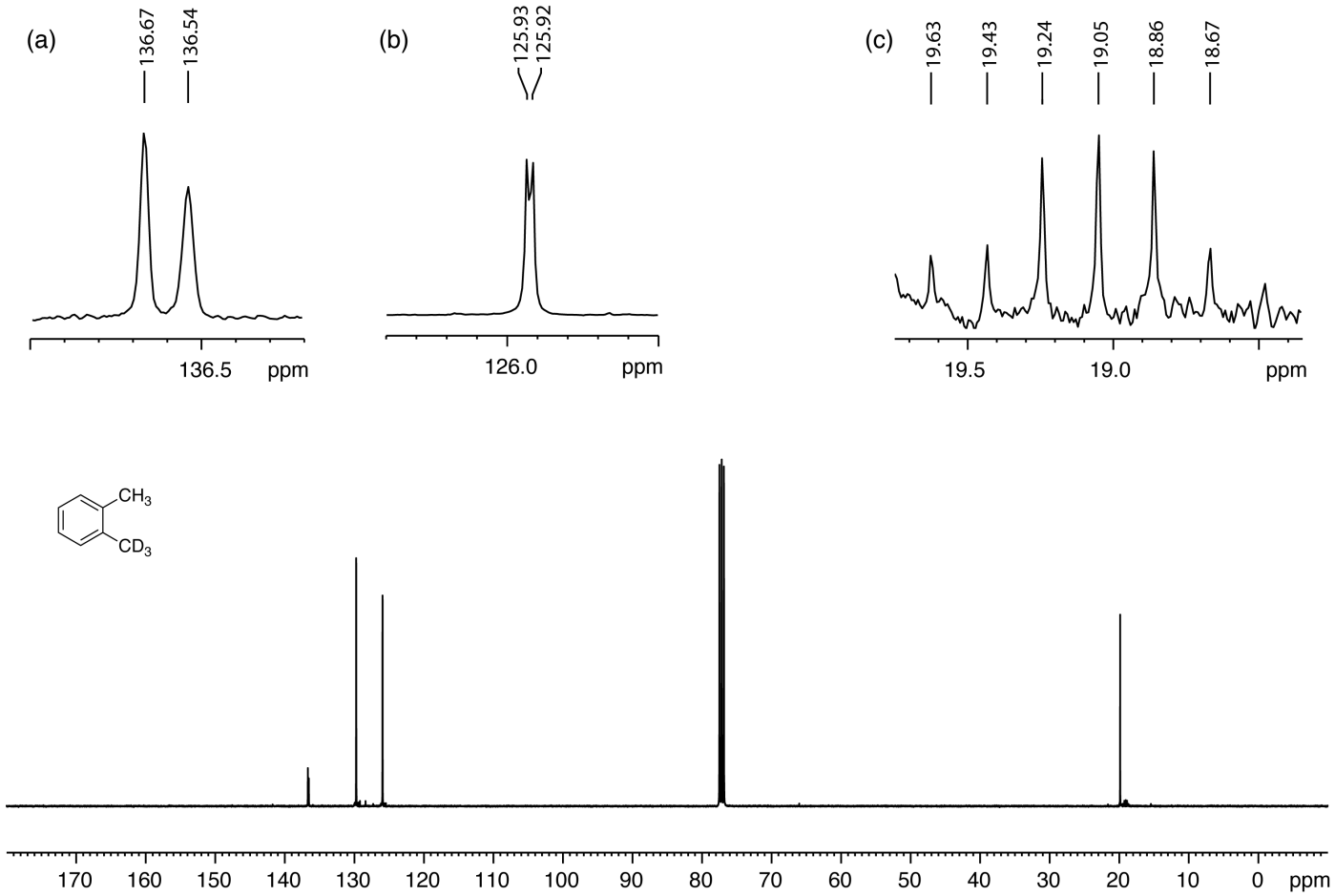

Figure IV-23. ^{13}C NMR spectrum of *o*-d_3-xylene acquired at 23 °C in $CDCl_3$. The insets show (a, b) $^{13}C_{ring}$ peaks and (c) ^{13}C–D coupling.

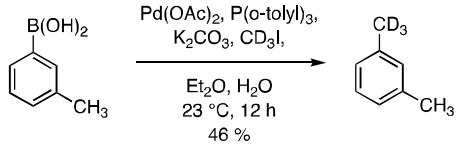

Synthesis of *m*-d_3-Xylene *m*-d_3-Xylene was prepared according to procedure above for *o*-d_3-xylene, with the exception that *m*-tolylboronic acid was used as starting material. *m*-d_3-Xylene was isolated by fractional distillation and was dried over $MgSO_4$ to afford 0.757 g title compound as a colorless liquid (46% yield). ^{1}H NMR (δ, 23 °C, $CDCl_3$): 7.15 (t, J = 7.6 Hz, 1H), 6.97–7.01 (m, 3H), 2.32 (s, 3H). ^{13}C NMR (δ, 23 °C, $CDCl_3$): 137.9 (s), 137.8 (s), 130.1 (s), 128.3 (s), 126.2 (s), 21.5 (s), 20.7 (septet, J = 19.1 Hz). The recorded ^{1}H and ^{13}C spectra are shown in **Figure IV-24** and **Figure IV-25**. The measured spectral data are in excellent agreement with *m*-xylene with the exception of the signals attributable to sites of deuteration.[276]

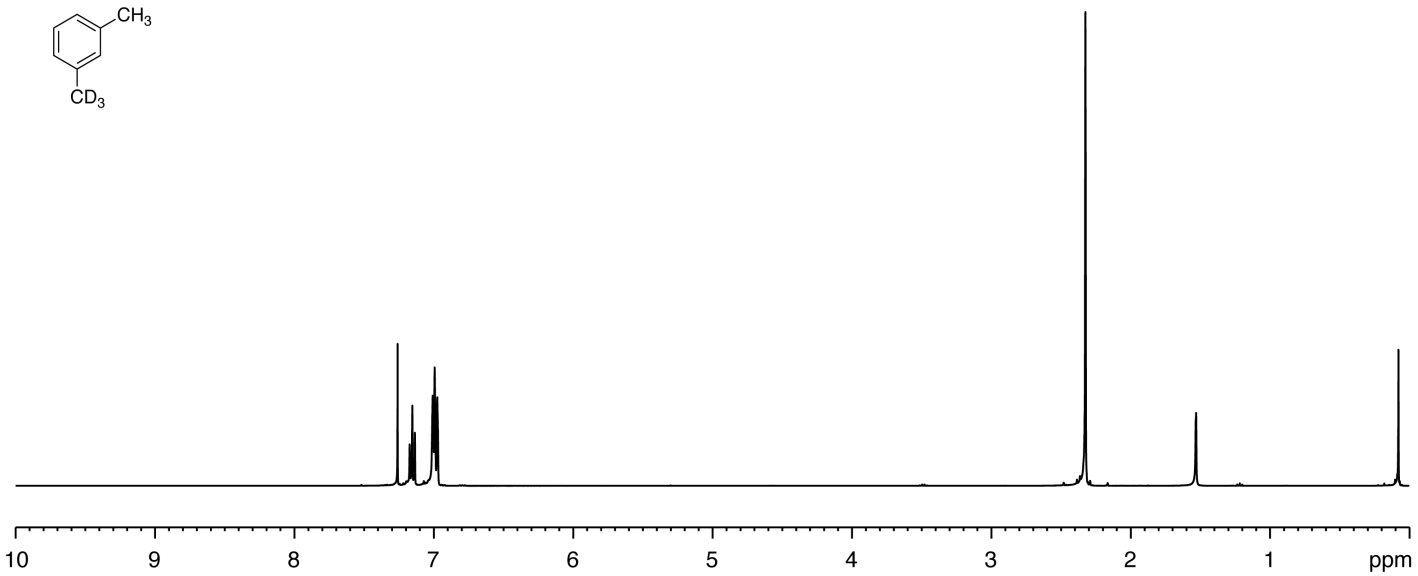

Figure IV-24. ^{1}H NMR spectrum of *m*-d_3-xylene acquired at 23 °C in $CDCl_3$.

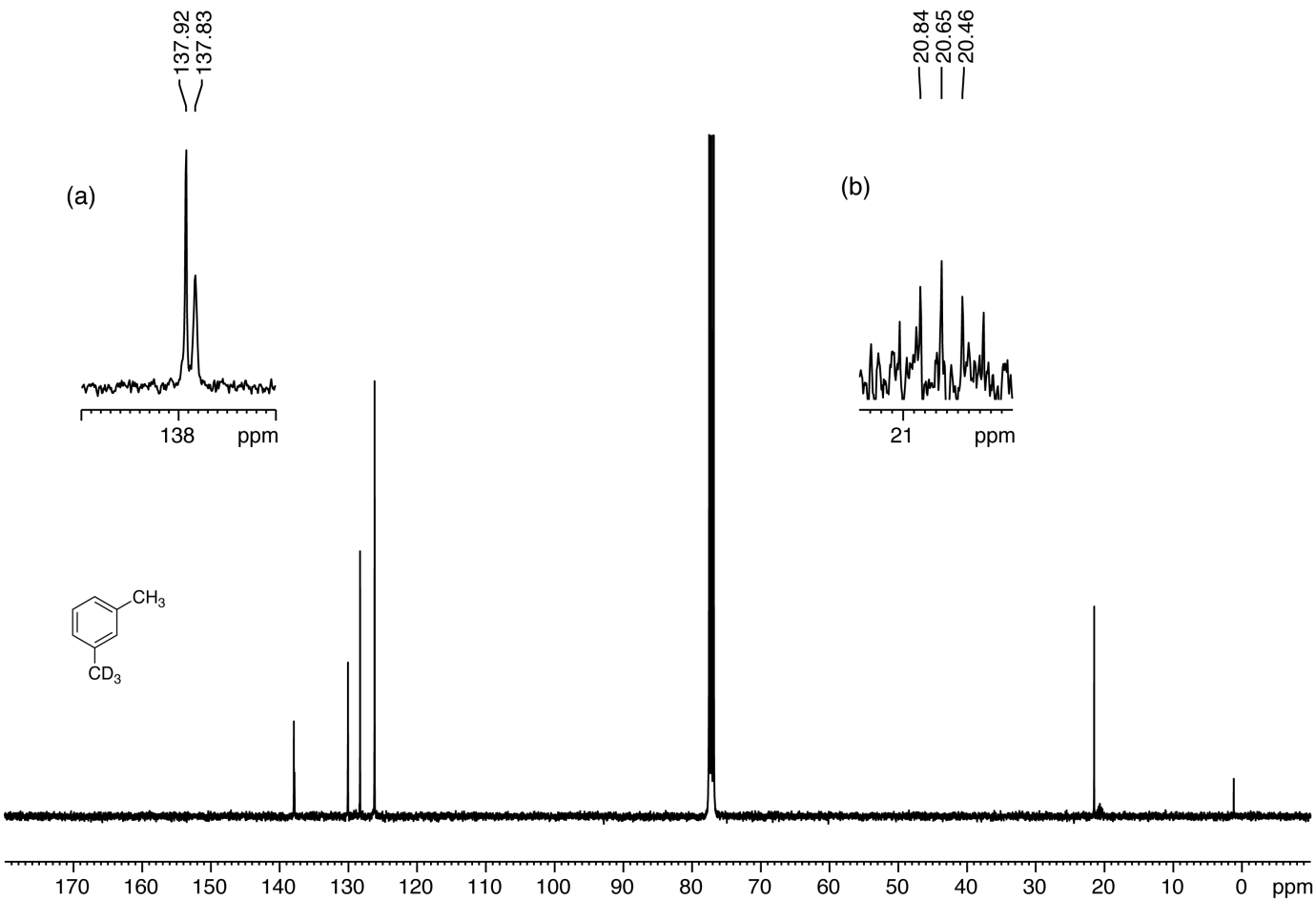

Figure IV-25. ^{13}C NMR spectrum of *m*-d_3-xylene acquired at 23 °C in $CDCl_3$. The insets show (a) $^{13}C_{ring}$-CD_3 and (b) ^{13}C–D coupling.

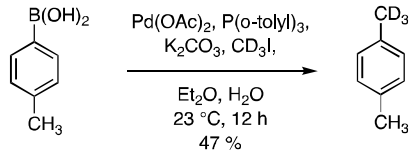

Synthesis of *p*-d_3-Xylene *p*-d_3-Xylene was prepared according to procedure above for *o*-d_3-xylene, with the exception that *p*-tolylboronic acid was used as starting material. *p*-d_3-Xylene was isolated by fractional distillation and was dried over $MgSO_4$ to afford 0.773 g title compound as a colorless liquid (47% yield). ^{1}H NMR (δ, 23 °C, $CDCl_3$): 7.08 (s, 4H), 2.33 (s, 3H). ^{13}C NMR (δ, 23 °C, $CDCl_3$): 134.8 (s), 134.7 (s), 129.0 (s), 21.1 (s), 20.3 (septet, J = 19.5 Hz). The measured spectral data are in excellent agreement with those reported for *p*-d_3-xylene.[277]

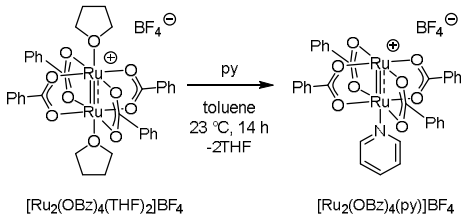

Synthesis of $[Ru_2(OBz)_4(py)]BF_4$ A 20 mL scintillation vial was charged with a stir bar, $[Ru_2(OBz)_4(THF)_2]BF_4$ (0.059 g, 0.064 mmol, 1 equiv), pyridine (5.2 μL, 0.064 mmol, 1 equiv), and toluene (3.0 mL). The resulting mixture was stirred at 23 °C for 14 h. The resulting solid was isolated by filtration and washed with hexane (3.0 mL × 2). The solid was dried under vacuum to afford 0.052 g of $[Ru_2(OBz)_4(py)]BF_4$ as a light-yellow powder (95% yield). ^{1}H NMR (δ, 23 °C, d_6-DMSO, Figure S21): 31.47 (br, 8H), 19.60 (br, 4H), 8.59 (m, 2H), 7.80 (m, 1H), 7.55 (br, 8H), 7.40 (m, 2H). Solid state UV-vis-NIR spectrum of this compound was collected and compared with its starting material (**Figure IV-26a**).

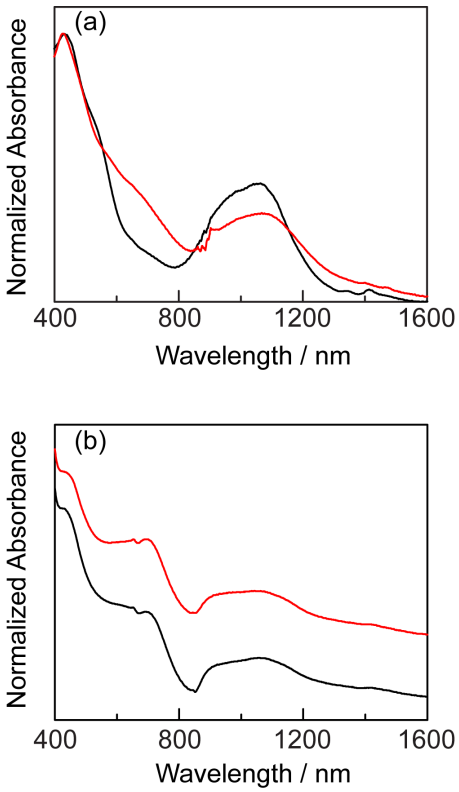

Figure IV-26. Solid-state UV-vis-NIR spectra. (a) Solid-state UV-vis-NIR spectra of $[Ru_2(OBz)_4(THF)_2]BF_4$ (—) and $[Ru_2(OBz)_4(py)]BF_4$ (—). (b) Solid-state UV-vis-NIR spectra of $[Ru_6(btc)_4Cl_3]$ (—) and $[Ru_6(btc)_x(pydc)_{4-x}Cl_3]$ (S_{meso}/S_{micro} = 0.39) (—). The axial pyridine coordination to the Ru_2 unit changed its electronic structure, recorded by solid state UV-vis-NIR. In contrast, no electronic structure change was observed by including 3,5-pyridinedicarboxylic acid into $[Ru_6(btc)_x(pydc)_{4-x}Cl_3]$.

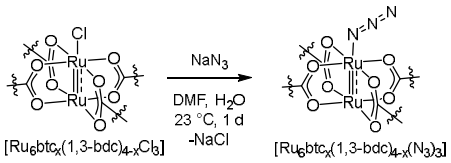

Synthesis of $[Ru_6(btc)_x(1,3\text{-}bdc)_{4-x}(N_3)_3]$ A 20-mL vial was charged with $[Ru_6(btc)_x(1,3\text{-}bdc)_{4-x}Cl_3]$ (0.0400 g), NaN_3 (0.0400 g, 0.615 mmol, > 30.0 equiv), H_2O (3.20 mL), and DMF (16.0 mL). The resulting mixture was allowed to stand at 23 °C for 1 d. At this time, the supernatant was decanted and the remaining solids were washed with MeOH (10.0 mL × 3). The solids were then soaked in MeOH (20.0 mL) at 23 °C for 3 d (refreshed three times per day), solvent was decanted, and the solids were allowed to air-dry to give 33.0 mg of the title compound as a dark brown powder. IR (cm^{-1}): 2042–2046 (m), 1645 (m), 1616 (m), 1555 (m), 1432 (m), 1365 (s), 1111 (m), 1022 (m), 937 (w), 730 (s), 687 (w). PXRD data for samples prepared by this procedure are collected in **Figure IV-27**. For gas adsorption studies, $[Ru_6(btc)_x(1,3\text{-}bdc)_{4-x}C(N_3)_3]$ was soaked in CH_2Cl_2 for 2 d (refreshed three times per day) and then activated at 23 °C under active vacuum for 24 h. N_2 adsorption isotherms are collected in **Figure IV-28**. Unlike for syntheses with H_2pydc, this procedure provided a fairly narrow range of mesoporosities (S_{meso} / S_{micro} = 0.44–0.51) and thus extensive analysis of porosity-dependent KIEs was not possible.

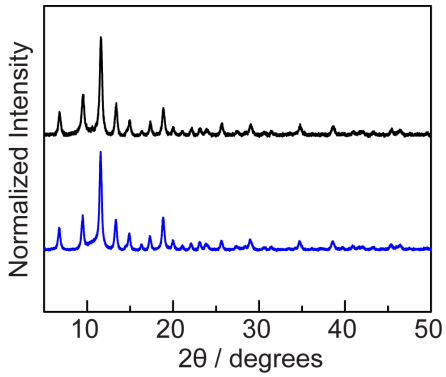

Figure IV-27. Powder X-ray diffraction patterns for $[Ru_6(btc)_x(1,3\text{-}bdc)_{4-x}(N_3)_3]$: S_{meso}/S_{micro} = 0.44 (—) and S_{meso}/S_{micro} = 0.51 (—).

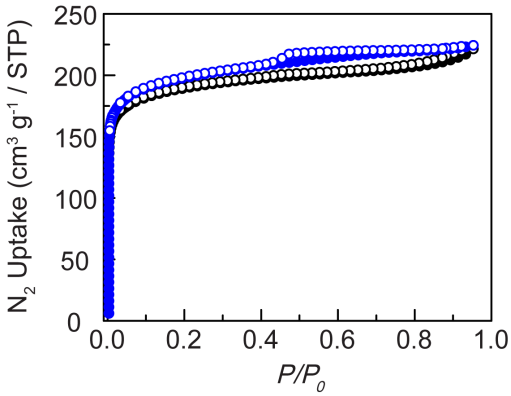

Figure IV-28. N_2 adsorption isotherms. Obtained at 77 K for $[Ru_6(btc)_x(1,3\text{-}bdc)_{4-x}(N_3)_3]$: S_{meso}/S_{micro} = 0.44 ((adsorption (●), desorption (○)) and S_{meso}/S_{micro} = 0.51 ((adsorption (●), desorption (○)).

IV.5.3 Additional Data

Figures IV-29 – IV-31 and Tables IV-16–IV-17 contain additional relevant data.

Table IV-16 Reaction yields for amination of toluene using $Ru_6(btc)_{3.83}(pydc)_{0.17}(OH)_{1.98}Cl_{0.54}(N_3)_{0.48}(H_2O)_{23}$ (S_{meso}/S_{micro} = 0.16) and $Ru_6(btc)_{2.80}(pydc)_{1.20}(OH)_{2.35}Cl_{0.23}(N_3)_{0.42}(H_2O)_{24}$ (S_{meso}/S_{micro} = 0.61)
Yields in parentheses are without toluene soaking prior to amination. Mesitylene is used as the internal standard and the integration of aromatic protons on mesitylene between benzylic protons on benzylamine is calculated by ^{1}H NMR. The amount of reactive [Ru_2N_3] sites is determined by elemental analysis.

Mesoporosity	Yield (soaking) / %	Yield (without soaking) / %
0.16	23.9	2.6
0.61	28.0	3.3

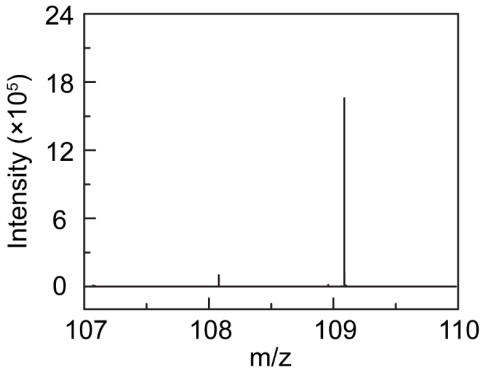

Figure IV-29. Mass spec trace for the intramolecular KIE determination. The m/z of benzylamine ($C_7H_{10}N^+$, ESI positive) is 108.0808; the m/z of deuterated benzylamine ($C_7H_9DN^+$, ESI positive) is 109.0871. The reported KIEs are calculated using the equation below that accounts for the 1 : 2 ratio of C–D and C–H bonds in d_1-toluene.

$$\text{Intramolecular KIE} = \frac{Area\ of\ deuterated\ benzylamine\ (109.0871)}{Area\ of\ benzylamine\ (108.0808)} \times \frac{1}{2}$$

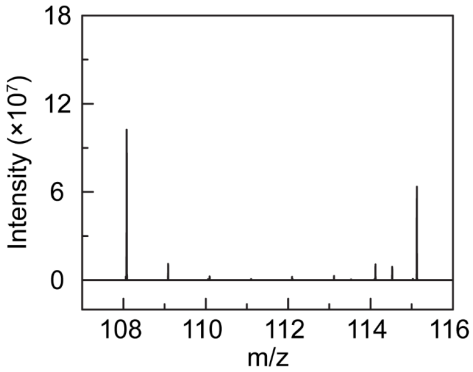

Figure IV-30. Mass spec trace for the intermolecular KIE determination. The m/z of benzylamine ($C_7H_{10}N^+$, ESI positive) is 108.0808; m/z of deuterated benzylamine ($C_7H_3D_7N^+$, ESI positive) is 115.1247. Reported KIEs are calculated using the equation below. The ratio of d_8/H_8-toluene is determined by gas chromatography (GC).

Intermolecular KIE

$$= \frac{Area\ of\ benzylamine\ (108.0808)}{Area\ of\ deuterated\ benzylamine\ (115.1247)} \times \frac{d8 - toluene}{h8 - toluene}$$

The frequency of a bond vibration is given by the following equation:

$$\nu = \frac{1}{2\pi c}\sqrt{\frac{k}{\mu}}$$

where c = speed of light, k = spring constant for the bond, and μ = the reduced mass.

The reduced mass is given by the equation:

$$\mu = \frac{m_A m_B}{m_A + m_B}$$

Analysis of the reduced mass for d_8- and d_3-toluene provides μ = 1.97361 and 1.97147, respectively. Analysis of the impact of this reduced mass on the zero-point energy of the C–D bond in d_8- and d_3-toluene reveals the change in deuteration patter has less

than 1% impact of the vibrational frequency of the benzylic C–D (*i.e.* the bond being cleaved):

$$\frac{\nu(D3)}{\nu(D8)} = \sqrt{\frac{1.97361}{1.97147}} = 1.0005$$

Given the commercial availability of d_8-toluene, and the indistinguishable effect of the isotopic substitution of the phenyl group on the analysis of KIEs, we have pursued all of our analysis with d_8-toluene.

Table IV-17 Time-dependent intramolecular KIEs at 100 °C
The data below were collected by heating a sample of $Ru_6(btc)_x(pydc)_{4-x}(N_3)_3$ (40 mg, S_{meso}/S_{micro} = 0.41) in d_1-toluene. At 12 h increments the reaction vial was removed from oil bath and allowed to cool to 23 °C. A portion of the $[Ru_6(btc)_x(pydc)_{4-x}(N_3)_3]$ (~10 mg) was removed and worked up as described above. The remaining reaction mixture was again heated at 75 °C. The KIE values tabulated below were determined by high resolution ESI. The data demonstrate that the measured KIEs are independent on the consumption of the substrates. The average of k_H/k_D in this experiment is 7.7(3). The percent error is comparable to that of the most mesoporous material 3.4(1).

Sample S_{meso}/S_{micro}	Time / h	k_H/k_D
0.41	12	7.63
	24	8.17
	36	7.32
	48	7.55

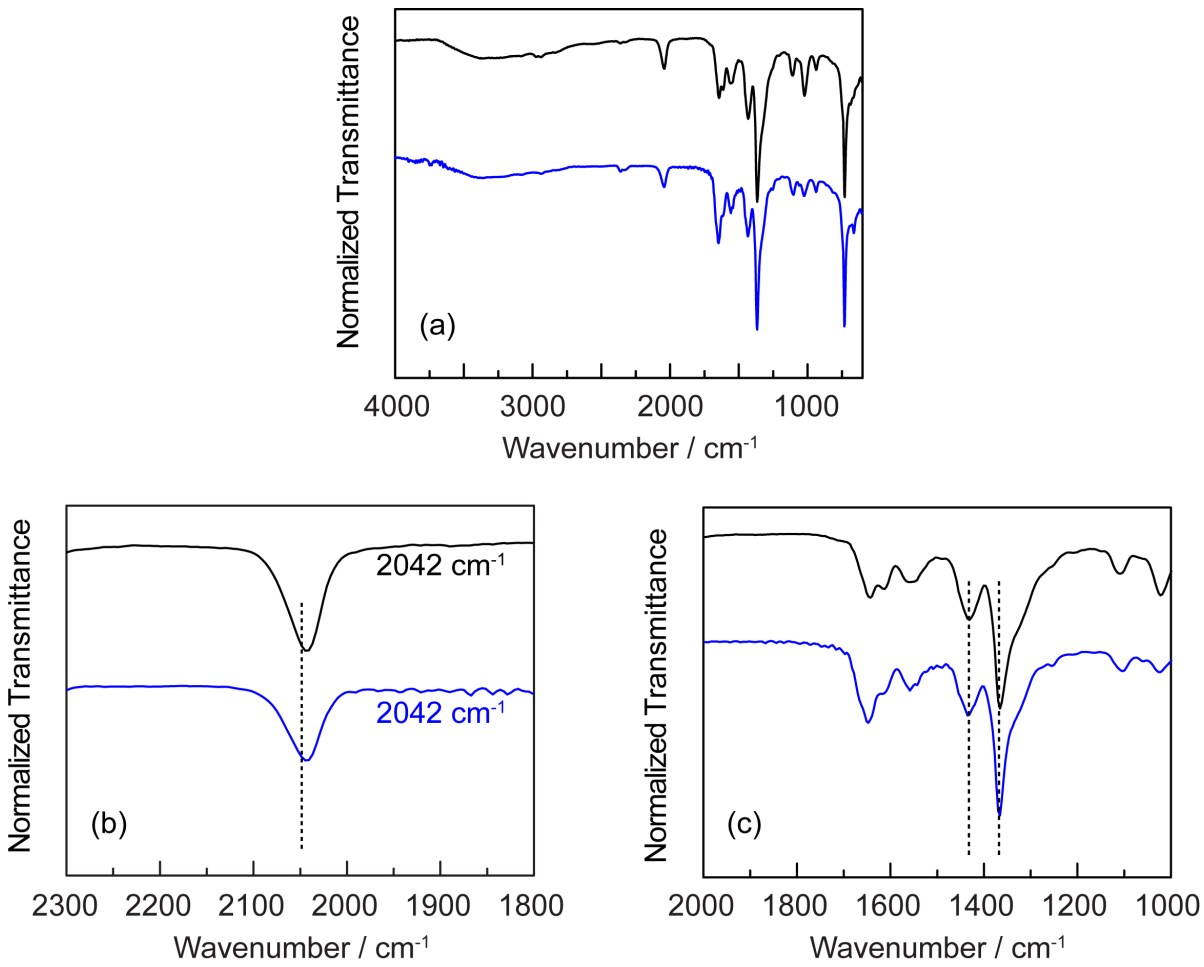

Figure IV-31. IR spectra of $[Ru_6(btc)_x(1,3\text{-}bdc)_{4-x}(N_3)_3]$. Spectra recorded as a function of mesoporosity (S_{meso}/S_{micro} = 0.44 (—); 0.51 (—)) used during synthesis of these materials. (a) Full spectral range; (b) expansion of azide with υ_{N3} labeled and (c) carboxylate stretching (υ_{asym} = 1433 cm^{-1}, υ_{sym} = 1366 cm^{-1}) region.

CHAPTER V

CONCLUDING REMARKS AND FUTURE DIRECTIONS

General strategies to control geometry of discrete aggregates advance the development of catalysts for C–H bond activation. We have demonstrated the stabilization and synthesis of Pd_2 tetracarboxylate sites that are metastable in solution phase by cation metathesis within porous materials. The proximity of two palladiums enforces the interaction between the two d_z^2 orbitals which renders Pd_2 tetracarboxylate a nucleophile. We have also revealed the role of solvated solvent in the lattice during cation metathesis chemistry. We anticipate the developed cation metathesis and strategies to synthesize the catalyst with metastable geometry will contribute to the advancement of novel polynuclear catalysts.

Site-isolation of the reactive Ru_2 nitride intermediates prevents bimolecular nitride coupling which is facile at homogeneous Ru_2 tetracarboxylate complexes and provides a platform for intermolecular C–H functionalization reactions that are challenging to achieve in the homogeneous milieu. Substrate diffusion rate on interstitial substrate functionalization can be investigated by the developed intermolecular NAT reaction. Intra- and intermolecular KIEs suggests that while substantial C–H cleavage is involved in the C–H amination transition state, substrate diffusion through the microporous network is slow relative to the amination process.

To address the impact of network structure on the confinement of substrates during interstitial chemistry, a series of Ru_2 MOFs with various mesoporosity are synthesized. Inter- and intramolecular KIEs reveal that the substrates are less confined as the pore size increases. These data resemble the enzymatic C−H activation in which substrates are highly confined in the cavity. We believe that the presented KIE analyses represent useful new tools in understanding the impact of substrate diffusion on interstitial chemistry and will provide critical guidance in designing new porous materials for interstitial MOF catalysis.

Future directions regarding this work mainly focus on the development of a diffusion-free catalyst to realize a broader scope of C−H functionalization. Synthetic strategy for this area is lacking and the availability of solid-state Ru_2 catalyst is limited. To address this challenge, 1) synthesis of Ru_2 catalyst by mechanochemical metallopolymerization as a new strategy to synthesize the novel MOF with a larger pore size and 2) use of mesoporous silica as a solid support to accommodate Ru_2, are currently being pursued in our laboratory. Efforts will be made to discover a system in which the substrate diffusion is not limited and the presence of confinement effect prevents possible side reactions such as bimolecular nitride coupling. We anticipate these novel materials will broaden the substrate scope of the catalysis for fine chemical synthesis.

REFERENCES

(1) Zhang, X.; Houk, K. N. Why Enzymes Are Proficient Catalysts: Beyond the Pauling Paradigm. *Acc. Chem. Res.* **2005**, *38*, 379–385.

(2) Gao, J.; Ma, S.; Major, D. T.; Nam, K.; Pu, J.; Truhlar, D. G. Mechanisms and Free Energies of Enzymatic Reactions. *Chem. Rev.* **2006**, *106*, 3188–3209.

(3) Shu, L.; Nesheim, J. C.; Kauffmann, K.; Münck, E.; Lipscomb, J. D.; Que, L. An $Fe_2^{IV}O_2$ Diamond Core Structure for the Key Intermediate Q of Methane Monooxygenase. *Science* **1997**, *275*, 515–518.

(4) Tshuva, E. Y.; Lippard, S. J. Synthetic Models for Non-Heme Carboxylate-Bridged Diiron Metalloproteins: Strategies and Tactics. *Chem. Rev.* **2004**, *104*, 987–1012.

(5) Friedle, S.; Reisner, E.; Lippard, S. J. Current Challenges of Modeling Diiron Enzyme Active Sites for Dioxygen Activation by Biomimetic Synthetic Complexes. *Chem. Soc. Rev.* **2010**, *39*, 2768–2779.

(6) Trehoux, A.; Mahy, J.-P.; Avenier, F. A Growing Family of O_2 Activating Dinuclear Iron Enzymes with Key Catalytic Diiron(III)-Peroxo Intermediates: Biological Systems and Chemical Models. *Coord. Chem. Rev.* **2016**, *322*, 142–158.

(7) Tinberg, C. E.; Lippard, S. J. Dioxygen Activation in Soluble Methane Monooxygenase. *Acc. Chem. Res.* **2011**, *44*, 280–288.

(8) Eady, R. R. Structure−Function Relationships of Alternative Nitrogenases. *Chem. Rev.* **1996**, *96*, 3013–3030.

(9) Burgess, B. K.; Lowe, D. J. Mechanism of Molybdenum Nitrogenase. *Chem. Rev.* **1996**, *96*, 2983–3012.

(10) Rutledge, H. L.; Tezcan, F. A. Electron Transfer in Nitrogenase. *Chem. Rev.* **2020**, DOI:10.1021/acs.chemrev.9b00663 10.1021/acs.chemrev.9b00663.

(11) Lee, S. C.; Holm, R. H. The Clusters of Nitrogenase: Synthetic Methodology in the Construction of Weak-Field Clusters. *Chem. Rev.* **2004**, *104*, 1135–1158.

(12) Lee, S. C.; Lo, W.; Holm, R. H. Developments in the Biomimetic Chemistry of Cubane-Type and Higher Nuclearity Iron–Sulfur Clusters. *Chem. Rev.* **2014**, *114*, 3579–3600.

(13) Bjornsson, R.; Neese, F.; Schrock, R. R.; Einsle, O.; DeBeer, S. The Discovery of Mo(III) in FeMoco: Reuniting Enzyme and Model Chemistry. *J. Biol. Inorg. Chem.* **2015**, *20*, 447–460.

(14) Shah, V. K.; Brill, W. J. Isolation of an Iron-Molybdenum Cofactor from Nitrogenase. *Proc. Natl. Acad. Sci.* **1977**, *74*, 3249–3253.

(15) Brown, C. J.; Toste, F. D.; Bergman, R. G.; Raymond, K. N. Supramolecular Catalysis in Metal–Ligand Cluster Hosts. *Chem. Rev.* **2015**, *115*, 3012–3035.

(16) Fang, Y.; Powell, J. A.; Li, E.; Wang, Q.; Perry, Z.; Kirchon, A.; Yang, X.; Xiao, Z.; Zhu, C.; Zhang, L.et al. Catalytic Reactions within the Cavity of Coordination Cages. *Chem. Soc. Rev.* **2019**, *48*, 4707–4730.

(17) Miners, S. A.; Rance, G. A.; Khlobystov, A. N. Chemical Reactions Confined within Carbon Nanotubes. *Chem. Soc. Rev.* **2016**, *45*, 4727–4746.

(18) Fu, Q.; Bao, X. Surface Chemistry and Catalysis Confined under Two-Dimensional Materials. *Chem. Soc. Rev.* **2017**, *46*, 1842–1874.

(19) Wang, Y.; Mao, J.; Meng, X.; Yu, L.; Deng, D.; Bao, X. Catalysis with Two-Dimensional Materials Confining Single Atoms: Concept, Design, and Applications. *Chem. Rev.* **2019**, *119*, 1806–1854.

(20) Nagel, Z. D.; Klinman, J. P. Update 1 of: Tunneling and Dynamics in Enzymatic Hydride Transfer. *Chem. Rev.* **2010**, *110*, PR41–PR67.

(21) Leenders, S. H. A. M.; Gramage-Doria, R.; de Bruin, B.; Reek, J. N. H. Transition Metal Catalysis in Confined Spaces. *Chem. Soc. Rev.* **2015**, *44*, 433–448.

(22) Minton, A. P. Confinement as a Determinant of Macromolecular Structure and Reactivity. *Biophys. J.* **1992**, *63*, 1090–1100.

(23) Goettmann, F.; Sanchez, C. How Does Confinement Affect the Catalytic Activity of Mesoporous Materials? *J. Mater. Chem.* **2007**, *17*, 24–30.

(24) Sastre, G.; Corma, A. The Confinement Effect in Zeolites. *J. Mol. Catal. A Chem.* **2009**, *305*, 3–7.

(25) Corma, A. From Microporous to Mesoporous Molecular Sieve Materials and Their Use in Catalysis. *Chem. Rev.* **1997**, *97*, 2373–2420.

(26) Pompliano, D. L.; Peyman, A.; Knowles, J. R. Stabilization of a Reaction Intermediate as a Catalytic Device: Definition of the Functional Role of the Flexible Loop in Triosephosphate Isomerase. *Biochemistry* **1990**, *29*, 3186–3194.

(27) Koblenz, T. S.; Wassenaar, J.; Reek, J. N. H. Reactivity within a Confined Self-Assembled Nanospace. *Chem. Soc. Rev.* **2008**, *37*, 247–262.

(28) Ringe, D.; Petsko, G. A. How Enzymes Work. *Science* **2008**, *320*, 1428–1429.

(29) Albery, W. J.; Knowles, J. R. Efficiency and Evolution of Enzyme Catalysis. *Angew. Chem. Int. Ed. Engl.* **1977**, *16*, 285–293.

(30) Li, X.; Wu, J.; He, C.; Meng, Q.; Duan, C. Asymmetric Catalysis within the Chiral Confined Space of Metal–Organic Architectures. *Small* **2019**, *15*, 1804770.

(31) Samantaray, M. K.; D'Elia, V.; Pump, E.; Falivene, L.; Harb, M.; Ould Chikh, S.; Cavallo, L.; Basset, J.-M. The Comparison between Single Atom Catalysis and Surface Organometallic Catalysis. *Chem. Rev.* **2020**, *120*, 734–813.

(32) Yoshizawa, M.; Tamura, M.; Fujita, M. Diels-Alder in Aqueous Molecular Hosts: Unusual Regioselectivity and Efficient Catalysis. *Science* **2006**, *312*, 251–254.

(33) Zarra, S.; Wood, D. M.; Roberts, D. A.; Nitschke, J. R. Molecular Containers in Complex Chemical Systems. *Chem. Soc. Rev.* **2015**, *44*, 419–432.

(34) Leung, D. H.; Bergman, R. G.; Raymond, K. N. Scope and Mechanism of the C−H Bond Activation Reactivity within a Supramolecular Host by an Iridium Guest: A Stepwise Ion Pair Guest Dissociation Mechanism. *J. Am. Chem. Soc.* **2006**, *128*, 9781–9797.

(35) Bierschenk, S. M.; Bergman, R. G.; Raymond, K. N.; Toste, F. D. A Nanovessel-Catalyzed Three-Component Aza-Darzens Reaction. *J. Am. Chem. Soc.* **2020**, *142*, 733–737.

(36) Kaphan, D. M.; Toste, F. D.; Bergman, R. G.; Raymond, K. N. Enabling New Modes of Reactivity via Constrictive Binding in a Supramolecular-Assembly-Catalyzed Aza-Prins Cyclization. *J. Am. Chem. Soc.* **2015**, *137*, 9202–9205.

(37) Bender, T. A.; Bergman, R. G.; Raymond, K. N.; Toste, F. D. A Supramolecular Strategy for Selective Catalytic Hydrogenation Independent of Remote Chain Length. *J. Am. Chem. Soc.* **2019**, *141*, 11806–11810.

(38) Hong, C. M.; Morimoto, M.; Kapustin, E. A.; Alzakhem, N.; Bergman, R. G.; Raymond, K. N.; Toste, F. D. Deconvoluting the Role of Charge in a Supramolecular Catalyst. *J. Am. Chem. Soc.* **2018**, *140*, 6591–6595.

(39) Zhou, H.-C. J.; Kitagawa, S. Metal–Organic Frameworks (MOFs). *Chem. Soc. Rev.* **2014**, *43*, 5415–5418.

(40) Hendon, C. H.; Rieth, A. J.; Korzyński, M. D.; Dincă, M. Grand Challenges and Future Opportunities for Metal–Organic Frameworks. *ACS Cent. Sci.* **2017**, *3*, 554–563.

(41) Davis, M. E. Zeolite-based catalysts for chemicals synthesis. *Microporous Mesoporous Mater.* **1998**, *21*, 173–182.

(42) Vogt, E. T. C.; Weckhuysen, B. M. Fluid catalytic cracking: recent developments on the grand old lady of zeolite catalysis. *Chem. Soc. Rev.* **2015**, *44*, 7342–7370.

(43) Smit, B.; Maesen, T. L. M. Towards a molecular understanding of shape selectivity. *Nature* **2008**, *451*, 671–678.

(44) Phan, A.; Czaja, A. U.; Gándara, F.; Knobler, C. B.; Yaghi, O. M. Metal–Organic Frameworks of Vanadium as Catalysts for Conversion of Methane to Acetic Acid. *Inorg. Chem.* **2011**, *50*, 7388–7390.

(45) Santos, V. P.; Wezendonk, T. A.; Jaén, J. J. D.; Dugulan, A. I.; Nasalevich, M. A.; Islam, H.-U.; Chojecki, A.; Sartipi, S.; Sun, X.; Hakeem, A. A.et al. Metal organic

framework-mediated synthesis of highly active and stable Fischer-Tropsch catalysts. *Nat. Commun.* **2015**, *6*, 6451.

(46) Ikuno, T.; Zheng, J.; Vjunov, A.; Sanchez-Sanchez, M.; Ortuño, M. A.; Pahls, D. R.; Fulton, J. L.; Camaioni, D. M.; Li, Z.; Ray, D.et al. Methane Oxidation to Methanol Catalyzed by Cu-Oxo Clusters Stabilized in NU-1000 Metal–Organic Framework. *J. Am. Chem. Soc.* **2017**, *139*, 10294–10301.

(47) Metzger, E. D.; Brozek, C. K.; Comito, R. J.; Dincă, M. Selective Dimerization of Ethylene to 1-Butene with a Porous Catalyst. *ACS Cent. Sci.* **2016**, *2*, 148–153.

(48) Park, H. D.; Dincă, M.; Román-Leshkov, Y. Continuous-Flow Production of Succinic Anhydrides via Catalytic β-Lactone Carbonylation by Co(CO)4⊂Cr-MIL-101. *J. Am. Chem. Soc.* **2018**, *140*, 10669–10672.

(49) Li, Z.; Schweitzer, N. M.; League, A. B.; Bernales, V.; Peters, A. W.; Getsoian, A. B.; Wang, T. C.; Miller, J. T.; Vjunov, A.; Fulton, J. L.et al. Sintering-Resistant Single-Site Nickel Catalyst Supported by Metal–Organic Framework. *J. Am. Chem. Soc.* **2016**, *138*, 1977–1982.

(50) Comito, R. J.; Fritzsching, K. J.; Sundell, B. J.; Schmidt-Rohr, K.; Dincă, M. Single-Site Heterogeneous Catalysts for Olefin Polymerization Enabled by Cation Exchange in a Metal-Organic Framework. *J. Am. Chem. Soc.* **2016**, *138*, 10232–10237.

(51) Liu, J.; Chen, L.; Cui, H.; Zhang, J.; Zhang, L.; Su, C.-Y. Applications of Metal–Organic Frameworks in Heterogeneous Supramolecular Catalysis. *Chem. Soc. Rev.* **2014**, *43*, 6011–6061.

(52) Zhu, L.; Liu, X.-Q.; Jiang, H.-L.; Sun, L.-B. Metal–Organic Frameworks for Heterogeneous Basic Catalysis. *Chem. Rev.* **2017**, *117*, 8129–8176.

(53) Huang, Y.-B.; Liang, J.; Wang, X.-S.; Cao, R. Multifunctional metal–organic framework catalysts: synergistic catalysis and tandem reactions. *Chem. Soc. Rev.* **2017**, *46*, 126–157.

(54) Cirujano, F. G. MOFs vs. Zeolites: Carbonyl Activation with M(IV) Catalytic Sites. *Catal. Sci. Technol.* **2017**, *7*, 5482–5494.

(55) Hartmann, M.; Machoke, A. G.; Schwieger, W. Catalytic Test Reactions for the Evaluation of Hierarchical Zeolites. *Chem. Soc. Rev.* **2016**, *45*, 3313–3330.

(56) R. J. Wijngaarden, A. K., K. R. Westerterp *Industrial Catalysis: Optimizing Catalysts and Processes*; Wiley-VCH: Weinheim, 1998.

(57) Titze, T.; Lauerer, A.; Heinke, L.; Chmelik, C.; Zimmermann, N. E. R.; Keil, F. J.; Ruthven, D. M.; Kärger, J. Transport in Nanoporous Materials Including MOFs: The Applicability of Fick's Laws. *Angew. Chem. Int. Ed.* **2015**, *54*, 14580–14583.

(58) Schneider, D.; Mehlhorn, D.; Zeigermann, P.; Kärger, J.; Valiullin, R. Transport Properties of Hierarchical Micro–Mesoporous Materials. *Chem. Soc. Rev.* **2016**, *45*, 3439–3467.

(59) Krishna, R. Describing the Diffusion of Guest Molecules Inside Porous Structures. *The Journal of Physical Chemistry C* **2009**, *113*, 19756–19781.

(60) Krishna, R. Diffusion in Porous Crystalline Materials. *Chem. Soc. Rev.* **2012**, *41*, 3099–3118.

(61) Petersen, E. E. Diffusion in a Pore of Varying Cross Section. *AIChE J.* **1958**, *4*, 343–345.

(62) Satterfield, C. N. *Mass Transfer in Heterogeneous Catalysis*; M.I.T. Press: Cambridge, 1970.

(63) Kärger, J. Transport Phenomena in Nanoporous Materials. *ChemPhysChem* **2015**, *16*, 24–51.

(64) Han, S.; Wei, Y.; Valente, C.; Lagzi, I.; Gassensmith, J. J.; Coskun, A.; Stoddart, J. F.; Grzybowski, B. A. Chromatography in a Single Metal−Organic Framework (MOF) Crystal. *J. Am. Chem. Soc.* **2010**, *132*, 16358–16361.

(65) Karge, H. G.; Nießen, W. A New Method for the Study of Diffusion and Counter-Diffusion in Zeolites. *Catal. Today* **1991**, *8*, 451–465.

(66) Heinke, L.; Chmelik, C.; Kortunov, P.; Ruthven, D. M.; Shah, D. B.; Vasenkov, S.; Kärger, J. Application of Interference Microscopy and IR Microscopy for Characterizing and Investigating Mass Transport in Nanoporous Materials. *Chem. Eng. Technol.* **2007**, *30*, 995–1002.

(67) Heinke, L.; Tzoulaki, D.; Chmelik, C.; Hibbe, F.; van Baten, J. M.; Lim, H.; Li, J.; Krishna, R.; Kärger, J. Assessing Guest Diffusivities in Porous Hosts from Transient Concentration Profiles. *Phys. Rev. Lett.* **2009**, *102*, 065901.

(68) Zhao, Z.; Li, Z.; Lin, Y. S. Adsorption and Diffusion of Carbon Dioxide on Metal−Organic Framework (MOF-5). *Ind. Eng. Chem. Res.* **2009**, *48*, 10015–10020.

(69) Zybaylo, O.; Shekhah, O.; Wang, H.; Tafipolsky, M.; Schmid, R.; Johannsmann, D.; Wöll, C. A Novel Method to Measure Diffusion Coefficients in Porous Metal–Organic Frameworks. *Phys. Chem. Chem. Phys.* **2010**, *12*, 8093–8098.

(70) Zhao, Z.; Li, X.; Huang, S.; Xia, Q.; Li, Z. Adsorption and Diffusion of Benzene on Chromium-Based Metal Organic Framework MIL-101 Synthesized by Microwave Irradiation. *Ind. Eng. Chem. Res.* **2011**, *50*, 2254–2261.

(71) Tovar, T. M.; Zhao, J.; Nunn, W. T.; Barton, H. F.; Peterson, G. W.; Parsons, G. N.; LeVan, M. D. Diffusion of CO_2 in Large Crystals of Cu-BTC MOF. *J. Am. Chem. Soc.* **2016**, *138*, 11449–11452.

(72) Eic, M.; Ruthven, D. M. A New Experimental Technique for Measurement of Intracrystalline Diffusivity. *Zeolites* **1988**, *8*, 40–45.

(73) Liu, J.; Wang, Y.; Benin, A. I.; Jakubczak, P.; Willis, R. R.; LeVan, M. D. CO_2/H_2O Adsorption Equilibrium and Rates on Metal−Organic Frameworks: HKUST-1 and Ni/DOBDC. *Langmuir* **2010**, *26*, 14301–14307.

(74) Jobic, H.; Kärger, J.; Bée, M. Simultaneous Measurement of Self- and Transport Diffusivities in Zeolites. *Phys. Rev. Lett.* **1999**, *82*, 4260–4263.

(75) Salles, F.; Jobic, H.; Ghoufi, A.; Llewellyn, P. L.; Serre, C.; Bourrelly, S.; Férey, G.; Maurin, G. Transport Diffusivity of CO_2 in the Highly Flexible Metal–Organic Framework MIL-53(Cr). *Angew. Chem. Int. Ed.* **2009**, *48*, 8335–8339.

(76) Stejskal, E. O.; Tanner, J. E. Spin Diffusion Measurements: Spin Echoes in the Presence of a Time-Dependent Field Gradient. *J. Chem. Phys.* **1965**, *42*, 288–292.

(77) J. Kärger, H. P., W. Heink *Advances in Magnetic and Optical Resonance, Vol. 12 (Ed.: J. S. Waugh)*; Academic Press: San Diego.

(78) Brandani, S.; Hufton, J.; Ruthven, D. Self-Diffusion of Propane and Propylene in 5A and 13X Zeolite Crystals Studied by the Tracer ZLC Method. *Zeolites* **1995**, *15*, 624–631.

(79) Schumacher, R. R.; Anderson, B. G.; Noordhoek, N. J.; de Gauw, F. J. M. M.; de Jong, A. M.; de Voigt, M. J. A.; van Santen, R. A. Tracer-Exchange Experiments with Positron Emission Profiling: Diffusion in Zeolites. *Microporous and Mesoporous Mater.* **2000**, *35-36*, 315–326.

(80) Chmelik, C.; Enke, D.; Galvosas, P.; Gobin, O.; Jentys, A.; Jobic, H.; Kärger, J.; Krause, C. B.; Kullmann, J.; Lercher, J.et al. Nanoporous Glass as a Model System for a Consistency Check of the Different Techniques of Diffusion Measurement. *ChemPhysChem* **2011**, *12*, 1130–1134.

(81) J. Kärger, D. M. R., D. N. Theodorou *Diffusion in Nanoporous Materials, Vol. 1*; Wiley-VCH: Weinheim, 2012.

(82) Zapilko, C.; Liang, Y.; Nerdal, W.; Anwander, R. A General Strategy for the Rational Design of Size-Selective Mesoporous Catalysts. *Chem. Eur. J.* **2007**, *13*, 3169–3176.

(83) Gu, J.-M.; Kim, W.-S.; Huh, S. Size-Dependent Catalysis by DABCO-Functionalized Zn-MOF with One-Dimensional Channels. *Dalton Trans.* **2011**, *40*, 10826–10829.

(84) Fan, W.; Wang, Y.; Xiao, Z.; Zhang, L.; Gong, Y.; Dai, F.; Wang, R.; Sun, D. A Stable Amino-Functionalized Interpenetrated Metal–Organic Framework Exhibiting Gas Selectivity and Pore-Size-Dependent Catalytic Performance. *Inorg. Chem.* **2017**, *56*, 13634–13637.

(85) Dewaele, A.; Van Berlo, B.; Dijkmans, J.; Jacobs, P. A.; Sels, B. F. Immobilized Grubbs catalysts on Mesoporous Silica Materials: Insight into Support Characteristics and Their Impact on Catalytic Activity and Product Selectivity. *Catal. Sci. Technol.* **2016**, *6*, 2580–2597.

(86) Holm, R. H.; Kennepohl, P.; Solomon, E. I. Structural and Functional Aspects of Metal Sites in Biology. *Chem. Rev.* **1996**, *96*, 2239–2314.

(87) McEvoy, J. P.; Brudvig, G. W. Water-Splitting Chemistry of Photosystem II. *Chem. Rev.* **2006**, *106*, 4455–4483.

(88) Fontecilla-Camps, J. C.; Volbeda, A.; Cavazza, C.; Nicolet, Y. Structure/Function Relationships of [NiFe]- and [FeFe]-Hydrogenases. *Chem. Rev.* **2007**, *107*, 4273–4303.

(89) Hoffman, B. M.; Lukoyanov, D.; Yang, Z.-Y.; Dean, D. R.; Seefeldt, L. C. Mechanism of Nitrogen Fixation by Nitrogenase: The Next Stage. *Chem. Rev.* **2014**, *114*, 4041–4062.

(90) Zambelli, T.; Wintterlin, J.; Trost, J.; Ertl, G. Identification of the "Active Sites" of a Surface-Catalyzed Reaction. *Science* **1996**, *273*, 1688–1690.

(91) Schlögl, R. Heterogeneous Catalysis. *Angew. Chem. Int. Ed.* **2015**, *54*, 3465–3520.

(92) Krogman, J. P.; Thomas, C. M. Metal–Metal Multiple Bonding in C3-Symmetric Bimetallic Complexes of the First Row Transition Metals. *Chem. Commun.* **2014**, *50*, 5115–5127.

(93) Kornecki, K. P. B., J. F.; Powers, D. C.; Ritter, T. Metal–Metal Bond-Containing Complexes as Catalysts for C–H Functionalization. *Prog. Inorg. Chem.* **2014**, *58*, 223–302.

(94) Powers, I. G.; Uyeda, C. Metal–Metal Bonds in Catalysis. *ACS Catal.* **2017**, *7*, 936–958.

(95) Pye, D. R.; Mankad, N. P. Bimetallic Catalysis for C–C and C–X Coupling Reactions. *Chem. Sci.* **2017**, *8*, 1705–1718.

(96) Berry, J. F.; Thomas, C. M. Multimetallic Complexes: Synthesis and Applications. *Dalton Trans.* **2017**, *46*, 5472–5473.

(97) Mankad, N. P. Diverse Bimetallic Mechanisms Emerging from Transition Metal Lewis Acid/Base Pairs: Development of Co-Catalysis with Metal Carbenes and Metal Carbonyl Anions. *Chem. Commun.* **2018**, *54*, 1291–1302.

(98) Powers, D. C.; Ritter, T. Bimetallic Redox Synergy in Oxidative Palladium Catalysis. *Acc. Chem. Res.* **2012**, *45*, 840–850.

(99) Velian, A.; Lin, S.; Miller, A. J. M.; Day, M. W.; Agapie, T. Synthesis and C−C Coupling Reactivity of a Dinuclear Ni^{I}–Ni^{I} Complex Supported by a Terphenyl Diphosphine. *J. Am. Chem. Soc.* **2010**, *132*, 6296–6297.

(100) Powers, T. M.; Fout, A. R.; Zheng, S.-L.; Betley, T. A. Oxidative Group Transfer to a Triiron Complex to Form a Nucleophilic μ^3-Nitride, $[Fe3(\mu3\text{-}N)]^-$. *J. Am. Chem. Soc.* **2011**, *133*, 3336–3338.

(101) Rudd, P. A.; Liu, S.; Planas, N.; Bill, E.; Gagliardi, L.; Lu, C. C. Multiple Metal–Metal Bonds in Iron–Chromium Complexes. *Angew. Chem. Int. Ed.* **2013**, *52*, 4449–4452.

(102) Kuppuswamy, S.; Powers, T. M.; Krogman, J. P.; Bezpalko, M. W.; Foxman, B. M.; Thomas, C. M. Vanadium–Iron Complexes Featuring Metal–Metal Multiple Bonds. *Chem. Sci.* **2013**, *4*, 3557–3565.

(103) Flowers, S. E.; Cossairt, B. M. Mono- and Dimetalation of a Tridentate Bisimidazole-Phosphine Ligand. *Organometallics* **2014**, *33*, 4341–4344.

(104) Lee, Y.; Anderton, K. J.; Sloane, F. T.; Ermert, D. M.; Abboud, K. A.; García-Serres, R.; Murray, L. J. Reactivity of Hydride Bridges in High-Spin $[3M–3(\mu\text{-}H)]$ Clusters ($M = Fe^{II}$, Co^{II}). *J. Am. Chem. Soc.* **2015**, *137*, 10610–10617.

(105) Diccianni, J. B.; Hu, C.; Diao, T. N−N Bond Forming Reductive Elimination via a Mixed-Valent Nickel(II)–Nickel(III) Intermediate. *Angew. Chem., Int. Ed.* **2016**, *55*, 7534–7538.

(106) Porai-Koshits, M. A. A., A. S. The Structure of Rhodium Acetate Complexes. *Dokl. Akad. Nauk SSSR* **1962**, *146*, 1102–1105.

(107) Cotton, F. A.; DeBoer, B. G.; Laprade, M. D.; Pipal, J. R.; Ucko, D. A. Multiple Chromium(II)-Chromium(II) and Rhodium(II)-Rhodium(II) Bonds. *J. Am. Chem. Soc.* **1970**, *92*, 2926–2927.

(108) Nakamura, E.; Yoshikai, N.; Yamanaka, M. Mechanism of C−H Bond Activation/C−C Bond Formation Reaction between Diazo Compound and Alkane Catalyzed by Dirhodium Tetracarboxylate. *J. Am. Chem. Soc.* **2002**, *124*, 7181–7192.

(109) van Niekerk, J. N.; Schoening, F. R. L. The Crystal Structures of Nickel Acetate, $Ni(CH_3COO)_2 \cdot 4H_2O$, and Cobalt Acetate, $Co(CH_3COO)_2 \cdot 4H_2O$. *Acta Crystallogr.* **1953**, *6*, 609–612.

(110) Downie, T. C.; Harrison, W.; Raper, E. S.; Hepworth, M. A. A Three-Dimensional Study of the Crystal Structure of Nickel Acetate Tetrahydrate. *Acta Crystallogr., Sect. B: Struct. Crystallogr. Cryst. Chem.* **1971**, *27*, 706–712.

(111) Stephenson, T. A.; Morehouse, S. M.; Powell, A. R.; Heffer, J. P.; Wilkinson, G. Carboxylates of Palladium, Platinum, and Rhodium, and Their Adducts. *J. Chem. Soc.* **1965**, DOI:10.1039/JR9650003632 10.1039/JR9650003632, 3632–3640.

(112) Skapski, A. C.; Smart, M. L. The Crystal Structure of Trimeric Palladium(II) Acetate. *J. Chem. Soc. D* **1970**, DOI:10.1039/C2970000658B 10.1039/C2970000658B, 658–659.

(113) Bakhmutov, V. I.; Berry, J. F.; Cotton, F. A.; Ibragimov, S.; Murillo, C. A. Non-Trivial Behavior of Palladium(II) Acetate. *Dalton Trans.* **2005**, DOI:10.1039/B502122G 10.1039/B502122G, 1989–1992.

(114) Nosova, V. M.; Ustynyuk, Y. A.; Bruk, L. G.; Temkin, O. N.; Kisin, A. V.; Storozhenko, P. A. Structure of Complexes Formed by Dissolution of Palladium

Diacetate in Methanol and Chloroform. In Situ NMR Study. *Inorg. Chem.* **2011**, *50*, 9300–9310.

(115) Adrio, L. A.; Nguyen, B. N.; Guilera, G.; Livingston, A. G.; Hii, K. K. Speciation of $Pd(OAc)_2$ in Ligandless Suzuki–Miyaura Reactions. *Catal. Sci. Technol.* **2012**, *2*, 316–323.

(116) Carole, W. A.; Bradley, J.; Sarwar, M.; Colacot, T. J. Can Palladium Acetate Lose Its "Saltiness"? Catalytic Activities of the Impurities in Palladium Acetate. *Org. Lett.* **2015**, *17*, 5472–5475.

(117) Pakula, R. J.; Srebro-Hooper, M.; Fry, C. G.; Reich, H. J.; Autschbach, J.; Berry, J. F. Palladium Acetate Revisited: Unusual Ring-Current Effects, One-Electron Reduction, and Metal–Metal Bonding. *Inorg. Chem.* **2018**, *57*, 8046–8049.

(118) Kirik, S. D.; Mulagaleev, R. F.; Blokhin, A. I. $[Pd(CH_3COO)_2]_n$ from X-Ray Powder Diffraction Data. *Acta Crystallogr., Sect. C: Cryst. Struct. Commun.* **2004**, *60*, M449–M450.

(119) Carrondo, M. A. A. F. d. C. T.; Skapski, A. C. A Square-Cluster Platinum Complex with Short Metal–Metal Bonds: X-Ray Crystal Structure of the Tetragonal form of Cyclo-Tetrakis[di-μ-Acetato-Platinum(II)]. *Acta Crystallogr., Sect. B: Struct. Crystallogr. Cryst. Chem.* **1978**, *34*, 1857–1862.

(120) O'Reilly, M. E.; Kim, R. S.; Oh, S.; Surendranath, Y. Catalytic Methane Monofunctionalization by an Electrogenerated High-Valent Pd Intermediate. *ACS Cent. Sci.* **2017**, *3*, 1174–1179.

(121) Powers, D. C.; Ritter, T. Bimetallic Pd(III) Complexes in Palladium-Catalysed Carbon–Heteroatom Bond Formation. *Nat. Chem.* **2009**, *1*, 302–309.

(122) Powers, D. C.; Geibel, M. A. L.; Klein, J. E. M. N.; Ritter, T. Bimetallic Palladium Catalysis: Direct Observation of Pd(III)−Pd(III) Intermediates. *J. Am. Chem. Soc.* **2009**, *131*, 17050–17051.

(123) Deprez, N. R.; Sanford, M. S. Synthetic and Mechanistic Studies of Pd-Catalyzed C−H Arylation with Diaryliodonium Salts: Evidence for a Bimetallic High Oxidation State Pd Intermediate. *J. Am. Chem. Soc.* **2009**, *131*, 11234–11241.

(124) Powers, D. C.; Xiao, D. Y.; Geibel, M. A. L.; Ritter, T. On the Mechanism of Palladium-Catalyzed Aromatic C−H Oxidation. *J. Am. Chem. Soc.* **2010**, *132*, 14530–14536.

(125) Powers, D. C.; Lee, E.; Ariafard, A.; Sanford, M. S.; Yates, B. F.; Canty, A. J.; Ritter, T. Connecting Binuclear Pd(III) and Mononuclear Pd(IV) Chemistry by Pd–Pd Bond Cleavage. *J. Am. Chem. Soc.* **2012**, *134*, 12002–12009.

(126) Canty, A. J.; Ariafard, A.; Sanford, M. S.; Yates, B. F. Mechanism of Pd-Catalyzed Ar–Ar Bond Formation Involving Ligand-Directed C–H Arylation and Diaryliodonium Oxidants: Computational Studies of Orthopalladation at Binuclear Pd(II) Centers, Oxidation To Form Binuclear Palladium(III) Species, and Ar···Ar Reductive Coupling. *Organometallics* **2013**, *32*, 544–555.

(127) Broclawik, E.; Yamauchi, R.; Endou, A.; Kubo, M.; Miyamoto, A. Density Functional Study on the Activation of Methane over Pd_2, PdO, and Pd_2O Clusters. *Int. J. Quantum Chem.* **1997**, *61*, 673–682.

(128) Lang, S. M.; Frank, A.; Bernhardt, T. M. Activation and Catalytic Dehydrogenation of Methane on Small Pd_x^+ and Pd_xO^+ Clusters. *J. Phys. Chem. C* **2013**, *117*, 9791–9800.

(129) White, P. B.; Jaworski, J. N.; Fry, C. G.; Dolinar, B. S.; Guzei, I. A.; Stahl, S. S. Structurally Diverse Diazafluorene-Ligated Palladium(II) Complexes and Their Implications for Aerobic Oxidation Reactions. *J. Am. Chem. Soc.* **2016**, *138*, 4869–4880.

(130) Cook, A. K.; Sanford, M. S. Mechanism of the Palladium-Catalyzed Arene C–H Acetoxylation: A Comparison of Catalysts and Ligand Effects. *J. Am. Chem. Soc.* **2015**, *137*, 3109–3118.

(131) Khranenko, S. P.; Shusharina, E. A.; Gromilov, S. A.; Korenev, S. V. Two Crystalline Modifications of $Pd_2(\mu\text{-ac})_2(acac)_2$. *J. Struct. Chem.* **2011**, *52*, 544.

(132) Hirano, T.; Uehara, K.; Kamata, K.; Mizuno, N. Palladium(II) Containing γ-Keggin Silicodecatungstate That Efficiently Catalyzes Hydration of Nitriles. *J. Am. Chem. Soc.* **2012**, *134*, 6425–6433.

(133) Pandey, R. N.; Henry, P. M. Interaction of Palladium(II) Acetate with Sodium and Lithium Acetate in Acetic Acid. *Can. J. Chem.* **1974**, *52*, 1241–1247.

(134) Kragten, D. D.; van Santen, R. A.; Crawford, M. K.; Provine, W. D.; Lerou, J. J. A Spectroscopic Study of the Homogeneous Catalytic Conversion of Ethylene to Vinyl Acetate by Palladium Acetate. *Inorg. Chem.* **1999**, *38*, 331–339.

(135) Kragten, D. D.; van Santen, R. A.; Neurock, M.; Lerou, J. J. A Density Functional Study of the Acetoxylation of Ethylene to Vinyl Acetate Catalyzed by Palladium Acetate. *J. Phys. Chem. A* **1999**, *103*, 2756–2765.

(136) Yang, Y.-F.; Cheng, G.-J.; Liu, P.; Leow, D.; Sun, T.-Y.; Chen, P.; Zhang, X.; Yu, J.-Q.; Wu, Y.-D.; Houk, K. N. Palladium-Catalyzed Meta-Selective C–H Bond Activation with a Nitrile-Containing Template: Computational Study on Mechanism and Origins of Selectivity. *J. Am. Chem. Soc.* **2014**, *136*, 344–355.

(137) Haines, B. E.; Xu, H.; Verma, P.; Wang, X.-C.; Yu, J.-Q.; Musaev, D. G. Mechanistic Details of Pd(II)-Catalyzed C–H Iodination with Molecular I_2: Oxidative Addition vs Electrophilic Cleavage. *J. Am. Chem. Soc.* **2015**, *137*, 9022–9031.

(138) Enman, L. J.; Burke, M. S.; Batchellor, A. S.; Boettcher, S. W. Effects of Intentionally Incorporated Metal Cations on the Oxygen Evolution Electrocatalytic Activity of Nickel (Oxy)hydroxide in Alkaline Media. *ACS Catal.* **2016**, *6*, 2416–2423.

(139) Dincă, M.; Long, J. R. High-Enthalpy Hydrogen Adsorption in Cation-Exchanged Variants of the Microporous Metal−Organic Framework $Mn_3[(Mn_4Cl)_3(BTT)_8(CH_3OH)_{10}]_2$. *J. Am. Chem. Soc.* **2007**, *129*, 11172–11176.

(140) Mi, L.; Hou, H.; Song, Z.; Han, H.; Xu, H.; Fan, Y.; Ng, S.-W. Rational Construction of Porous Polymeric Cadmium Ferrocene-1,1′-disulfonates for Transition Metal Ion Exchange and Sorption. *Cryst. Growth Des.* **2007**, *7*, 2553–2561.

(141) Brozek, C. K.; Dincă, M. Ti^{3+}-, $V^{2+/3+}$-, $Cr^{2+/3+}$-, Mn^{2+}-, and Fe^{2+}-Substituted MOF-5 and Redox Reactivity in Cr- and Fe-MOF-5. *J. Am. Chem. Soc.* **2013**, *135*, 12886–12891.

(142) Liu, L.; Li, L.; DeGayner, J. A.; Winegar, P. H.; Fang, Y.; Harris, T. D. Harnessing Structural Dynamics in a 2D Manganese–Benzoquinoid Framework To Dramatically Accelerate Metal Transport in Diffusion-Limited Metal Exchange Reactions. *J. Am. Chem. Soc.* **2018**, *140*, 11444–11453.

(143) Lalonde, M.; Bury, W.; Karagiaridi, O.; Brown, Z.; Hupp, J. T.; Farha, O. K. Transmetalation: Routes to Metal Exchange within Metal–Organic Frameworks. *J. Mater. Chem. A* **2013**, *1*, 5453–5468.

(144) Brozek, C. K.; Dincă, M. Cation Exchange at the Secondary Building Units of Metal–Organic Frameworks. *Chem. Soc. Rev.* **2014**, *43*, 5456–5467.

(145) Deria, P.; Mondloch, J. E.; Karagiaridi, O.; Bury, W.; Hupp, J. T.; Farha, O. K. Beyond Post-Synthesis Modification: Evolution of Metal–Organic Frameworks via Building Block Replacement. *Chem. Soc. Rev.* **2014**, *43*, 5896–5912.

(146) Bosch, M.; Yuan, S.; Rutledge, W.; Zhou, H.-C. Stepwise Synthesis of Metal–Organic Frameworks. *Acc. Chem. Res.* **2017**, *50*, 857–865.

(147) Cohen, S. M. The Postsynthetic Renaissance in Porous Solids. *J. Am. Chem. Soc.* **2017**, *139*, 2855–2863.

(148) Kim, M.; Cahill, J. F.; Fei, H.; Prather, K. A.; Cohen, S. M. Postsynthetic Ligand and Cation Exchange in Robust Metal–Organic Frameworks. *J. Am. Chem. Soc.* **2012**, *134*, 18082–18088.

(149) Das, S.; Kim, H.; Kim, K. Metathesis in Single Crystal: Complete and Reversible Exchange of Metal Ions Constituting the Frameworks of Metal−Organic Frameworks. *J. Am. Chem. Soc.* **2009**, *131*, 3814–3815.

(150) Huang, S.; Li, X.; Shi, X.; Hou, H.; Fan, Y. Structure Extending and Cation Exchange of Cd(II) and Co(II) Materials Compounds inducing Fluorescence Signal Mutation. *J. Mater. Chem.* **2010**, *20*, 5695–5699.

(151) Mukherjee, G.; Biradha, K. Post-Synthetic Modification of Isomorphic Coordination Layers: Exchange Dynamics of Metal Ions in a Single Crystal to Single crystal Fashion. *Chem. Commun.* **2012**, *48*, 4293–4295.

(152) Lee, C.; Yang, W.; Parr, R. G. Development of the Colle-Salvetti Correlation-Energy Formula into a Functional of the Electron Density. *Phys. Rev. B: Condens. Matter Mater. Phys.* **1988**, *37*, 785–789.

(153) Becke, A. D. A New Mixing of Hartree–Fock and Local Density-Functional Theories. *J. Chem. Phys.;* **1993**, *98*, 1372–1377.

(154) Becke, A. D. Density-Functional Thermochemistry. III. The Role of Exact Exchange. *J. Chem. Phys.* **1993**, *98*, 5648–5652.

(155) Stephens, P. J.; Devlin, F. J.; Chabalowski, C. F.; Frisch, M. J. Ab Initio Calculation of Vibrational Absorption and Circular Dichroism Spectra Using Density Functional Force Fields. *J. Phys. Chem.* **1994**, *98*, 11623–11627.

(156) Hay, P. J.; Wadt, W. R. Ab Initio Effective Core Potentials for Molecular Calculations. Potentials for K to Au including the Outermost Core Orbitals. *J. Chem. Phys.* **1985**, *82*, 299–310.

(157) Ehlers, A. W.; Böhme, M.; Dapprich, S.; Gobbi, A.; Höllwarth, A.; Jonas, V.; Köhler, K. F.; Stegmann, R.; Veldkamp, A.; Frenking, G. A Set of f-Polarization Functions for Pseudo-Potential Basis Sets of the Transition Metals Sc·Cu, Y·Ag and La·Au. *Chem. Phys. Lett.* **1993**, *208*, 111–114.

(158) Roy, L. E.; Hay, P. J.; Martin, R. L. Revised Basis Sets for the LANL Effective Core Potentials. *J. Chem. Theory Comput.* **2008**, *4*, 1029–1031.

(159) Ditchfield, R.; Hehre, W. J.; Pople, J. A. Self-Consistent Molecular-Orbital Methods. IX. An Extended Gaussian-Type Basis for Molecular-Orbital Studies of Organic Molecules. *J. Chem. Phys.* **1971**, *54*, 724–728.

(160) Hehre, W. J.; Ditchfield, R.; Pople, J. A. Self—Consistent Molecular Orbital Methods. XII. Further Extensions of Gaussian—Type Basis Sets for Use in Molecular Orbital Studies of Organic Molecules. *J. Chem. Phys.* **1972**, *56*, 2257–2261.

(161) Hariharan, P. C.; Pople, J. A. The Influence of Polarization Functions on Molecular Orbital Hydrogenation Energies. *Theor. Chim. Acta* **1973**, *28*, 213–222.

(162) Zhao, Y.; Truhlar, D. G. The M06 Suite of Density Functionals for Main Group Thermochemistry, Thermochemical Kinetics, Noncovalent Interactions, Excited States, and Transition Elements: Two New Functionals and Systematic Testing of Four M06-Class Functionals and 12 other Functionals. *Theor. Chem. Acc.* **2008**, *120*, 215–241.

(163) Dolg, M.; Wedig, U.; Stoll, H.; Preuss, H. Energy-Adjusted ab initio Pseudopotentials for the First Row Transition Elements. *J. Chem. Phys.* **1987**, *86*, 866–872.

(164) Andrae, D.; Häußermann, U.; Dolg, M.; Stoll, H.; Preuß, H. Energy-Adjusted ab initio Pseudopotentials for the Second and Third Row Transition Elements. *Theor. Chem. Acc.* **1990**, *77*, 123–141.

(165) Krishnan, R.; Binkley, J. S.; Seeger, R.; Pople, J. A. Self-Consistent Molecular Orbital Methods. XX. A Basis Set for Correlated Wave Functions. *J. Chem. Phys.* **1980**, *72*, 650–654.

(166) Marenich, A. V.; Cramer, C. J.; Truhlar, D. G. Universal Solvation Model Based on Solute Electron Density and on a Continuum Model of the Solvent Defined by the Bulk Dielectric Constant and Atomic Surface Tensions. *J. Phys. Chem. B* **2009**, *113*, 6378–6396.

(167) Wade, C. R.; Dincă, M. Investigation of the Synthesis, Activation, and Isosteric Heats of CO_2 Adsorption of the Isostructural Series of Metal–Organic Frameworks $M_3(BTC)_2$ (M = Cr, Fe, Ni, Cu, Mo, Ru). *Dalton Trans.* **2012**, *41*, 7931–7938.

(168) Das, A.; Reibenspies, J. H.; Chen, Y.-S.; Powers, D. C. Direct Characterization of a Reactive Lattice-Confined Ru2 Nitride by Photocrystallography. *J. Am. Chem. Soc.* **2017**, *139*, 2912–2915.

(169) Wang, C.-H.; Das, A.; Gao, W.-Y.; Powers, D. C. Probing Substrate Diffusion in Interstitial MOF Chemistry with Kinetic Isotope Effects. *Angew. Chem. Int. Ed.* **2018**, *57*, 3676–3681.

(170) Chui, S. S.-Y.; Lo, S. M.-F.; Charmant, J. P. H.; Orpen, A. G.; Williams, I. D. A Chemically Functionalizable Nanoporous Material $[Cu_3(TMA)_2(H_2O)_3]_n$. *Science* **1999**, *283*, 1148–1150.

(171) Song, X.; Jeong, S.; Kim, D.; Lah, M. S. Transmetalations in Two metal–Organic Frameworks with Different Framework Flexibilities: Kinetics and Core–Shell Heterostructure. *CrystEngComm* **2012**, *14*, 5753–5756.

(172) Akhmadullina, N. S.; Cherkashina, N. V.; Kozitsyna, N. Y.; Stolarov, I. P.; Perova, E. V.; Gekhman, A. E.; Nefedov, S. E.; Vargaftik, M. N.; Moiseev, I. I. Synthesis of Palladium(II) 3d-Metal(II) Paddlewheel Ccetate-Bridged Heterodimetallic Complexes: Unexpected Catalysis by Water Molecules. *Inorg. Chim. Acta* **2009**, *362*, 1943–1951.

(173) Brozek, C. K.; Michaelis, V. K.; Ong, T.-C.; Bellarosa, L.; López, N.; Griffin, R. G.; Dincă, M. Dynamic DMF Binding in MOF-5 Enables the Formation of Metastable Cobalt-Substituted MOF-5 Analogues. *ACS Cent. Sci.* **2015**, *1*, 252–260.

(174) Hong, S.; Oh, M.; Park, M.; Yoon, J. W.; Chang, J.-S.; Lah, M. S. Large H_2 Storage Capacity of a New Polyhedron-Based Metal–Organic Framework with High Thermal and Hygroscopic Stability. *Chem. Commun.* **2009**, 5397–5399.

(175) Zhao, D.; Yuan, D.; Sun, D.; Zhou, H.-C. Stabilization of Metal−Organic Frameworks with High Surface Areas by the Incorporation of Mesocavities with Microwindows. *J. Am. Chem. Soc.* **2009**, *131*, 9186–9188.

(176) Boldog, I.; Domasevitch, K. V.; Sanchiz, J.; Mayer, P.; Janiak, C. 1,3,5,7-Tetrakis(tetrazol-5-yl)-Adamantane: the Smallest Tetrahedral Tetrazole-Functionalized Ligand and its Complexes Formed by Reaction with Anhydrous M(II)Cl_2 (M = Mn, Cu, Zn, Cd). *Dalton Trans.* **2014**, *43*, 12590–12605.

(177) Kim, H. K.; Yun, W. S.; Kim, M.-B.; Kim, J. Y.; Bae, Y.-S.; Lee, J.; Jeong, N. C. A Chemical Route to Activation of Open Metal Sites in the Copper-Based Metal–Organic Framework Materials HKUST-1 and Cu-MOF-2. *J. Am. Chem. Soc.* **2015**, *137*, 10009–10015.

(178) Shimizu, K.-i.; Kamiya, Y.; Osaki, K.; Yoshida, H.; Satsuma, A. The Average Pd Oxidation State in Pd/SiO2 Quantified by L3-Edge XANES Analysis and its Effects on Catalytic Activity for CO Oxidation. *Catal. Sci. Technol.* **2012**, *2*, 767–772.

(179) Sahibed-Dine, A.; Aboulayt, A.; Bensitel, M.; Mohammed Saad, A. B.; Daturi, M.; Lavalley, J. C. IR Study of CS_2 Adsorption on Metal Oxides: Relation with their Surface Oxygen Basicity and Mobility. *J. Mol. Catal. A: Chem.* **2000**, *162*, 125–134.

(180) Bercaw, J. E.; Durrell, A. C.; Gray, H. B.; Green, J. C.; Hazari, N.; Labinger, J. A.; Winkler, J. R. Electronic Structures of PdII Dimers. *Inorg. Chem.* **2010**, *49*, 1801–1810.

(181) Berry, J. F.; Cotton, F. A.; Ibragimov, S. A.; Murillo, C. A.; Wang, X. Searching for Precursors to Metal−Metal Bonded Dipalladium Species: A Study of Pd24+ Complexes. *Inorg. Chem.* **2005**, *44*, 6129–6137.

(182) Zhang, W.; Chen, Z.; Al-Naji, M.; Guo, P.; Cwik, S.; Halbherr, O.; Wang, Y.; Muhler, M.; Wilde, N.; Gläser, R.et al. Simultaneous Introduction of Various Palladium Active Sites into MOF via One-Pot Synthesis: Pd@$[Cu_{3-x}Pd_x(BTC)_2]_n$. *Dalton Trans.* **2016**, *45*, 14883–14887.

(183) Malpass, J. R.; Hemmings, D. A.; Wallis, A. L.; Fletcher, S. R.; Patel, S. Synthesis and Nicotinic Acetylcholine-Binding Properties of Epibatidine Homologues: Homoepibatidine and Dihomoepibatidine. *J. Chem. Soc., Perkin Trans. 1* **2001**, 1044–1050.

(184) Macikenas, D.; Skrzypczak-Jankun, E.; Protasiewicz, J. D. A New Class of Iodonium Ylides Engineered as Soluble Primary Oxo and Nitrene Sources. *J. Am. Chem. Soc.* **1999**, *121*, 7164–7165.

(185) Fulmer, G. R.; Miller, A. J. M.; Sherden, N. H.; Gottlieb, H. E.; Nudelman, A.; Stoltz, B. M.; Bercaw, J. E.; Goldberg, K. I. NMR Chemical Shifts of Trace Impurities: Common Laboratory Solvents, Organics, and Gases in Deuterated Solvents Relevant to the Organometallic Chemist. *Organometallics* **2010**, *29*, 2176–2179.

(186) Aujard, I.; Baltaze, J.-P.; Baudin, J.-B.; Cogné, E.; Ferrage, F.; Jullien, L.; Perez, É.; Prévost, V.; Qian, L. M.; Ruel, O. Tetrahedral Onsager Crosses for Solubility Improvement and Crystallization Bypass. *J. Am. Chem. Soc.* **2001**, *123*, 8177–8188.

(187) Farha, O. K.; Özgür Yazaydın, A.; Eryazici, I.; Malliakas, C. D.; Hauser, B. G.; Kanatzidis, M. G.; Nguyen, S. T.; Snurr, R. Q.; Hupp, J. T. De novo Synthesis of

a Metal–Organic Framework Material featuring Ultrahigh Surface Area and Gas Storage Capacities. *Nat. Chem.* **2010**, *2*, 944–948.

(188) Dhakshinamoorthy, A.; Alvaro, M.; Chevreau, H.; Horcajada, P.; Devic, T.; Serre, C.; Garcia, H. Iron(III) Metal–Organic Frameworks as Solid Lewis Acids for the Isomerization of α-Pinene Oxide. *Catal. Sci. Technol.* **2012**, *2*, 324–330.

(189) Goel, N.; Kumar, N. A Dual-Functional Luminescent Tb(III) Metal–Organic Framework for the Selective Sensing of Acetone and TNP in Water. *RSC Adv.* **2018**, *8*, 10746–10755.

(190) Hu, D.; Kluger, R. Efficient Generation of Dendritic Arrays of Cross-Linked Hemoglobin: Symmetry and Redundancy. *Org. Biomol. Chem.* **2008**, *6*, 151–156.

(191) Eubank, J. F.; Nouar, F.; Luebke, R.; Cairns, A. J.; Wojtas, L.; Alkordi, M.; Bousquet, T.; Hight, M. R.; Eckert, J.; Embs, J. P.et al. On Demand: The Singular rht Net, an Ideal Blueprint for the Construction of a Metal–Organic Framework (MOF) Platform. *Angew. Chem. Int. Ed.* **2012**, *51*, 10099–10103.

(192) Zhang, S.; Ma, J.; Zhang, X.; Duan, E.; Cheng, P. Assembly of Metal–Organic Frameworks Based on 3,3′,5,5′-Azobenzene-tetracarboxylic Acid: Photoluminescences, Magnetic Properties, and Gas Separations. *Inorg. Chem.* **2015**, *54*, 586–595.

(193) Zou, Y.; Park, M.; Hong, S.; Lah, M. S. A Designed Metal–Organic Framework Based on a Metal–Organic Polyhedron. *Chem. Commun.* **2008**, 2340–2342.

(194) Wallar, B. J.; Lipscomb, J. D. Dioxygen Activation by Enzymes Containing Binuclear Non-Heme Iron Clusters. *Chem. Rev.* **1996**, *96*, 2625–2658.

(195) Banerjee, R.; Proshlyakov, Y.; Lipscomb, J. D.; Proshlyakov, D. A. Structure of the Key Species in the Enzymatic Oxidation of Methane to Methanol. *Nature* **2015**, *518*, 431–434.

(196) Castillo, R. G.; Banerjee, R.; Allpress, C. J.; Rohde, G. T.; Bill, E.; Que, L.; Lipscomb, J. D.; DeBeer, S. High-Energy-Resolution Fluorescence-Detected X-ray Absorption of the Q Intermediate of Soluble Methane Monooxygenase. *J. Am. Chem. Soc.* **2017**, *139*, 18024–18033.

(197) Murray, L. J.; Lippard, S. J. Substrate Trafficking and Dioxygen Activation in Bacterial Multicomponent Monooxygenases. *Acc. Chem. Res.* **2007**, *40*, 466–474.

(198) Wang, W.; Liang, A. D.; Lippard, S. J. Coupling Oxygen Consumption with Hydrocarbon Oxidation in Bacterial Multicomponent Monooxygenases. *Acc. Chem. Res.* **2015**, *48*, 2632–2639.

(199) Priestley, N. D.; Floss, H. G.; Froland, W. A.; Lipscomb, J. D.; Williams, P. G.; Morimoto, H. Cryptic Stereospecificity of Methane Monooxygenase. *J. Am. Chem. Soc.* **1992**, *114*, 7561–7562.

(200) Brazeau, B. J.; Wallar, B. J.; Lipscomb, J. D. Unmasking of Deuterium Kinetic Isotope Effects on the Methane Monooxygenase Compound Q Reaction by Site-Directed Mutagenesis of Component B. *J. Am. Chem. Soc.* **2001**, *123*, 10421–10422.

(201) Ambundo, E. A.; Friesner, R. A.; Lippard, S. J. Reactions of Methane Monooxygenase Intermediate Q with Derivatized Methanes. *J. Am. Chem. Soc.* **2002**, *124*, 8770–8771.

(202) Rataj, M. J.; Kauth, J. E.; Donnelly, M. I. Oxidation of Deuterated Compounds by High Specific Activity Methane Monooxygenase from Methylosinus Trichosporium. Mechanistic Implications. *J. Biol. Chem.* **1991**, *266*, 18684–18690.

(203) Liu, K. E.; Johnson, C. C.; Newcomb, M.; Lippard, S. J. Radical Clock Substrate Probes and Kinetic Isotope Effect Studies of the Hydroxylation of Hydrocarbons by Methane Monooxygenase. *J. Am. Chem. Soc.* **1993**, *115*, 939–947.

(204) Meunier, B.; de Visser, S. P.; Shaik, S. Mechanism of Oxidation Reactions Catalyzed by Cytochrome P450 Enzymes. *Chem. Rev.* **2004**, *104*, 3947–3980.

(205) Montellano, P. R. O. d. *Cytochrome P450: Structure, Mechanism, and Biochemistry*; Plenum Publishers: New York, 2005.

(206) Rittle, J.; Green, M. T. Cytochrome P450 Compound I: Capture, Characterization, and C–H Bond Activation Kinetics. *Science* **2010**, *330*, 933–937.

(207) Rohde, J.-U.; In, J.-H.; Lim, M. H.; Brennessel, W. W.; Bukowski, M. R.; Stubna, A.; Münck, E.; Nam, W.; Que, L. Crystallographic and Spectroscopic Characterization of a Nonheme Fe(IV)=O Complex. *Science* **2003**, *299*, 1037–1039.

(208) Pestovsky, O.; Bakac, A. Reactivity of Aqueous Fe(IV) in Hydride and Hydrogen Atom Transfer Reactions. *J. Am. Chem. Soc.* **2004**, *126*, 13757–13764.

(209) Puri, M.; Que, L. Toward the Synthesis of More Reactive S = 2 Non-Heme Oxoiron(IV) Complexes. *Acc. Chem. Res.* **2015**, *48*, 2443–2452.

(210) Pap, J. S.; DeBeer George, S.; Berry, J. F. Delocalized Metal–Metal and Metal–Ligand Multiple Bonding in a Linear Ru·Ru·N Unit: Elongation of a Traditionally Short Ru·N Bond. *Angew. Chem. Int. Ed.* **2008**, *47*, 10102–10105.

(211) Musch Long, A. K.; Yu, R. P.; Timmer, G. H.; Berry, J. F. Aryl C−H Bond Amination by an Electrophilic Diruthenium Nitride. *J. Am. Chem. Soc.* **2010**, *132*, 12228–12230.

(212) Long, A. K. M.; Timmer, G. H.; Pap, J. S.; Snyder, J. L.; Yu, R. P.; Berry, J. F. Aryl C–H Amination by Diruthenium Nitrides in the Solid State and in Solution at Room Temperature: Experimental and Computational Study of the Reaction Mechanism. *J. Am. Chem. Soc.* **2011**, *133*, 13138–13150.

(213) Xiao, D. J.; Bloch, E. D.; Mason, J. A.; Queen, W. L.; Hudson, M. R.; Planas, N.; Borycz, J.; Dzubak, A. L.; Verma, P.; Lee, K.et al. Oxidation of ethane to ethanol by N2O in a metal–organic framework with coordinatively unsaturated iron(II) sites. *Nat. Chem.* **2014**, *6*, 590–595.

(214) Zhang, T.; Manna, K.; Lin, W. Metal–Organic Frameworks Stabilize Solution-Inaccessible Cobalt Catalysts for Highly Efficient Broad-Scope Organic Transformations. *J. Am. Chem. Soc.* **2016**, *138*, 3241–3249.

(215) Thacker, N. C.; Lin, Z.; Zhang, T.; Gilhula, J. C.; Abney, C. W.; Lin, W. Robust and Porous β-Diketiminate-Functionalized Metal–Organic Frameworks for Earth-Abundant-Metal-Catalyzed C–H Amination and Hydrogenation. *J. Am. Chem. Soc.* **2016**, *138*, 3501–3509.

(216) Wang, L.; Agnew, D. W.; Yu, X.; Figueroa, J. S.; Cohen, S. M. A Metal–Organic Framework with Exceptional Activity for C−H Bond Amination. *Angew. Chem. Int. Ed.* **2018**, *57*, 511–515.

(217) Song, F.; Wang, C.; Falkowski, J. M.; Ma, L.; Lin, W. Isoreticular Chiral Metal−Organic Frameworks for Asymmetric Alkene Epoxidation: Tuning Catalytic Activity by Controlling Framework Catenation and Varying Open Channel Sizes. *J. Am. Chem. Soc.* **2010**, *132*, 15390–15398.

(218) Wang, C.; Lin, W. Diffusion-Controlled Luminescence Quenching in Metal−Organic Frameworks. *J. Am. Chem. Soc.* **2011**, *133*, 4232–4235.

(219) Cardenal, A. D.; Jeong Park, H.; Chalker, C. J.; Ortiz, K. G.; Powers, D. C. cis-Decalin Oxidation as a Stereochemical Probe of in-MOF versus on-MOF Catalysis. *Chem. Commun.* **2017**, *53*, 7377–7380.

(220) Timmer, G. H.; Berry, J. F. Electrophilic aryl C–H Amination by Dimetal Nitrides: Correlating Electronic Structure with Reactivity. *Chem. Sci.* **2012**, *3*, 3038–3052.

(221) Zhang, T.; Song, F.; Lin, W. Blocking Bimolecular Activation Pathways Leads to Different Regioselectivity in Metal–Organic Framework Catalysis. *Chem. Commun.* **2012**, *48*, 8766–8768.

(222) Anderson, J. S.; Gallagher, A. T.; Mason, J. A.; Harris, T. D. A Five-Coordinate Heme Dioxygen Adduct Isolated within a Metal–Organic Framework. *J. Am. Chem. Soc.* **2014**, *136*, 16489–16492.

(223) Gallagher, A. T.; Kelty, M. L.; Park, J. G.; Anderson, J. S.; Mason, J. A.; Walsh, J. P. S.; Collins, S. L.; Harris, T. D. Dioxygen Binding at a Four-Coordinate

Cobaltous Porphyrin Site in a Metal–Organic Framework: Structural, EPR, and O_2 Adsorption Analysis. *Inorg. Chem. Front.* **2016**, *3*, 536–540.

(224) Man, W.-L.; Tang, T.-M.; Wong, T.-W.; Lau, T.-C.; Peng, S.-M.; Wong, W.-T. Highly Electrophilic (Salen)ruthenium(VI) Nitrido Complexes. *J. Am. Chem. Soc.* **2004**, *126*, 478–479.

(225) Kozachuk, O.; Yusenko, K.; Noei, H.; Wang, Y.; Walleck, S.; Glaser, T.; Fischer, R. A. Solvothermal Growth of a Ruthenium Metal–Organic Framework Featuring HKUST-1 Structure Type as Thin Films on Oxide Surfaces. *Chem. Commun.* **2011**, *47*, 8509–8511.

(226) Zhang, W.; Kozachuk, O.; Medishetty, R.; Schneemann, A.; Wagner, R.; Khaletskaya, K.; Epp, K.; Fischer, R. A. Controlled SBU Approaches to Isoreticular Metal-Organic Framework Ruthenium-Analogues of HKUST-1. *Eur. J. Inorg. Chem.* **2015**, *2015*, 3913–3920.

(227) Peterson, V. K.; Southon, P. D.; Halder, G. J.; Price, D. J.; Bevitt, J. J.; Kepert, C. J. Guest Adsorption in the Nanoporous Metal–Organic Framework Cu_3(1,3,5-Benzenetricarboxylate)$_2$: Combined *In Situ* X-ray Diffraction and Vapor Sorption. *Chem. Mater.* **2014**, *26*, 4712–4723.

(228) Goel, S.; Wu, Z.; Zones, S. I.; Iglesia, E. Synthesis and Catalytic Properties of Metal Clusters Encapsulated within Small-Pore (SOD, GIS, ANA) Zeolites. *J. Am. Chem. Soc.* **2012**, *134*, 17688–17695.

(229) Luo, Y. R. *Comprehensive Handbook of Chemical Bond Energies*; CRC Press: Boca Raton, FL, 2007.

(230) Liu, B.; Yin, P.; Yi; Gao, S.; Zheng, L.-M. Template- and pH-Directed Assembly of Diruthenium Diphosphonates with Different Topologies and Oxidation States. *Inorg. Chem.* **2006**, *45*, 4205–4213.

(231) Blanksby, S. J.; Ellison, G. B. Bond Dissociation Energies of Organic Molecules. *Acc. Chem. Res.* **2003**, *36*, 255–263.

(232) Tian, Z.; Fattahi, A.; Lis, L.; Kass, S. R. Cycloalkane and Cycloalkene C−H Bond Dissociation Energies. *J. Am. Chem. Soc.* **2006**, *128*, 17087–17092.

(233) Bell, R. P. *The Tunnel Effect in Chemistry*; Chapman and Hall: New York, 1980.

(234) Pangborn, A. B.; Giardello, M. A.; Grubbs, R. H.; Rosen, R. K.; Timmers, F. J. Safe and Convenient Procedure for Solvent Purification. *Organometallics* **1996**, *15*, 1518–1520.

(235) Bain, G. A.; Berry, J. F. Diamagnetic Corrections and Pascal's Constants. *J. Chem. Educ.* **2008**, *85*, 532.

(236) Mitchell, R. W.; Spencer, A.; Wilkinson, G. Carboxylato-Triphenylphosphine Complexes of Ruthenium, Cationic Triphenylphosphine Complexes Derived from Them, and Their Behaviour as Homogeneous Hydrogenation Catalysts for Alkenes. *J. Chem. Soc., Dalton Trans.* **1973**, DOI:10.1039/DT9730000846 10.1039/DT9730000846, 846–854.

(237) Lindsay, A. J.; Wilkinson, G.; Motevalli, M.; Hursthouse, M. B. The Synthesis, Magnetic, Electrochemical, and Spectroscopic Properties of Diruthenium(II,II) tetra-μ-Carboxylates and Their Adducts. X-Ray Structures of $Ru_2(O_2CR)_4L_2$ (R =

Me, L = H_2O or Tetrahydrofuran; R = Et, L = Me_2CO). . *J. Chem. Soc., Dalton Trans.* **1985**, DOI:10.1039/DT9850002321 10.1039/DT9850002321, 2321–2326.

(238) Zhang, W.; Freitag, K.; Wannapaiboon, S.; Schneider, C.; Epp, K.; Kieslich, G.; Fischer, R. A. Elaboration of a Highly Porous $Ru^{II,II}$ Analogue of HKUST-1. *Inorg. Chem.* **2016**, *55*, 12492–12495.

(239) Furukawa, S.; Kitagawa, S. Neutral Paddlewheel Diruthenium Complexes with Tetracarboxylates of Large π-Conjugated Substituents: Facile One-Pot Synthesis, Crystal Structures, and Electrochemical Studies. *Inorg. Chem.* **2004**, *43*, 6464–6472.

(240) Chisholm, M. H.; Christou, G.; Folting, K.; Huffman, J. C.; James, C. A.; Samuels, J. A.; Wesemann, J. L.; Woodruff, W. H. Solution Studies of $Ru_2(O_2CR)_4^{n+}$ Complexes (*n* = 0, 1; O2CR = Octanoate, Crotonate, Dimethylacrylate, Benzoate, *p*-Toluate) and Solid-State Structures of $Ru_2(O_2C$-*p*-tolyl$)_4(THF)_2$, $[Ru_2(O_2C$-*p*-tolyl$)_4(THF)_2]^+[BF4]^-$, and $Ru_2(O_2C$-*p*-tolyl$)_4(CH_3CN)_2$: Investigations of the Axial Ligation of the Ru_2 Core. *Inorg. Chem.* **1996**, *35*, 3643–3658.

(241) Blangetti, M.; Fleming, P.; O'Shea, D. F. Homo- and Hetero-oxidative Coupling of Benzyl Anions. *J. Org. Chem.* **2012**, *77*, 2870–2877.

(242) Wesener, J. R.; Günther, H. Deuterium-Induced Perturbation of Hyperconjugation ? - A Carbon-13 NMR Study. *Tetrahedron Lett.* **1982**, *23*, 2845–2848.

(243) Benkovic, S. J.; Hammes-Schiffer, S. A Perspective on Enzyme Catalysis. *Science* **2003**, *301*, 1196–1202.

(244) Ortiz de Montellano, P. R. Hydrocarbon Hydroxylation by Cytochrome P450 Enzymes. *Chem. Rev.* **2010**, *110*, 932–948.

(245) Huang, X.; Groves, J. T. Oxygen Activation and Radical Transformations in Heme Proteins and Metalloporphyrins. *Chem. Rev.* **2018**, *118*, 2491–2553.

(246) Northrop, D. B. In *Methods Enzymol.*; Purich, D. L., Ed.; Academic Press, 1982; Vol. 87.

(247) Kim, Y.; Kreevoy, M. M. The Experimental Manifestations of Corner-Cutting Tunneling. *J. Am. Chem. Soc.* **1992**, *114*, 7116–7123.

(248) Klinman, J. P.; Offenbacher, A. R. Understanding Biological Hydrogen Transfer Through the Lens of Temperature Dependent Kinetic Isotope Effects. *Acc. Chem. Res.* **2018**, *51*, 1966–1974.

(249) Lee, J.; Farha, O. K.; Roberts, J.; Scheidt, K. A.; Nguyen, S. T.; Hupp, J. T. Metal–Organic Framework Materials as Catalysts. *Chem. Soc. Rev.* **2009**, *38*, 1450–1459.

(250) Gu, Z.-Y.; Park, J.; Raiff, A.; Wei, Z.; Zhou, H.-C. Metal–Organic Frameworks as Biomimetic Catalysts. *ChemCatChem* **2014**, *6*, 67–75.

(251) Nath, I.; Chakraborty, J.; Verpoort, F. Metal Organic Frameworks Mimicking Natural Enzymes: a Structural and Functional Analogy. *Chem. Soc. Rev.* **2016**, *45*, 4127–4170.

(252) Rogge, S. M. J.; Bavykina, A.; Hajek, J.; Garcia, H.; Olivos-Suarez, A. I.; Sepúlveda-Escribano, A.; Vimont, A.; Clet, G.; Bazin, P.; Kapteijn, F.et al. Metal–Organic and Covalent Organic Frameworks as Single-Site Catalysts. *Chem. Soc. Rev.* **2017**, *46*, 3134–3184.

(253) Yang, D.; Gates, B. C. Catalysis by Metal Organic Frameworks: Perspective and Suggestions for Future Research. *ACS Catal.* **2019**, *9*, 1779–1798.

(254) Pascanu, V.; González Miera, G.; Inge, A. K.; Martín-Matute, B. Metal–Organic Frameworks as Catalysts for Organic Synthesis: A Critical Perspective. *J. Am. Chem. Soc.* **2019**, *141*, 7223–7234.

(255) Marx, S.; Kleist, W.; Baiker, A. Synthesis, Structural Properties, and Catalytic Behavior of Cu-BTC and Mixed-Linker Cu-BTC-PyDC in the Oxidation of Benzene Derivatives. *J. Catal.* **2011**, *281*, 76–87.

(256) Fang, Z.; Dürholt, J. P.; Kauer, M.; Zhang, W.; Lochenie, C.; Jee, B.; Albada, B.; Metzler-Nolte, N.; Pöppl, A.; Weber, B.et al. Structural Complexity in Metal–Organic Frameworks: Simultaneous Modification of Open Metal Sites and Hierarchical Porosity by Systematic Doping with Defective Linkers. *J. Am. Chem. Soc.* **2014**, *136*, 9627–9636.

(257) Kozachuk, O.; Luz, I.; Llabrés i Xamena, F. X.; Noei, H.; Kauer, M.; Albada, H. B.; Bloch, E. D.; Marler, B.; Wang, Y.; Muhler, M.et al. Multifunctional, Defect-Engineered Metal–Organic Frameworks with Ruthenium Centers: Sorption and Catalytic Properties. *Angew. Chem. Int. Ed.* **2014**, *53*, 7058–7062.

(258) Li, Y.; Miao, J.; Sun, X.; Xiao, J.; Li, Y.; Wang, H.; Xia, Q.; Li, Z. Mechanochemical Synthesis of Cu-BTC@GO with Enhanced Water Stability and Toluene Adsorption Capacity. *Chem. Eng. J.* **2016**, *298*, 191–197.

(259) Simmons, E. M.; Hartwig, J. F. On the Interpretation of Deuterium Kinetic Isotope Effects in C–H Bond Functionalizations by Transition-Metal Complexes. *Angew. Chem. Int. Ed.* **2012**, *51*, 3066–3072.

(260) Dubkov, K. A.; Sobolev, V. I.; Talsi, E. P.; Rodkin, M. A.; Watkins, N. H.; Shteinman, A. A.; Panov, G. I. Kinetic Isotope Effects and Mechanism of Biomimetic Oxidation of Methane and Benzene on FeZSM-5 Zeolite. *J. Mol. Catal. A: Chem.* **1997**, *123*, 155–161.

(261) Ribeiro, G.; Vichi, F. M.; de Oliveira Silva, D. Synthesis, Characterization and Adsorption Properties of Porous Mixed Valent Diruthenium(II,III)-Terephthalate and Diruthenium(II,III)-Adipate Polymers. *J. Mol. Struct.* **2008**, *890*, 209–214.

(262) Takamizawa, S.; Yamaguchi, K.; Mori, W. The Gas-Occlusion Properties of Dicarboxylate (Fumarate, trans-trans-Muconate and Terephthalate) Ruthenium(II,III) Dinuclear Complexes. *Inorg. Chem. Commun.* **1998**, *1*, 177–178.

(263) Kato, C. N.; Ono, M.; Hino, T.; Ohmura, T.; Mori, W. Room Temperature Oxidation of Alcohols with 1atm Dioxygen and Air Catalyzed by a Novel Three-Dimensional Microporous Ruthenium(II,III) 4,4′,4″,4‴-(21H,23H-Porphine-5,10,15,20-Tetrayl)tetrakisbenzoate Tetrafluoroborate. *Catal. Commun.* **2006**, *7*, 673–677.

(264) Miyazaki, Y.; Kataoka, Y.; Mori, W. Nitrogen and Hydrogen Gas Adsorption Properties of Microporous Ruthenium Coordination Polymers. *Trans. Mater. Res. Soc. Japan* **2010**, *35*, 665–667.

(265) Mori, W.; Takamizawa, S. Microporous Materials of Metal Carboxylates. *J. Solid State Chem.* **2000**, *152*, 120–129.

(266) Kataoka, Y.; Sato, K.; Miyazaki, Y.; Masuda, K.; Tanaka, H.; Naito, S.; Mori, W. Photocatalytic Hydrogen Production from Water Using Porous Material $[Ru_2(p\text{-}BDC)_2]_n$. *Energy Environ. Sci.* **2009**, *2*, 397–400.

(267) Gao, W.-Y.; Ezazi, A. A.; Wang, C.-H.; Moon, J.; Abney, C.; Wright, J.; Powers, D. C. Metallopolymerization as a Strategy to Translate Ligand-Modulated Chemoselectivity to Porous Catalysts. *Organometallics* **2019**, *38*, 3436–3443.

(268) Slaughter, L. M.; Wolczanski, P. T.; Klinckman, T. R.; Cundari, T. R. Inter- and Intramolecular Experimental and Calculated Equilibrium Isotope Effects for $(silox)_2(tBu_3SiND)TiR + RH$ ($silox = tBu_3SiO$): Inferred Kinetic Isotope Effects for RH/D Addition to Transient $(silox)_2TiNSitBu_3$. *J. Am. Chem. Soc.* **2000**, *122*, 7953–7975.

(269) Jonsson, T.; Glickman, M. H.; Sun, S.; Klinman, J. P. Experimental Evidence for Extensive Tunneling of Hydrogen in the Lipoxygenase Reaction: Implications for Enzyme Catalysis. *J. Am. Chem. Soc.* **1996**, *118*, 10319–10320.

(270) Crossetti, G. L.; Dias, M. L.; Queiroz, B. T.; Silva, L. P.; Ziglio, C. M.; Bomfim, J. A. S.; Filgueiras, C. A. L. Ethylene Polymerization with Imine and Phosphine Nickel Complexes Containing Isothiocyanate. *Appl. Organomet. Chem.* **2004**, *18*, 331–336.

(271) Peralta, D.; Barthelet, K.; Pérez-Pellitero, J.; Chizallet, C.; Chaplais, G.; Simon-Masseron, A.; Pirngruber, G. D. Adsorption and Separation of Xylene Isomers: CPO-27-Ni vs HKUST-1 vs NaY. *J. Phys. Chem. C* **2012**, *116*, 21844–21855.

(272) Zhang, W.; Kauer, M.; Halbherr, O.; Epp, K.; Guo, P.; Gonzalez, M. I.; Xiao, D. J.; Wiktor, C.; LIabrés i Xamena, F. X.; Wöll, C.et al. Ruthenium Metal–Organic Frameworks with Different Defect Types: Influence on Porosity, Sorption, and Catalytic Properties. *A. Chem. Eur. J.* **2016**, *22*, 14297–14307.

(273) Agirrezabal-Telleria, I.; Luz, I.; Ortuño, M. A.; Oregui-Bengoechea, M.; Gandarias, I.; López, N.; Lail, M. A.; Soukri, M. Gas Reactions under Intrapore Condensation Regime within Tailored Metal–Organic Framework Catalysts. *Nat. Commun.* **2019**, *10*, 2076.

(274) Barrett, E. P.; Joyner, L. G.; Halenda, P. P. The Determination of Pore Volume and Area Distributions in Porous Substances. I. Computations from Nitrogen Isotherms. *J. Am. Chem. Soc.* **1951**, *73*, 373–380.

(275) Kruk, M.; Jaroniec, M.; Sayari, A. Application of Large Pore MCM-41 Molecular Sieves To Improve Pore Size Analysis Using Nitrogen Adsorption Measurements. *Langmuir* **1997**, *13*, 6267–6273.

(276) Krüger, T.; Vorndran, K.; Linker, T. Regioselective Arene Functionalization: Simple Substitution of Carboxylate by Alkyl Groups. *Chem. Eur. J.* **2009**, *15*, 12082–12091.

(277) Zhu, H.; Meyer, M. P. Cationic Intermediates in Friedel–Crafts Acylation: Structural Information from Theory and Experiment. *Chem. Commun.* **2011**, *47*, 409–411.